Laser-induced surface texturing of electrodes for obtaining hydrophobic surfaces in electrochemical ammonia synthesis

Master of Science in Technology Thesis

Mechanical Engineering

Digital Manufacturing

Department of Mechanical and Materials Engineering

Author:

Eter Tourunen B. Sc.

11.12.2025

Turku

The originality of this thesis has been checked in accordance with the University of Turku quality assurance system using the Turnitin Originality Check service.

Master's thesis

Subject: Mechanical Engineering
Author: Eter Tourunen
Title: Laser-induced surface texturing of electrodes for obtaining hydrophobic surfaces in electrochemical ammonia synthesis
Supervisor: Senior researcher Heidi Piili, D.Sc. (Tech.)
Advisor: Postdoctoral researcher Georgy Givirovskiy D.Sc. (Tech.), Postdoctoral Nikhil Kambol D.Sc. (Tech)
Number of pages: 166 pages
Date: 11.12.2025

Hydrophobicity and coating adhesion are critical surface properties in electrochemical applications, where stainless steel electrodes are often used as structural substrates. Conventional stainless steel surfaces are naturally hydrophilic due to their oxide layer, which limits their suitability without additional modification. Laser surface texturing has emerged as a potential method to improve these properties by creating controlled micro- and nanostructures.

The aim of this thesis was to examine whether a 100 W nanosecond fibre laser can be applied to generate hydrophobic surface features and enhance the adhesion of cobalt hydroxide coatings on stainless steel. The experimental design focused on two texture geometries (line and grid patterns) produced at two fluence levels (35 J/mm² and 141 J/mm²), allowing systematic evaluation of the effects of processing parameters.

The stainless steel specimens were characterised using a combination of macro imaging, scanning electron microscopy analysis, 3D surface topography and areal roughness measurements. Functional performance was assessed through static contact angle measurements and with tape adhesion tests. Cobalt hydroxide coatings were deposited to investigate coating distribution and interfacial stability on both laser-treated and untreated reference surfaces.

Results demonstrated that laser texturing significantly altered surface morphology and wettability. The untreated reference surface was hydrophilic, with a contact angle of 82°, whereas laser-treated surfaces achieved contact angles up to 135° (grid pattern, 35 J/mm²). Line patterns produced anisotropic wetting, with orientation-dependent differences up to 32 %, while grid patterns resulted in isotropic wetting. However, after coating deposition, hydrophobicity was strongly diminished or entirely lost, with the G2 surface showing superhydrophilicity. Roughness analyses confirmed that grid textures produced the most pronounced features (*Sa* up to 16.4 µm, *Sz* up to 124 µm), but excessive remelting at higher fluence reduced their effectiveness. Adhesion testing revealed that line textures provided enhanced coating stability (grades 2–3), while grid textures performed poorly, with G2 showing complete detachment (grade 0). SEM analyses further indicated that cobalt hydroxide deposition was less effective on laser-treated surfaces, likely due to oxide formation during processing, whereas the untreated reference surface showed more homogeneous and continuous coating coverage.

Future work should focus on optimising laser parameters to balance beneficial roughness with controlled oxide formation, as well as exploring combined surface treatments or alternative deposition strategies to achieve both strong hydrophobicity and reliable coating adhesion. These findings provide new insight into how laser-induced surface structures can be tailored for functional stainless steel electrodes, but also highlight the limitations of cobalt hydroxide deposition on laser-textured substrates.

Key words: laser surface texturing, nanosecond fibre laser, stainless steel, hydrophobicity, surface roughness, contact angle, coating adhesion, cobalt hydroxide deposition, surface morphology, electrode modification

Acknowledgements

I would like to begin by expressing my gratitude to the University of Turku and the Department of Mechanical Engineering for providing me the opportunity to work in an academic environment and contribute to scientific research. This thesis was carried out as part of the Green-AM project, with the aim of producing new insights related to sustainable development.

My deepest thanks go to Docent Heidi Piili, who served as my supervisor. She has been both a mentor and a source of constant support throughout the thesis process and beyond. Her trust, guidance, and encouragement have allowed me the freedom and resources to explore my ideas and grow as a researcher. I would also like to express my sincere gratitude to Nikhil Kamboj, who acted as the second advisor of this thesis and provided valuable insights, constructive feedback, and encouragement throughout the work.

I also wish to thank Georgy Givirovskiy and Daria Givirovskaia from LUT University for their valuable help in the design, evaluation, and coating of the specimens. In addition, I am grateful to the many people from the Departments of Physics, Chemistry, and Mechanical Engineering who have supported this work in different ways. Special thanks to Sari, Ermei, Mikko, Antti, Erno, and everyone else who contributed their expertise and time.

Warm thanks also go to my former colleague Inka Väisänen, who acted as both an experienced advisor and an unofficial co-supervisor during this journey.

Finally, I want to thank my family and loved ones. Thank you, Mom and Dad, for raising me to be persistent and a little creatively crazy. And to my beloved partner Anton – your unwavering support throughout this thesis and my studies has meant everything. I could not have done this without you. On to the next adventure!

Table of contents

Nomenclature

Abbreviation	Explanation
AFM	Atomic force microscopy
AM	Additive manufacturing
CVD	Chemical vapor deposition
EAS	Electrochemical ammonia synthesis
EDS	Energy dispersive X-ray spectroscopy
ePTFE	Expanded polytetrafluoroethylene
ETD	Everhart-Thornley detector
FCC	Face-centerer cubic
FE	Faradaic efficiency
FE-SEM	Field-emission scanning electron microscope
FEG	Field emission gun
FIB-SEM	Focused ion beam scanning electron microscopy
GDL	Gas diffusion layer
HER	Hydrogen evolution reaction
LaSAT	Laser shock adhesion test
LIPSS	Laser-induced periodic surface structures
NRR	Nitrogen reduction reaction
OER	Oxygen evolution reaction
PDMS	Microfabricated silicon polymer, polydimethylsiloxane
PEM	Polymer exchange membrane
PFTEOS	Modified epoxy coating with fluorinated silanes
PMMA	Poly(methyl methacrylate)
PTFE	Fluoridated polymer, polytetrafluoroethylene
SE/BSE	Secondary electrons and backscattered electrons
SEM	Scanning electron microscopy
STEM	Scanning transmission electron
T1	High-angle backscattered electron detector
T3	Secondary electron detector
UV-Vis	Ultraviolet-visible spectroscopy
XPS	X-ray photoelectron spectroscopy

Symbol	Unit	Explanation
α	^{o}	Tilting angle
A	mm^2	Laser beam cross-section area

a	m	Droplet radius
F	J/mm^2	Laser fluence
f	-	Fraction of the wet solid contact angle
g	m/s^2	Gravitational acceleration
H	º	Hysteresis
k	-	Geometric factor
m	kg	Mass
P	W	Laser power
r	µm	Roughness coefficient
Ra	µm	Arithmetic average roughness (linear)
Rz	µm	Mean peak-to-valley height (linear)
Sa	µm	Arithmetic average roughness (areal)
Sz	µm	Mean peak-to-valley height (areal)
τ	N	Line tension
t	s	Pulse length
θ	º	Contact angle
γ	N/m	Interfacial tension
ω	m	Width of the contact area of the droplet

1 Introduction

The urgent need to reduce greenhouse gas emissions and decouple chemical production from fossil resources has intensified the search for more sustainable alternatives. Among emerging solutions, Power-to-X technologies offers a promising route by enabling the conversion of renewable electricity into chemical energy carriers such as hydrogen (H_2), ammonia (NH_3) and synthetic fuels. In general, Power-to-X refers to processes that convert electrical energy into storable and transportable chemical forms. These approaches are central to future carbon-neutral energy systems and rely on advances in electrochemical process design. [1], [2], [3]

One key step of Power-to-X is H_2 production through water electrolysis; a process that uses electricity to split water into H_2 and oxygen (O_2). This process involves Hydrogen Evolution Reaction (HER) and Oxygen Evolution Reaction (OER), whose efficiency can be limited by sluggish reaction kinetics and overpotentials, making the design of active, stable, and conductive electrode materials crucial for overall performance [4]. Water electrolysis performance is critically dependent on the electrode and catalyst materials, whose surface characteristics influence reaction kinetics, overpotentials and the efficiency of HER at the cathode and OER at the anode [5], [6]. Accordingly, the design of efficient, selective, and stable electrode surfaces remains a major focus in electrochemical engineering. [7], [8]

Within this framework, Electrochemical Ammonia Synthesis (EAS) represents one possible Power-to-X pathway and has emerged as a potential alternative to the traditional Haber–Bosch process. EAS enables NH_3 production under ambient conditions using water and nitrogen (N_2) as feedstocks, powered by renewable electricity. [6] While attractive in principle, this method is still limited by low Faradaic efficiency (FE), poor selectivity for N_2 reduction compared to the competing HER – which is thermodynamically and kinetically more favourable – and instability of catalyst materials [9]. Addressing these limitations not only requires improvements in catalyst activity and stability but also careful optimization of the reaction interface. For this reason, precise control over the electrode surface – and particularly its ability to manage multiphase contact between gas, liquid, and solid phases– acts as a key factor in enabling efficient and selective NH_3 synthesis. [10]

Among the surface properties that govern these interfacial dynamics, wettability is one of the factors that may influence gas–liquid–solid interactions and thereby affect the overall efficiency of EAS [11]. In this thesis, wetting refers to the interfacial interaction between a liquid and a

solid surface, reflecting how easily liquid spreads or beads up on the surface. It is the surface property that encompasses both hydrophilic behaviours, where water spreads and wets the surface, and hydrophobic behaviour, where water minimizes contact by forming droplets with high contact angles. Surface wettability influences mass transport, interfacial reaction rates, bubble adhesion and access to catalytic sites. Surfaces with hydrophobic characteristics, for instance, can modulate the local gas–liquid interface in ways that potentially enhance the Nitrogen Reduction Reaction (NRR) – the cathodic half-reaction in EAS that converts N_2 to NH_3 – while suppressing competing reactions [11], [12], [13]

Surface modification techniques are required, to control and tailor such surface characteristics. Traditional methods, such as chemical etching or mechanical abrasion, often suffer from limited control, chemical waste and poor reproducibility [14], [15], [16]. In contrast, laser-based surface functionalization offers a highly controllable, clean and scalable solution for modifying surface morphology and chemistry. [17] In this thesis, laser surface functionalization refers to the use of laser irradiation to induce localized physical and chemical changes on surface of material, thereby modifying its interaction with surrounding media. More specifically, laser surface texturing involves the creation of micro- and nanostructures that influence surface energy, topography and wettability. [18], [19] The key advantage of laser processing lies in its non-contact nature and ability to fabricate fine features in a programmable and reproducible manner, without any chemical additives [20].

Beyond the technical motivation, there is also growing economic and scientific interest in this field. According to recent market studies, the global demand for advanced surface technologies, including laser-based techniques, is expected to grow in the coming years. [21] Additionally, a rising number of academic publications focusing on laser-induced wettability and surface functionalization, shows that this research area is rapidly expanding and well-aligned with current scientific priorities (as illustrated in Figure 1).

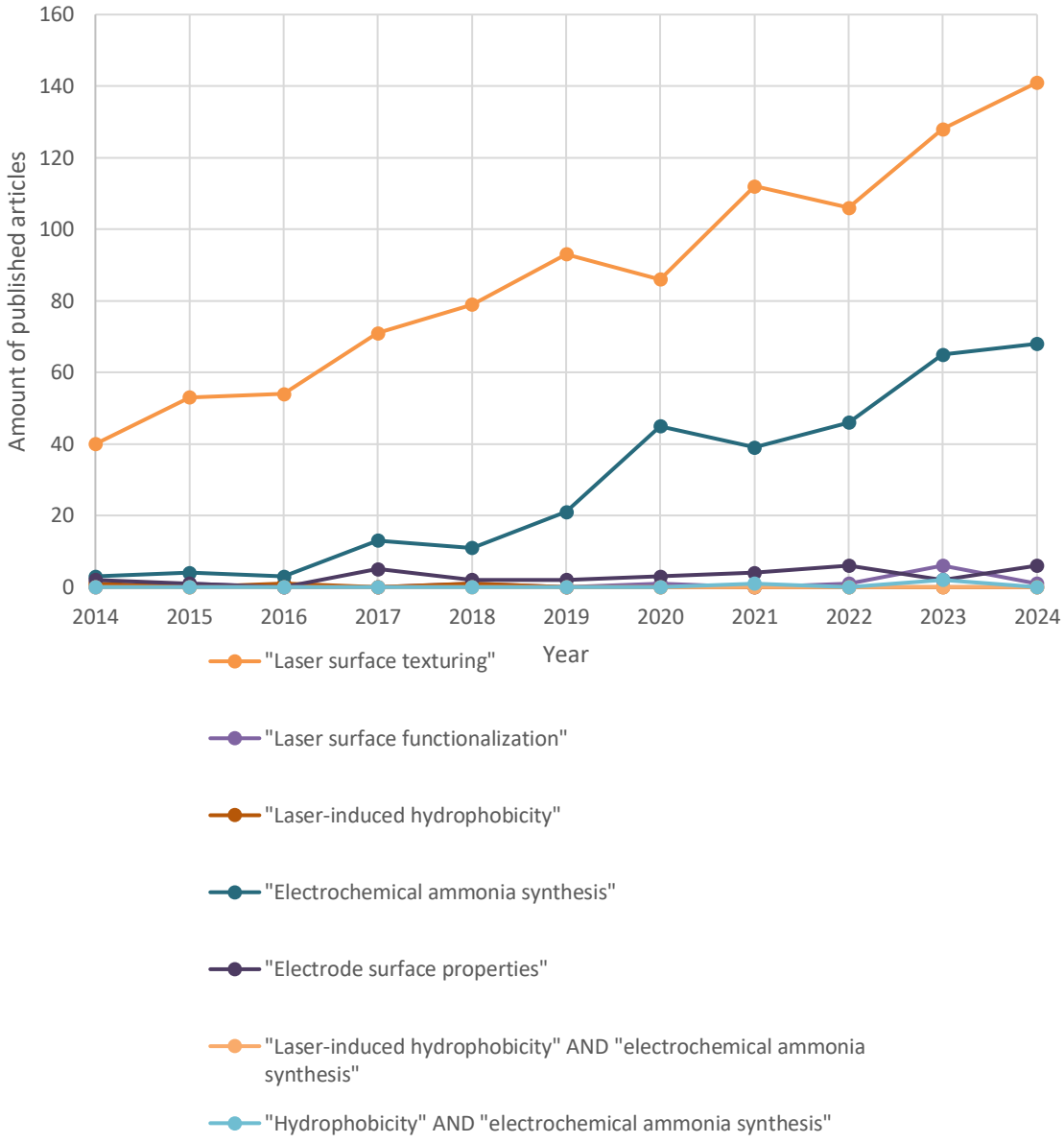

Figure 1 Yearly number of publications per topic based on Scopus search results using different keywords.

As shown in Figure 1, the number of publications using the keyword “Laser surface texturing” has increased proportionally over the past decade. In 2014, around 40 papers were published on this topic, whereas by 2024 the number had grown to approximately 140, resulting in an increase of over 250 %. This trend reflects continued and growing interest in laser-based surface engineering methods. According to publication data, the second most active area, is “Electrochemical ammonia synthesis”, which has shown particularly sharp growth since 2018. The annual number of publications rose from fewer than 10 in 2016 to over 60 in 2023 and up-to nearly 70 in 2024.

In contrast, search terms such as “Laser-induced hydrophobicity”, “Electrode surface properties”, and “Laser surface functionalization” have remained below 10–15 publications per year. Notably, combinations like “Laser-induced hydrophobicity” AND “electrochemical ammonia synthesis” or “Hydrophobicity” AND “electrochemical ammonia synthesis” have resulted in only 0–2 annual publications. This indicates that while both laser surface engineering and EAS are independently active research areas, their intersection, especially in the context of hydrophobic surface-texturing for electrode applications, remains still largely unexplored.

This thesis investigates whether such laser surface structuring can be used to tune the wettability of electrode materials for EAS. A 100 W pulsed nanosecond fibre laser is used to generate controlled surface textures on 316L stainless steel substrates. Stainless steel was chosen as the substrate due to its mechanical strength, corrosion resistance, and relevance in electrochemical device integration. The study examines how different laser surface texturing geometries influence surface hydrophobicity, and whether these surface features affect the adhesion of coating layers, which may be applied in further electrode functionalization.

Through this work, the feasibility of laser-induced electrode surface modification applications is evaluated. The following research questions are addressed:

1. *Can a nanosecond fibre laser be used to improve hydrophobic properties on stainless steel surfaces?*
2. *How do different surface texturing geometries affect the hydrophobicity of the surface of stainless steel electrodes?*
3. *Can laser surface texturing improve the adhesion of catalytic coatings to stainless steel electrodes?*

By answering these questions, this thesis aims to contribute to the development of scalable and sustainable electrode surface engineering strategies for next-generation electrochemical energy technologies.

This thesis was executed as part of project “Production of Green Ammonia by Electrochemical Reactors Realized with Additive Manufacturing (Green-AM)” which is funded by Research Council of Finland’s Proof of Concept Funding (decision number 365515). This project started 1.1.2025, and it will end 31.12.2026. Project partners are Research Group of Hydro-metallurgy for Urban Miningof School of Engineering Science at Lappeenranta-Lahti University of

Technology LUT and Research Group of Digital Manufacturing and Surface Engineering (DMS) of Mechanical Engineering in Faculty of Technology at University of Turku. The Green-AM project aims to develop a decentralized, sustainable ammonia (NH_3) production process using electrosynthesis powered by renewable energy, replacing the energy-intensive Haber-Bosch method. Its purpose is to support Finland's transition to carbon neutrality by enabling green NH_3-based fertilizers and energy carriers, fostering innovation, self-sufficiency, and clean energy access.

2 Surface functionality

2.1 Overview of surface functionality

Surface functionality is an emergent property of surface, based on materials surface structure and chemistry [22], [23]. This property enables different physical, chemical, biological or optical response in specific environments [24], [25], [26], [27]. Functionality can appear as passive or as active property by giving a respond to external stimulus [28]. Passive surface functionality implies to a surface where the functionality is always present, the property being independent of any external stimulus or changes in environmental conditions, and it is based on stable surface structure or chemistry. Passive surface functionalities are used, for example, in motor bearing, where hard coating and surface structure reduces friction and wear of the part. Active functionality implies to a surface property which can change or activate due to an external stimulus, such as light, heat, electricity, magnetic field or chemical environment. This active response is based on, for example, changes in material phases or ionic response. [29] These types of surfaces with active functional properties are often called smart materials and can be used in various applications, one example being smart glass, where the glass material responses to UV light [30], [31]. Table 1 shows the common surface functionalities, their key properties and example applications, compiled from [32], [33], [34], [35], [36], [37], [38], [39].

Table 1 Common surface functionalities, their key properties and applications [32], [33], [34], [35], [36], [37], [38], [39].

Surface functionality	Key properties	Applications	Reference
Water-repellent properties	Hydrophobicity, hydrophilicity	Self-cleaning surfaces, anti-fogging surfaces	[32]
Friction and wear control	Reduced coefficient of friction, enhanced wear resistance, surface hardness	Machinery parts, medical implants	[33]
Optical functionalities	Anti-reflectivity, photocatalytic surface, wavelength-selective absorption	Solar panels, air and water purification	[34]
Conductive properties	Electrical conductivity, thermal conductivity	Conductive polymers, insulators	[35]
Biological functionalities	Antimicrobial activity, bio-inertness, cell adhesion control	Surgical instruments, implants, biosensors	[36]
Adhesion properties	Tunable surface energy, enhanced bonding, anti-adhesive (non-stick) behavior	Coating adhesion, adhesives, release liners, non-stick cookware	[37]
Other liquid-repellent properties	Oleophobicity, lipophobicity, chemical resistance to oils and organic solvents	Anti-smudge coatings, protective screens, fluid barriers	[38]
Stimuli-responsive surfaces	Changes in properties under external stimuli (light, heat, electric/magnetic field)	Smart windows, sensors, actuators, tunable optical devices	[39]

As shown in Table 1, different surface functionalities are based on specific physical and chemical properties, such as hydrophobicity, electrical conductivity, wear durability or biological activity. These functional properties allow the application of surfaces in well-defined applications, such as medical implants, optical systems or mechanical components. [24], [25] Controlled implementation of these functionalities, for example, through micro- and nanostructures, surface chemistry or intelligent material responses, acts as a key factor in optimising material performance across industries.

Surface functionalities can be explained through four main factors: (1) chemical composition, (2) surface roughness, (3) topographical structure, and (4) external stimulus-responsiveness. All four factors are closely linked to the micro- and nanoscale, and to some extent, with its macroscale features, such as overall surface waviness, geometric form, or large-scale roughness variations. [25], [40]

The atomic-level composition of a surface directly influences its surface energy, interactions with surrounding substances, physical responses, and electrochemical activity. Functional groups, such as $–CH_3$, –OH, $–NH_2$, —CHO and –COOH, play a key role in determining surface wettability, adhesion, and biocompatibility (the material's ability to perform in a living system without triggering toxic, allergic, or harmful immune responses). [41] Chemical surface energy governs how the surface interacts with liquids and biological molecules, affecting phenomena such as spreading, adsorption, and protein binding. Additionally, reactive species, such as O_2 radicals, can modulate biological responses and are closely associated with material-induced toxicity [42]. Chemical coatings, including silanes and oxide layers, are used to tailor surface properties, particularly to enhance water repellence or to improve coating adhesion [37], [43]. Ding et al. (2020) [37] demonstrated that the application of a silane coupling agent enhanced the adhesion between asphalt and acidic granite aggregates by modifying the surface chemistry and forming a stable interfacial layer, thereby improving both the water repellence and bonding performance.

Microscopic roughness of a surface, has an impact on the behaviour of liquids and particles interacting with the surface, as well as on the optical and mechanical properties of the surface. High surface roughness can promote hydrophobicity, provided that the liquid cannot penetrate into the surface asperities, as described by the Cassie–Baxter model [41]. This model demonstrates the relation of contact angle (θ_R) on a rough surface to the equilibrium contact angle (θ) (the angle at the solid–liquid–vapor boundary when a droplet is at rest, reflecting the balance of interfacial tensions between the phases) on a smooth surface and the fraction of the liquid–solid contact angle (*f*), as below Equation 1 shows.

$$\cos\theta_R = -1 + f(1 + \cos\theta) \tag{1}$$

This model shows that increased surface porosity, with the value of *f* being low, causes a larger apparent contact angle, contributing to superhydrophobic behaviour. A classic example is the superhydrophobicity of the lotus leaf, which caused from a hierarchical microstructure composed of short and wide surface pillars [44]. Furthermore, controlled surface roughness plays an important role in tribological performance, as regular texture patterns can be engineered to optimize friction behaviour, lubricant retention, and load distribution in mechanical systems [45], [46], [47].

The geometric structure of a surface, including micro- and nanostructures, hierarchical architectures, and high aspect ratio features, can be engineered to elicit physical responses. In

particular, high aspect ratio structures, have been shown to reduce the degradation of biological components such as von Willebrand factor (a glycoprotein in the blood essential for the process of clot formation), underscoring the critical role of surface topography in modulating bifunctionality. [48] The modelling and fabrication of multiscale surface textures enable precise control over friction behaviour and lubricant dynamics in mechanically demanding or dynamic applications. A well-known example is the use of pyramidal surface textures in solar panels, which minimize light reflection and thereby enhance optical absorption efficiency. [49]

In addition to single-layered modifications, surface functionalities can also emerge from multi-layered architectures or from materials that exhibit responsiveness to external stimuli. With multilayer systems, each layer is tailored to fulfil a specific role, such as mechanical reinforcement, chemical interfacing, or active functional behaviour. [45] Furthermore, stimuli-responsive coatings, which for example react to light, temperature, or electric fields, can provide adaptive performance and dynamic tunability, as exemplified in technologies such as smart windows and sensing interfaces [31].

Functional surfaces can be fabricated using methods such as Chemical Vapor Deposition (CVD) (a high-temperature process in which gaseous precursors react to form a thin solid film directly on a substrate) [50], sol-gel processing (a wet-chemical method for producing high-purity ceramics or glasses by transforming a liquid precursor into a solid network through hydrolysis and condensation, followed by drying and heat treatment) [51] and photolithography (a technique that uses UV light, a photomask, and a photoresist to produce micrometre-scale patterns on substrates through steps such as spin coating, exposure, and development) [52]. These techniques enable control over surface energy and allow the creation of micro- and nanostructures that influence properties like wettability (a surface property describing how a liquid interacts with a solid surface) [53], adhesion a surface property describing the tendency of dissimilar materials or surfaces to stick to each other) [54], or corrosion resistance a material property that defines its ability to resist degradation caused by chemical reactions with the surrounding environment) [55]. Plasma etching (a microfabrication technique where reactive ionized gas (plasma) is directed onto a surface to remove material from thin films) [56] can generate hierarchical textures on metals or polymers, enhancing their functional behaviour. Functional surface structures can also be produced using additive manufacturing (AM), known also as industrial 3D printing, where the surface geometry is intentionally designed into a digital model. By adjusting parameters such as texture height, spacing, and orientation, it is possible to achieve surface functionalities, such as water repellence or guided fluid flow, directly during

the printing process. [57] Figure 2 shows AM surfaces with functional micropatterning [58], [59], [60].

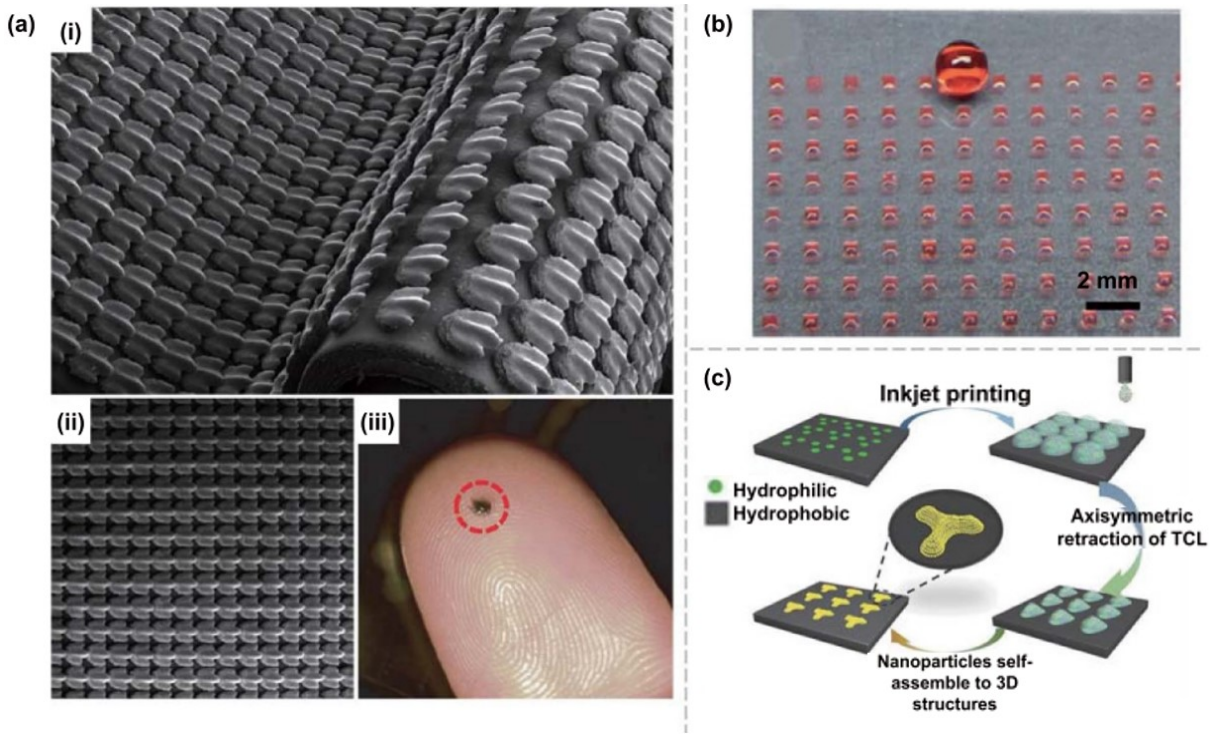

Figure 2 Examples of micropatterned AM surfaces for wettability control: (a) multi-jet printed shark skin structures, shown as membrane, pattern layout, and individual denticle; (b) inkjet-printed hydrophilic polydopamine squares on a hydrophobic substrate; and (c) patterned photonic crystals on a hydrophobic silicon wafer with hydrophilic micropatterns created by inkjet printing. Reproduced from [58], [59], [60] which are under an open access Creative Common CC BY licence.

As shown in Figure 2, panel (a) presents an AM microstructure surface inspired by biological textures, where precise control of the feature orientation and density enables the replication of complex natural designs for applications such as drag reduction and wear resistance. Panel (b) demonstrates the hydrophilic–hydrophobic contrast patterns that regulate droplet spreading and positioning, offering potential use in microfluidic devices and lab-on-chip systems. Panel (c) shows inkjet-printed nanoparticle assemblies that self-organize into three-dimensional structures, illustrating how additive manufacturing can be combined with nanoscale material control to create multifunctional surfaces for use in optical, biomedical, and anti-fouling applications. [58], [59], [60]

2.2 Hydrophobic surfaces

Hydrophobicity of surfaces is the ability of surface to repel water, which is a key functional feature in different natural and technical systems. This phenomenon is emerged from a high contact angle in the interface of liquid and solid materials, when water does not spread to the

surface, but creates a rounded droplet, as illustrated in Figure 3. Hydrophobicity is influenced by both the chemical properties of the surface and the physical structures of the surface, especially properties such as roughness, porosity and topography. Several theories have been developed to model this functional phenomenon, the most important beng the models of Young, Wenzel and Cassie-Baxter. These theorems describe the relation between liquid and surface, taking into account the physical and structural influencing factors, such as surface energy of interfaces and surface roughness. [13], [61], [62] Hydrophobicity can be also induced by chemical and external factors, such as light and thermal impact, which can influence the wetting properties of the surface.

Wettability of a surface can be evaluated by measuring the contact angle between the interface of a droplet of liquid and a solid plane, as illustrated in Figure 3 [63].

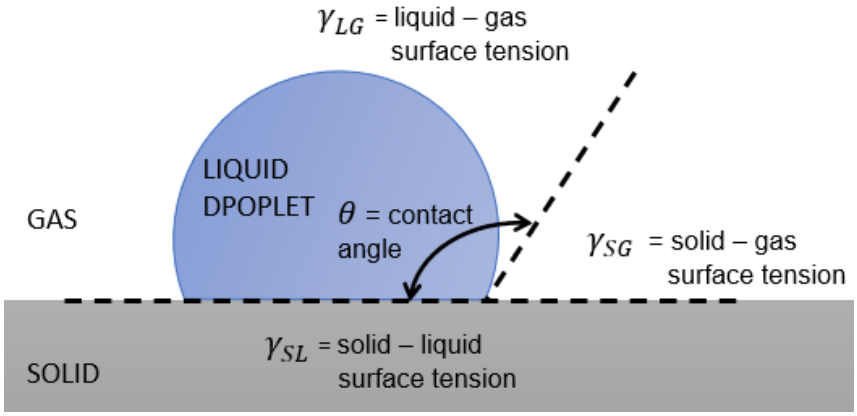

Figure 3 Contact angle between the interface of a liquid droplet and a solid plane. Reproduced from [63] which is under an open access Creative Common CC BY licence.

As shown above in Figure 3, a liquid droplet rests on a solid surface while being surrounded by a gas phase. The contact angle (θ) is formed at the point where the three phases (liquid, gas, and solid) meet. The image illustrates the interfacial tensions acting at this point: γ_{LG} representing the surface tension between the liquid and gas, γ_{SL} between the solid and liquid, and γ_{SG} between the solid and gas. [63]

The value of contact angle determines the wettability of a solid surface. The magnitude of the angle is determined by the balance between adhesive and cohesive forces acting between the surface and the liquid: the smaller the angle, the better the liquid wets the surface. [64], [65] Angles below 90° indicate good wettability, that is, a hydrophilic surface where the liquid spreads widely. Angles above 90°, on the other hand, indicates poor wettability, where the liquid forms a compact droplet and the surface is considered as hydrophobic. If the contact

angle exceeds 150°, the surface is classified as superhydrophobic. In this case, the liquid barely touches the surface and the droplet easily rolls off. The opposite of superhydrophobic behaviour is with a superhydrophilic surface, where the contact angle is less than 10°, often approaching 0°. On such surfaces, water spreads rapidly and evenly due to very strong adhesive forces. [12]

Young's equation (1805), shown in Equation 2, describes the relationship between the contact angle and a surface tension of droplets on ideal, smooth and homogenic surface.

$$\cos\theta_Y = \frac{\gamma_{SG}-\gamma_{SL}}{\gamma_{LG}} \tag{2}$$

where θ_Y is the contact angle by Young's model and γ_{SG}, γ_{SL} and γ_{LG} are surface energies of the solid-gas, solid-liquid and liquid-gas interfaces [61]. This model was later modified by Gibbs to take into account the volumetric dependence of the contact angle, as Equation 3 shows.

$$\cos\theta_Y = \frac{\gamma_{SG}-\gamma_{SL}}{\gamma_{LG}} + \frac{\tau}{\gamma_{LG}}\frac{1}{a} \tag{3}$$

where τ is the line tension and a is the droplet radius [66].

The Wenzel model (1936) accounts for the fact that solid surfaces are typically not ideally smooth, but exhibit surface roughness that influences wetting behaviour, as shown in Equation 4.

$$\cos\theta_R = r\cos\theta_Y \tag{4}$$

where r is roughness coefficient. According to the theory of Wenzel, surface roughness enhances the inherent wetting tendency of a material: hydrophilic surfaces show improved spreading of water, whereas hydrophobic surfaces exhibit increased resistance to wetting. [62]

The previously referred Cassie-Baxter model (1944) describes the relation of the contact angle on a rough surface to the equilibrium contact angle (see Equation 1). This model also describes situation, where liquid does not fill the unevenness of the surface, but partly floats by air on top of microstructures. This model is based on the distribution of the interfaces, as shown in Equation 5.

$$\cos\theta_{CB} = f_s\cos\theta_Y - f_a \tag{5}$$

where f_s is the proportion of the solids under the liquid and f_a is the air proportion. When $f_s + f_a = 1$, the equation described above reduces to the form of Equation 1. This equation shows, that the microstructures and porosity of the surfaces can increase the contact angle. [13]

In order for the surface to be hydrophobic, the surface needs to have appropriate topography, porosity and often a hieratic structure, meaning that the surface features must be dimensionally and spatially optimized to support water repellence, by minimizing contact with water and maximise air trapping. These structures combine micro- and nanoscale features that reduce the contact area between the liquid and the solid, allowing air to remain trapped beneath droplets and thereby promoting a Cassie–Baxter wetting state. [67], [68] Previous studies have shown that combining micro- and nanostructures into hierarchical entities can improve both the degree of water repellent and mechanical stability [69]. In such structures, water does not penetrate into the pores but instead rests on air pockets, which is referred to as the Cassie–Baxter state. By reducing the solid–liquid contact area, this state enables the droplet to maintain a high contact angle, resulting in superhydrophobic behaviour. [70] Long et al. (2016) [70] systematically investigated the stability of the Cassie–Baxter state on structured copper surfaces and found that although many surfaces display high contact angles and low sliding angles under ambient conditions. These properties deteriorate under condensation or external pressure if the surface lacks sufficient nanoscale texture. Their results indicate that hierarchical micro- and nanostructures, especially those with densely packed nanoscale features, enhance the stability of the Cassie–Baxter state even under low temperatures and during droplet evaporation, preventing transitions to the metastable. This structural stability facilitates robust water repellence, critical for applications such as anti-icing and sustained dropwise condensation. Moreover, their evaporation experiments demonstrated that only surfaces with dense hierarchical features could sustain spherical droplet geometry under increasing Laplace pressure, indicating persistent low adhesion and stable Cassie–Baxter state. Similar conclusions were drawn by Yoon et al. (2014) [69], who emphasized that natural and artificial surfaces with dual micro- and nanoscale roughness consistently yield superhydrophobic behaviour by trapping air beneath droplets, thereby reducing solid–liquid contact. Their review reinforced the idea that both topography and surface chemistry must be engineered in concert to achieve reliable non-wetting behaviour. The principle is illustrated in Figure 4, where scanning electron microscopy (SEM) images show the hierarchical morphology of a natural lotus leaf alongside an artificially fabricated PDMS surface. [69]

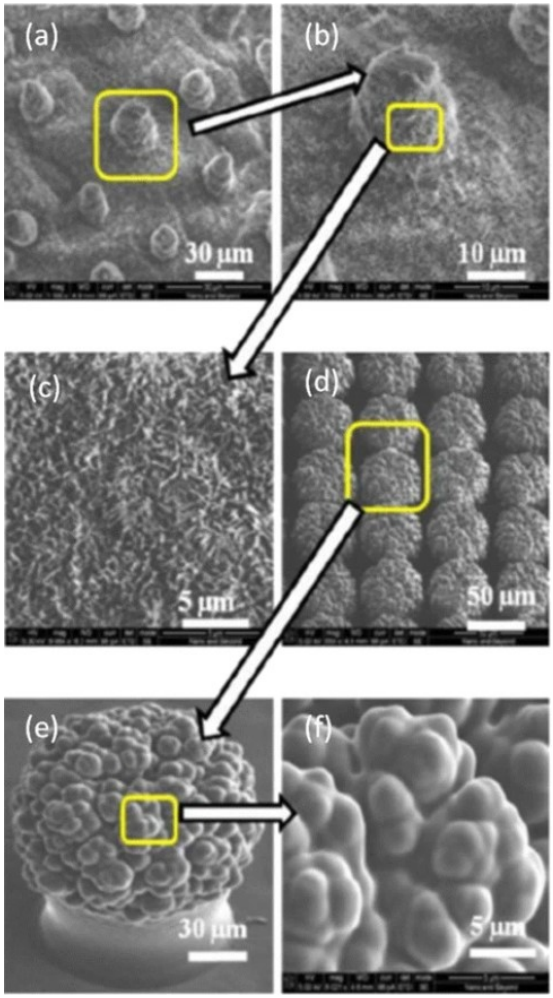

Figure 4 SEM images showing superhydrophobic surface morphology: (a–c) a natural lotus leaf, and (d–f) an artificial PDMS-based surface with similar wetting behaviour. Image sourced from [69] which is under an open access Creative Common CC BY licence.

As seen in Figure 4, the artificial structure, created via a one-step replication process using an underbaked, underexposed photoresist mould, exhibiting a broccoli-like micro/nanotexture. This randomly distributed surface architecture closely mimics the natural lotus leaf and enables high water contact angles (>160°), confirming its superhydrophobic nature. [69]

Surface hydrophobicity is dependent on contact angle hysteresis (H), defined as the difference between an advancing (θ_A) and a receding contact angle (θ_R), as shown in Equation 6 [71].

$$H = \theta_A - \theta_R \tag{6}$$

This difference indicates how strongly the liquid adheres to the surface. [72], [73] Low hysteresis allows the droplet to roll off easily, enabling self-cleaning, whereas high hysteresis causes the droplet to remain pinned. [74], [75]

Figure 5 illustrates the concept of contact angle hysteresis on a tilted surface. The advancing angle (θ_A) appears at the droplet front as it spreads, while the receding angle (θ_R) appears at the rear as it detaches. Their difference represents hysteresis, while the tilting angle (α) indicates the minimum inclination needed for the droplet to move. [76]

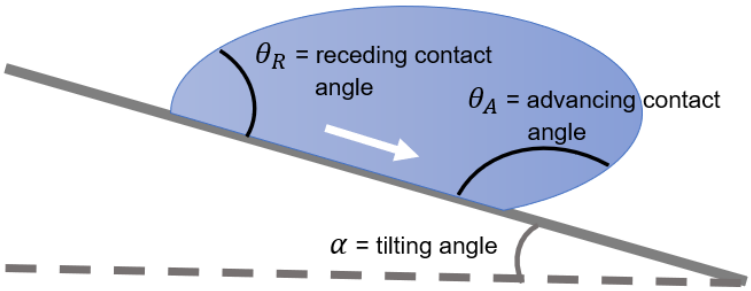

Figure 5 Advancing and receding contact angle between the interface of a liquid droplet and a solid plane, and the effect of hysteresis due to tilted plane. Reproduced from [76] which is under an open access Creative Common CC BY licence.

As shown in Figure 5, a tilted plane can be used to measure advancing and receding contact angles. By tilting the plane, gravitation gradually increases and the droplet starts to slide. [76] Values of each angle can be calculated using gravitational force, as shown in Equation (7).

$$\sin \alpha = \frac{\omega \gamma_{LG} k}{mg} (\cos \theta_R - \cos \theta_A) \quad (7)$$

where ω is the width of the contact area of the droplet, k is a geometric factor, m is the mass of the droplet and g is the gravitational acceleration. [77], [78] He et al. (2004) [79] conducted direct measurements on microfabricated silicon polymer, polydimethylsiloxan (PDMS), surfaces and found that Cassie droplets (groplets that sits on roughness peaks with air pockets and rolls easily off the surface) exhibited lower hysteresis compared to Wenzel droplets (droplets that penetrate grooves of roughness and sticks strongly to the surface). Specifically, the advancing contact angle for a Cassie droplet was 152–153°, and the receding angle was 132°, causing a hysteresis of about 20°. In contrast, Wenzel droplets on the same surface showed advancing angles of 142–143°, but the receding angle continuously decreased with volume reduction, indicating no stable value and thus very high hysteresis. These results confirm that the wetting state strongly affects hysteresis and that Cassie droplets, resting on air

pockets, are more desirable in self-cleaning or droplet-transport applications due to their enhanced mobility. [79]

The hydrophobic behaviour of a surface is influenced by a set of structural parameters that determine how water interacts with the surface both statically and dynamically [80]. One key factor being surface roughness, which can be measured by: *Ra* (arithmetic average roughness) describing the linear average roughness of the surface, and *Rz* (mean peak-to-valley height) describing the linear average height difference between the largest peak and the deepest valley [81], [82]. In the study by Kubiak et al. (2011) [83], the influence of surface roughness on wettability was systematically evaluated using six different materials: (1) aluminium alloy, (2) titanium alloy, (3) steel alloy, (4) copper alloy, (5) ceramic, and (6) poly(methyl methacrylate) (PMMA). The surface roughness was controlled by polishing samples with abrasives of varying grit sizes, causing *Ra* values ranging from 0.15 µm to 7.74 µm. Apparent water contact angles were measured 20 seconds after droplet deposition to capture the quasi-static wetting behaviour. Results showed that the relationship between surface roughness and contact angle was not linear but material-dependent and often non-monotonic. As illustrated in Figure 6, each material exhibited a characteristic trend. [83]

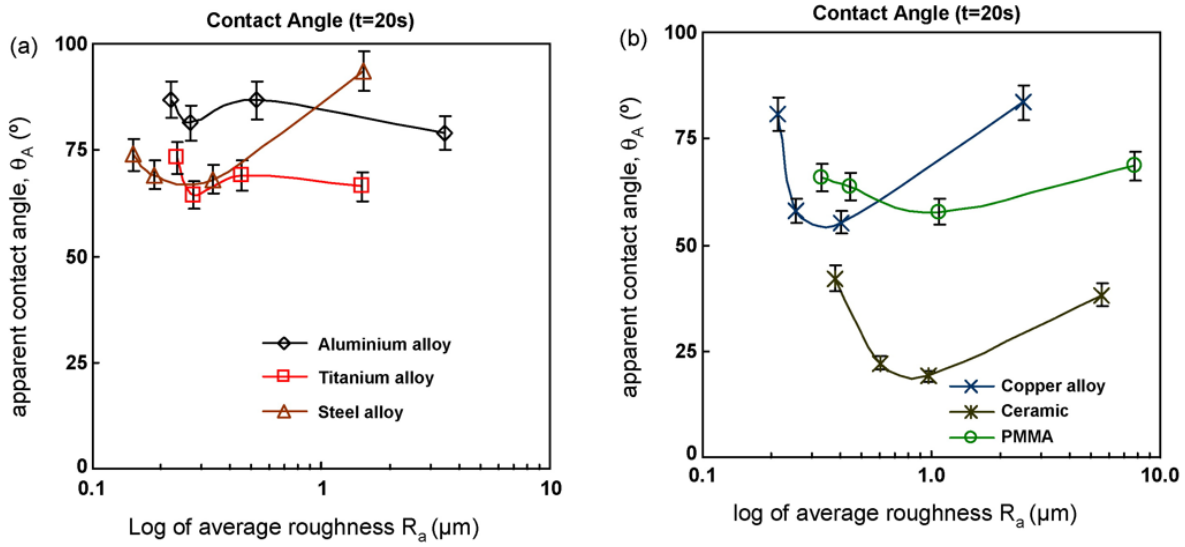

Figure 6 Apparent contact angle (θ_A) measured 20 seconds after droplet deposition as a function of linear average surface roughness (*Ra*). (a) Results for aluminium, titanium, and steel alloys. (b) Results for copper alloy, ceramic, and PMMA surfaces. Image sourced from [83] which is under an open access Creative Common CC BY licence.

As seen in Figure 6, titanium and steel alloys showed increasing contact angles with increasing roughness, whereas copper alloy and ceramic surfaces exhibited a minimum contact angle at intermediate roughness values. In the case of ceramic, contact angles as low as 20° were

observed at *Ra* values of ~1 μm, indicating enhanced spreading. PMMA surfaces showed a more gradual change, with contact angles increasing with roughness. These trends suggest that while increased surface roughness can promote air entrapment and enhance hydrophobicity, it may also lead to increased wetting depending on the surface chemistry and morphology. The authors also emphasized that roughness alone cannot predict wetting behaviour reliably; rather, it must be evaluated in conjunction with surface material properties and topographical complexity. [83]

Another parameter having an effect on surface hydrophobicity, is pore geometry and order. If the pores are regularly arranged, for example in a micropillar structure, they can produce a mechanically stable Cassie–Baxter state where water cannot fill the pores, but instead remains above them. In contrast, occasional or irregular porosity can lead to unstable wetting behaviour and trigger a contact angle hysteresis phenomenon, in which droplet propagation and withdrawal occur at different angles. The influence of pore geometry and ordering on hydrophobicity has been confirmed both computationally and experimentally. [68], [84], [85] Bushuev (2025) [68] used molecular dynamics simulations to study hierarchical Menger sponge nanoparticles and observed that particles with isolated micropores (2–3 nm) exhibited more stable non-wetting behaviour and higher intrusion pressures compared to those with interconnected mesopores (5–10 nm). Irregular connectivity promoted premature water infiltration and weakened H_2 bonding networks, leading to transitions away from the Cassie–Baxter state. In contrast, more symmetric and closed pore networks enhanced air entrapment and supported stable droplet suspension. Supporting these findings, Bernardoni and Fadeev (2011) [86] fabricated structured alumina surfaces with either hexagonally ordered (~100 nm) or randomly distributed pores and evaluated their wetting properties after silanization (chemical surface modification process where organosilane molecules are covalently attached to the surface to create functional properties). Surfaces with regular pore arrangements exhibited higher contact angles (up to 162°) and lower contact angle hysteresis, while disordered surfaces showed reduced angles (~145°) and increased droplet pinning. These results demonstrate that pore symmetry and spatial order enhance both the static and dynamic aspects of surface hydrophobicity by stabilising the Cassie–Baxter regime and minimising wetting transitions.

Although surface structure plays an important role in hydrophobicity, the chemical composition of the surface must also be considered [87]. The free surface energy of the surface and the functional groups attached to it determine how strongly water interacts with solid matter. A surface with low free energy does not provide enough thermodynamic energy for water

molecules to spread, causing a high contact angle and hydrophobicity. [88], [89] Chang et al. (2022) [90] demonstrated that by modifying epoxy coatings with fluorinated silanes (PFTEOS) reduced the surface free energy of solid and increased the contact angle of water droplet from 107.2° to 114.4° on flat surfaces. On rough nanocomposite surfaces, the contact angle further increased from 143.6° (Zn40-1:5) to 148.2° (ZnF40-1:5) and from 150.2° (Zn40-1:9) to 153.4° (ZnF40-1:9) after fluorination. The corresponding 3D surface topographies of Zn40-1:5, Zn40-1:9, ZnF40-1:5, and ZnF40-1:9 coatings are shown in Figure 7. [90]

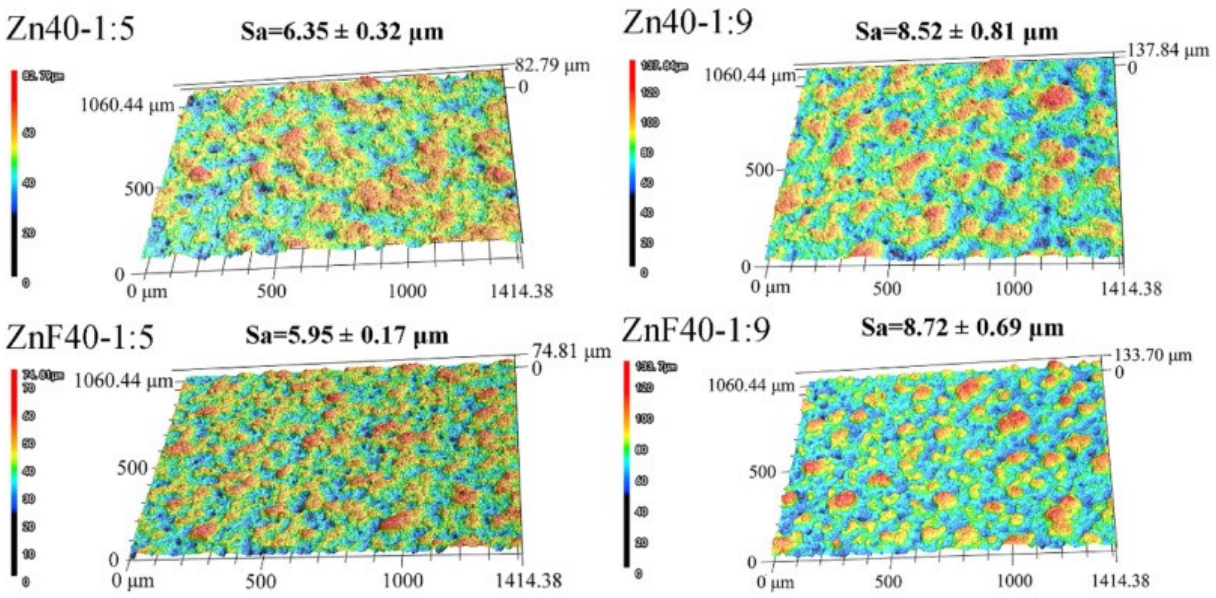

Figure 7 Three-dimensional surface profiles and average surface roughness (*Sa*) of the fabricated nanocomposite coatings. Image sourced from [90] which is under an open access Creative Common CC BY licence.

Figure 7 shows the 3D surface topographies of Zn40-1:5, Zn40-1:9, ZnF40-1:5, and ZnF40-1:9 coatings and measured surface roughness values [90]. The *Sa* values confirm that fluorination with PFTEOS did not alter the micro/nanostructural features, as surfaces with identical ZnO nanoparticle concentrations and size ratios exhibit comparable roughness. The increase in *Sa* from the 1:5 to the 1:9 ratio reflects the higher proportion of larger ZnO particles, indicating that surface topography is primarily dictated its nanofiller characteristics rather than the chemical modification. Since the surface topography remained nearly unchanged, these increases were attributed directly to the chemical composition. The introduction of $-CF_2$ and $-CF_3$ groups lowered the surface energy, stabilizing Cassie–type wetting and decreasing contact angle hysteresis, down to 3.39° in the most hydrophobic coating (ZnF40-1:9). These findings confirm that lowering surface energy via functional group modification is a key mechanism for enhancing hydrophobicity. [90] In technical applications, such where low-

energy surfaces are implemented, for example, by fluoridated polymers such as PTFE (polytetrafluoroethylene), or by the use of silane-based coatings that form hydrophobic structures. For example, these materials include CH_3 (methyl group), CF_3 (trifluoromethyl) and $Si(CH_3)_3$ (trimethylsiloxane) groups, which are known for their ability to lower surface energy and thus increase water repellent. [91], [92]

External stimuli can affect or even actively regulate the hydrophobic nature of the surface. For example, in the electrowetting phenomenon (an external electric field dynamically reducing the contact angle) enabling controlled movement of the liquid in microchannels. Similar responses can also be achieved by light (optowetting) or heat (thermoresponsive coatings), where the surface reacts to changes in environmental conditions and changes its wetting property accordingly. [93] Zhu et al. (2024) demonstrated that surface wettability can be dynamically controlled using a terahertz-frequency electric field. When a field of 0.8 V/nm at ~33 THz was applied to a surface coated with a sub nanoscale water layer, the contact angle dropped from 51.7° to 0°, indicating a switch from hydrophilic to superhydrophilic. This reversible transition was frequency-specific and driven by disruption of the H_2 bonding network, showing that wettability can be tuned also without changing surface chemistry or structure. [94]

3 Laser surface functionalization

3.1 Overview of laser surface functionalization

Laser surface functionalization is a technique used for the controlled modification of material surfaces by using laser energy to create physical or chemical changes at levels of micro- and nanoscales [95]. This approach enables the generation of functional properties with high precision and reproducibility [96]. For instance, laser surface texturing can enhance optical characteristics, such as anti-reflective properties or light trapping (confinement of light within a material by repeated internal reflections, which increases its absorption), which are useful in photovoltaics (technology were light is converted into electricity) and sensor design [97]. Surfaces modified with laser techniques can also be tailored to influence friction and wear, making them more suitable for tribological applications where durability and reduced mechanical losses are required [98], [99]. Laser treatment can alter the chemical reactivity of surfaces, either by exposing reactive sites or by enabling selective coating adhesion, which is important for material integration and the deposition of protective layers [100], [101]. Functionalization may further be used to adjust thermal and electrical conductivities or to modify surface-driven fluid flow behaviour [102], [103].

Laser surface functionalization is caused from physical and chemical interactions between laser energy and the material [95]. One of the key mechanisms is the formation of micro- and nanostructures as a result of local melting, ablation and rapid recrystallization [104]. Such surface structures – including wells, grooves, and regular ridges – can influence the optical, tribological, and biological properties of the material [105], [106]. Laser treatment also changes the chemical composition of the surface, for example through oxidation or other reactions that occur with air, shielding gas or other additives. These chemical modifications enable the adjustment of surface energy, corrosion resistance, and biocompatibility. Rapid temperature variations may induce phase transformations and refine the microstructure, enhancing properties such as surface hardness and fatigue strength. [107] Ultra-short pulses can be used to create laser-induced periodic surface structures (LIPSS), which influence, among other things, the scattering of light, the orientation of cells, or the wetting behaviour of the surfaces [97]. In addition, residual stresses and localized hardening may form under laser irradiation, improving wear resistance [99]. Laser processing further enables selective removal or melting of material with high precision, making it possible to fabricate multi-layer or hybrid structures and with minimal material consumption [108]. Because it is a non-contact method, laser

processing is particularly well suited for the clean and accurate modification of delicate or geometrically complex surfaces [96].

Laser surface structuring can be achieved in two primary ways, depending on both the pulse characteristics – such as pulse width and frequency – and scanning method. When using longer pulses and a laser beam with small diameter at the focal point, individual grooves or microchannels are formed, with a depth ranging from several nanometres to micrometres directly as the beam ablates material along the scanning path. This creates defined patterns based on the movement of the beam, as shown in Figure 8a [104][92]. When using ultrashort pulses, such as femtosecond pulses, LIPSS can form on the surface during scanning process, as shown in Figure 8b [105]. These self-organized nanoscale ripples are typically oriented perpendicular to the laser polarization and arise from the interference between the incident beam and surface electromagnetic waves. The formation of LIPSS is influenced by parameters such as laser wavelength, fluence, number of pulses, and polarization direction. [97] Such structures enhance surface functionality, including wettability, adhesion, and optical behaviour [97], [109].

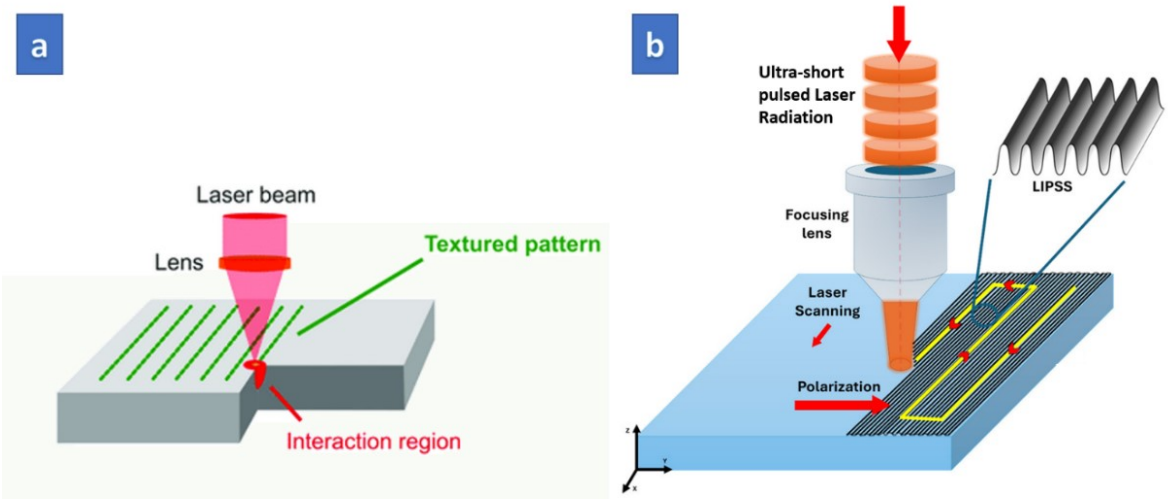

Figure 8 Laser surface structuring methods: (a) Long pulsed scanning method and (b) LIPSS method with ultrashort pulses. Images sourced from [97], [109] which are under an open access Creative Common CC BY licence.

Figure 8 presents the two laser-based approaches to surface texturing [97], [109]. In Figure 8a, long-pulse laser irradiation is used to ablate material and to produce well-defined microstructures, such as dimples or grooves, with dimensions ranging from tens to hundreds of micrometres depending on the beam diameter. These features are generated by scanning the laser beam across the surface, either through the movement of the beam itself or by introducing

a relative motion between the laser system and the substrate [110], [111] Figure 8b illustrates the formation of LIPSS using ultra-short pulsed laser radiation, for example femtosecond pulsed laser system. Here material removal does not occur in the conventional sense; instead, periodic nanostructures are self-organized due to interference between the incoming laser wave and surface-scattered waves. These ripples are oriented perpendicular to the polarization of the laser and are highly sensitive to processing parameters such as laser fluence, pulse number, and wavelength. [97], [109]

Laser surface texturing has been shown to improve the tribological performance of mechanical components by reducing the friction and wear through the introduction of micro-dimples on contact surfaces, which can be used as hydrodynamic bearings or lubricant reservoirs under various lubrication regimes [98], [99]. Etsion (2004) [99] reported both theoretical modelling and experimental validation of laser surface texturing applied to mechanical seals, piston rings, and thrust bearings. In case of mechanical seals, laser textured surfaces with hemispherical dimples (∼100 μm diameter, ∼10 μm depth, 20% area density) achieved a friction torque reduction of up to 65 % at low unit loads compared to non-textured references. Partially textured seals provided an even greater effect, reducing friction by more than 90% at 12 bar sealed pressure. More recently, Lin et al. (2025) [112] investigated the effect of laser surface texturing on the wear resistance of laser-cladded WC–Ni composite coatings. A picosecond laser device producing a laser beam with a wavelength of 1064 nm, an average power of 25 W, a scanning speed of 200 mm/s, and a pulse frequency of 100 kHz was used for laser texturing. Circular pit textures were applied to coatings containing 20 wt% WC (WC20) and compared with both untextured coatings and coatings with higher WC content (60 wt%). Figure 9 shows representative images of the textured surfaces, highlighting the uniform pit geometry produced by the picosecond laser processing. [112]

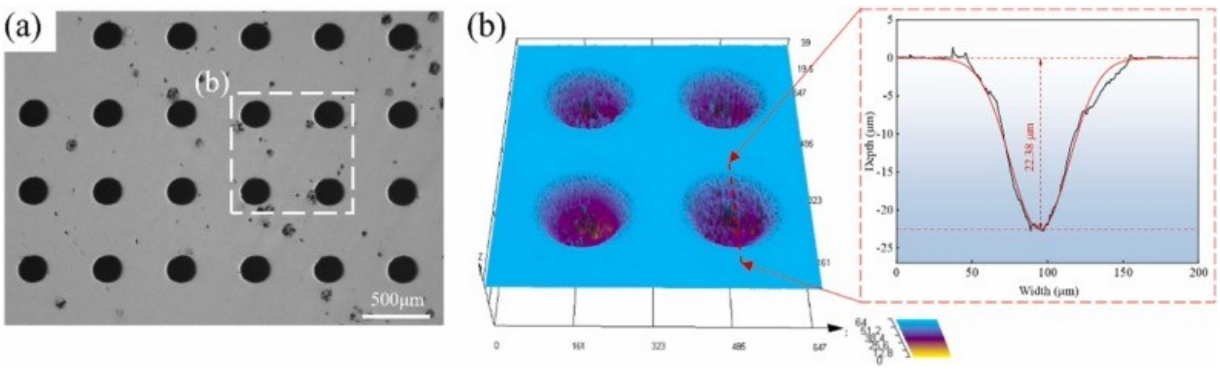

Figure 9 (a) Optical microscopy image of laser textured surface. (b) 3D image and corresponding centre section profile of laser textured surface. Image sourced from [112] which is under an open access Creative Common CC BY licence.

Figure 9 shows the textured WC–Ni composite surfaces, where the optical micrograph illustrates the regular distribution of circular pits, and the 3D profilometry image confirms an average pit diameter of ~100 μm and a depth of ~22 μm. The darker peripheral zones visible around the pits reflect localized thermal effects during laser processing. The tribological tests demonstrated that wear resistance was enhanced by surface texturing. In particular, the textured WC20 coatings (WC20-LT) showed a 29.24 % reduction in average friction coefficient and a 53.56 % reduction in wear rate compared to untextured WC20 coatings. This improvement is attributed to the function of the micro-pits as reservoirs for wear debris and lubricants, which mitigated abrasive and adhesive wear while supporting hydrodynamic lubrication under wet sliding conditions. Microstructural analysis further indicated that the laser-induced texture preserved the overall phase composition but promoted grain refinement and localized hardening in the binder phase, especially near pit edges, where microhardness values exceeded 500 $HV_{0.2}$. As a result, the wear tracks of textured coatings were shallower and smoother, with improved lubricant retention and reduced crack propagation, confirming the protective effect of the laser-generated microstructures. [112]

Several studies have demonstrated that laser processing can alter the electrical conductivity of a surface through controlled texturing and chemical modification [113]. Stolz and Poprawe (1999) [113], investigated this effect on ceramic substrates, specifically Al_2O_3 and AIN, by generating conductive micro-traces with CO_2 and excimer laser irradiation. Al_2O_3 was modified using continuous wave CO_2 laser radiation (wavelength of 10.6 μm) with scanning velocity between 10 and 300 mm min^{-1}, and laser powers from 25 W to 1 kW. In contrast, excimer laser radiation at 248 nm was employed for AlN, with an effective pulse number ranging from 1 to 140 and fluences between 1.5 and 6 J cm^{-2}. The process reduced the resistivity of Al_2O_3 from

values exceeding $10^{14}\,\Omega$ cm to approximately $0.5\,\Omega$ cm, corresponding to an improvement of 14 orders of magnitude. This modification was achieved through carbonization and crystalline transformations in ethanol environment, forming offstoichiometric phases (such as $\alpha - Al_2O_3$) and introducing amorphous carbon. Figure 10 shows resistance per length as a function of process velocity for Al_2O_3 samples of different purities, showing that higher velocities were generally associated with lower resistance. [113]

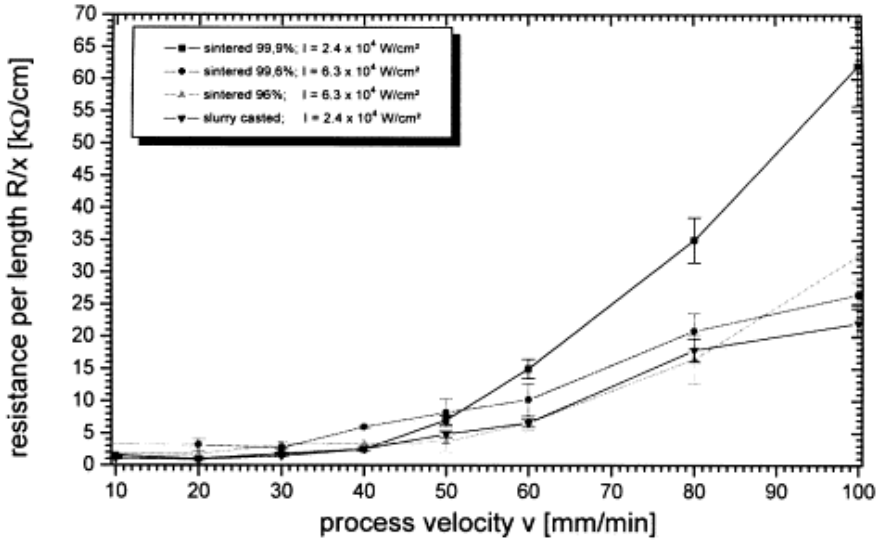

Figure 10 Electrical resistance per unit length as a function of processing velocity for various Al_2O_3 grades. Image sourced from [113] which are under an open access Creative Common CC BY licence.

As shown in Figure 10, at scanning velocities of ≤40 mm/min the resistance remains low and nearly constant across all Al_2O_3 purities. When the velocity exceeds 50 mm/min, the resistance increases sharply, most notably for the 99.9% sintered Al_2O_3. In comparison, slurry-cast and lower-purity sintered materials retain a lower resistance over a wider velocity range, indicating a greater tolerance to high scanning velocities without conductivity loss. For AlN, laser modification decreased resistivity to values of 50–300 mΩ cm, depending on the pulse number. This improvement was associated with grain boundary alterations that enhanced conductivity without complete metallization of the surface. The changes were attributed to microstructural rearrangements and the possible formation of N-rich secondary phases, confirming that laser irradiation can selectively adjust the electrical behaviour of dielectric ceramics. [113]

Laser processing can also be applied to enhance the electromagnetic shielding effectiveness of materials. Electromagnetic shielding refers to the ability of a material to block or attenuate external electromagnetic fields, including radio waves and static electric fields. Tunakova et al. (2018) [114], investigated this effect by treating electrically conductive hybrid fabrics

composed of stainless steel fibres with a CO_2 laser device. This laser system operated at a wavelength of 10.6 µm, a power of 100 W, and a frequency of 5 kHz. The study demonstrated that laser patterning increased the shielding effectiveness measured at 1.5 GHz from approximately 10 dB to more than 40 dB. This improvement was attributed to laser-induced carbonization and localized conductivity enhancement, achieved without the need for additional coatings. For detailed control of the surface modification, the grayscale method was applied, in which pixel intensity in the input image determines the delivered laser energy: darker regions receive higher doses, enabling precise and localized structuring [115]. While high laser intensity led to brittleness and changes in mechanical performance in some patterns, optimization within the 20–35 % grayscale range maintained the integrity of the fabric while improving both shielding capability and visual appearance. These results demonstrate that laser structuring provides a promising strategy for tailoring the electromagnetic performance of flexible electronic textiles. [114]

Laser-induced surface functionalization has been shown to influence fluid–structure interactions, particularly in relation to hydrodynamic cavitation. Cavitation refers to the formation, growth, and collapse of vapor bubbles in a liquid flow, often occurring when local pressures drop below the vapor pressure of the liquid. [116] Petkovšek et al. (2020) [117] investigated this phenomenon by fabricating five distinct microstructural topographies (dimpled, velvet, oxidized, waved, and grooved) on stainless-steel cylinders using a nanosecond fibre laser. This laser operated at a wavelength of 1060 nm with pulse durations between 10 ns and 28 ns, repetition frequencies ranging from 90 kHz to 900 kHz, and average powers between 3.7 W and 19 W. Scanning speeds varied between 300 mm/s and 540 mm/s, with line spacings from 0.9 µm to 130 µm depending on the pattern. The results demonstrated that laser texturing delayed the onset of cavitation and reduced its intensity compared to polished reference surfaces, especially during the early stages of cavitation development. Among the tested textures, dimpled and velvet surfaces produced the smallest cavitation extent and lowest pressure oscillations, indicating that well-designed microfeatures can mitigate cavitation-induced erosion and noise. In contrast, the grooved surface, with the highest roughness (*Sa* value of 18.3 µm), promoted the most intense cavitation activity and the longest cavitation lengths, confirming that high roughness enhances vapor bubble generation. Frequency analysis of pressure fluctuations further supported these findings by showing that laser-induced texturing altered both the shedding frequency and amplitude of cavitation clouds. This outcome indicate that surface texturing affects cavitation not only through roughness or wettability, but

also via the interplay of microgeometry, material response, and flow dynamics. The results highlight the potential of laser texturing as a functionalization strategy: it can suppress cavitation where it is harmful, such as in turbines and pumps, or enhance it in applications where bubble activity is beneficial, such as water purification and emulsification. [117]

The functionalization of stainless steel surfaces through the formation of LIPSS, was explored by Saqib et al. (2022) [118], focusing particularly on corrosion resistance and biocompatibility. Using a picosecond laser system with wavelengths of 1064 nm and 532 nm, the researchers fabricated distinct nanopatterns on AISI 316 stainless steel, including linear LIPSS formed parallel to the laser polarization (L1064 and L532) and crosshatched groove patterns (LGV). These nanostructures differed in both spatial period and morphology: L1064 patterns exhibit wider, less densely packed ripples, L532 produces finer, high-frequency ripples with smaller feature spacing, and LGV combines two orthogonal sets of grooves to create a grid-like texture. Electrochemical tests in Hanks' Balanced Salt Solution (Figure 11) revealed substantial differences in corrosion behaviour among the surface types. [118]

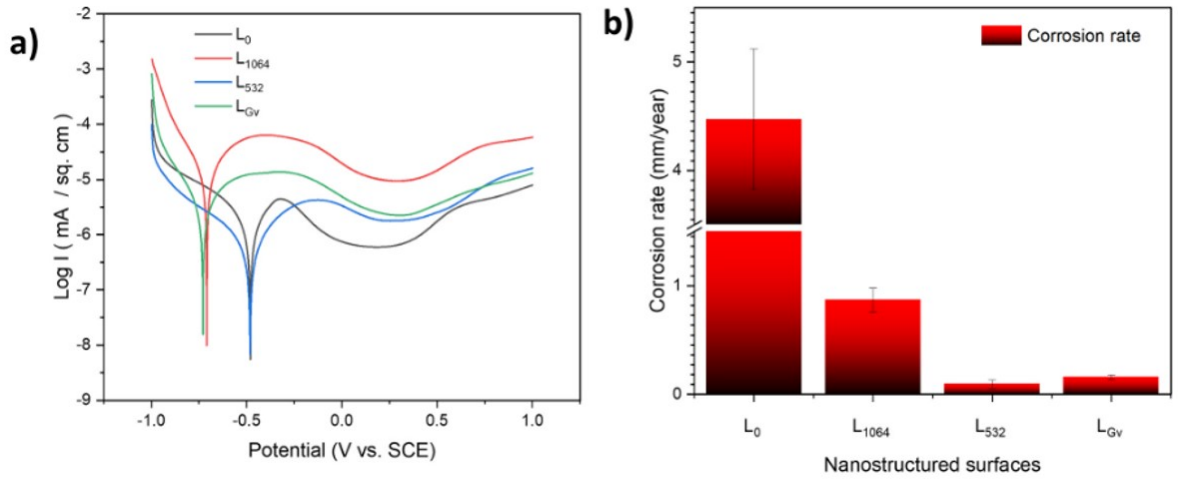

Figure 11 Corrosion performance of LIPSS-treated surfaces: (a) potentiodynamic polarization curves, (b) comparison of corrosion rates in bar chart form. Reproduced from [118] which is under an open access Creative Common CC BY licence.

The potentiodynamic polarization curves in Figure 11a show that L532 exhibited the most noble corrosion potential, meaning it shifted toward more positive values, which indicates a higher resistance to the initiation of corrosion, and the lowest current density in the passive region, demonstrating superior passivation. The LGV surface also performed well, with currents higher than L532 but clearly reduced compared to the untreated reference (L0). By contrast, L1064 provided only a moderate improvement, with current densities higher than L532 but still lower than L0. The quantitative comparison in Figure 11b confirmed these trends: the L532 surface

achieved the lowest corrosion rate (0.09 mm/year), nearly 50 times lower than the untreated reference. LGV followed closely, while L1064 achieved only partial reduction. The enhanced corrosion resistance was attributed to laser-induced microstructural changes, including grain refinement and oxide modification, as well as physical entrapment of air within the nanostructures, which served as barriers against corrosive ion penetration. Biocompatibility tests with human umbilical cord mesenchymal stem cells were also performed. All textured surfaces were shown to support cell adhesion and proliferation, but the L1064 surface promoted superior alignment and confluence of cells along the linear nanogrooves. These findings indicate that LIPSS can be tailored not only to enhance corrosion resistance but also to guide cellular behaviour, making them highly relevant for biomedical applications such as stents where both durability and biocompatibility are critical. [118]

In addition to creating surface textures, laser processing can also impart functional properties by modifying the surface chemistry of a material. Laser-induced surface functionalization was explored not only for controlling wettability but also for engineering functional flow channels on flat glass surfaces in a study done by Aono et al. (2016) [98]. Chemical surface treatment with terminal functional groups ($-CF_3$ or $-(CH_3)_2$) was combined with localized infrared laser irradiation. By this approach, invisible, non-textured flow channels were created without physical engraving. A CO_2 marking laser with a wavelength of 9.3 μm, a power of 20 W, and a scanning speed of 2000 mm/s was used in the experiments. The laser modified channels preserved both the transparency and the surface integrity of the glass, as verified by SEM and ultraviolet-visible (UV–vis) spectroscopy. The concept of self-transportation flow channels was introduced, where droplets were driven autonomously along the surface due to a gradient in wettability. This behaviour was achieved by controlling the decomposition of terminal functional groups through tailored laser parameters. As the surface locally transitioned from hydrophobic to hydrophilic, a contact angle gradient was generated, and the resulting hysteresis was sufficient to induce fluid motion without external actuation. These results demonstrate that laser-induced functionalization can be used to manipulate fluid dynamics on glass surfaces through chemical composition control, offering potential for applications in microfluidics, lab-on-a-chip systems, and passive liquid transport technologies. [103]

3.2 Laser-induced hydrophobicity

Hydrophobic functionality can be induced to solid surfaces through laser irradiation, particularly by employing pulsed lasers with ultra-short pulses, such as femtosecond pulsed

laser devices. This laser-based method enables the formation of controlled micro- and nanostructured topographies that alter the wetting characteristics of the material surface. Following laser irradiation, surface morphology becomes hierarchically textured, consisting of conical spikes, grooves, or dimpled features, which trap air beneath water droplets and reduce the effective contact area between the solid and the liquid phase. This geometric configuration facilitates the transition from a Wenzel-type wetting state, where the droplet fully penetrates the surface texture, to a Cassie–Baxter state, where the droplet partially rests on air pockets. As a result, the contact angle between the water droplet and substrate surface increases and may, in certain cases, exceed 150°, at which point the surface is classified as superhydrophobic. [119], [120], [121]

The degree of hydrophobicity achieved by laser texturing is governed by several interdependent processing parameters, including laser fluence, pulse duration, scanning speed, and hatch spacing. By adjusting the laser fluence, the extent of material ablation and surface modification can be controlled with high precision. Moderate to high fluences enable the formation of well-defined microcavities and hierarchical textures, which contribute to air entrapment beneath liquid droplets and support stable Cassie–Baxter wetting states. [121] Use of lower fluences causes shallower surface features or incomplete pattern development, leading to reduced contact angles and less stable wetting behaviour. The transition from superhydrophilic to hydrophobic behaviour is time-dependent and driven by post-irradiation surface chemistry evolution, notably the gradual adsorption of airborne hydrocarbons and reduction in surface free energy. [122] Immediately after texturing, surfaces typically exhibit hydrophilic states with contact angles below 10°, which can spontaneously evolve into stable hydrophobic or superhydrophobic surfaces over the course of days or weeks under ambient conditions. [121] This time-dependent wetting transition has been experimentally verified by Dongre et al. (2021) [123]. Surfaces were prepared by using a nanosecond laser texturing of stainless steel 316 using a fibre laser operating at a wavelength of 1064 nm, a pulse duration of 200 ns, a repetition rate of 30 kHz, a scanning speed of 100 mm/s, and a fluence of approximately 2.5 J/cm². Contact angle as a function of time (days) was measured in order to review the time-dependence of surface wetting, as shown in Figure 12. [123]

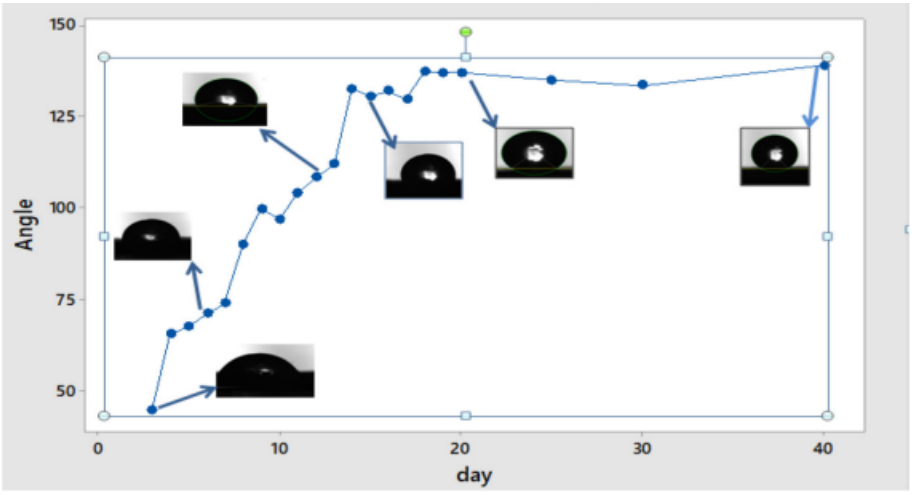

Figure 12 Time (days) as a function of contact angle. Image sourced from [123] which is under an open access Creative Common CC BY licence

As shown in Figure 12, the measured contact angle was evaluated as a function of time. The scatterplot shows how the contact angle increased from below 90° to a maximum of 153° within 40 days, after which no further changes were recorded after 20 days, indicating stabilization of the surface state. The plotted data are complemented by optical microscopy images of sessile droplets at different time points, clearly illustrating the gradual transition from complete wetting to strong water repellence. SEM analysis has confirmed that the surface modifications are consistent with partial oxidation and the formation of nanostructured particulate layers. The increase in contact angle was attributed to a combined effect of oxide crystallization and adsorption of airborne contaminants, both of which reduce the surface energy and promote non-wetting behaviour. [123]

Coatings with low surface energy, such as fluorinated silanes or plasma-deposited CF_X layers, can be applied onto laser-treated surfaces of substrates to accelerate and stabilize the wettability transitions. These coatings reduce surface energy while conformally preserving the underlying topography. [120], [122] The combination of laser-generated micro- and nanostructures with such coatings has been shown to increase contact angles and decrease hysteresis, thereby enhancing droplet mobility and reducing the pinning effects. Surfaces with hierarchical dual-scale roughness have demonstrated higher resilience in dynamic wetting conditions, such as droplet impact or ice nucleation (process where molecules of liquid water start to form into clusters). [120], [122] In anti-icing applications, laser textured and fluorinated aluminium surfaces have exhibited extended freezing delay times [122]. Rico et al. (2019) [122] observed that Cassie–Baxter surfaces delayed freezing for longer times compared to Wenzel-type geometries with similar roughness. Their findings highlighted that surface morphology and air

entrapment play a more decisive role than roughness amplitude alone in suppressing heterogeneous nucleation.

The durability and functional longevity of laser-induced hydrophobicity have been systematically investigated. Surfaces fabricated with dense and uniform nanostructures have demonstrated improved resistance to mechanical abrasion, chemical attack, and thermal cycling. In particular, stainless steel surfaces textured with a nanosecond pulsed fibre laser and subsequently coated with a thin silane-based hydrophobic layer were shown to maintain hydrophobicity even after prolonged exposure to saline environments, confirming potential for maritime and industrial applications. [120] Rafieazad et al. (2018) [120] have reported that the laser textured surfaces exhibited contact angles up to 145°, indicating the formation of water-repellent surface features. However, electrochemical testing in a 3.5 wt.% NaCl solution revealed a decrease in corrosion resistance compared to untreated or solely silane-coated references. The corrosion current density of the laser textured and coated surface was 8.51 x 10^{-7} A/cm², which was higher than that of the untreated substrate (5.17 x 10^{-7} A/cm²) and the silane-coated reference (2.44 x 10^{-7} A/cm²). These findings indicate that the laser-induced microstructures, while effective in achieving hydrophobicity, did not maintain air entrapment under full immersion, which increased the effective contact area with the electrolyte. Although wettability remained unchanged after corrosion testing, the structural design alone was insufficient to provide corrosion protection in aqueous environments. Effective mitigation of immersion-induced corrosion requires the development of stable superhydrophobic geometries with hierarchical roughness, capable of sustaining the Cassie–Baxter wetting state and preventing electrolyte infiltration into surface recesses. [120]

Stainless steel surfaces treated with femtosecond pulsed laser devices have shown long-term stability of contact angles when the micro-cone density and aspect ratio were optimized, highlighting the importance of precise control over texture dimensions and uniformity [119]. Kam et al. (2012) [119] have demonstrated that by tailoring the scanning speed (120 to 2400 mm s^{-1}) and fluence (from 0.253 to 1.014 J cm²) during femtosecond laser processing (wavelength of 1043 nm) of AISI 316L stainless steel surface, micro-cone structures with different micro-cone densities and geometries could be fabricated, as shown in Figure 13.

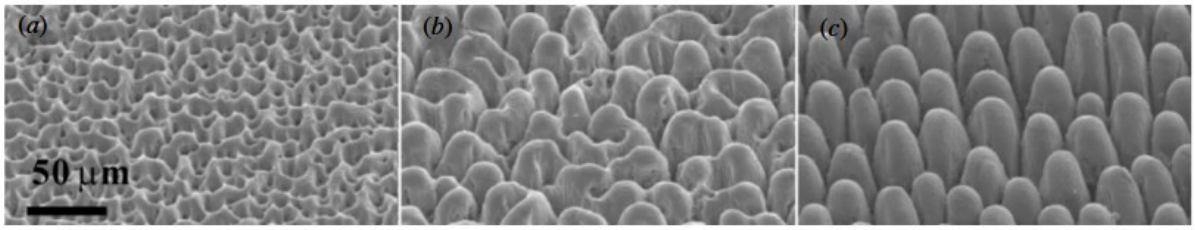

Figure 13 SEM images of the 316L stainless steel surface following processing with (a) N = 8, (b) N = 40, and (c) N = 300 scanned layers. The textures were generated using laser pulses at a fluence of approximately 1.014 J cm^{-2} (8 µJ at focus) with a repetition rate of 1000 kHz and a scanning speed of 600 mm s^{-1}. Image sourced from [119] which is under an open access Creative Common CC BY licence.

Figure 13 presents SEM images of surfaces fabricated under high-fluence conditions (F ≈ 1.014 J/cm^2) at varying numbers of scanned layers: (a) N = 8, (b) N = 40, and (c) N = 300. At low N, the cones are shorter and more widely spaced, while increasing N produces taller structures with higher aspect ratios and more uniform distribution. These variations in geometry directly influenced wettability, with contact angles ranging from superhydrophilic (0°) to hydrophobic (~113°) without chemical treatment, and up to ~150° after silane coating. The images highlight how controlled adjustment of scanning parameters allows precise tuning of micro-cone density and aspect ratio, enabling tailored wetting behaviour on stainless steel surfaces. [119]

The geometry and configuration of laser-induced surface textures have been shown to influence the wetting behaviour of metallic surfaces, since different texturing strategies generate distinct microstructural and chemical modifications that directly affect surface wettability. [124]. In a systematic study, Yang et al. (2016) [125] have fabricated three types of textures (line, grid and spot) on pure titanium surfaces, using a nanosecond pulsed laser system with a wavelength of 1064 nm, a pulse width of 6 ns and an output power of 1.2 W. The distance between lines and spots varied from 50 to 100 µm. Immediately after processing, all surfaces displayed superhydrophilic behaviour with contact angles below 90°, which was attributed to increased surface energy and oxide formation. Over time, contact angles increased as surface chemistry evolved. After stabilization, the surfaces textured with line pattern achieved the highest contact angle of 157.2°, followed by grid (153°) and spot (132.5°) patterns. The transition was linked to the combined effects of hierarchical roughness and gradual accumulation of carbonaceous species. Surface roughness analysis confirmed that line and grid textures produced higher *Ra* values (value of 6.7 µm), particularly when spacing was minimized (50–60 µm), thereby enhancing air pocket formation beneath droplets. Spot patterns, in contrast, showed the lowest roughness (*Ra* value of 0.2 µm) and correspondingly weaker hydrophobicity. Morphological observations further revealed that grid textures produced the most complex topography due to

overlapping laser passes, whereas spot textures generated isolated features with limited interconnection. X-ray photoelectron spectroscopy (XPS) measurements showed an increase in surface carbon content from 48.6% (untreated) to 60.7% (line), 58.7% (grid), and 52.0% (spot), demonstrating that both surface morphology and chemical composition contributed to enhanced water repellence. These results confirm that texture type and spatial density critically determine the wetting state. In particular, continuous and intersecting patterns such as lines and grids support stable Cassie–Baxter wetting by increasing roughness and enabling air trapping.

4 Functional properties of electrodes needed in electrochemical ammonia synthesis

Ammonia synthesis is the process by which N_2 and H_2 are formed into NH_3, usually under catalytically controlled conditions [126]. Industrially, this is traditionally accomplished through the Haber-Bosch process, which requires high temperature (400-500 °C) and pressure (20-40 MPa), and high energy based on fossil fuels [127], [128]. The method contributes to approximately 1.8 % of global carbon emissions, making it a critical target for sustainable technological reform [129].

In recent years, particular interest has been attracted by the so-called green ammonia, in which the NH_3 is produced by using H_2, which has been produced with renewable energy. This approach supports climate goals as it can reduce the carbon footprint of the synthesis. As a result, research is oriented towards electrochemical synthesis methods in which NH_3 can be produced directly from water and air at ambient conditions. These methods offer a promising alternative to energy-intensive Haber-Bosch process, with energy-efficient and environmentally sustainable NH_3 production. [130]

EAS is based on the principle of driving NRR at the cathode using electrons and protons generated from water oxidation at the anode. As illustrated in Figure 14 [131], water molecules are split at the anode into protons (H^+) and electrons (e^-) via the reaction

$$2H_2O \rightarrow 02^+ + 4H^+ + 4e^-. \quad (7)$$

As shown in Figure 14 the protons migrate through the electrolyte, while the electrons flow through an external circuit to the cathode. At the cathode, N_2 gas reacts with the supplied protons and electrons to produce NH_3, according to the reaction

$$N_2 + 6H^+ + 6e^- \rightarrow 2NH_3. \quad (8)$$

This electrochemical route enables decentralized NH_3 production under ambient conditions and offers a promising, sustainable alternative to the conventional Haber-Bosch process. [132], [133]

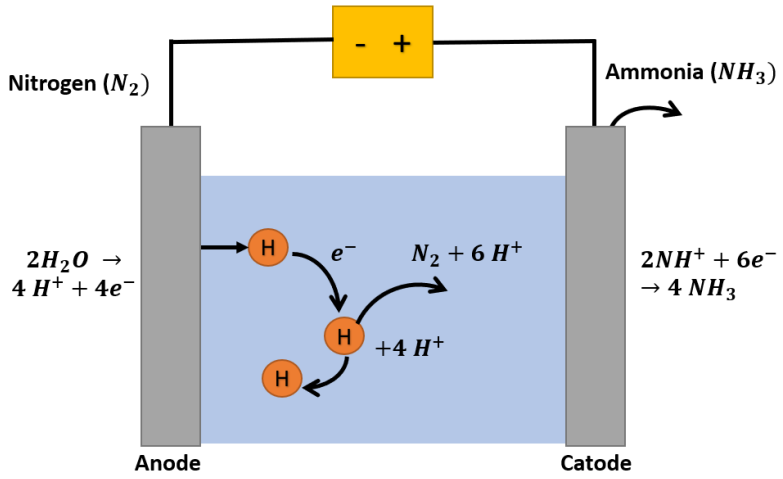

Figure 14 Schematic of EAS. Reproduced from [131] which is under an open access Creative Common CC BY licence.

As illustrated in Figure 14, the EAS system consists of several components, among which the electrodes play a central role [131]. The anode and cathode not only facilitate the respective oxidation and reduction reactions but also directly influence the overall reaction efficiency, selectivity, and stability. Therefore, the development of advanced electrode materials and the careful selection of their surface properties are critical in improving the performance of the process. Optimized electrode design can enhance reaction kinetics, promote N_2 adsorption and activation, and reduce competing side reactions such as HER. [8], [134]

The properties of electrode materials in EAS are decisive for determining the overall performance and efficiency of the system [135]. Electrodes must exhibit high selectivity for the NRR to suppress competing side reactions, particularly HER, which often dominates in aqueous electrolytes [136], [137]. Good electrical conductivity is also required to ensure efficient charge transfer between the external circuit and catalytic sites. Another critical factor is strong catalytic activity toward N_2 activation, which is frequently the rate-limiting step due to the inertness of the N≡N triple bond [138]. To address this challenge, electrodes should provide a large surface area to increase the exposure of active sites and enhance mass transport [139]. Long-term chemical and structural stability in the electrolytic environment is equally important to prevent degradation or leaching during operation [140], [141]. A wide range of material classes has been investigated to meet these requirements, including metal-based catalysts (e.g., Fe, Mo, or Ru), composites that combine complementary functionalities, polymers with tunable chemical properties, and biobased materials that provide environmentally sustainable alternatives [142], [143]. The integration of these material properties is central to the design of efficient and scalable electrodes for EAS.

4.1 Hydrophobic surface

Surface processing of electrodes, such as surface texturing, enables the tailoring of functional properties that directly influence electrochemical performance [7]. By modifying surface microstructure and chemistry, it is possible to enhance catalytic activity, electrical conductivity, and wettability [144], [145]. One such functional property is hydrophobicity, which can be deliberately introduced to improve interfacial behaviour during electrochemical reactions [146].

Hydrophobic surface modification of electrodes, particularly the cathode, has been identified as a promising strategy to improve the efficiency, selectivity, and durability of EAS systems [147], [148]. Since the NRR occurs at the cathode, where N_2 competes with protons (H^+) and electrons (e^-) for access to catalytic sites [149], a hydrophobic surface plays a key role. Hydrophobicity helps to maintain gas-accessible pathways by limiting water intrusion, which is essential for efficient N_2 transport to the electrode [150]. Restricting water accumulation at the surface, hydrophobicity suppresses HER, the competing side reaction that reduces NH_3 yield. As a result, hydrophobic cathodes improve NRR selectivity, increase the Faradaic efficiency (FE), defined as the fraction of charge used for the desired reaction, and contribute to electrode stability under electrochemical operating conditions. [151], [152], [153] On hydrophilic electrodes, the electrolyte wets the surface readily, leading to a continuous washing effect that enhances proton availability but simultaneously intensifies competition from HER. By contrast, hydrophobic surfaces limit direct electrolyte contact, which reduces proton flooding and increases local N_2 availability at the reaction sites, thereby improving NH_3 selectivity. However, if the hydrophobicity becomes excessive, ionic contact with the electrolyte may be restricted, resulting in diminished conductivity and reduced overall current density. [154]

Effective NRR at the cathode requires balancing the delivery of N_2 and protons to active sites while suppressing HER [155]. Hydrophobic surfaces support this by limiting liquid water penetration into the catalyst or gas diffusion layer (GDL), thereby preserving gas pathways and promoting stable three-phase boundary formation. Expanded polytetrafluoroethylene (ePTFE) membranes are used as hydrophobic GDLs, as they combine high gas permeability with strong water repellence [156]. Goldman et al. (2024) [156], demonstrated that incorporating ePTFE into a zero-gap CO_2 electrolyser, stable operation is maintained with high Faradaic performance. The cell achieved voltages of 2.5 V and FE above 90% for C_2^+ products at 200

mA cm^{-2}. This highlights how hydrophobic GDLs prevent electrolyte flooding, sustain mass transport, and ensure long-term stability. Such benefits are transferable to EAS systems, where efficient gas diffusion and interface stability are critical for high performance [141].

Hydrophobicity has also been shown to enhance mass transport under pressurized conditions [157]. Controlled wettability allows higher current densities without sacrificing the selectivity [158]. Vediyappan et al. (2024) [158], have demonstrated how the integration of a hydrophobic gas diffusion layer (hydrophobic-GDL) in a pressurized polymer exchange membrane (PEM) water electrolyser, mass transport characteristics are enhanced under elevated water pressure. Hydrophobic-GDL prevents water from penetrating into the carbon paper, thus maintaining effective separation between gas and liquid phases at the electrode surface. This structural configuration enables efficient gas evolution and minimizes membrane dehydration. The results have shown that increasing water pressure from 0.1 to 0.4 MPa lead to a consistent rise in current density, from 64 to 117 mA cm^{-2} at 25 °C, and up to 237 mA cm^{-2} at 80 °C with a cell voltage of 1.6 V, indicating improve in water availability and reduce of mass transport limitations. These findings support the argument that hydrophobicity, particularly under pressurized conditions, facilitates enhanced mass transport by preventing electrolyte flooding and improving reactant access at the catalyst interface, thereby enabling higher operating current densities without compromising efficiency or selectivity. This is especially relevant in high-rate electrolysis setups, with water electrolysis done with high current density, where excessive water accumulation would otherwise lead to performance degradation [159], [160].

In addition to improving transport and selectivity, hydrophobic layers can extend the operational lifetime of electrodes [156]. By reducing continuous exposure to electrolyte, hydrophobic surfaces protect catalytic materials and support structures during prolonged operation. Hydrophobic layers act as a protective barrier against electrolyte-induced damage while maintaining gas access, which slows down degradation and extends electrode/catalyst lifetime. [162], [163] The study done by Khorsand et al. (2014) [163] provides support for the protective role of hydrophobic surfaces in enhancing the durability of electrodes in electrochemical environments. Carbon-based gas diffusion electrodes modified with hydrophobic agents, specifically polytetrafluoroethylene (PTFE), were investigated and their performance was evaluated during long-term electrolysis. The results have shown that hydrophobic PTFE-treated electrodes exhibit structural integrity improvement and operational stability compared to the untreated samples. Over extended operation, the untreated electrodes suffer from electrolyte flooding, catalyst layer delamination, and performance degradation. The

hydrophobic layer act as a physical barrier that minimized prolonged exposure to aqueous electrolytes. The results indicate that hydrophobic treatment not only enhances initial electrochemical performance but also prolong the functional lifetime of electrode by maintaining stable gas–liquid interfaces and by protecting the underlying catalytic structure from chemical and mechanical deterioration.

Hydrophobic surface functionalities at the cathode represent an effective strategy for improving EAS efficiency and electrode lifetime. By supporting efficient gas diffusion, stabilizing electrochemical interfaces, and protecting against degradation, hydrophobic electrodes contribute to the development of high-performance and sustainable systems. [141], [150], [163] These advances support objectives in green NH_3 production, by providing possible solutions for material and component selection, which additionally help to reduce energy consumption and carbon emissions of the process.

4.2 Coating properties and adhesion

Electrode surfaces must exhibit catalytic functionality in EAS to enable efficient NRR while maintaining stability during continuous operation [164]. Unlike inert conductive substrates, functional electrodes require surface characteristics that actively promote NRR, suppress competing reactions, and support long-term durability. These properties are often introduced by applying catalytically active coatings tailored to enhance electrocatalytic efficiency, selectivity toward NH_3, and resistance to degradation in electrolyte environments [165]. When the substrate lacks inherent catalytic activity or stability, the coating provides the necessary functional properties, while the substrate mainly serves as a conductive and structural support [166]. Nevertheless, substrate features such as surface topography or microstructure introduced during fabrication or surface treatment can still influence electrode performance by affecting mass transport, adhesion or local reaction environments [167].

Most important requirements for catalytic coatings are in high electrocatalytic efficiency, strong selectivity toward NH_3 formation, and stability under electrochemical conditions [168], [169], [170]. However, another significant aspect is mechanical durability of the electrode, which depends on the structural and electronic design of the catalyst, including the distribution of active sites and favourable metal combinations that facilitate charge transfer and accelerate reaction kinetics [171], [172]. Wang et al. (2024) [173] have used RuMo alloy nanoflower structures with a face-centred cubic (fcc) phase. Nanoflower structures resemble flower

morphology in microscopic scale [174]. The results have shown that the nanostructures enhance nitrate-to-ammonia conversion, achieving high FE of 95.2 % and durability due to favourable electron redistribution and an optimized d-band center, which improve electroactivity and electron transfer of the electrode surface. Guo et al. (2025) [175] have fabricated catalysts composed of copper nanowires encapsulated in ZIF67 (CuNW@ZIF67) structures. These structures demonstrate enhanced catalytic performance with FE of 93.7 % and high energy efficiency of over 30 %, due to their optimized morphology and synergistic electron interactions. Equally important is the ability of the catalyst to selectively direct the reaction pathway toward NH_3, minimizing the formation of undesired by-products. Yan et al. (2024) [176] have shown that a catalyst made of phosphorus-doped copper clusters combined with cobalt hydroxide nanosheets ($P-Cu/Co(OH)_2$) achieved this by managing both steps (NO_3^- to NO_2^- and NO_2^- to NH_3) of the nitrate-to-ammonia conversion. The phosphorus doping improved the electronic properties of the catalyst, helping to keep the nitrite intermediate on the surface long enough for it to be fully converted to NH_3. This design resulted in a high FE of 97.04 % and reduced the formation of unwanted by-products. The electrocatalytic coatings also need to remain chemically and structurally stable under the electrochemical conditions [177]. Materials like Cu/PTS, CoW/CF, and titanium hydride have been shown to maintain high activity and stability over extended use. These materials could be therefore used as electrode coating materials in practical applications when designing a system for NH_3 synthesis. [172], [176], [178]

Coatings need to remain structurally stable and firmly bonded to the substrate surface during operation [179]. Weakly bonded or structurally unstable coatings are prone to delamination (separation of a layered material into individual layers), dissolution (material dissolves into a solvent to form a homogeneous solution), or restructuring under harsh electrochemical conditions, leading to a loss of activity and reduced electrode lifetime [180], [181], [182]. Coatings acts as a protective barrier for substrate material, preventing for example corrosion in NH_3 environment [183]. Effective surface preparation before coating deposition improves adhesion and is therefore a critical step in electrode manufacturing [184].

A key mechanism that governs the coating adhesion is mechanical interlocking, which relies on the interaction between the coating and the microscopic irregularities of the substrate surface. Features – such as ridges, valleys, pores, and micro- or nano-scale roughness – allow the coating material to penetrate and anchor physically into the substrate topography. [185] This improves wetting of the coating onto the surface and establishes physical anchoring points that

resist shear forces and delamination. As a result, the effective bonding area is increased and local stress concentrations are reduced, leading to enhanced adhesion strength, durability, and coating stability. [186] This is particularly important for electrocatalytic systems operating under continuous cycling and in harsh chemical environments, where strong interfacial bonding ensures long-term performance and reliability [140], [141].

Surface texturing with laser systems has emerged as an effective approach for enhancing coating adhesion and stability through both physical and chemical surface modification. Controlled laser irradiation produces micro- and nanostructures that enlarge the surface area and promote mechanical interlocking of the coating. [187] These textured surfaces reduce local stress concentrations and improve the mechanical anchoring of the catalytic layer, thereby minimizing the risk of delamination under cyclic loading or thermal expansion [188]. The study by Kromer et al. (2015) [189] has shown that laser surface texturing improves coating adhesion by creating micro-dimpled patterns that enhance mechanical interlocking. A pulsed fibre laser with a wavelength of 1064 nm, a pulse duration of 100 ns and repetition rate from 20 to 100 Hz, was used to laser surface texturing process. In tensile adhesion tests, laser-treated aluminium substrates reached adhesion strengths of up to 60 MPa, compared to only 20 MPa for grit-blasted references. In laser shock adhesion tests (LaSAT), the textured surfaces withstood laser pulse energies up to 2.5 J, whereas untreated samples delaminated at 0.8 J. The increased adhesion was attributed to micro-dimple arrays that improved mechanical interlocking and enlarged the bonding area, confirming the effectiveness of laser surface texturing in improving coating durability.

In EAS, electrodes are continuously exposed to pressurized electrolytes, reactive intermediates, and potential cycling. Under such conditions, the combination of catalytic coatings and laser pre-treatment is highly valuable. This strategy enhances both catalytic performance and mechanical robustness, ensuring long-term stability. Applying laser treatment before catalyst deposition therefore represents a key enabling step for advanced electrode materials in sustainable NH_3 production.

5 Aim and purpose of experimental part

The aim of the experimental part is to investigate how laser surface texturing can be used to fabricate hydrophobic surface structures on stainless steel substrate. The primary objective is to understand how micro- and nanoscale surface features generated by laser processing affect the surface wettability, topography and coating behaviour. These aspects are essential for tailoring surface properties for applications where control over water repellence and surface interactions is critical.

The experimental part of the thesis is divided into three main stages, as illustrated in Figure 15. Each stage includes specific characterization steps that support the final analysis.

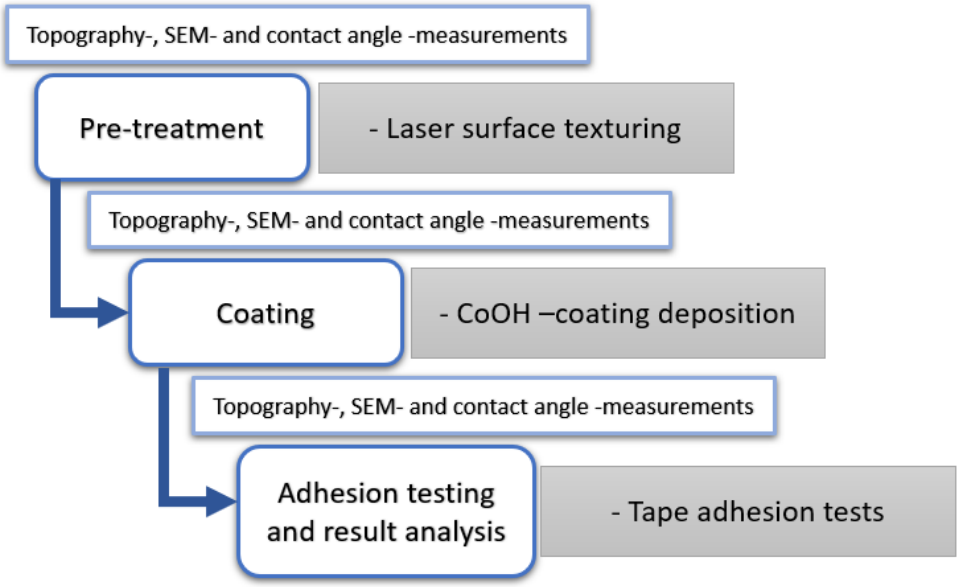

Figure 15 Steps of experiments for this thesis.

In the first part (see Figure 15), laser surface texturing as a pre-treatment is applied to stainless steel surfaces using selected parameter sets. Surface characterization is then performed, including topographic profiling, SEM and contact angle measurements. These techniques provide a comprehensive understanding of the resulting surface textures and wettability before coating.

The second part of the experiments (see Figure 15) involves applying the CoOH -coating to the laser textured surfaces. After coating, the same set of surface analyses is repeated to evaluate how the coating interacts with the underlying textures and whether any changes occur in wettability or morphology.

In the final stage, adhesion testing is conducted on the coated surfaces, as shown in Figure 15. The goal is to assess whether laser texturing improves the coating adhesion and to identify which surface features contribute most effectively to mechanical interlocking. The results are then analysed in the context of the earlier surface characterizations to establish correlations between structure, wetting behaviour and adhesion strength.

An important part of the study is the comparison of different surface patterns, which are fabricated with different laser surface texturing parameters. These patterns differ in their geometry, spacing and line structure, and are designed to investigate how the characteristics of surface texture influence the ability to induce hydrophobic behaviour. The laser-induced textures include both line and grid patterns, enabling evaluation of how directional features and intersecting topographies affect liquid–solid surface interaction. The work aims to determine which types of surface textures most effectively promotes water repellence, both on bare metal surfaces and when coated.

In addition to laser-induced hydrophobicity, the study also examines how a coating applied to the laser textured surfaces interacts with the underlying patterns. This includes assessing (1) whether the coating modifies or preserves the wetting behaviour of surface, and (2) how well the coating adheres to different textured structures. The influence of surface roughness, feature size, and pattern uniformity on coating performance is also explored. The relationship between surface morphology and coating adhesion is analysed to evaluate whether laser texturing can enhance the durability, consistency, or the functional performance of the coating under conditions where surface wettability plays a critical role.

6 Experimental setup

6.1 Material

The material used in the experimental work is AISI 316L austenitic stainless steel, supplied by Acerinox Europa. This material was chosen due to its chemical stability, corrosion resistance, and mechanical integrity, which are desirable properties for electrodes used in EASs. Its low carbon content and alloying elements – such as chromium, nickel and molybdenum – contribute to its resistance against localized corrosion in electrolytic environments. These characteristics make it a practical substrate for surface modification studies, where the objective is to tailor the electrode surface to improve wettability, chemical compatibility, or the electrochemical performance. [190]

The stainless steel was supplied as 5.0 mm thick sheets with a 2B surface finish according to the EN 10088-2 material standard. The chemical composition of the steel, as confirmed by spectrometric analysis, is presented in Table 2. The three main alloying elements besides iron are chromium (16.5 %), nickel (10.0 %), and molybdenum (3.00 %), with iron being in balance, all of which contribute to the corrosion resistance and stability of material. The low carbon content (0.018 %) helps prevent sensitization during welding or heat exposure. [191]

Table 2 Nominal chemical composition-% of 316L stainless steel.

Elements	C	Cr	Mn	Mo	N	Ni	P	S	Si
316L	0.018	16.5	1.34	2.10	0.043	10.0	0.031	0.008	0.472

Mechanical properties of the material were determined by the supplier and are shown in Table 3. The offset yield strength ($Rp_{0.2}$) was measured as 338.56 MPa, the proof strength ($Rp_{1.0}$) as 378.49 MPa and the ultimate tensile strength (Rm) as 598.01 MPa. The elongation break with 50 mm gauge ($A50$) was 55.50 % and with 5 mm gauge ($A5$) was 56.6 %, indicating good ductility, and the Rockwell hardness was measured as 84 HB. These values confirm that the material has sufficient mechanical strength while retaining formability, which is essential in experimental processes involving surface structuring and mechanical testing.

Table 3 Mechanical properties determined by the supplier of the 316L stainless steel.

Rm (MPa)	$Rp_{0.2}$ (MPa)	$Rp_{1.0}$ (MPa)	A50 (%)	A5 (%)	HRB
598	339	379	55.5	56.6	84.0

The material was delivered in accordance with the EN 10088-2 standard and underwent a solution annealing heat treatment between 1050–1100 °C and cooling with air. All values were verified by a third-party laboratory in accordance with ISO 17025 methodology.

6.2 Hardware

Nanosecond pulsed fibre laser

The laser system used in this thesis for surface texturing is the IPG YLPN nanosecond pulsed fibre laser, which has an integrated 2D scanner head. The laser operates within a wavelength range of 1055–1075 nm, with a typical average? wavelength of 1064 nm, and delivers a maximum average power of 100 W. The focal distance is 283 mm from the lens, resulting in a beam diameter of approximately 60 µm at the focal point.

The processing area is enclosed by a metal shielding on all sides to ensure working safety, as shown in see Figure 16. Although the system operates under standard indoor air conditions, the combination of ambient air and localized heating from laser pulses can cause unwanted surface oxidation. Argon gas was introduced into the work area to prevent oxidation during laser processing at a flow rate of 20 l/min, serving as a protective and inert atmosphere. The complete experimental setup for laser surface texturing is shown in Figure 16.

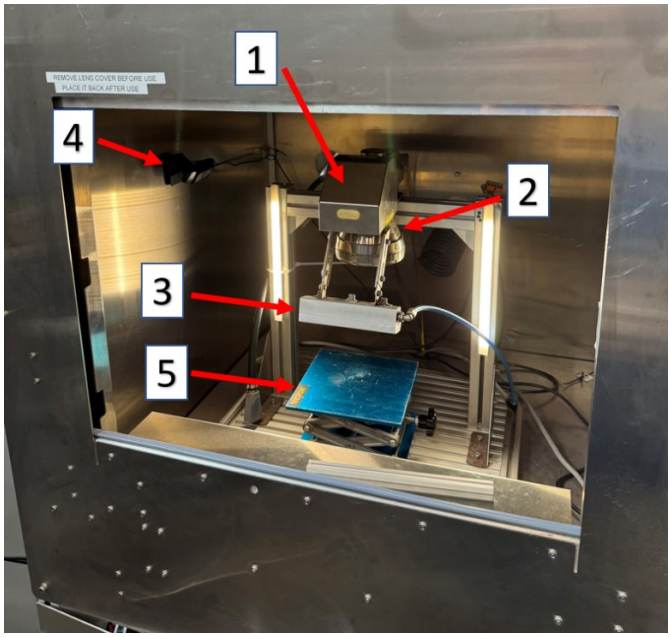

Figure 16 Laser system and setup used in experimental part.

As shown in Figure 16, the laser setup consists of the scanner head (1) mounted above the working area and connected to the laser system. The laser output (2) is directed vertically

through the scanner optics onto the sample surface. An air blade (3) blows room air across the optical path, deflecting fumes and particles to prevent contamination or thermal damage to the optics. A web camera (4) is used to monitor the process in real time. The working area is on tops of an adjustable platform (5) which can be then raised or lowered to align the sample with the focal plane of the laser.

Figure 17 shows a close-up image of the laser system used in the study.

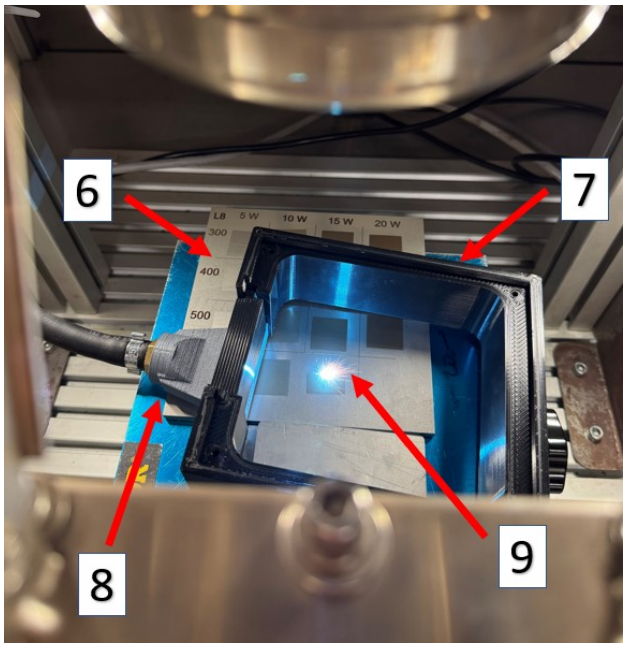

Figure 17 Closeup of the laser setup used in the experiments.

A close-up view is shown in Figure 17, where the workpiece (6) is positioned within the gas barrier (7). The gas barrier helps to retain the protective atmosphere over the treated surface during processing. Argon gas is introduced via the argon outlet (8), flowing steadily over the workpiece to minimize oxidation during laser processing. The laser beam (9) is visible in the centre of the treated area. While it appears as a bright (there is a broad spot in the image due to rapid scanning and exposure), the actual focused beam diameter is approximately 60 µm.

Laser fluence refers to the amount of laser energy delivered per unit area, expressed in joules per square centimetre (J/cm²) or joules per square millimetre (J/mm²) (SI unit). It is a key parameter governing the extent of material interaction, such as melting, ablation, or surface modification. [192] For the laser system used in this study, fluence can be calculated using Equation (8).

$$F = \frac{P}{t \cdot A} \tag{8}$$

where P is the laser pulse power, t is the pulse length and A is the beam cross-section area.

Microscopy imaging system

The optical microscopy system used in this thesis for surface inspection and imaging was the Motic AE2000MET inverted metallurgical microscope, shown in Figure 18. This microscope is designed for examining polished cross-sections and bulky metallic samples that are too large for conventional upright microscopes. It enables detailed analysis for applications such as material characterization, quality control, and failure analysis.

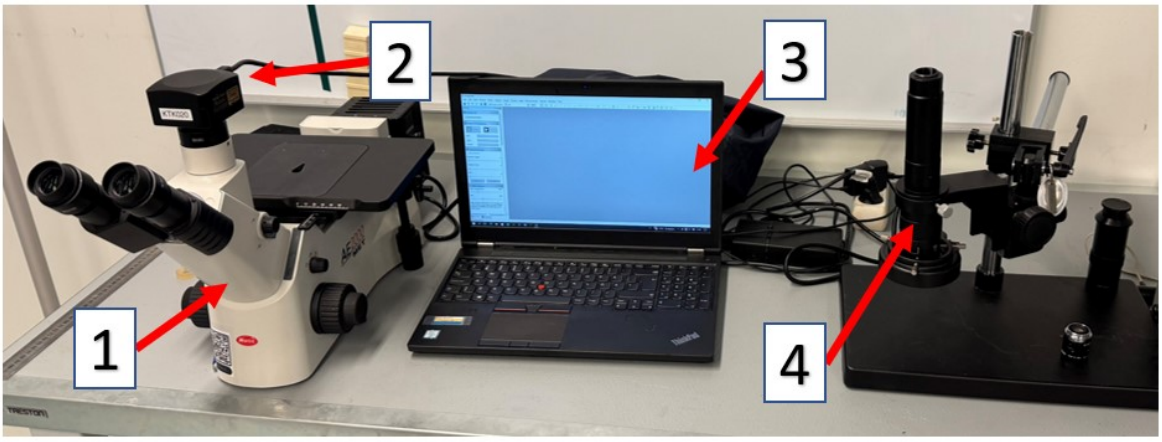

Figure 18 Optical microscope used in the experimental part.

As shown in Figure 18, the setup consists of the inverted metallurgical microscope (1) equipped with a trinocular head, providing magnifications from 5x to 100x. A digital camera (2) mounted on the trinocular port transfers live images to the connected computer for both real-time observation and image capture. The computer (3) is used for image analysis and documentation of the saved micrographs. For additional flexibility, the system includes a macro-imaging unit (4) with interchangeable magnification heads, such as a 1x lens, allowing capture of wider field-of-view images to complement the high-magnification optical analysis.

Coating system

Coating deposition in this thesis was carried out using a CEM Discover 2.0 Microwave Synthesizer. The system is designed for controlled chemical reactions and thin film depositions under microwave irradiation. It combines a single-mode 300 ml microwave cavity with a 900

W magnetron, enabling rapid and uniform volumetric heating of liquid and solid-phase samples.

The instrument is equipped with Activent technology, which provides automated pressure management by releasing gaseous by-products during processing, thereby preventing vessel failures and ensuring safe high-pressure operation. The temperature is monitored by a patented iWave sensor, a non-contact infrared sensor capable of measuring sample temperature directly through glass or Teflon vessels, ensuring accurate and reproducible heating without fragile thermocouples.

Figure 19 shows the coating deposition system used in the study.

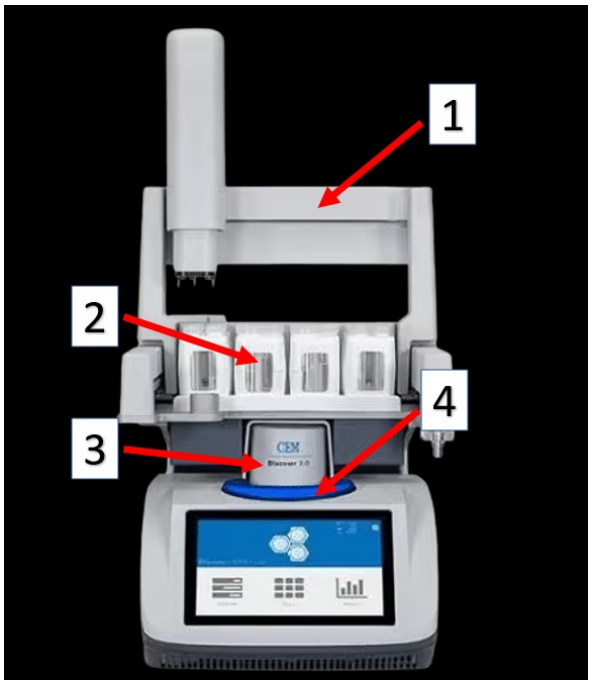

Figure 19 Coating deposition system used in the experimental part.

As shown in Figure 19, the main system components include the automatic sampler (1) for handling multiple vessels, reaction vessels (2) where coating deposition takes place, the attenuator port (3) for coupling microwave energy into the cavity, and the Activent pressure device (4) for controlled venting. The integrated touch-screen interface enables programming of coating cycles and monitoring of reaction progress in real time.

3D surface measurement system

Surface topography measurements in this thesis were performed using a Bruker Alicona InfiniteFocus G6 optical 3D surface measurement system (see Figure 20). The device operates

based on non-contact, optical, three-dimensional metrology, using Advanced Focus Variation (Smart Flash 2.0) and Vertical Focus Probing technologies. This enables high-resolution imaging and accurate characterization of both rough and polished surfaces, regardless of reflectivity.

The system is capable of acquiring up to 4.6 million measurement points per scan, with a positioning volume of 200 x 200 x 100 mm, tilt range from –15° to +90°, and compatibility with objects weighing up to 30 kg (with special mounting). In this thesis, the system was used to evaluate the surface structure of laser textured stainless steel surfaces by capturing 3D topography and analysing areal surface roughness parameters *Sa* (arithmetical average roughness) and *Sz* (mean peak-to-valley height).

The analysis of the 3D point cloud data was carried out using MetMax: Laboratory Measurement Module, version 10.0.2, which allowed for precise extraction of surface roughness metrics as well as 2D profile sections from the measured data. This enabled comparison between different surface texturing strategies and supported quantitative assessment of the effects of laser texturing.

Figure 20 shows the surface measurement system used in the study.

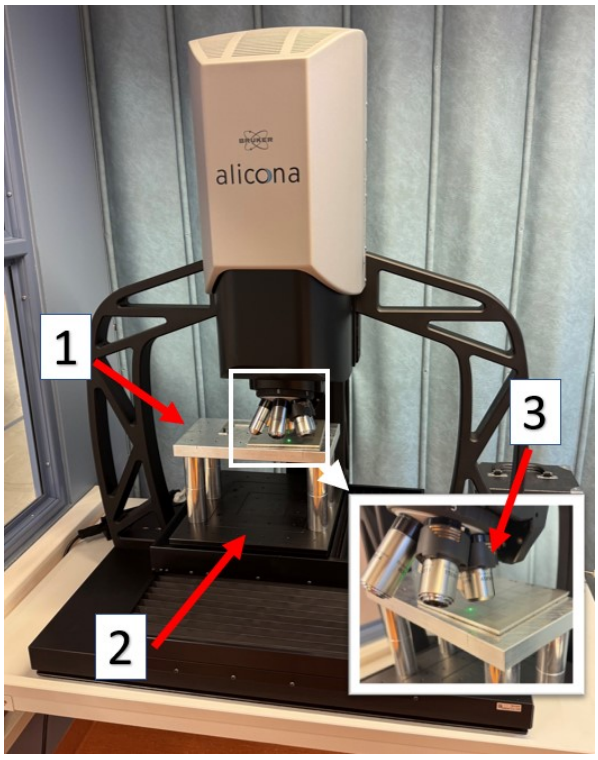

Figure 20 Bruker Alicona InfiniteFocus G6 optical 3D surface measurement system.

As shown in Figure 20, the Alicona measurement system includes the sample holder (1), where the specimen is fixed during scanning. The motorized platform (2) enables precise X, Y, and Z positioning of the surface of sample to align the measurement area accurately. The objective lenses (3) mounted on a rotating turret offer magnification options ranging from 5x to 100x, allowing both wide-field and high-resolution imaging of surface features.

Scanning electron microscope

SEM analysis in this thesis was performed using a Thermo Scientific Apreo S field-emission scanning electron microscope (FE-SEM), equipped with multiple advanced imaging and analysis capabilities. The system features a Schottky field emission gun (FEG) electron source, providing high beam stability and resolution with an acceleration voltage range from 0.2 kV to 30 kV and beam currents from 1 pA to 400 nA. The microscope supports both high and low vacuum operation (LoVac: 10–500 Pa with H_2O), and its compound lens system enables variable imaging modes, including electrostatic, field-free magnetic, and magnetic immersion lens configurations.

The Apreo S microscope is equipped with a wide range of detectors, including three in-lens and in-column secondary electron and backscatter electron (SE/BSE) detectors, an Everhart-Thornley detector, low-vacuum SE, and lens-mounted BSE detectors, as well as retractable scanning transmission electron (STEM) and cathodoluminescence detectors. For elemental analysis, the system includes an Oxford Instruments Ultim Max 100 EDS spectrometer, with a 100 mm^2 Peltier-cooled sensor, enabling rapid live chemical imaging, particle analysis, and element mapping from beryllium (Be) to californium (Cf). The microscope uses AZtec 6.1 software, which includes advanced modules for automated large-area mapping, image registration, and feature classification. The imaging chamber is monitored with an integrated IR camera and navigation tools for precise sample positioning. FE-SEM system used in this study is presented in Figure 21.

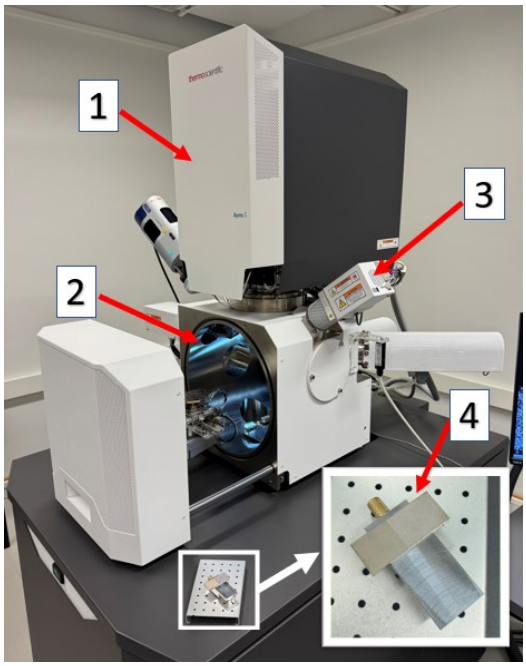

Figure 21 Thermo Scientific Apreo S FE-SEM.

As shown in Figure 21, the microscope includes the electron column (1), which houses the Schottky FEG source and beam optics. The sample chamber (2) is centrally located and provides access to the multi-axis stage and internal detectors. The system is equipped with multiple detectors (3), including those used for secondary electron, backscattered electron, and X-ray signal collection. The inset image shows the sample holder (4) used to mount the stainless steel specimens during imaging and energy dispersive X-ray spectroscopy (EDS) analysis.

Contact angle measuring system

Contact angle measurements in this study were performed using the Attension Theta optical tensiometer, a precision instrument for characterizing surface wettability and surface free energy. The measurement system used in this study is presented in Figure 13.

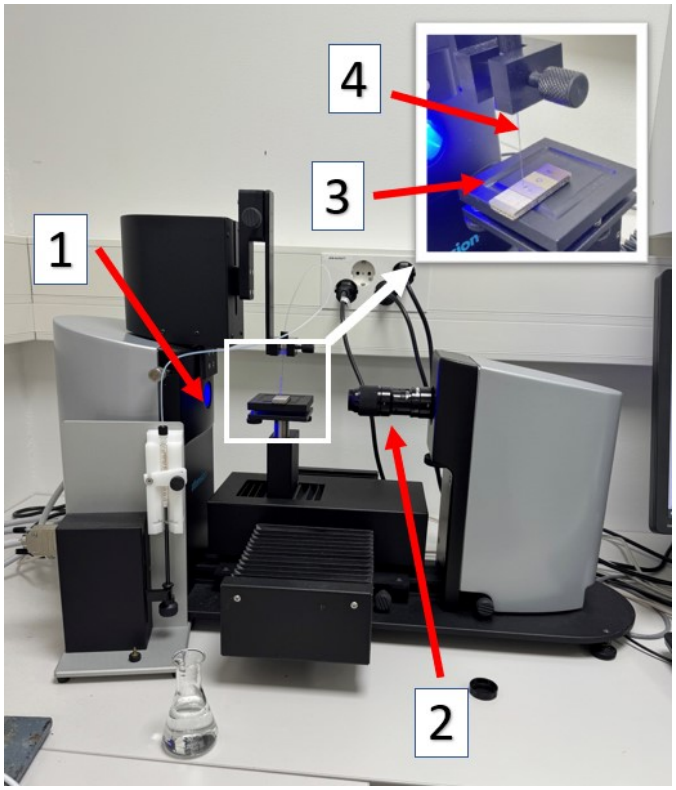

Figure 22 Attension Theta optical tensiometer.

The system employs a high-resolution drop shape analysis by capturing side-profile images of liquid droplets on solid surfaces. A monochromatic cold LED light source (1) ensures consistent illumination while minimizing sample evaporation, and a high-resolution digital camera combined with precision optics (2) provides an accurate image capture of the droplet contour. The instrument is equipped with a motorized sample stage (3) for precise alignment and positioning, and a syringe mechanism (4) for dispensing controlled volumes of test liquids onto the sample surface.

Measurement is based on fitting the droplet profile to a theoretical shape model, accounting for the effects of surface tension, gravity, and liquid density. All measurements and analyses were performed using the OneAttension software, which supports automated droplet detection, baseline adjustment, and contact angle fitting.

Adhesion measurement setup

Adhesion measurements test were done in this thesis using a standardized tape test set up. Measurement setup is presented in Figure 23.

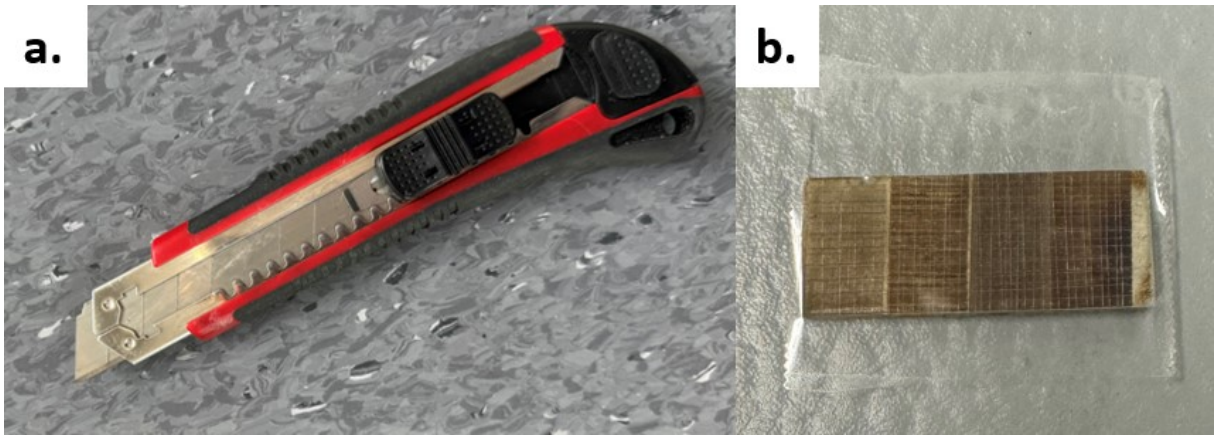

Figure 23 Adhesion testing set ups, including a) exacto knife used in surface scoring, and b) tape piece layer on top of coated surfaces.

Figure 23 shows the adhesion measurements setup used in the study. The setup consisted of a precision exacto knife (a) for scoring the coating layer and a pressure-sensitive adhesive tape (b) to evaluate the coating detachment from the laser-textured stainless steel specimens. Together, these components provide a hardware configuration for assessing coating adhesion according to established grading scales.

7 Experimental procedure

7.1 Pre-treatment

The objective of the pre-treatment stage was to evaluate the suitability of various laser parameters for generating micro- and sub microscale surface textures capable of modifying the surface wettability of stainless steel. Surface texturing was carried out using a nanosecond pulsed fibre laser system, operated under ambient atmospheric conditions with Argon-gas as additional shielding gas during laser processing. The majority of laser processed surfaces were stored in ambient air for a period of 20 days prior to the characterization and coating, to account for realistic handling and testing conditions. This storage was intended to simulate practical exposure-related aging effects such as mild oxidation or airborne contamination. In addition, freshly textured surfaces were included in the inspection to enable a preliminary comparison between aged and fresh surfaces, providing an insight into possible time-dependent changes in hydrophobic behaviour. While the potential impact of atmospheric exposure was not quantitatively analysed in this study, it was acknowledged as an important factor for future research.

A matrix of 30 discrete parameter combinations were designed, for exploring the wide parameter space. The parameters varied in laser power (10–40 W), pulse width (1 ns – 100 ns), pulse frequency (20–100 kHz), scanning speed (1500–2000 mm/s), fill pitch (0.02–0.5 mm), and number of repetitions (1–7). Each combination was applied to a 2 x 2 cm square section of the substrate, resulting in a 6 x 5 array of test surfaces. The complete matrix on preliminary tests is provided in Appendix 1.

Surface wettability was preliminarily evaluated using a qualitative droplet inspection method. Water droplets were gently dispensed on the centre of each laser textured surface using a pipette to avoid impact-driven spreading. The droplet profiles were then inspected visually from a low angle to estimate contact angle and symmetry. This approach enabled rapid screening of all 30 surfaces and was justified by the exploratory nature of this phase. Figure 24 illustrates typical results of this inspection, showing droplets resting on differently textured surfaces. Qualitative differences in droplet shape, including contact angle, were used as indicators of hydrophobicity.

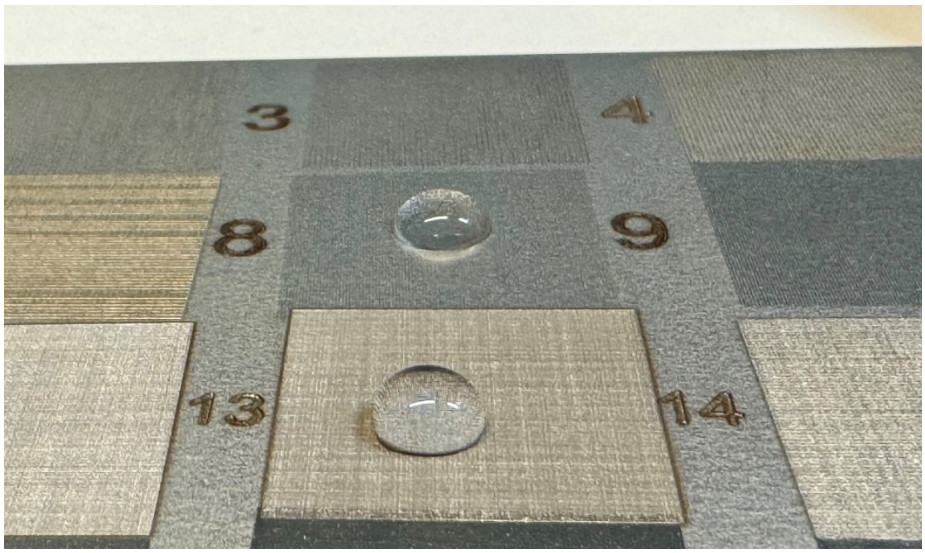

Figure 24 Prelimany testing of hydrophobicity for laser textured surfaces.

Figure 24 shows two water droplets resting on differently textured surface areas. This image was captured from a low angle to emphasize differences in droplet shape and contact angle. The droplet on top of the surface (numbered as eight) appears more flattened compared to the other droplet on top of the surface (numbered as 13), indicating a lower contact angle and thus lower hydrophobicity. In contrast, the droplet (on top of the surface 13) maintains a more spherical shape, suggesting a higher degree of water repellence. The distinct surface finishes in the numbered squares affect the spreading and wetting behaviour of the surface. These qualitative observations support the initial selection of processing parameters for further analysis.

Figure 25 shows a schematic illustration of the two laser scanning strategies used in this study: line pattern (a) and grid pattern (b).

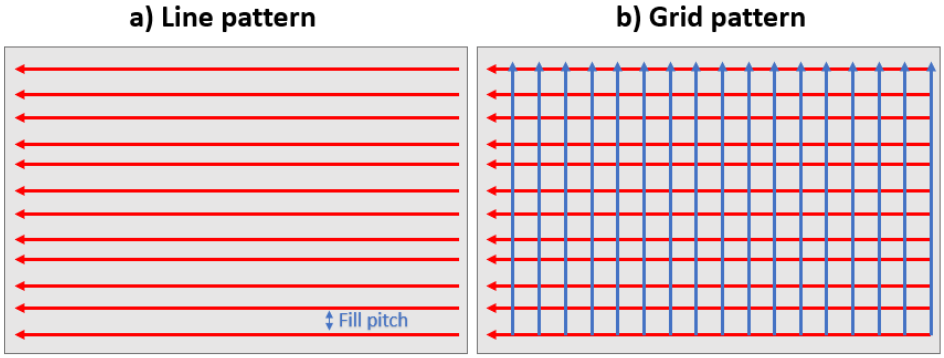

Figure 25 Laser surface texturing patterns: a) line and b) grid pattern.

As seen in Figure 25, for the line pattern, laser scanning is performed unidirectionally with parallel scan lines separated by a constant fill pitch, resulting in a series of evenly spaced laser

tracks. In the grid pattern, the same area is scanned twice, first in the horizontal and then in the vertical direction, producing a crosshatched texture where features overlap in two orthogonal directions. The fill pitch, indicated by the blue arrow, defines the spacing between adjacent scan lines and directly influences the density and resolution of the textured surface. These scanning strategies were employed to investigate the effect of the pattern geometry on surface topography and wettability.

Four parameter combinations, two with line patterns and two with grid patterns, were selected based on preliminary visual droplet inspection and structural assessment by optical microscopy. These surfaces displayed hydrophobic behaviour in the initial tests and were therefore chosen to allow the direct comparison between line and grid geometries. The selection also considered the surface uniformity and structural integrity. The final laser parameters used in this study are presented in Table 4.

Table 4 Laser parameters for laser texuring of surfaces.

	Pattern	Power (W)	Pulse duration (ns)	Frequency (kHz)	Scanning speed (mm/s)	Fill pitch (mm)	Repetition times	Fluence (J/mm^2)
L1	Line	10.0	100	20.0	1500	0.02	7	35.0
L2	Line	40.0	100	100	2000	0.10	5	141
G1	Grid	10.0	100	20.0	1500	0.02	7	35.0
G2	Grid	40.0	100	100	2000	0.10	5	141

As shown in Table 4, surfaces L1 and L2 represent the surfaces processed with line pattern and surfaces G1 and G2 with grid pattern. The L1 and G1 surfaces were processed using laser parameters of power 10 W, pulse duration 100 ns, pulse frequency 20 kHz, scanning speed 1500 mm/s, fill pitch 0.02 mm and repetition times 7. For the L2 and G2 surfaces, the parameters were power 40 W, pulse duration 100 ns, pulse frequency 100 kHz, scanning speed 2000 mm/s, fill pitch 0.1 mm and repetition times 5. Fluences for surfaces L1, L2, G1 and G2 was calculated using Equation (8). Example calculation of fluence is in Appendix 2.

The stainless steel was cut to plates of 18 x 45 mm to fit the coating and measurements systems. Each plate was processed to have surfaces L1, L2, G1 and G2. The processing area for these surfaces was 10 x 18 mm, as shown in Figure 26.

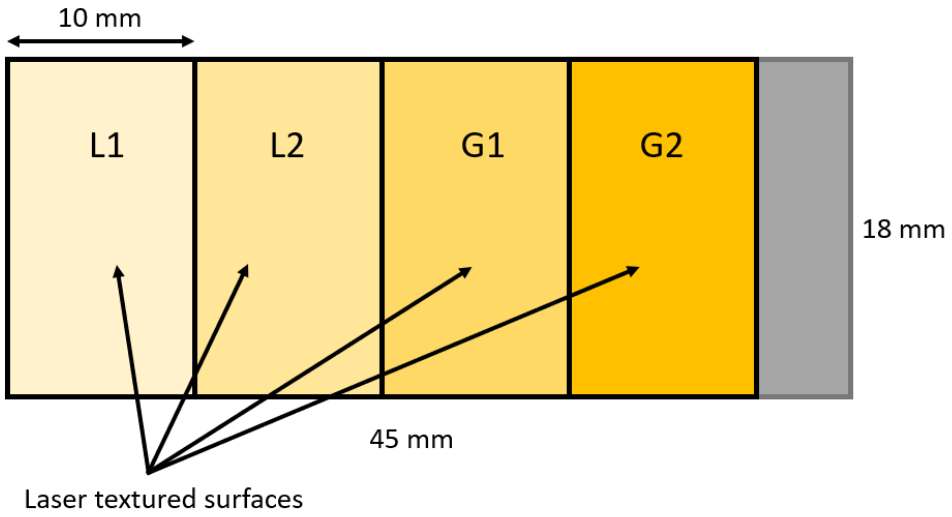

Figure 26 Laser processing areas for laser texturing of the surfaces.

As shown in Figure 26, the laser textured zones were positioned sequentially along the SS plate, with each surface (L1, L2, G1, and G2) occupying an area of 10 × 18 mm. This arrangement enabled a direct comparison of surfaces with line pattern (L1, L2) and with grid pattern (G1, G2) regions under identical material and processing conditions. The grey area represents an unprocessed section on the right side of the plate.

All laser textured plates had identical surface structures and were prepared on the same day, ensuring that all measurements could be repeated on comparable samples to obtain reliable averages, and that the time-dependency of hydrophobicity was consistent throughout all surfaces. Surfaces were the cleaned using compressed air immediately after laser processing, in order to remove dust and other derbies. After laser processing, the plates were exposed ambient air in room temperature and humidity for 20 days, to induce hydrophobicity. This exposure period was chosen based on literature [123], where comparable time frames have been reported as sufficient for wettability transition, while a longer period was not feasible due to the time constraints of this thesis. These plates with laser textured surfaces were used for further analyses, including topography, SEM characterization, and adhesion testing. Four plates were left untreated to act as reference surfaces for measurements and analysis.

7.2 Coating

Cobalt(II) hydroxide (CoOH) coatings were deposited on stainless steel substrates using a CEM Discover 2.0 microwave reactor. Prior to deposition, the stainless steel specimens were cleaned in an ultrasonic bath, first in acetone for 10 min and then in absolute ethanol for 10 min, to

remove any organic contaminants and to ensure good coating adhesion. The deposition solution consisted of 50 mL of deionized water containing 1.46 g of cobalt nitrate hexahydrate ($Co(NO_3)_2 \cdot 6H_2O$) and 0.15 g of urea. The coated samples were prepared under microwave-assisted hydrothermal conditions at 90 °C with a power setting of 150 W for 12 h. After the reaction, the specimens were rinsed with ethanol to remove residual precursors and subsequently dried at 70 °C overnight to stabilize the coatings.

7.3 3D topography

Topographic features of the laser textured surfaces were analysed using optical focus-variation microscopy, which enables quantitative three-dimensional surface reconstruction by capturing height data from changes in optical focus. This technique is suitable for characterizing microscale surface textures, as it provides both colour-coded height maps and numerical line profiles with a vertical resolution of ± 1 µm, depending on the lens and measurement settings.

Figure 27 shows an example image of the measurement results provided from optical 3D topography measurements.

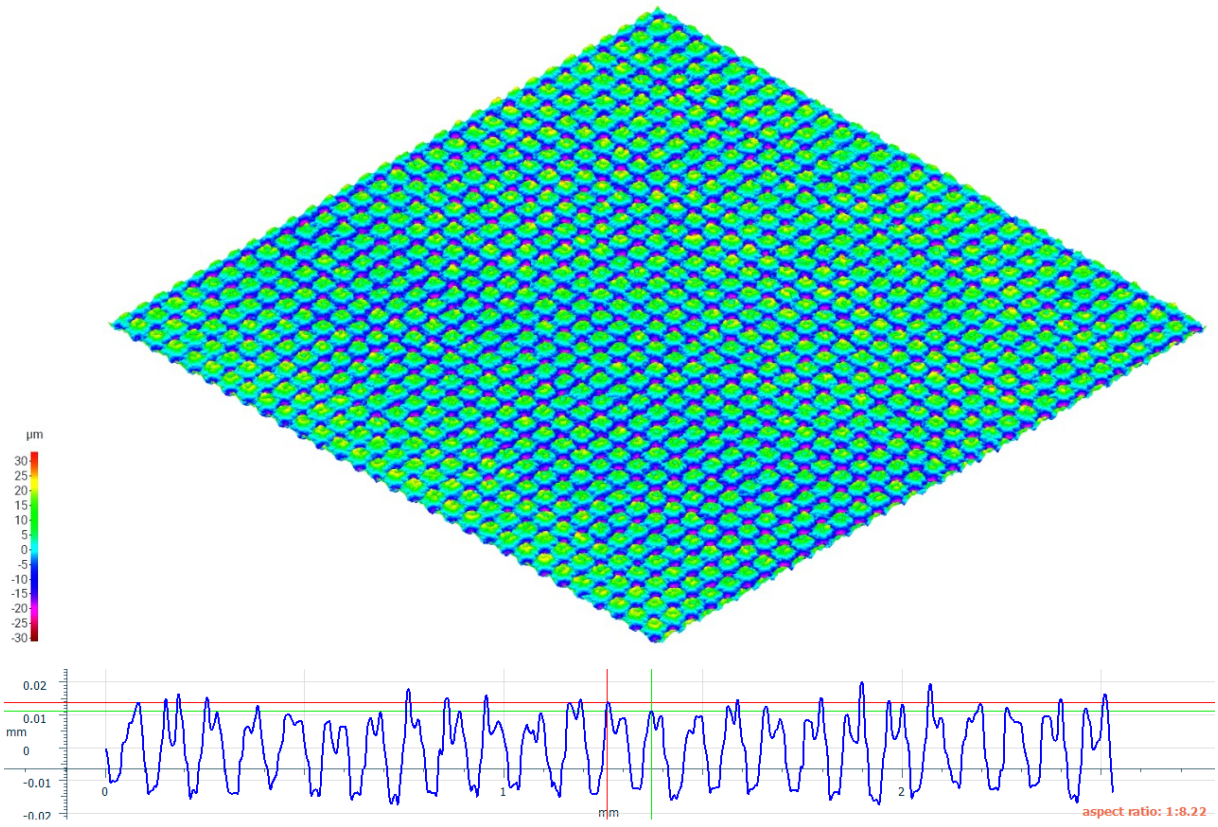

Figure 27 Colour-coded image of surface topography and numerical line profile from optical 3D measurements system used in this thesis.

As shown in Figure 27, the colour-coded map represents the measured surface height variations, where different colours correspond to different elevation levels. The accompanying line profile illustrates the cross-sectional height data along a selected path. This example demonstrates the type of three-dimensional surface information obtained with the optical focus-variation microscope, combining both qualitative visualisation with quantitative numerical data.

The arithmetical average roughness (*Sa*) and mean peak-to-valley height (*Sz*) values were measured for each textured surface (L1, L2, G1 and G2) and nontreated reference surface, to characterize surface roughness on a quantitative scale.

Prior to analysing the laser treated surfaces, a reference profile was measured on a non-treated 316L stainless steel surface to provide a baseline for comparison. Due to the visually smooth and isotropic nature of the non-treated reference surface, only a single cross-sectional profile was extracted in a random direction. This profile served to confirm the surface flatness and the low roughness, offering a point of contrast for the highly structured laser textured regions.

Line pattern analysis

Detailed surface profile analysis was conducted for the surfaces treated using line pattern (L1 and L2). The three different measured line profiles for surfaces textured with line pattern are shown in Figure 28.

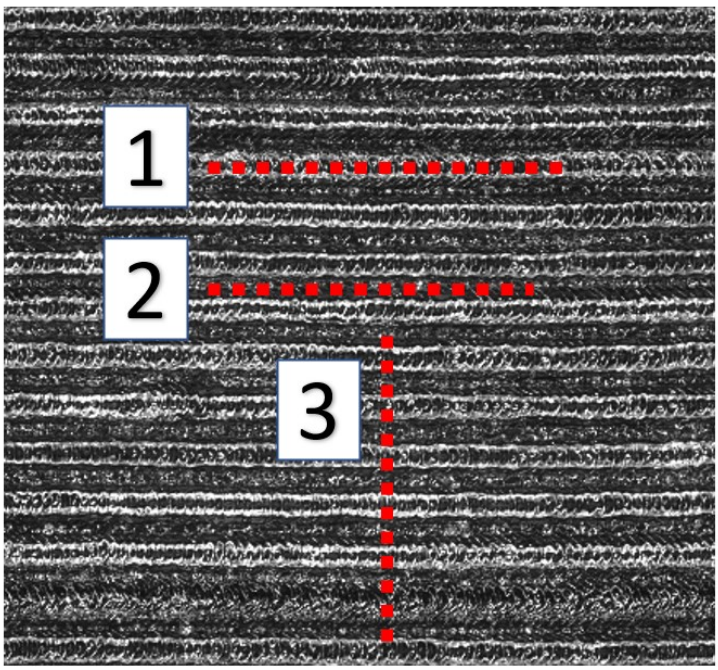

Figure 28 Topographic map of laser textured surface with line pattern. Red profile lines represent: (1) along the laser tracks, (2) between the laser tracks, and (3) across laser tracks.

As shown in Figure 28, three red-dotted profile lines represent the profiles used to characterize the periodic structure of the surfaces:

- Profile 1 – Along laser tracks: This profile follows the crest lines of individual laser tracks, allowing the assessment of surface morphology along the irradiated zones. It reveals the uniformity of track peaks and highlights variations in melt flow or pulse overlap along the scan direction.

- Profile 2 – Between laser tracks: Positioned in the troughs separating adjacent tracks, this profile captures the valley structure between scan lines. It is useful for evaluating the fill pitch regularity and the depth consistency of the unirradiated or minimally affected regions.

- Profile 3 – Across laser tracks: This cross-sectional profile intersects multiple laser tracks perpendicularly, providing a comprehensive view of the surface modulation caused by texturing. It reflects the combined height variation across peaks and valleys and offers an insight into the periodicity and symmetry of the overall pattern.

These profiles are essential for determining whether the surface exhibits consistent texture geometry, which is critical for surface functionalities such as directional wetting or anisotropic adhesion. Uniformity of crest spacing and trough depth directly influence how surface features interact with water droplets or coatings.

Grid pattern analysis

A detailed surface profile analysis was also performed for the laser textured surfaces with grid pattern (G1 and G2), which were produced using bidirectional laser scanning to generate intersecting structures. Figure 29 presents two measured line profiles of surfaces textured with a grid pattern.

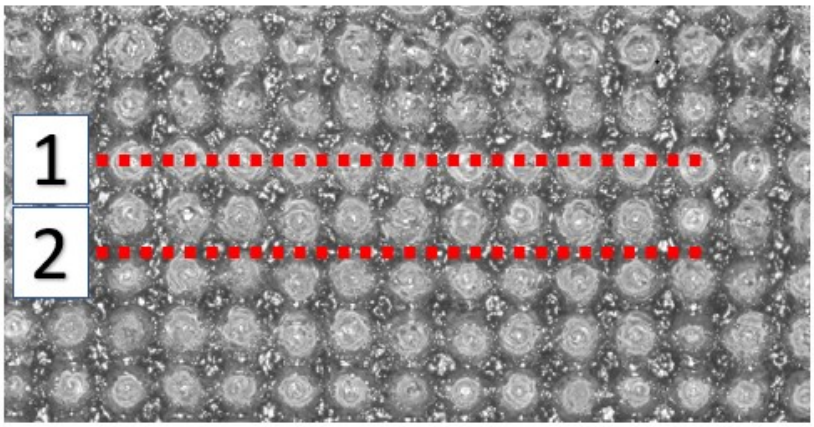

Figure 29 Topographic map of laser textured surface with grid pattern. Red profile lines represent: (1) on top of laser tracks and (2) between laser tracks.

The topographic image of a grid-textured surface is shown in Figure 29, with two red-dotted profile lines used to characterize the resulting two-dimensional periodic pattern:

- Profile 1 – Along laser tracks: This line follows the path of the laser scanning direction, traversing the topography formed along each track. It captures the periodicity and height variation introduced by repeated pulses along a single scanning direction.

- Profile 2 – Between laser tracks: Oriented perpendicularly to Profile 1, this line runs between adjacent laser tracks, enabling assessment of the track spacing, valley depth, and consistency across the orthogonal scan direction.

These profiles help to confirm the fidelity of the grid pattern, ensuring that the structure is formed symmetrically and with consistent energy distribution. The ability to extract height variation in multiple orientations allows an in-depth evaluation of pattern symmetry, which is essential when assessing isotropic properties such as omnidirectional hydrophobicity or uniform surface adhesion.

7.4 SEM

SEM was used to characterize the surface morphology of stainless steel surfaces after laser treatment. The imaging was performed using a Thermo Scientific Apreo S FE-SEM, under high-vacuum conditions, utilizing the OptiPlan mode to optimize image quality and depth of field during imaging. SEM was chosen due to its ability to provide detailed visualization of surface structures at both micro- and nanoscales, which is essential for evaluating the effects of surface modification.

To obtain comprehensive surface information, each surface (non-treated reference, L1, L2, G1 and G2 surface) was imaged using three different detectors: ETD, T1 and T3. These detectors differ in their detection angles and the type of electrons that they collect, enabling complementary contrast modes and visualization of various surface properties.

- ETD (Everhart–Thornley detector) collects low-angle backscattered electrons, which are highly sensitive to surface topography. Images captured with ETD detector were used in this thesis to visualize the topography (overall texture, step heights and fine morphological details) of the surface.

- T1 collects high-angle backscattered electrons, which are primarily used for generating atomic number contrast (Z-contrast). Images captured with the T1 detector were used to qualitatively assess compositional variations on the surface, particularly in areas where surface treatments or contamination may have caused local differences in elemental composition.

- T3 detector is a secondary electron detector that collects electrons at a relatively high take-off angle, enhancing the visibility of inclined surfaces and complex microstructures. In this study, T3 was used to capture detailed images of the laser textured surfaces, allowing subtle topographical features and edge contrasts to be observed with improved clarity.

All images were acquired using a consistent accelerating voltage of 2 kV and with a beam current of 25 pA to minimize surface charging and ensure high surface sensitivity. Magnifications ranged from 500x to 1500x, allowing both general and detailed visualization of the surface features. The representative regions were selected away from edges of the plates to avoid mechanical or mounting artifacts. Scale bars were added to the obtained images using Fiji ImageJ software to provide an accurate spatial reference for the observed surface features. This enables a quantitative comparison of texture dimensions and ensures that structural characteristics which can be reliably interpreted and reported in the analysis. An example image of laser textured surface captured with SEM device used in this thesis, as shown Figure 30.

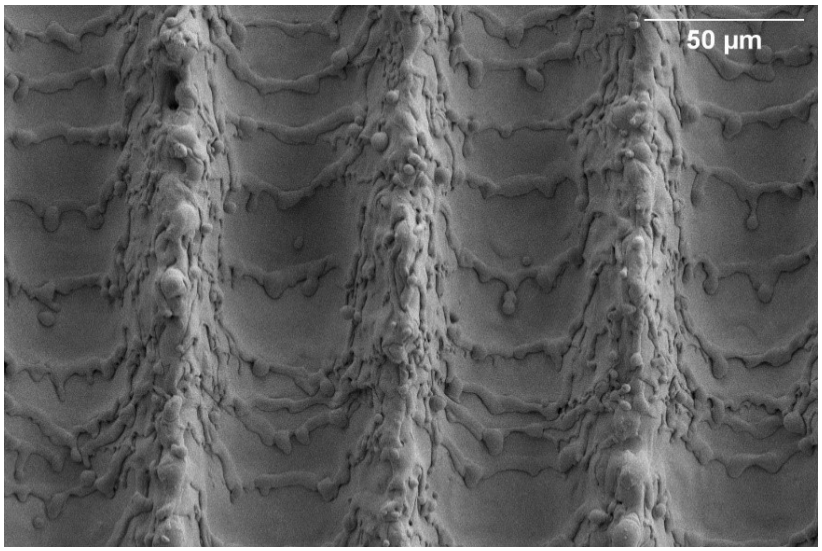

Figure 30 Image of laser textured surface captured with SEM.

As Figure 30 shows, SEM provides high-resolution images of the laser textured surfaces, enabling a clear visualization of both the overall texture pattern and finer surface details. These representative images illustrate the type of data acquired for subsequent morphological assessment.

Micrographs were analysed qualitatively to assess the effects of surface treatments on morphology, including changes in roughness, feature shape and uniformity. The use of multiple detectors enabled a more complete interpretation of the surface characteristics by combining topographical and compositional contrast information.

7.5 Contact angle measurements

Surface wettability was evaluated by measuring the static contact angle of water droplets using an Attension Theta optical tensiometer (Biolin Scientific), equipped with a high-resolution camera and monochromatic cold LED illumination. Measurements were conducted under ambient laboratory conditions using quartz double-distilled water as test liquid. A droplet volume of 5 µl was used in all measurements, dispensed at a controlled rate of 0.1 µl/s to ensure a smooth and reproducible drop formation.

Each measurement followed a standardized procedure illustrated in Figure 31.

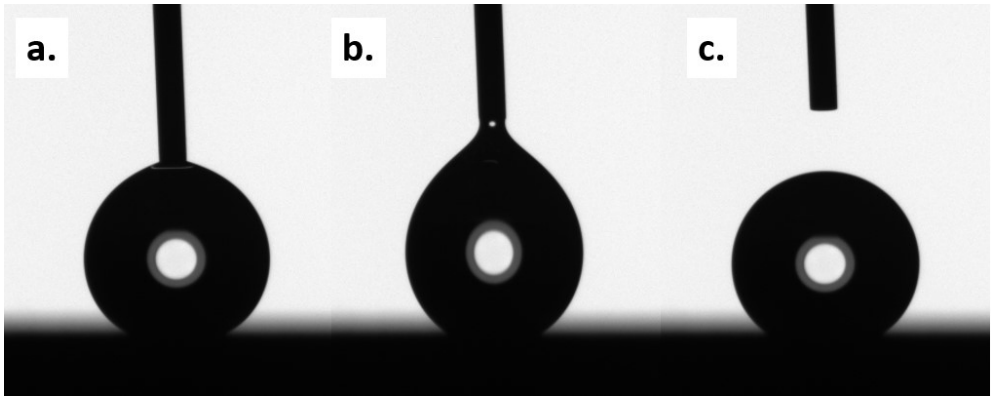

Figure 31 Illustration of contact angle measurement procedure.

As shown in Figure 31, a droplet was first formed at the tip of the vertically aligned dispensing syringe (a), brought into contact with the surface (b), and released with minimal impact (c). The droplet profile was recorded immediately after release to avoid errors caused by evaporation or spreading dynamics. For each surface, four droplets were measured at separate locations to account for local surface variability. The average of these measurements was then calculated and used as the representative value for subsequent analysis of surface wettability.

Contact angles were determined using the Young–Laplace fitting method in Analyse mode within the OneAttension software. The software automatically detected the droplet baseline and fitted the drop contour using the Young–Laplace equation, calculating the left and right contact angles, which were then averaged for each droplet, as shown in Figure 32.

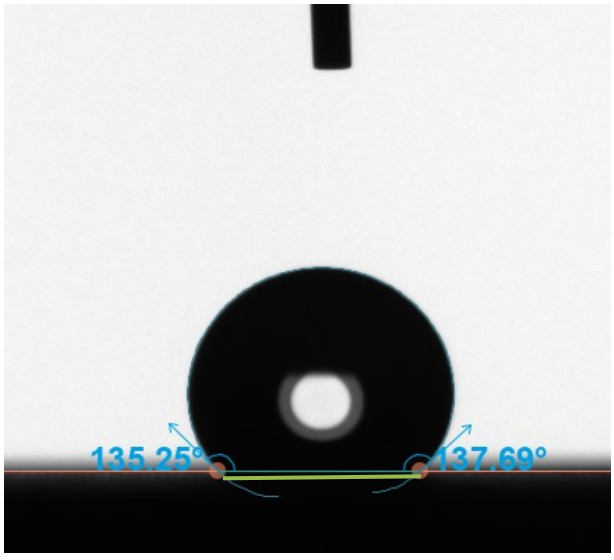

Figure 32 Droplet baseline (green line) and fitted contact angles measured with Attension Theta optical tensiometer.

As shown in Figure 32, the measurement system used in this thesis for contact angle determination provides a clear profile of the droplet, with the left and right contact angles automatically calculated and displayed. This ensures a consistent and reproducible evaluation of surface wettability across all tested samples.

The mean of three droplets was reported as the representative contact angle for the surface. These values were used to classify surface wettability: contact angles below 90° were considered hydrophilic, whereas angles above 90° indicated hydrophobic behaviour. Contact angles exceeding 150° were interpreted as superhydrophobic.

For specimens with surfaces laser textured with line patterns (L1 and L2), anisotropic wetting behaviour was expected due to the directionality of the textured features. To capture this effect, contact angles were measured from two orthogonal viewing directions relative to the pattern orientation as shown in Figure 33.

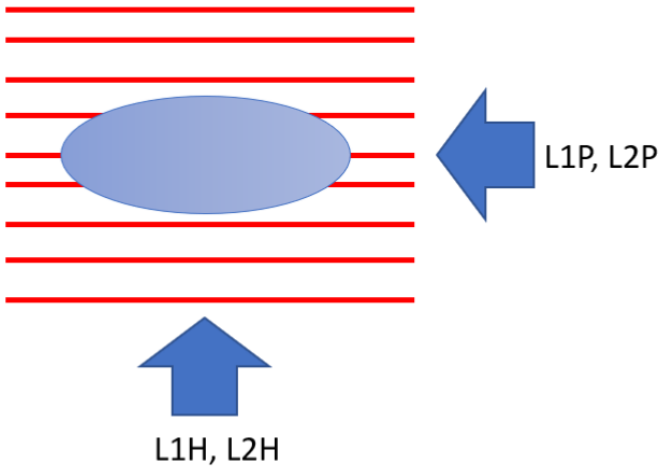

Figure 33 Schematics of contact angle measurements of surfaces laser textured with line patterns (L1 and L2) from two different directions: L1-H and L2-H horizontal to the laser track direction, and L1-P and L2-P perpendicular to the laser track direction.

As shown in Figure 33, measurements marked as "P" (L1-P, L2-P) were taken with the camera perpendicular to the line direction, and those marked as "H" (L1-H, L2-H) were taken horizontal to the line direction. This approach allowed an assessment of directional differences in droplet shape and contact angle caused by the anisotropic surface morphology.

7.6 Adhesion testing

The adhesion strength of the coatings was evaluated using the standardized cross-cut tape test according to ISO 2409:2020. In this method, the coating surface is scored with a series of

perpendicular cuts to form a cross-hatch pattern, penetrating through the coating layer into the substrate. The cuts were made at 1.5 mm intervals with a precision blade to ensure uniform depth and spacing across all surfaces. The procedure is illustrated in Figure 34, which schematically shows the sequence of cross-hatch scoring, application of adhesive tape, and subsequent evaluation of coating detachment.

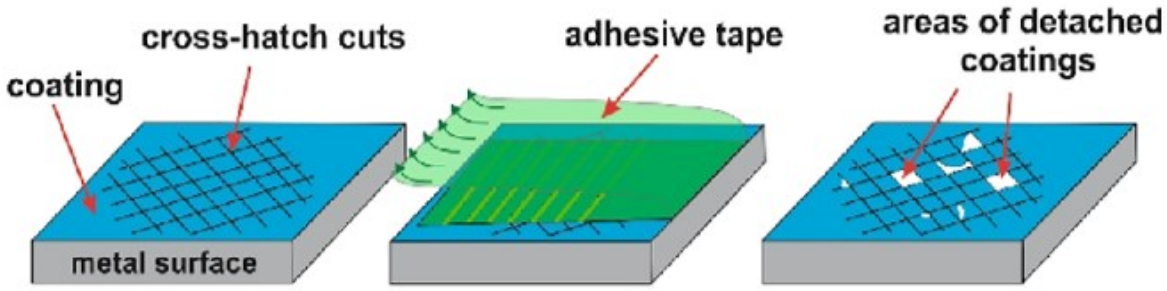

Figure 34 Schematic illustration of the cross-cut tape adhesion test procedure, showing cross-hatch scoring, application of adhesive tape, and evaluation of coating detachment. Image sourced from [193] which are under an open access Creative Common CC BY licence.

Figure 34 shows a schematic illustration of the cross-cut tape test procedure. In the first step, the coating is scored into a cross-hatch grid. In the second step, a pressure-sensitive adhesive tape is applied firmly over the scored area. Finally, the tape is removed in a controlled motion, and any detached coating fragments remain visible within the cross-hatched region. This schematic highlights the principle of the method, where poor adhesion results in larger areas of detached coating, whereas strong adhesion leaves the coating intact.

Following the schematic, the same procedure was applied to the studied samples. After scoring of the surfaces with exacto knife, a pressure-sensitive adhesive tape (Gorilla Tape Crystal Clear) was firmly applied to the cross-hatch area and then removed in a single smooth motion at a consistent angle and speed to reduce variability. After the tape removal, the tape surfaces were examined with optical microscope at 1x magnification to assess coating detachment.

The adhesion quality was evaluated using a custom grading method developed specifically for this work. The method involved visually estimating the proportion of coating detached from the cross-hatched areas after the tape test, as shown in Figure 35. Each surface was assessed by determining the percentage of coating loss within the grid squares, providing a direct indication of the coating–substrate adhesion strength: the greater the detachment, the weaker the adhesion.

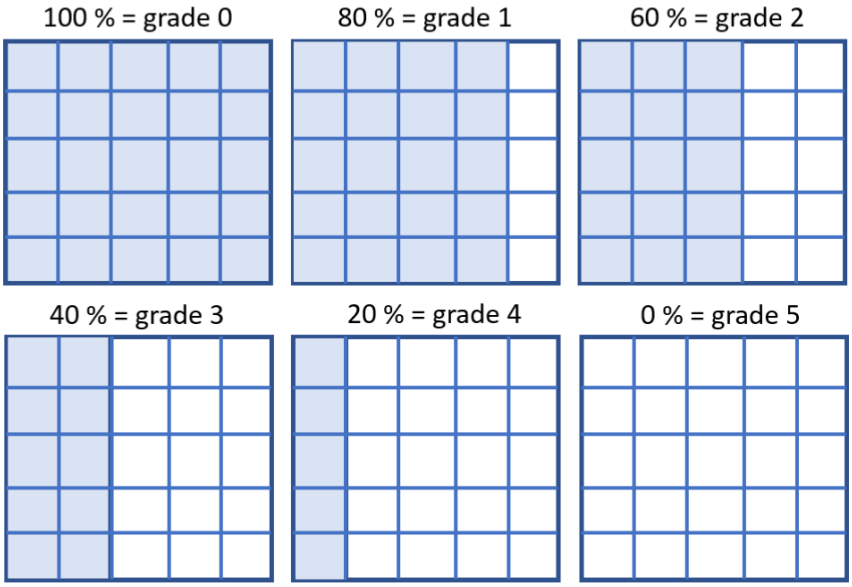

Figure 35 Reference chart for estimating coating removal percentage in the cross-cut tape test, used for determining adhesion.

Figure 35 presents the reference chart used for this evaluation. The grading scale ranged from grade 0 to grade 5, corresponding to 100 % to 0 % coating detachment, respectively. Intermediate grades represented 80 % (grade 1), 60 % (grade 2), 40 % (grade 3), and 20 % (grade 4) removal. This tailored visual system allowed consistent and quantitative comparison of adhesion performance across the tested surfaces.

8 Results and discussion

8.1 Pre-treatment

The laser surface texturing experiments (as a pre-treatment), were conducted on a stainless steel specimens divided into four distinct areas, labelled L1, L2, G1, and G2. The corresponding laser processing parameters for each area are listed in Table 4, and photograph of the textured surfaces is shown in Figure 36. The parameter sets were selected based on preliminary testing, as described in Section 7.1, to enable comparison between the different laser texturing pattern types (line and grid) and energy inputs (fluence of 35 J/mm² and 141 J/mm²).

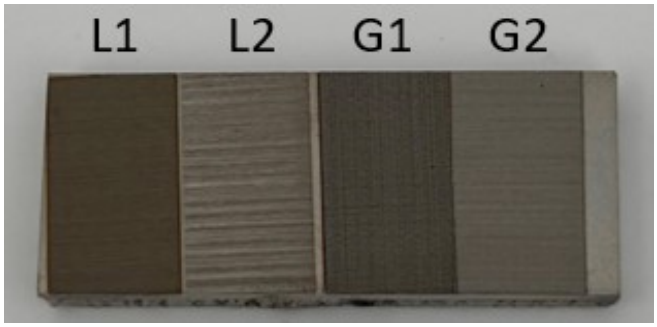

Figure 36 Photograph of laser textured surfaces L1 (line pattern, fluence 35 J/mm^2), L2 (line pattern, fluence 141 J/mm^2), G1 (grid pattern, fluence 35 J/mm^2), and G2 (grid pattern, fluence 141 J/mm^2).

Figure 36 presents a photograph of the laser processed stainless steel specimen, showing the four processed surface areas: linear patterns L1 and L2, and grid patterns G1 and G2. Visually, contrasts in colour and texture can be observed between the surfaces, reflecting variations in surface morphology and oxidation caused from the processing conditions. The L1 and G1 surfaces, both processed at a lower fluence of 35 J/mm², appear darker than L2 and G2, which were processed at a higher fluence of 141 J/mm². This difference in appearance may be related to changes in oxide layer thickness and surface roughness induced by the different energy inputs, as well as differences in heat accumulation due to the combination of scanning speed and repetition times. The line-patterned surfaces (L1, L2) exhibit distinct unidirectional features, whereas the grid-patterned surfaces (G1, G2) show intersecting structures that produce a more complex visual texture. The sharper boundary lines between adjacent areas indicate precise control of the laser processing, with minimal heat-affected zones extending beyond the intended regions. These observations can also be seen in macro image taken with 1x magnification in Figure 37.

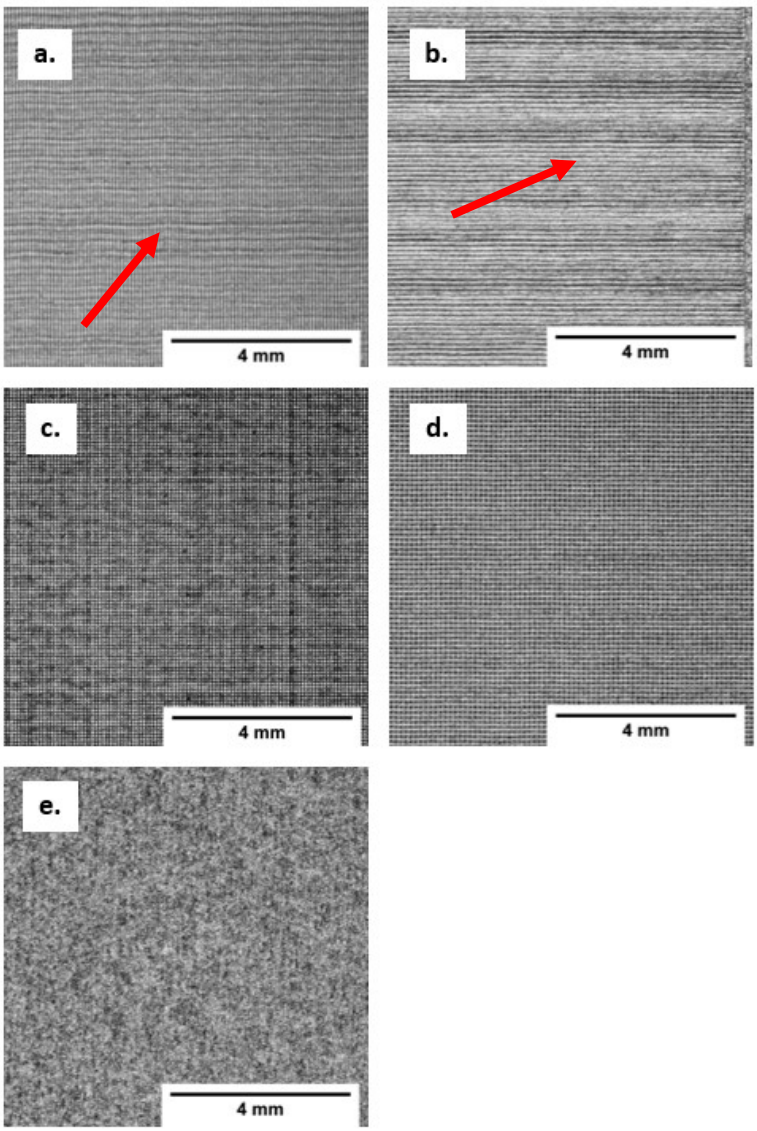

Figure 37 Macro image with 1x magnification of surfaces a) L1 (line pattern, fluence 35 J/mm^2), b) L2 (line pattern, fluence 141 J/mm^2), c) G1 (grid pattern, fluence 35 J/mm^2), d) G2 (grid pattern, fluence 141 J/mm^2), and e) non-treated reference surface.

Figure 37 shows 1x magnification macro images of the laser textured surfaces L1, L2, G1 and G2 (a–d) and the non-treated reference surface (e). L1 surface (a) was processed with line pattern and laser fluence of 35 J/mm^2, L2 (b) line pattern and laser fluence of 141 J/mm^2, G1 (c) has been processed with grid pattern and laser fluence of 35 J/mm^2, G2 (d) grid pattern and laser fluence of 141 J/mm^2. In L1 surface (a), vertical laser tracks are visible, with a diagonal waviness across the pattern, as indicated by the arrows in Figure 37. This diagonal waviness effect of the surface may be related to the lower pulse frequency (20 kHz), which increases the spacing between pulses and can accentuate small misalignments or scanning system vibrations. Additionally, the observed waviness could be influenced by the underlying surface topography of the substrate or by thermal distortion during processing. In the L2 surface (b), the arrows

highlight horizontal lines corresponding to the laser scanning direction. The surface exhibits non-uniformity, with darker lines in certain regions, which may result from local variations in heat accumulation or oxide formation during laser processing. The surface shows non-uniformity, with darker lines in certain areas, possibly due to local variations in heat accumulation or oxide layer formed during laser processing.

In G1 surface (c), the grid pattern is visible, but the surface appears non-homogeneity, suggesting variations in the laser–material interaction across the processed area. G2 surface (d) exhibits a uniform and well-defined grid structure, indicating stable process conditions and consistent substrate response during laser surface texturing. The non-treated reference surface (e) shows only the original surface of the stainless steel substrate, with no periodic or directional features, as shown in Figure 37. Furthermore, L1 (a) and G2 (d) surfaces appear more uniform compared to L2 and G1 surfaces, which could be related not only to differences in the initial substrate surface homogeneity but also to the number of passes and energy distribution associated with their respective pattern types. Macro images with higher magnification (5x) for corresponding surfaces are presented in Figure 38.

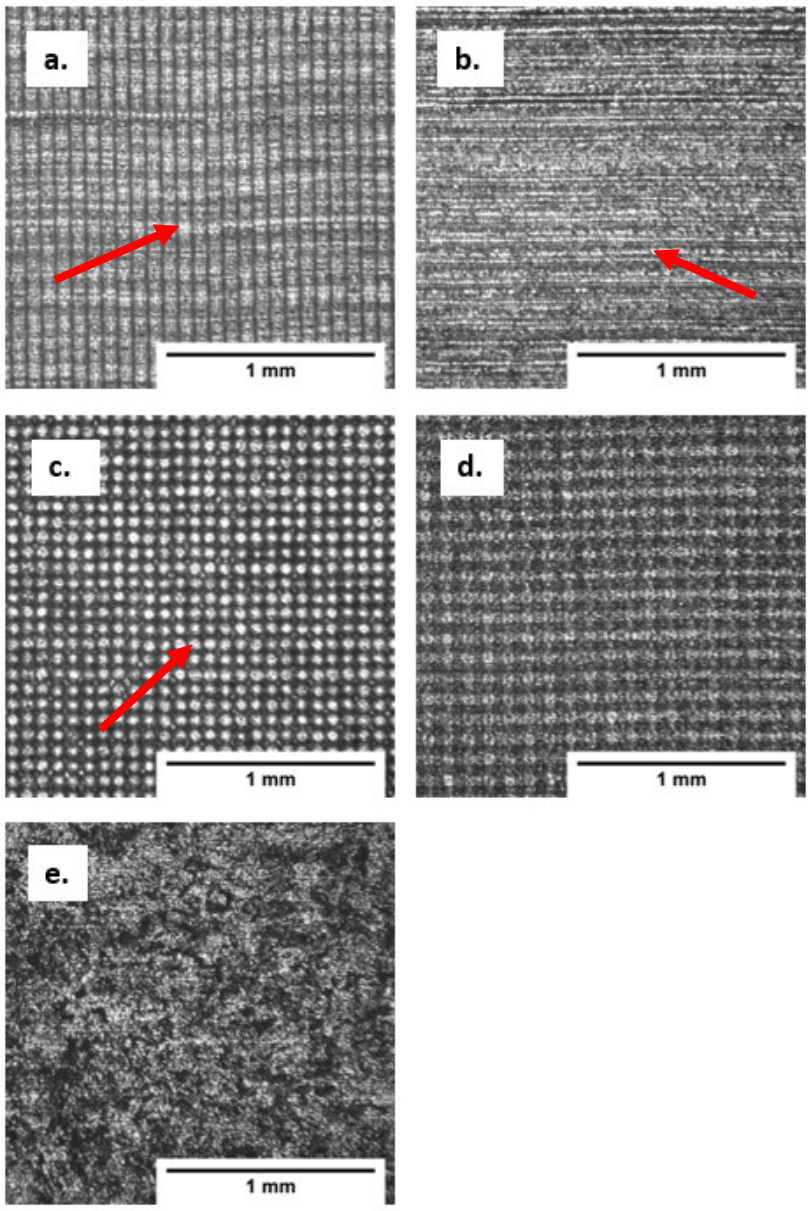

Figure 38 Macro image with 5x magnification of surfaces a) L1 (line pattern, fluence 35 J/mm^2), b) L2 (line pattern, fluence 141 J/mm^2), c) G1 (grid pattern, fluence 35 J/mm^2), d) G2 (grid pattern, fluence 141 J/mm^2), and e) non-treated reference surface.

Figure 38 presents 5x magnification macro images of the laser textured surfaces L1, L2, G1 and G2 (a–d) and the non-treated reference surface (e), providing a closer view of the laser textured features observed in Figure 37. L1 surface (a) was processed with line pattern and laser fluence of 35 J/mm^2, L2 (b) line pattern and laser fluence of 141 J/mm^2, G1 (c) has been processed with grid pattern and laser fluence of 35 J/mm^2, G2 (d) grid pattern and laser fluence of 141 J/mm^2. In L1 surface (a), distinct vertical lines corresponding to individual laser scanning tracks are visible. The uniformity of the spacing a suggests consistent beam positioning, although variations in brightness along the tracks may indicate fluctuations in energy delivery or local surface reflectivity. L2 surface (b) displays predominantly horizontal lines following

the laser scanning direction; however, these lines appear less defined than in L1 surface, which could be related to the higher scanning speed and fluence used, leading to a smoother melt layer and reduced visual contrast between adjacent tracks. In G1 surface (c), the grid pattern is pronounced, with bright, regularly spaced nodes at track intersections, as seen in Figure 38. The appearance suggests of localized material modification or oxide formation at the overlap points, where the laser beam passes twice. G2 surface (d) also shows a grid pattern but with more uniform brightness across the surface, consistent with stable processing at higher fluence and scanning speed. The non-treated reference surface (e) exhibits the inherent random roughness of the stainless steel substrate, with no directional or periodic structures present.

8.2 Coating

Photograph of laser textured surfaces L1, L2, G1 and G2 is shown in Figure 39.

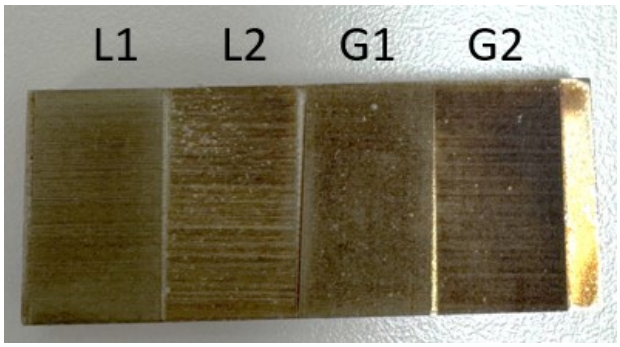

Figure 39 Photograph of laser textured and coated surfaces L1 (line pattern, fluence 35 J/mm^2), L2 (line pattern, fluence 141 J/mm^2), G1 (grid pattern, fluence 35 J/mm^2), and G2 (grid pattern, fluence 141 J/mm^2).

Figure 39 presents a photograph of the coated stainless steel specimen, showing the four laser textured surface areas: L1 and L2 surfaces laser textured with line pattern, and G1 and G2 surfaces with grid pattern. After coating, the visual contrasts between the areas remain evident, although the overall appearance is more uniform compared to the uncoated specimen. The darker tone of L1 and G1 surfaces, both processed at a lower fluence of 35 J/mm², is still distinguishable from the lighter appearance of L2 and G2 surfaces, which were processed at a higher fluence of 141 J/mm². This difference may be linked to the mechanical interlocking of the coating layer with the underlying oxide thickness and surface roughness. This can also be explained based on the reflectance and transmittance characteristics of the laser-processed regions, as the higher fluence tends to produce smoother and more reflective surfaces with thinner oxide layers, resulting in a lighter visual appearance. Conversely, lower fluence settings promote increased surface oxidation and roughness, which enhance light absorption and reduce

reflectivity, leading to a darker tone. The line-patterned surfaces (L1, L2) retain their characteristic unidirectional streaks, while the grid-patterned surfaces (G1, G2) display more complex intersecting textures. The boundaries between the coated sections remain sharp, indicating that the deposition process produced a conformal and homogeneous layer without spreading beyond the intended areas. These features confirm that the coating has adhered uniformly across the textured surfaces while preserving the distinct morphological characteristics generated by the laser device.

Figure 40 presents 1x magnification macro images of the coated laser textured surfaces L1, L2, G1 and G2, and coated non-treated reference surface.

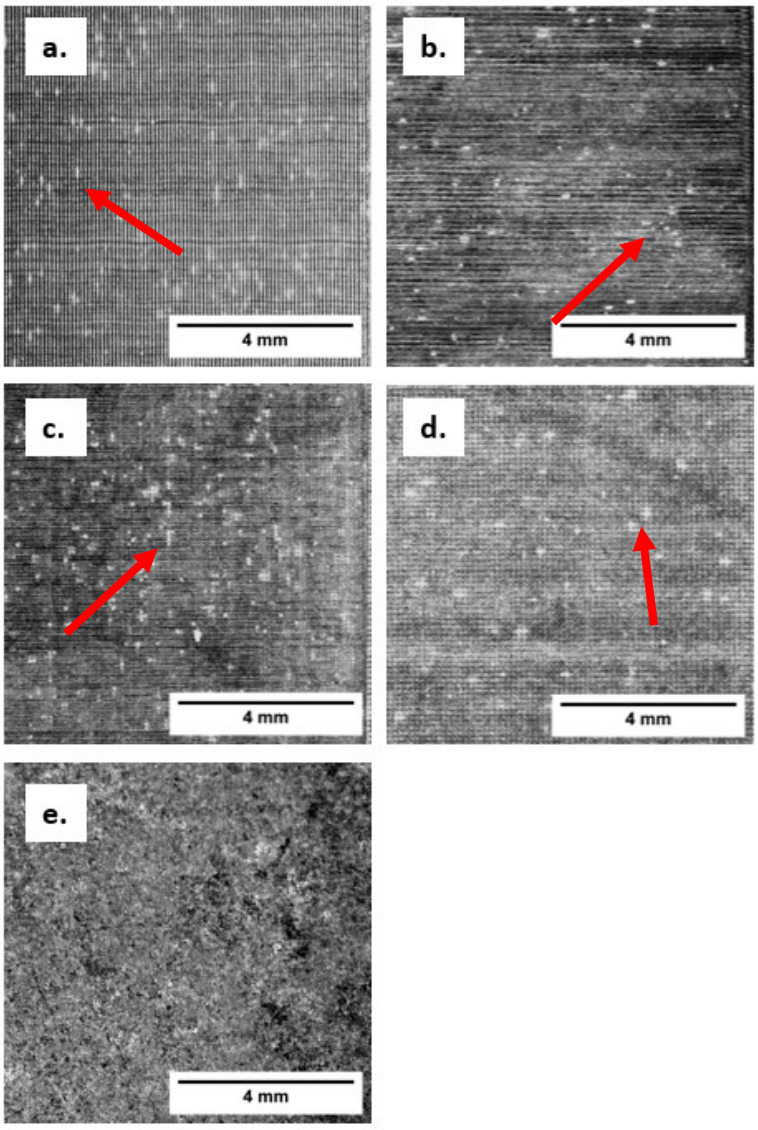

Figure 40 Macro image with 1x magnification of coated surfaces a) L1 (line pattern, fluence 35 J/mm^2), b) L2 (line pattern, fluence 141 J/mm^2), c) G1 (grid pattern, fluence 35 J/mm^2), d) G2 (grid pattern, fluence 141 J/mm^2), and e) non-treated reference surface.

Figure 40 shows 1x magnification macro images of the coated surfaces L1, L2, G1 and G2 (a–d) and the coated non-treated reference surface (e). L1 surface (a), processed with line pattern and fluence of 35 J/mm², displays visible unidirectional tracks that remain distinguishable after coating. The periodicity of the laser-induced grooves is preserved, although the coating layer gives the surface a more uniform and slightly smoother appearance compared to the uncoated condition. In L2 surface (b), produced with line pattern and fluence of 141 J/mm², horizontal features are observed, but the surface appears darker and less uniform than L1 surface. This may be related to increased local oxidation or differences in the coating wetting behaviour on the smoother but less topographically pronounced texture of L2 surface. G1 surface (c), processed with grid pattern at lower fluence (35 J/mm²), shows intersecting structures characteristic of the orthogonal scanning strategy, but the coated layer appears to highlight small-scale irregularities and local variations in reflectivity, suggesting slight heterogeneity in coating deposition. In contrast, G2 surface (d), produced at higher fluence (141 J/mm²), exhibits a more uniform grid pattern after coating, with well-defined intersecting nodes and consistent tonal contrast across the area. The coating seems to have spread homogeneously, preserving the hierarchical features introduced by the laser texturing. As marked in Figure 40 with arrows, all laser textured surfaces (L1, L2, G1 and G2) show light spots distributed across the surface. These features can be attributed to local variations in coating thickness, reflectivity, or surface oxidation, which are enhanced by the underlying microstructural roughness introduced during laser texturing. Their presence suggests heterogeneity in the coating deposition, although the overall pattern geometry and periodicity remain clearly preserved. The coated non-treated reference surface (e) shows the smooth stainless steel base without periodic features, with only fine-scale stochastic roughness visible. Compared to the laser textured surfaces (L1, L2, G1 and G2), the coating layer on non-treated reference surface appears more evenly distributed but lacks the structural features that contribute to functional roughness. Macro images with higher magnification (5x) for corresponding surfaces are presented in Figure 41.

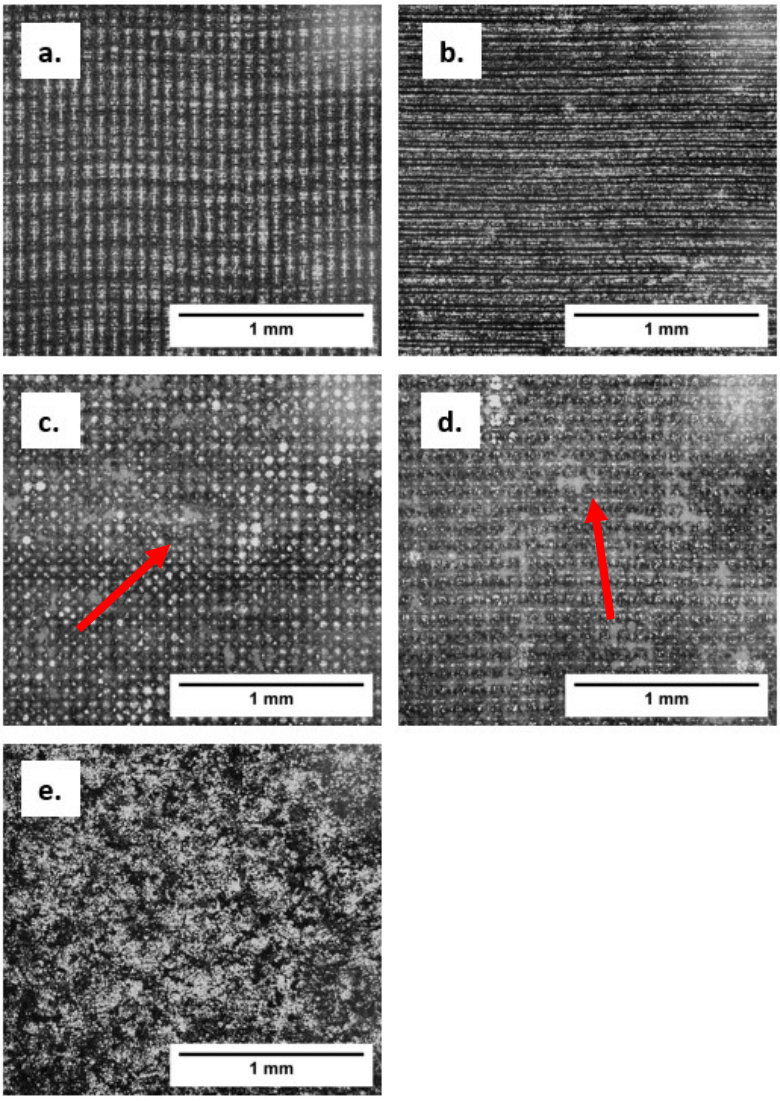

Figure 41 Macro image with 5x magnification of coated surfaces a) L1 (line pattern, fluence 35 J/mm^2), b) L2 (line pattern, fluence 141 J/mm^2), c) G1 (grid pattern, fluence 35 J/mm^2), d) G2 (grid pattern, fluence 141 J/mm^2), and e) non-treated reference surface.

Figure 41 shows 5x magnification macro images of the coated surfaces L1, L2, G1 and G2 (a–d) and the coated non-treated reference surface (e). L1 surface (a), processed with line pattern and fluence of 35 J/mm², exhibits well-defined parallel grooves that remain clearly visible through the coating. The periodicity of the line tracks is preserved, though the coating layer smoothens some of the sharper edges, giving the surface a slightly more uniform visual texture compared to the uncoated state.

L2 surface (b), produced at higher fluence (141 J/mm²), displays continuous horizontal lines along the scanning direction. The surface appears darker and more homogeneous than L1, with fewer small-scale irregularities visible. This may be related to stronger remelting during laser texturing, which produced smoother initial features, as well as to more uniform coating

deposition on the flatter texture. G1 surface (c), processed with a grid pattern at lower fluence (35 J/mm²), shows a pronounced array of bright circular spots corresponding to the laser pulse overlaps. The coating highlights these intersecting nodes, which appear as reflective points across the pattern, suggesting that the thin coating layer conforms closely to the underlying topography. In contrast, G2 surface (d), textured with a grid pattern at higher fluence (141 J/mm²), reveals a more uniform distribution of the grid intersections. The brighter nodes appear more rounded and less irregular than in G1 surface, consistent with increased remelting and smoothing effects of the higher energy input. As indicated by the arrows in Figure 41, the grid-patterned coated surfaces (G1 and G2) display localized regions where the coating appears less uniform, with areas of brighter contrast suggesting variations in layer thickness or reflectivity. These inhomogeneities may arise from small differences in laser-induced surface roughness at the ridge intersections, which influence the spreading and adhesion of the deposited coating. The coated non-treated reference surface (e) presents a fine-grained, stochastic texture without periodic features, where the coating forms a homogeneous but non-structured layer. Compared to the textured surfaces, the absence of directional or grid-like patterns results in a visually more random surface morphology.

8.3 3D topography

Pre-treatment

3D surface topography measurements and imaging were conducted for laser textures surfaces L1, L2, G1 and G2, and non-treated reference surface. Coloured topography images of these surfaces are presented in Figures 42-47.

The 3D topography image with angled view on non-treated reference surface and surface G1 is presented in Figure 42.

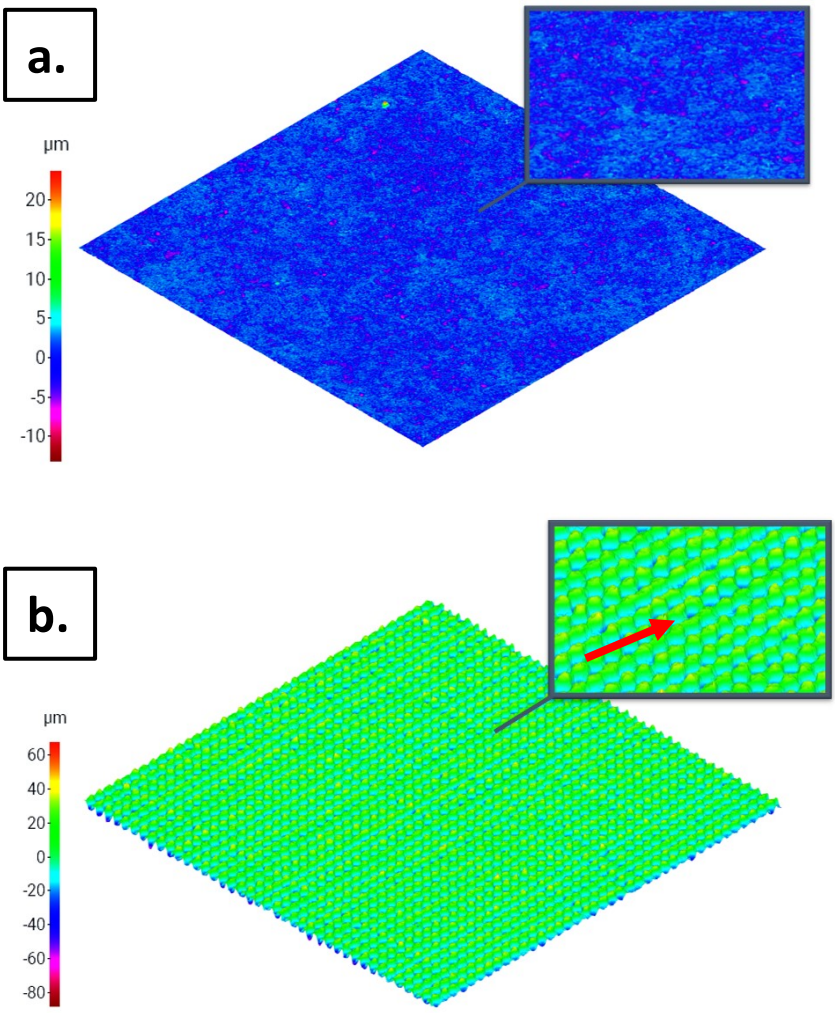

Figure 42 3D topography image of a) the non-treated reference surface and b) laser textured G1 surface, processed with grid pattern and laser fluence of 35 J/mm^2 surface.

As seen in Figure 42, the 3D surface topography of the non-treated reference surface (a) exhibits a fine, stochastic roughness pattern characteristic of the untreated stainless steel substrate, with no evidence of periodic or directional features. In contrast, the G1 surface (b), processed with a grid pattern at a fluence of 35 J/mm², reveals periodic microstructures with well-defined height variations across the patterned area. The inset provides a magnified view, confirming the uniformity and regular arrangement of the laser-induced features. Comparable 3D topography maps of the other textured surfaces (L1, L2, and G2) are presented in Appendix 3, where top-view representations are shown to enable detailed evaluation of height variations across the entire surface.

Surface topography image of non-treated reference surface is presented in Figure 43.

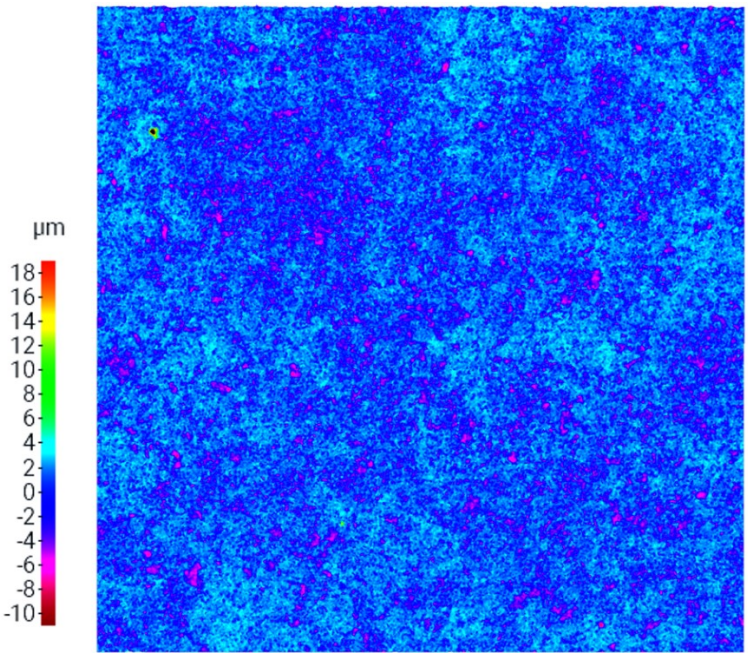

Figure 43 Topography image of the non-treated reference surface.

Figure 43 shows the 3D surface topography of the non-treated reference surface. The colour scale represents the surface height variations in micrometres, with blue tones indicating lower areas and red/yellow tones representing higher peaks. The surface exhibits a relatively fine, stochastic roughness pattern characteristic of the original stainless steel substrate, with height variations ranging approximately from -10 µm to +18 µm. No periodic or directional features are present, confirming the absence of prior surface texturing. The irregular distribution of peaks and valleys reflects the manufacturing and finishing processes of the base material, which serve as the baseline condition for evaluating the effects of laser surface texturing. This reference surface will be used as a comparative benchmark for assessing changes in roughness parameters (*Sa*, *Sz*) and morphological characteristics introduced by the different laser processing conditions.

The surface topography image of laser textured L1 surface is presented in Figure 44.

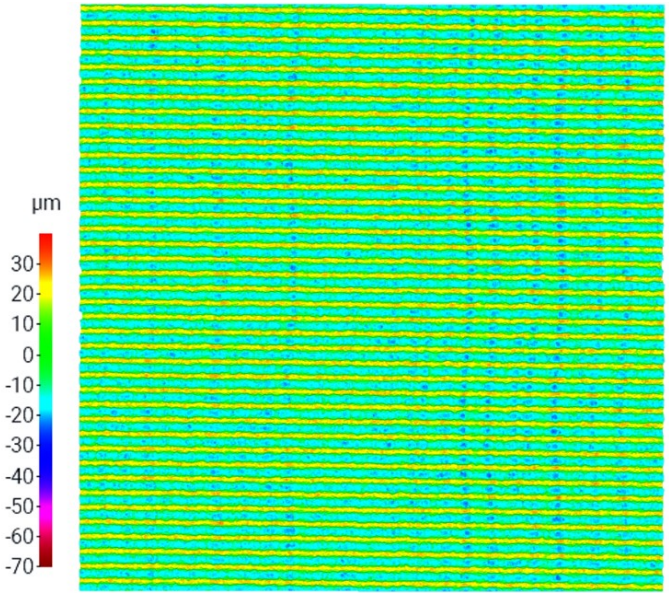

Figure 44 Topography image of the L1 surface processed with line pattern and laser fluence of 35 J/mm^2.

Figure 44 shows the 3D surface topography of the L1 surface, processed with a line pattern at a fluence of 35 J/mm² and a frequency of 20 kHz. The topography reveals a distinct series of parallel ridges and grooves aligned with the scanning direction, with height variations ranging from approximately -70 µm in the deepest valleys, to +30 µm at the highest peaks. These variations originate from the periodic energy input and thermal accumulation during successive laser passes. The higher peaks correspond to areas where local melting and re-solidification have occurred due to overlapping pulses, while the deeper valleys represent regions of more efficient ablation where material removal was dominant. The regularity of the pattern indicates stable beam positioning and consistent overlap between adjacent tracks, although minor periodic modulations along the ridges may be associated with the pulse spacing dictated by the low repetition frequency. The alternating high and low regions result from material ablation and localized melting–solidification, forming well-defined track boundaries. Compared to the non-treated reference surface (seen in Figure 43), L1 shows an increase in both peak-to-valley height and structural periodicity, features that are expected to influence wettability and surface functionality.

The surface topography image of laser textured L2 surface is presented in Figure 45.

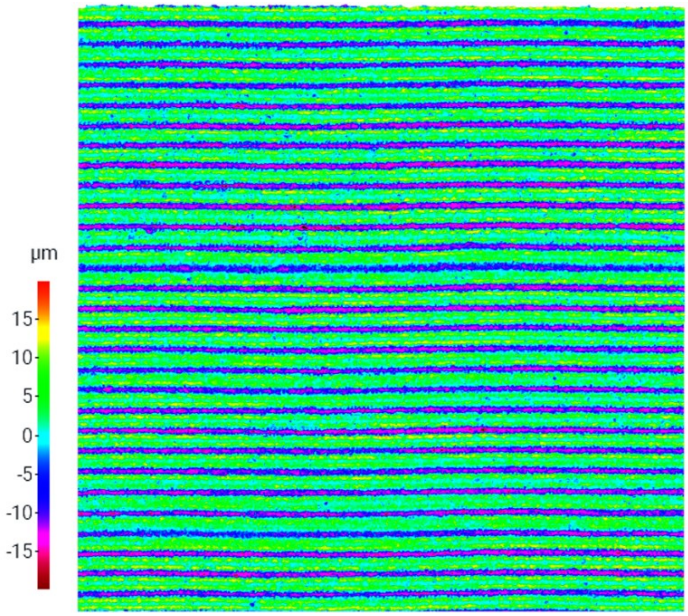

Figure 45 Topography image of the L2 surface processed with line pattern and laser fluence of 141 J/mm^2.

Figure 45 shows the 3D surface topography of the L2 surface, processed with a line pattern at a fluence of 141 J/mm² and a frequency of 100 kHz. The surface displays evenly spaced parallel ridges and grooves aligned with the scanning direction, with height variations ranging from approximately –15 µm to +15 µm. Compared to L1 (as seen in Figure 44), the amplitude of the surface features is smaller, indicating shallower structuring. This difference is likely explained by the higher repetition frequency (100 kHz) compared to surface L1 (20 kHz), which reduces pulse spacing. In addition, the higher scanning speed further promotes material removal and increased surface remelting. The ridges exhibit a continuous and uniform profile with minimal irregularities, producing even surface texture. While the periodicity remains well-defined, the reduced peak-to-valley, may limit the ability of surface L2 to trap air pockets compared to the deeper structures observed in L1, potentially affecting the caused wettability characteristics.

The surface topography image of laser textured G1 surface is presented in Figure 46.

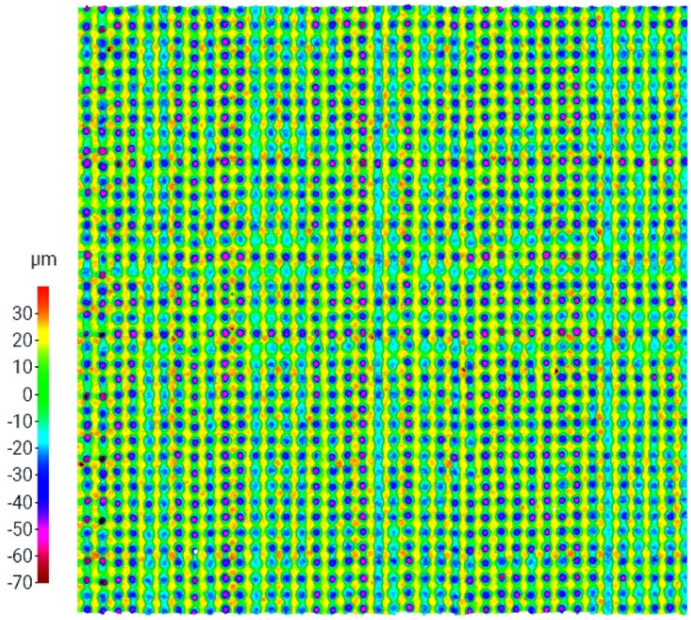

Figure 46 Topography image of the G1 surface processed with grid pattern and laser fluence of 35 J/mm^2.

Figure 46 shows the 3D surface topography of the G1 surface, processed with a grid pattern at a fluence of 35 J/mm² and a frequency of 20 kHz. The surface features a periodic array of intersecting ridges forming a distinct orthogonal grid pattern, with pronounced nodes at the intersection points. These nodes correspond to areas where the laser beam passes twice in each repetition times, causing an increaced local ablation depth and thermal modification. Height variations range from approximately -70 µm in the deepest valleys to +30 µm at the highest peaks, making this surface one of the most topographically pronounced among the tested patterns. The periodicity is consistent in both scanning directions, although variations in node shape and depth suggest minor fluctuations in energy delivery or beam overlap. The lower frequency (20 kHz) used for this pattern increases pulse spacing, potentially contributing to the more distinct separation between features and the deeper valleys compared to higher frequency (100 kHz) settings. This pronounced hierarchical topography is expected to strongly influence wettability by facilitating air entrapment between nodes and ridges, promoting Cassie–Baxter-type behaviour.

Surface topography image of laser textured G1 surface is presented in Figure 47.

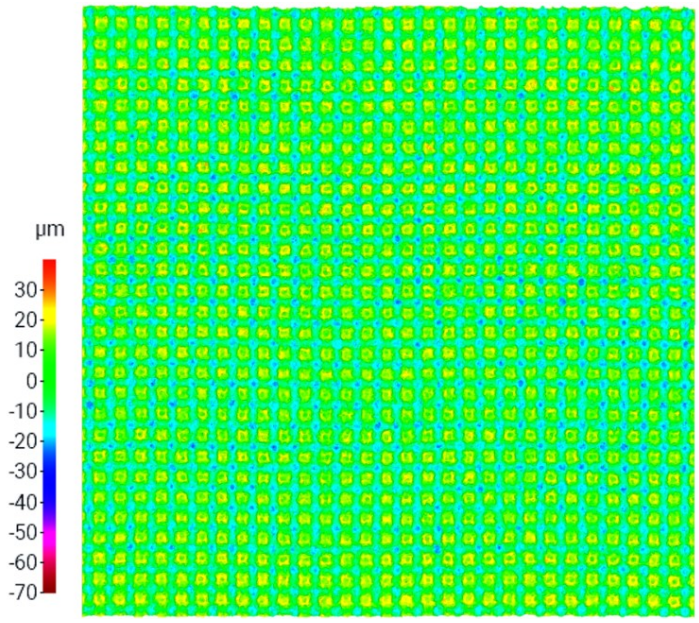

Figure 47 Topography image of the G2 surface processed with grid pattern and laser fluence of 141 J/mm^2.

Figure 47 shows the 3D surface topography of the G2 surface, processed with a grid pattern at a higher fluence of 141 J/mm² and a frequency of 100 kHz. The surface exhibits a regular array of square-shaped nodes formed at the intersections of the orthogonal scanning tracks, with uniform height and spacing across the entire measured surface area. Height variations range from approximately –70 µm in the deepest valleys to +30 µm at the highest peaks, similar to G1 (as seen in Figure 46), but with smoother transitions between features. The increased fluence combined with a higher repetition frequency causes more complete remelting at the intersection points, producing rounded and more uniform node edges compared to the sharper features seen in G1. The reduced variability in peak and valley heights suggests a more stable energy delivery and improved homogeneity of the substrate surface during processing. This consistent topography is expected to yield predictable wetting behaviour, with regular air pocket formation at the grid intersections supporting stable Cassie–Baxter wetting states.

Line profile extractions, were performed for the laser textured surfaces L1, L2, G1, and G2, as well as for the non-treated reference surface. The illustrated profiles of these surfaces are presented in Figures 48-52.

The line profiles along laser tracks of surfaces pattern L1 and L2 laser textured with line pattern, and non-treated reference surface are presented in Figure 48.

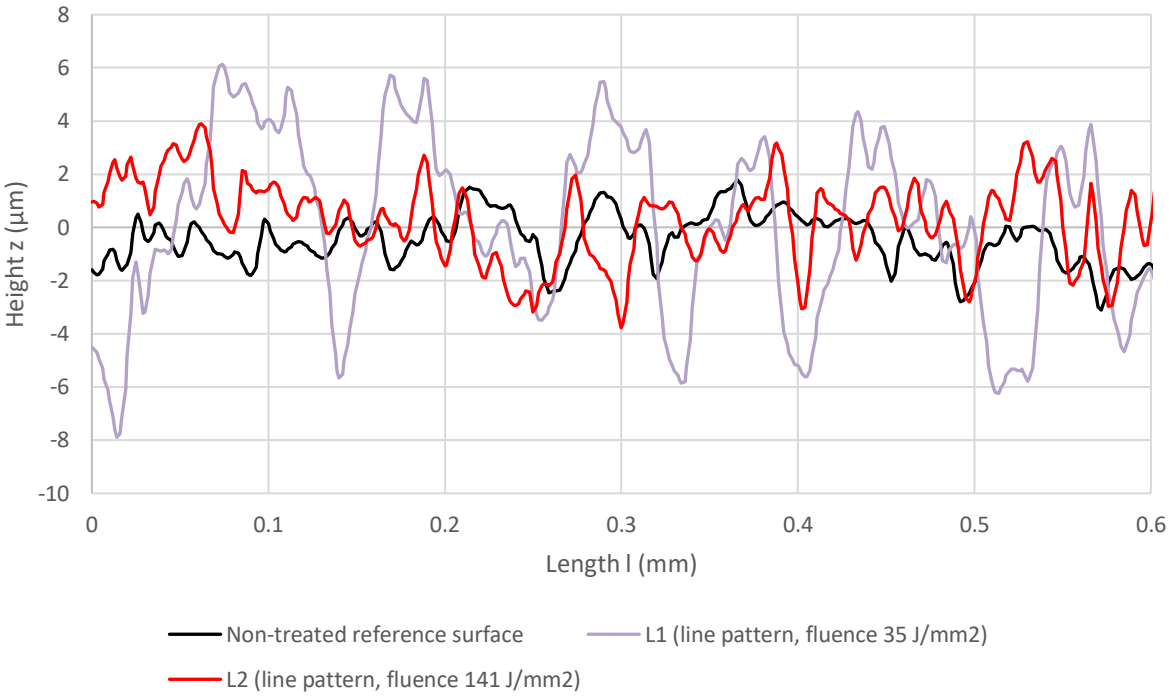

Figure 48 Line profiles along laser tracks of non-treated reference surface, and laser textured surfaces L1 and L2.

Figure 48 shows profile measurements of non-treated reference surface (black profile) and laser textured surfaces L1 (violet profile) and L2 (red profile). The L1 surface was processed with line pattern and laser fluence of 35 J/mm^2, and the L2 surface with line pattern and laser fluence of 141 J/mm^2. Line profiles were measured along the direction of the laser tracks (line pattern profile 1 see section 7.5), to evaluate surface height variations introduced by different scanning parameters. The reference surface (REF) exhibited only minor roughness fluctuations within ±4 µm, corresponding to the baseline texture of the stainless steel substrate. Surface L1 (fill pitch 0.02 mm, frequency of 20 kHz) displayed a clear periodic waviness along the scan direction, with peak-to-valley heights of approximately 11 µm. This regular pattern is likely related to the relatively large pulse spacing at 20 kHz, where each individual pulse produces a distinct surface depression, leading to a repeating topographic modulation. In contrast, surface L2 (fill pitch 0.1 mm, 100 kHz) did not exhibit such regular periodicity. The shorter pulse spacing at 100 kHz causes a higher degree of pulse overlap, producing a smoother track without distinct repetitive structures. As seen in Figure 48, the overall height variation in L2 surface was higher than the non-treated reference surface but lacked the uniform modulation seen in L1 surface. These observations indicate that pulse frequency and spacing have a direct influence

on the periodicity and amplitude of surface features, with lower frequencies producing more pronounced and regular topographic patterns.

The line profiles between laser tracks of surfaces pattern L1 and L2 laser textured with line pattern, and non-treated reference surface are presented in Figure 49.

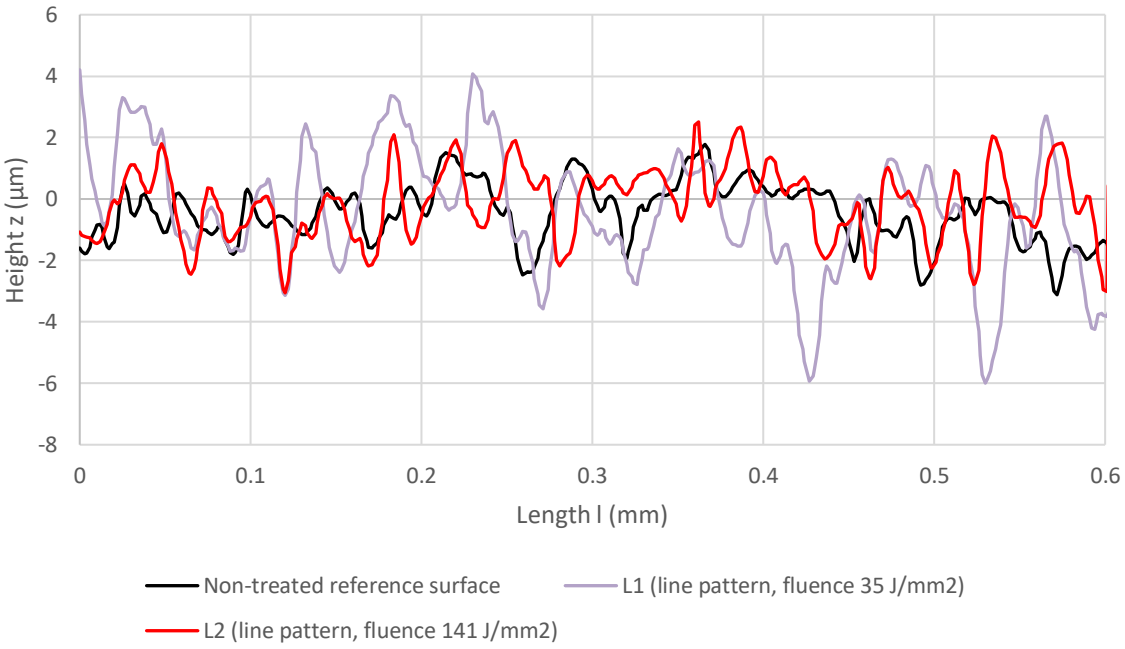

Figure 49 Line profiles between laser tracks of non-treated reference surface, and laser textured surfaces L1 and L2.

Figure 49 shows the profile measurements of the non-treated reference surface (black profile) and laser textured surfaces L1 (violet profile) and L2 (red profile). L1 surface was processed with line pattern and laser fluence of 35 J/mm^2, and L2 surface with line pattern and laser fluence of 141 J/mm^2. Line profiles were measured between the laser tracks (line pattern profile 2, see section 7.5) to evaluate the topography of the trough regions separating adjacent scan lines. Surface L2 (fill pitch 0.1 mm, 100 kHz) showed a profile closely matching the non-treated reference surface, indicating that the larger fill pitch left unprocessed regions between tracks. These valleys retained the original surface roughness of the stainless steel substrate without laser-induced modification. In contrast, surface L1 (fill pitch 0.02 mm, 20 kHz) displayed a modified ridge profile between adjacent tracks. The small fill pitch ensured full coverage, and the measured profile captured the morphology of the laser formed ridge. As seen in Figure 49, this ridge exhibited periodic waviness, with the modulation likely caused by the larger pulse spacing at 20 kHz, where individual pulses create localized surface undulations. These results demonstrate that fill pitch strongly determines whether inter-track regions remain unprocessed

or become part of the laser-modified topography, and that low pulse frequencies can imprint periodic features even in these ridge areas.

The line profiles perpendicular to laser tracks of surfaces pattern L1 and L2 laser textured with line, and non-treated reference surface are presented in Figure 50.

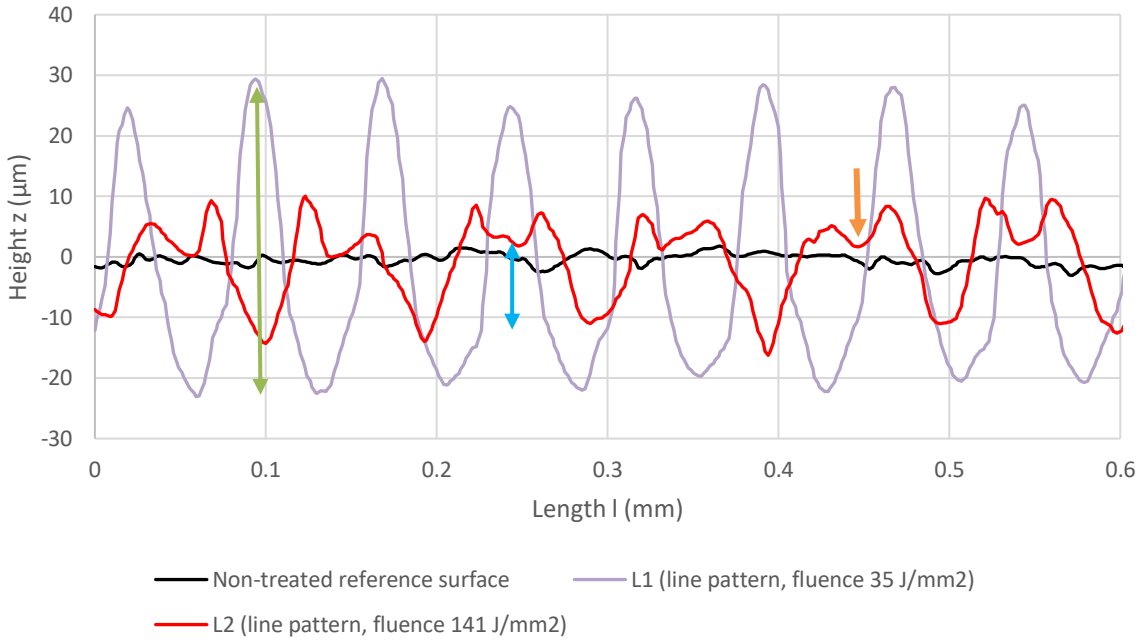

Figure 50 Line profiles perpendicular to laser tracks of non-treated reference surface, and laser textured surfaces L1 and L2. The peak-to-valley amplitude of L1 surface is indicated with green two-headed arrow, and peak-to-valley amplitude of L2 surface is indicated with blue two-headed arrow. Unprocessed area between L2 surface ridges is indicated with orange arrow.

Figure 50 shows profile measurements of the non-treated reference surface (black profile) and laser textured surfaces L1 (violet profile) and L2 (red profile). L1 surface was processed with line pattern and laser fluence of 35 J/mm^2, and L2 surface with line pattern and laser fluence of 141 J/mm^2. Line profiles were measured perpendicular to the laser tracks (line pattern profile 3, see section 7.5) to evaluate the depth and shape of the grooves and ridges formed between scan lines. Surface L1 (fill pitch 0.02 mm, 20 kHz) showed deep grooves with peak-to-valley amplitudes reaching approximately 50 µm (green two-headed arrow). These pronounced depressions are likely the result of material removal combined with ridge formation at the track edges, potentially caused by molten material displacement during processing. Surface L2 (fill pitch 0.1 mm, 100 kHz) exhibited shallower groove depths, with edge depths around 12 µm relative to the reference level (blue two-headed arrow). Between the ridges of L2 surface, unprocessed reference surface (orange arrow) remained visible, and ridge height above the reference surface was approximately 5 µm. As seen in Figure 50, the differences between L1

surface and L2 surface may be influenced by both the number of treatment times and the higher laser fluence in L2 (141 J/mm² vs. 35 J/mm² for L1 surface), affecting the extent of material displacement and melting. These results indicate that both fill pitch and laser fluence have a strong impact on the cross-track groove depth and ridge height, with tighter track spacing and lower frequency producing more prominent surface modulation.

The line profiles along laser tracks of surfaces G1 and G2 laser textured with grid pattern, and non-treated reference surface are presented in Figure 51.

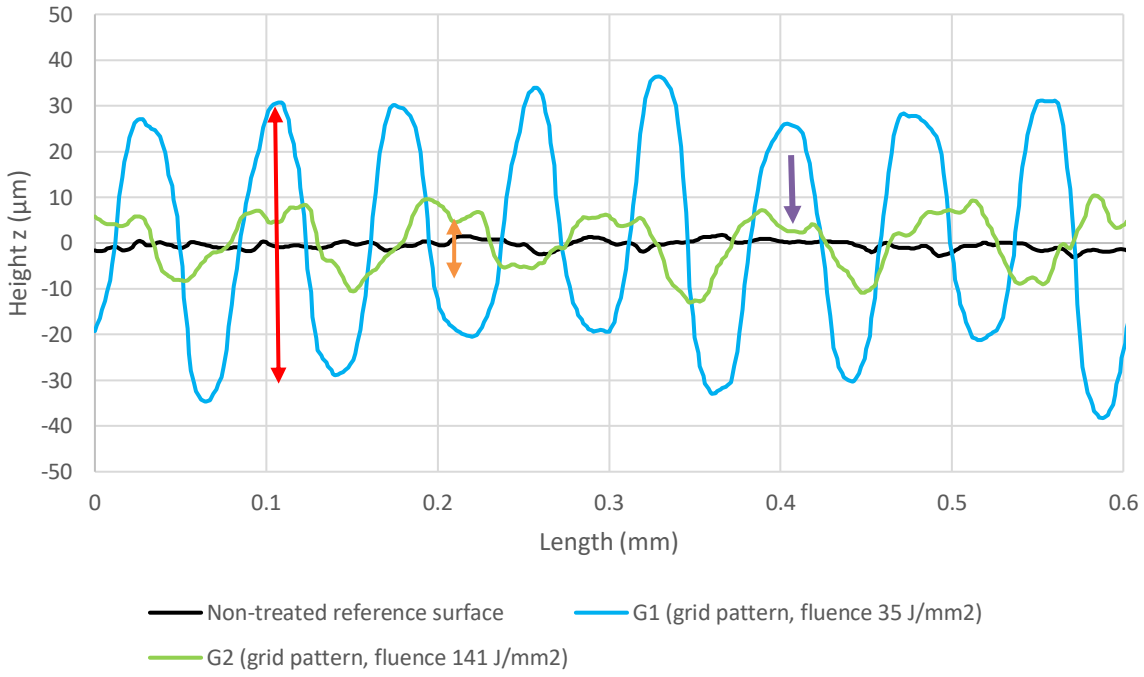

Figure 51 Line profiles along laser tracks of non-treated reference surface, and laser textured surfaces G1 and G2. The peak-to-valley amplitude of G1 surface is indicated with red two-headed arrow, and peak-to-valley amplitude of G2 surface is indicated with orange two-headed arrow. Unprocessed area between G2 surface ridges is indicated with violet arrow.

Figure 51 shows profile measurements of the non-treated reference surface (black profile) and laser textured grid pattern surfaces G1 (blue profile) and G2 (green profile). G1 surface was processed with grid pattern and laser fluence of 35 J/mm^2, and G2 surface with grid pattern and laser fluence of 141 J/mm^2. Line profiles were measured along the direction of the laser tracks (grid pattern profile 1, see section 7.5) to evaluate the height variations across the pulsed spots and ridges formed during grid pattern processing. Surface G1 (fill pitch 0.02 mm, 20 kHz) showed deep, regularly spaced grooves with peak-to-valley amplitudes of approximately 60 µm (red two-headed arrow). These pronounced features are likely the result of combined ablation and ridge formation, where molten material is displaced towards the edges of the laser-affected

zones. Surface G2 (fill pitch 0.1 mm, 100 kHz) displayed shallower grooves with depths of around 20 µm at the track edges (orange two-headed arrow). Between the ridges, the unprocessed reference surface remained (violet arrow), with ridge heights approximately 5 µm above the baseline. As seen in Figure 51, the difference in morphology between G1 and G2 is consistent with the larger fill pitch and shorter pulse spacing of G2, which reduce the degree of material displacement and produce a less pronounced surface modulation. Despite the higher nominal fluence in G2, the groove depth was smaller. This indicates that, within the present parameter window, fill pitch and pulse-to-pulse spacing dominates over fluence in controlling ridge formation and peak-to-valley amplitude.

The line profiles between the laser tracks of surfaces G1 and G2 laser textured with grid pattern, and non-treated reference surface are presented in Figure 52.

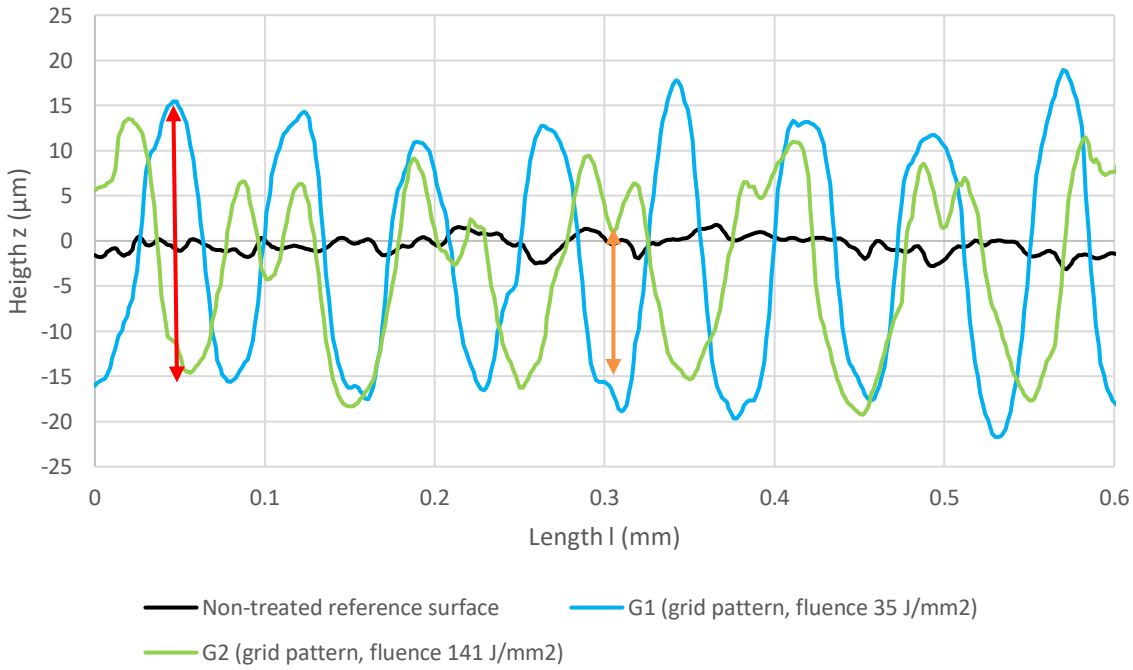

Figure 52 Line profiles between laser tracks of non-treated reference surface, and laser textured surfaces G1 and G2. The peak-to-valley amplitude of G1 surface is indicated with red two-headed arrow, and peak-to-valley amplitude of G2 surface is indicated with orange two-headed arrow.

Figure 52 shows line profiles measured between adjacent scan lines for the non-treated reference surface (black profile), G1 (blue profile) and G2 (green profile). G1 surface was processed with grid pattern and laser fluence of 35 J/mm^2, and G2 surface with grid pattern and laser fluence of 141 J/mm^2. Line profiles were measured between the laser tracks (grid pattern profile 2, see section 7.5). The reference profile is almost flat, with minor height variations within ±4 µm, corresponding to the baseline stainless steel substrate texture. Both G1 and G2

exhibit a repeating valley–ridge structure, but the measured groove depths are relatively close: approximately 30 µm for G1 (red two-headed arrow) and 25 µm for G2 (orange two-headed arrow), with ridge height between valleys in G2 being around 5 µm above the baseline. In G1, the small fill pitch results in full surface coverage, with overlap in the between-track regions, as seen in Figure 52. This promotes ridge build-up but also re-melts valley regions due to the orthogonal grid pass, which limits maximum valley depth despite the pronounced ridges. In G2, the larger fill pitch leaves baseline material between ridges. While the higher fluence produces deeper individual spots, the measurement path crosses both ridges and unprocessed baseline, causing shallower apparent valleys and smaller peak-to-valley height differences. These results indicate that, for between track measurements, surface coverage and overlap effects outweigh the influence of fluence in determining the apparent groove depth.

When comparing the line and grid patterns, clear differences in surface morphology and profile characteristics emerge. The surfaces laser textured with line patterns (L1 and L2) produced elongated, unidirectional grooves and ridges aligned with the scanning direction. L1 surface, processed at lower fluence (value of 35 J/mm^2) and frequency (value of 20 kHz), exhibited deeper and more pronounced peak-to-valley amplitudes, whereas L2 surface, processed at higher fluence (value of 141 J/mm^2) and frequency (value of 100 kHz), resulted in 76 % shallower structures with smoother ridge profiles and occasional unprocessed baseline areas. This demonstrates that in line textures, pulse frequency and fill pitch strongly control groove depth and ridge continuity. In contrast, the surfaces laser textured with grid patterns (G1 and G2) formed orthogonal structures with pronounced nodes at track intersections, creating a more isotropic topography. G1 surface, produced at lower fluence (value of 35 J/mm^2) and tighter fill pitch (value of 0.02 mm), showed the deepest and most periodic grooves, while G2, processed at higher fluence (value of 141 J/mm^2) and larger fill pitch (value of 0.1 mm), exhibited 67 % reduced valley depths and more uniform but less pronounced features. The groove depth of L1 surface vas 17 % lower when compared to G1 surface, similarly for surface L2 the groove depth was 40 % lower when compared to G2 surface. It can be observed, that laser texturing with grid textures is more effective in producing hierarchical roughness and isotropic structures, while using line textures emphasize anisotropic grooves whose dimensions are sensitive to processing parameters. The results confirm that pattern geometry plays a decisive role in determining both the directionality and magnitude of the surface features, which are expected to influence wetting behaviour and functional performance differently.

Coating

3D surface topography measurements and imaging were conducted for coated laser textures surfaces L1, L2, G1 and G2, and coated non-treated reference surface. Coloured topography images of these surfaces are presented in Figures 53 and 54. These images and line profile measurements can be compared to non-coated surfaces presented in previous section (see section 8.3 3D topography: Pre-treatment).

The surface topography image of coated non-treated reference surface is presented in Figure 53.

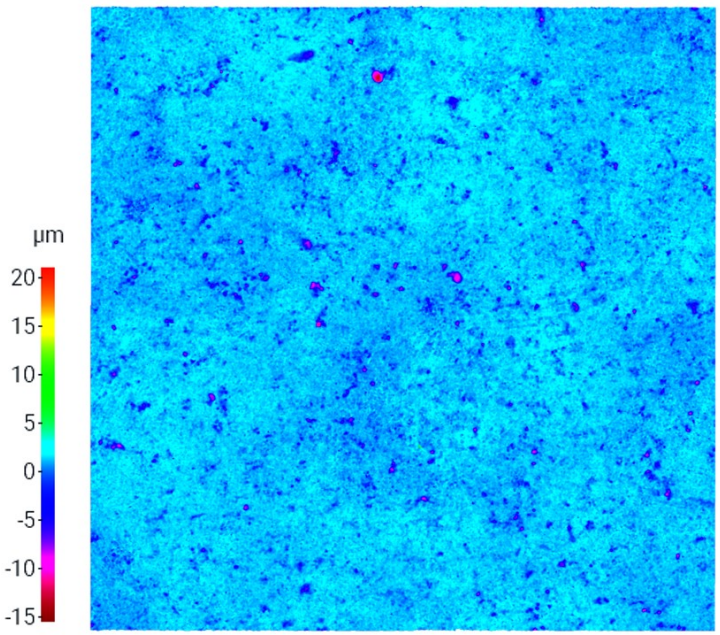

Figure 53 Topography image of the coated non-treated reference surface.

Figure 53 shows the 3D surface topography of the non-treated reference surface after coating. The colour scale indicates height variations between –15 µm and +20 µm. Compared to the non-treated reference surface before coating (Figure 43), the overall morphology remains fine and randomly distributed, as expected in the absence of laser texturing. After coating, the distribution of peaks and valleys appears more even and the sharpest extremes are reduced, giving the surface a slightly smoother and more homogeneous appearance. This suggests mechanical interlocking, where the coating has adhered effectively along both the crests and troughs of the stainless-steel surface, promoting strong interfacial bonding despite the relatively fine topography. The coating conforms closely to the underlying steel substrate without introducing any periodic or directional features, confirming that the modification is primarily conformal and chemical in nature rather than structural.

The surface topography image of coated surface L1 laser textured with line pattern is presented in Figure 54.

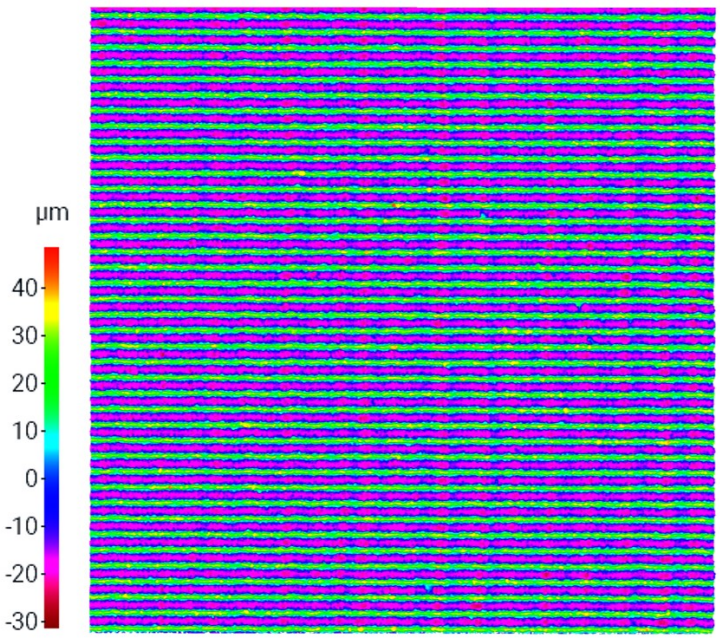

Figure 54 Topography image of the coated L1 surface processed with line pattern and laser fluence of 35 J/mm^2.

Figure 54 shows the 3D surface topography of the coated L1 surface. The line-patterned ridges and grooves created by laser texturing remain clearly visible, and no major changes in surface morphology can be observed compared to the uncoated L1 surface (Figure 44). The peaks and valleys appear nearly identical in shape and amplitude, indicating that the coating has formed a very thin and homogeneous layer across the textured surface. The colour scale supports this interpretation, showing that the characteristic periodic structure is preserved without significant smoothing or filling of valleys. This suggests that the coating process did not alter the micrometre-scale topography, but instead uniformly covered the surface, ensuring that functional behaviour can be directly compared before and after coating.

The same observation can be made in the 3D topography images of the other coated laser textured surfaces (L2, G1 and G2 surface) shown in Appendix 3. In these cases, no major changes in surface morphology are visible when compared to the uncoated counterparts. The ridges, grooves, and valleys generated by laser texturing remain clearly distinguishable, and the overall roughness values show only minor variations. This indicates that the coating layer is very thin and has spread homogeneously across the surfaces without significantly altering the microstructural features.

The minimal effect on roughness parameters suggests that the coating conforms closely to the existing topography rather than filling valleys or smoothing peaks. As a result, the functional textures created during laser processing are preserved, while the uniform coating ensures consistent chemical modification across the entire surface. This outcome is consistent with the expected behaviour of thin-film coatings, which form a continuous layer without substantially changing micrometre-scale features. It also highlights that the hydrophobic or functional improvements introduced by the coating arise primarily from changes in surface chemistry rather than large-scale modifications of topography.

The line profiles perpendicular to laser tracks of coated laser textured surfaces L1 and L2, and coated non-treated reference surface are presented in Figure 55.

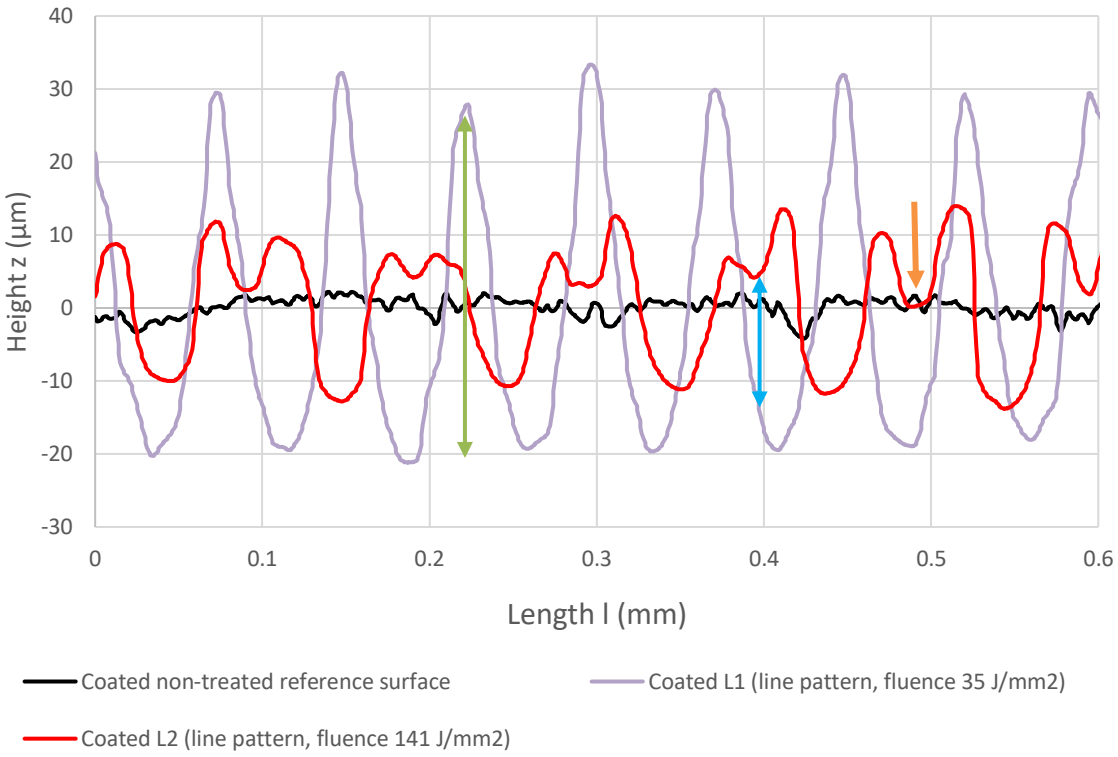

Figure 55 Line profiles perpendicular to laser tracks of coated non-treated reference surface, and coated laser textured surfaces L1 and L2. The peak-to-valley amplitude of L1 surface is indicated with green two-headed arrow, and peak-to-valley amplitude of L2 surface is indicated with blue two-headed arrow. Unprocessed area between L2 surface ridges is indicated with orange arrow.

Figure 55 shows the profile measurements of the coated non-treated reference surface and the coated laser textured surfaces L1 and L2. Line profiles were measured perpendicular to the laser tracks (line pattern profile 3, see section 7.5). The coated reference surface (black profile) remains nearly flat, with only minor fluctuations within ±2 µm, confirming the absence of laser-induced structures. Surface L1, processed with a line pattern at a fluence of 35 J/mm², displays

a clear periodic modulation with peak-to-valley amplitudes of about 50 µm (green two-headed arrow). Surface L2, processed with a line pattern at a fluence of 141 J/mm², shows shallower grooves with amplitudes of roughly 12 µm (blue two-headed arrow), and unprocessed baseline areas are still visible between ridges (orange arrow).

When compared with the uncoated profiles in Figure 50, no changes are observed after coating. The amplitudes of both L1 and L2 surface remain essentially the same, and the ridge–valley morphology is preserved. This indicates that the coating layer is very thin and deposited conformally, covering the textured surfaces without altering their geometry. The slight smoothing visible at the ridge crests suggests uniform film coverage, but the periodicity and characteristic structure remain unchanged. This confirms that the coating does not modify the laser-induced microstructure but rather forms a homogeneous, thin layer on top.

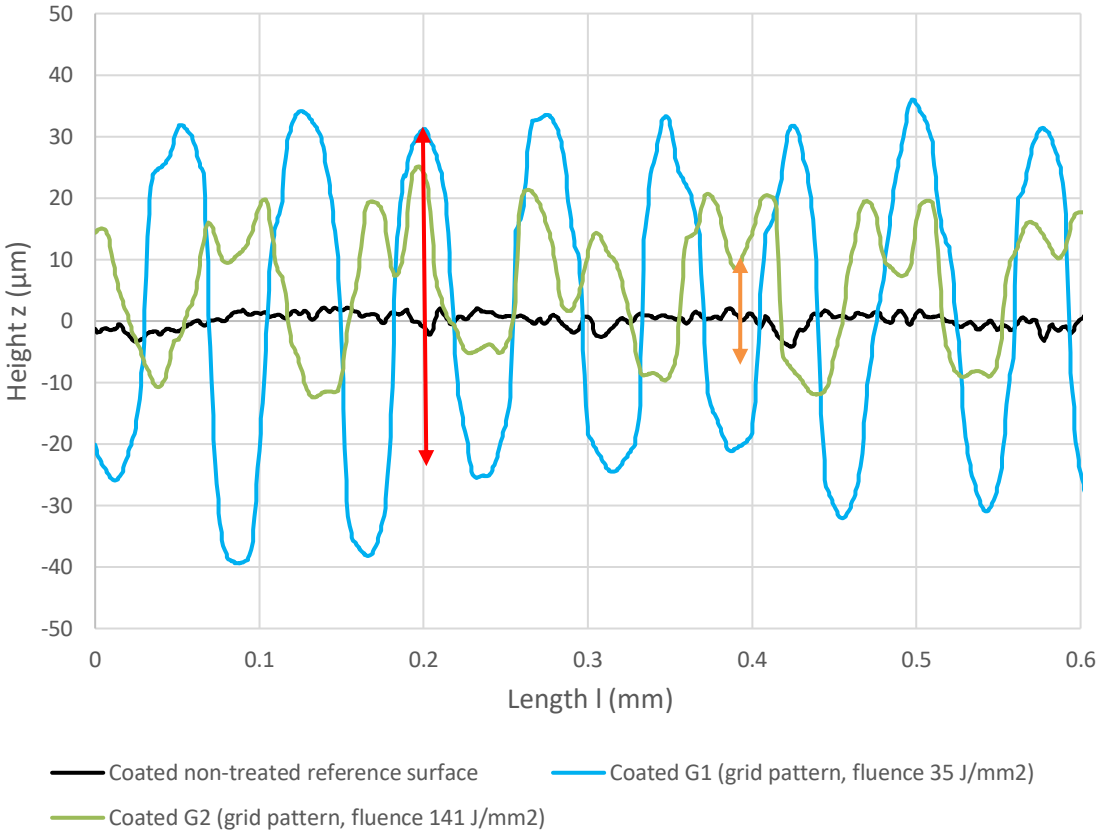

Figure 56 Line profiles along laser tracks of coated non-treated reference surface, and coated laser textured surfaces G1 and G2. The peak-to-valley amplitude of G1 surface is indicated with red two-headed arrow, and peak-to-valley amplitude of G2 surface is indicated with orange two-headed arrow.

Figure 56 shows profile measurements of the coated non-treated reference surface (black profile) and the coated laser textured grid pattern surfaces G1 (blue profile) and G2 (green profile). Line profiles were measured along the direction of the laser tracks (grid pattern profile

1, see section 7.5). The reference surface remains essentially flat, with only minor fluctuations within ±2 μm, confirming the absence of laser-induced structures. Surface G1, processed with a grid pattern at fluence of 35 J/mm², displays the same pronounced periodic peaks and valleys as observed before coating, with peak-to-valley amplitudes of approximately 60 μm (red two-headed arrow). Similarly, surface G2 (fluence of 141 J/mm²) maintains shallower grooves with depths around 20 μm (orange two-headed arrow), consistent with its original morphology prior to coating.

When comparing profiles of coated surfaces G1 and G2, as seen in Figure 57, to the uncoated profiles of surfaces in Figure 51, no changes are observed in either amplitude or periodicity, indicating that the coating layer is very thin and conformal. The sharp ridges, valleys, and unprocessed baseline regions remain visible, confirming that the coating deposited uniformly without altering the larger-scale geometry of the textured surfaces. These results suggest that the coating forms a homogeneous film across both the textured and untextured regions, preserving the functional topography generated by laser texturing.

The same trend was observed in the line profile measurements of the other coated laser textured surfaces, which are presented in Appendix 6. In each case, the coated profiles closely matched their uncoated counterparts, with no significant alterations in ridge height, groove depth, or overall periodicity. The characteristic structures created by the laser texturing process, such as the deep ridges of L1 and G1 surface (fluence of 35 J/mm²) or the shallower grooves of L2 and G2 surface (fluence of 141 J/mm²), remained clearly visible after coating. This confirms that the applied coating layer was very thin and uniformly distributed across the surfaces, conforming to the existing topography without filling valleys or levelling peaks.

The preservation of these microstructural features indicates that the primary influence of the coating lies in chemical surface modification rather than physical restructuring. As a result, the functional behaviour of the laser-textured patterns is maintained, while the thin film ensures a consistent hydrophobic layer across the entire surface. This outcome aligns with the expected behaviour of conformal thin coatings, which enhance surface functionality while leaving micrometre-scale roughness essentially unchanged.

Roughness measurements

Areal roughness measurements were conducted for laser textures surfaces L1, L2, G1 and G2, and non-treated reference surface. L1 surface was processed with line pattern and fluence of 35

J/mm², L2 surface was processed with line pattern and fluence of 141 J/mm², G1 surface was processed with grid pattern and fluence of 35 J/mm² and G2 surface was processed with grid pattern and fluence of 141 J/mm². The arithmetical average roughness values *Sa* for these surfaces are presented in

Figure 57 and mean peak-to-valley height values *Sz* in Figure 58. *Sa* and *Sz* roughness values are provided in Appendix 4. Areal roughness measurements were performed for coated laser textured surfaces L1, L2, G1 and G2, as well as for the coated non-treated reference surface. The arithmetical average roughness values (*Sa*) for these surfaces are presented in Figure 59, and the maximum peak-to-valley height values (*Sz*) in Figure 60. *Sa* and *Sz* roughness values are provided in Appendix 4.

The roughness values *Sa* of laser textured surfaces L1, L2, G1 and G2, and non-treated reference surface, are presented in Figure 57.

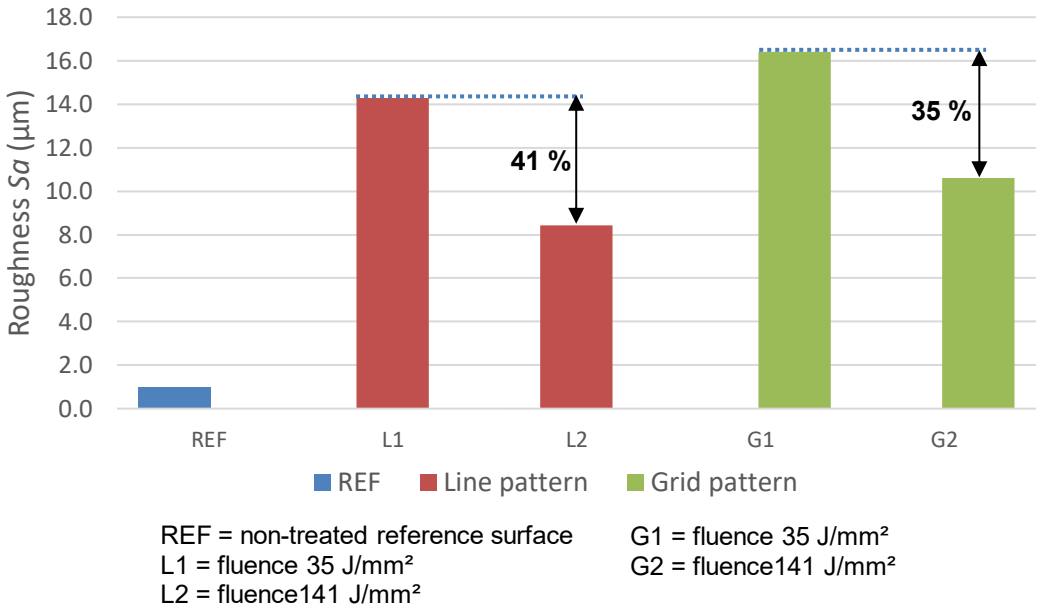

Figure 57 Roughness values *Sa* for laser textures surfaces L1, L2, G1 and G2, and non-treated reference surface.

Figure 57 presents the measured areal roughness values *Sa* for the non-treated reference surface and laser textured surfaces L1, L2, G1, and G2. The non-treated reference surface exhibited a roughness value *Sa* of 1.0 µm, consistent with the fine topography of the stainless steel substrate. All laser treated surfaces showed a substantial increase in roughness when compared to non-treated reference surface, reflecting the formation of distinct micro-scale features by laser ablation and material displacement. Among the line patterns, L1 surface (fill pitch 0.02 mm, frequency 20 kHz, fluence 35 J/mm²) recorded the higher *Sa* value of 14.3 µm, indicating

the presence of pronounced periodic waviness and ridge structures generated by the relatively large pulse spacing. L2 surface (fill pitch 0.1 mm, frequency 100 kHz, fluence 141 J/mm²) had a 41 % lower roughness value (*Sa* value of 8.4 µm) compared to L1 surface, consistent with the more uniform surface texture and reduced modulation due to higher pulse overlap.

As seen in Figure 57, the surfaces laser textured with grid pattern (surfaces G1 and G2), the roughness values were higher in comparison to surfaces textured with line pattern (surfaces L1 and L2), with surface G1 (fill pitch 0.02 mm, frequency 20 kHz, fluence 35 J/mm²) reaching a *Sa* value of 16.4 µm, the highest among all textured surfaces. This can be attributed to the combined effect of orthogonal scanning and small fill pitch, which maximizes overlap and promotes the formation of pronounced ridges at the intersections of scan lines. G2 surface (fill pitch 0.1 mm, frequency 100 kHz, fluence 141 J/mm²) exhibited a 35 % lower roughness (*Sa* value of 10.6 µm) compared to G1 surface, which reflects the reduced surface coverage and presence of baseline material between ridges. These results show that pattern geometry and fill pitch have a strong influence on the resulting surface roughness, with small fill pitches in both line and grid patterns producing the highest *Sa* values, whereas higher pulse overlap (higher frequency) tends to reduce roughness amplitude.

The roughness values *Sz* of laser textured surfaces L1, L2, G1 and G2, and non-treated reference surface are presented in Figure 58.

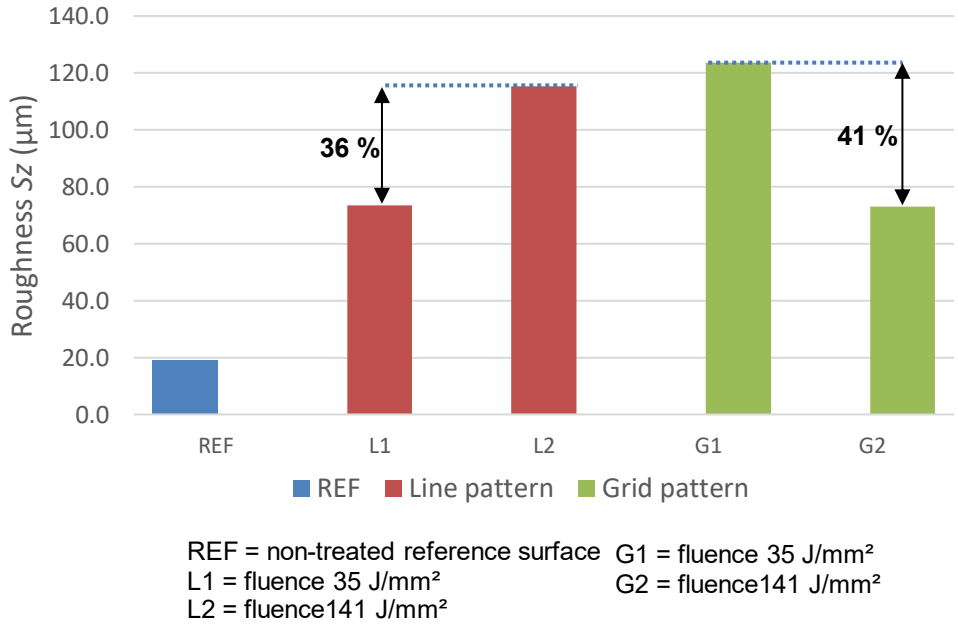

Figure 58 Roughness values *Sz* for laser textures surfaces L1, L2, G1 and G2, and non-treated reference surface.

Figure 58 presents the maximum height values *Sz* for the non-treated reference surface and laser textured surfaces L1, L2, G1, and G2. L1 surface was processed with line pattern and laser fluence of 35 J/mm^2, L2 line pattern and laser fluence of 141 J/mm^2, G1 with grid pattern and laser fluence of 35 J/mm^2, G2 grid pattern and laser fluence of 141 J/mm^2. The non-treated reference surface exhibited a *Sz* value of 19.1 µm, consistent with the minor peak-to-valley variations of the stainless steel substrate. All laser textured surfaces showed an increase in *Sz* values compared to non-treated reference surface, reflecting the introduction of deeper valleys and higher peaks through material removal and ridge formation. Among the surfaces textured with line patterns, L1 surface (*Sz* value of 73.4 µm) had a 36 % lower value of *Sz* than L2 surface (*Sz* value of 115.3 µm). This difference is primarily related to the larger fill pitch of L2 (value of 0.1 mm), which leaves untreated regions between tracks, producing deeper valleys that increase the overall vertical range. In contrast, smaller fill pitch (value of 0.02 mm) of L1 surface results in more continuous coverage and shallower valleys, even though its ridge structures are still prominent.

As seen in Figure 58, the surfaces laser textured with grid pattern exhibited the highest *Sz* values overall, with G1 surface reaching *Sz* value of 123.6 µm and G2 surface measuring *Sz* value of 73.0 µm. The combination of small fill pitch (value of 0.02 mm) and orthogonal scanning of G1 surface generated tall ridges at scan intersections and deep troughs between them, maximising the peak-to-valley range. In G2 surface, the larger fill pitch (value of 0.1 mm) reduced overlap between tracks in both x and y scanning directions, producing shallower ridges (value of ~5 µm above untreated areas) and lower value of *Sz*. These results demonstrate that maximum height value *Sz* is influenced by fill pitch and scanning geometry, with large untreated gaps and orthogonal scanning promoting higher maximum heights, while smaller fill pitch leads to more uniform but less vertically extreme surface topography.

The roughness values *Sa* of coated laser textured surfaces L1, L2, G1 and G2, and coated non-treated reference surface, are presented in Figure 59.

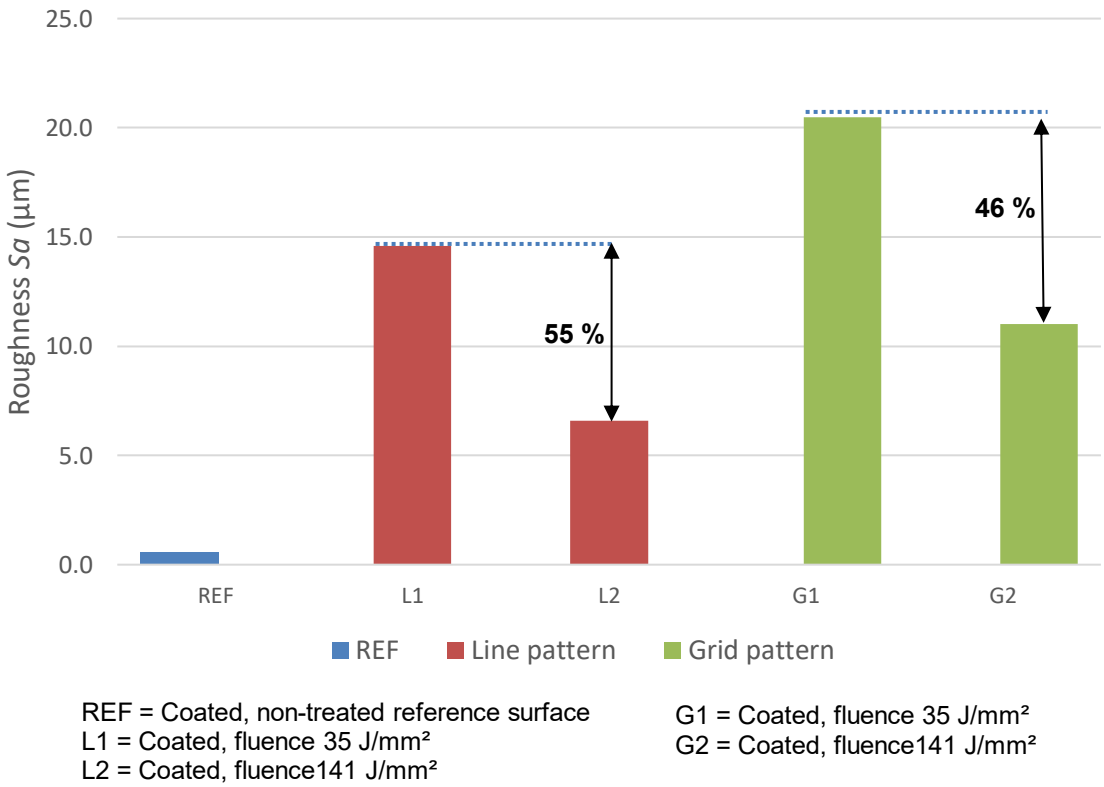

Figure 59 Roughness values *Sa* for coated laser textures surfaces L1, L2, G1 and G2, and coated non-treated reference surface.

As shown in Figure 59, the coated non-treated reference surface exhibited a low *Sa* value of 0.6 µm, consistent with the smooth stainless steel substrate morphology. All laser textured surfaces maintained higher *Sa* values after coating, demonstrating that the deposition process preserved the underlying microstructures generated during laser texturing. Among the laser textured surfaces processed with line pattern, L1 surface (fluence 35 J/mm²) exhibited a *Sa* value of 14.7 µm, while L2 surface (fluence 141 J/mm²) showed a lower value of 6.6 µm, corresponding to a 55 % reduction. This suggests that the higher fluence of L2 surface resulted in a smoother topography with reduced waviness compared to L1 surface. For the laser textured surfaces processed with grid pattern, G1 surface (fluence 35 J/mm²) reached the highest *Sa* value overall at 20.5 µm, while G2 surface (fluence 141 J/mm²) measured 11.0 µm, reflecting a 46 % reduction relative to G1 surface.

The roughness values *Sz* of coated laser textured surfaces L1, L2, G1 and G2, and coated non-treated reference surface, are presented in Figure 60.

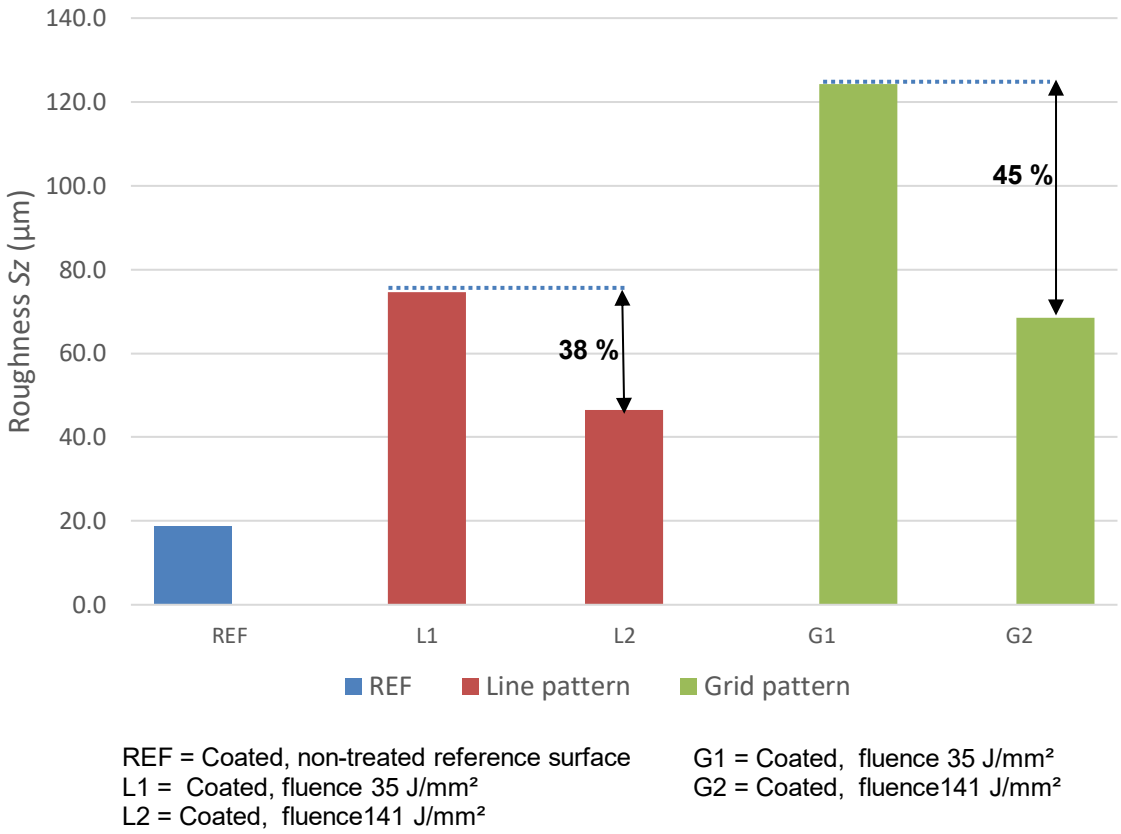

Figure 60 Roughness values *Sz* for coated laser textures surfaces L1, L2, G1 and G2, and coated non-treated reference surface.

The *Sz* values presented in Figure 60 provide additional insight into the vertical range of the structures. The coated non-treated reference surface exhibited a *Sz* of 19.1 µm, consistent with its flat baseline topography. Among the laser textured surfaces processed with line pattern, L1 surface (fluence 35 J/mm²) reached a *Sz* of 73.4 µm, while L2 surface (fluence 141 J/mm²) showed a higher *Sz* value of 115.3 µm, corresponding to a 38 % increase compared to L1 surface. For the surfaces laser textured with grid pattern, G1 surface exhibited the highest *Sz* value of all surfaces at 124.0 µm, while G2 surface measured 68.5 µm, a 45 % reduction compared to G1 surface. The high *Sz* of G1 reflects the combination of small fill pitch and orthogonal scanning, which produced tall ridges and deep troughs. In contrast, G2 surface, with larger fill pitch and higher frequency, showed shallower ridges and less vertical variation.

After coating, the roughness values of the laser-textured surfaces exhibited notable changes compared to the uncoated state. For the reference surface, both *Sa* and *Sz* values slightly

decreased (–45 % and –1.5 %, respectively), which can be attributed to the coating layer filling shallow valleys and smoothing the original substrate topography. Among the line-patterned surfaces, L1 showed minimal change in *Sa* (around +2 %), while *Sz* remained nearly constant (+1.6 %), indicating that the coating conformed to the existing ridge–valley structure without altering the overall height distribution. In contrast, L2 displayed a substantial reduction, with *Sa* decreasing by approximately –22 % and *Sz* by –60 %, suggesting that the coating filled the deeper valleys created by the larger fill pitch, reducing the vertical range of the surface features.

For the grid-patterned surfaces, G1 experienced an increase in Sa of about +25 %, while *Sz* remained almost unchanged (+0.8 %). This indicates that the coating amplified the average roughness by enhancing fine-scale asperities without altering the maximum peak-to-valley distances. Conversely, G2 showed a moderate increase in *Sa* (+3.8 %) but a considerable reduction in *Sz* (–41 %), highlighting that although the average surface roughness increased slightly, the coating effectively reduced the extreme height variations by partially leveling the deepest valleys.

These results demonstrate that the effect of coating on roughness depends on the underlying surface geometry. While smoother or more uniform structures (e.g., L1, G1) retained their morphology after coating, surfaces with larger valleys (L2, G2) exhibited reductions in *Sz*, indicating that the coating preferentially filled deeper features and reduced vertical extremes. This behaviour suggests that the coating can homogenize roughness and potentially influence subsequent surface functionality, particularly wettability and corrosion resistance.

8.4 SEM

Pre-treatment

SEM imaging and analysis were performed on the laser textured surfaces L1, L2, G1, and G2, as well as on the non-treated reference surface, which served as the baseline prior to the laser processing. Key results obtained using the ETD, T1, and T3 detectors of FE-SEM are presented in Figures 61-74.

The ETD-SEM image with 500x magnification of non-treated reference surface is presented in Figure 61.

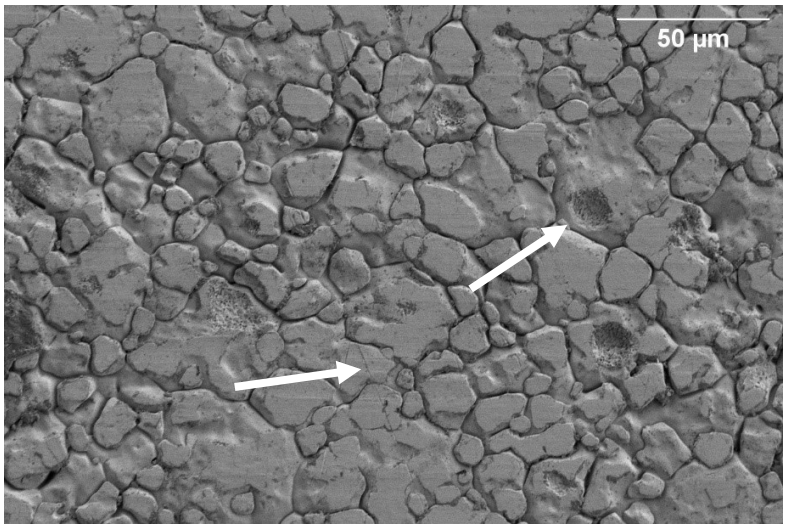

Figure 61 ETD-SEM image of non-treated reference surface with 500x magnification. Irregularities (pits and scratches) of the surface are highlighted with arrows.

Figure 61 presents an ETD-SEM image of the non-treated reference surface at 500x magnification, illustrating the overall granular microstructure characteristic of the stainless steel substrate surface. The grains are predominantly equiaxed, with diameters ranging from a few to several tens of micrometres. Grain boundaries are continuous and well-defined, forming an interconnected network across the stainless steel surface. Variations in the surface morphology are visible between grain interiors and boundaries, likely caused from mechanical finishing and the inherent crystallographic orientation of the grains. As shown in Figure 61, minor surface irregularities, such as shallow pits and scratches, are distributed across the surface, consistent with polishing marks or handling-induced defects. This low-magnification overview establishes the baseline morphology for later comparison with laser treated surfaces, where deviations in boundary sharpness, depth differences of the surface structure, and microstructural uniformity may indicate melting, ablation, or re-solidification effects.

The ETD-SEM image with 1500x magnification of non-treated reference surface is presented in Figure 62.

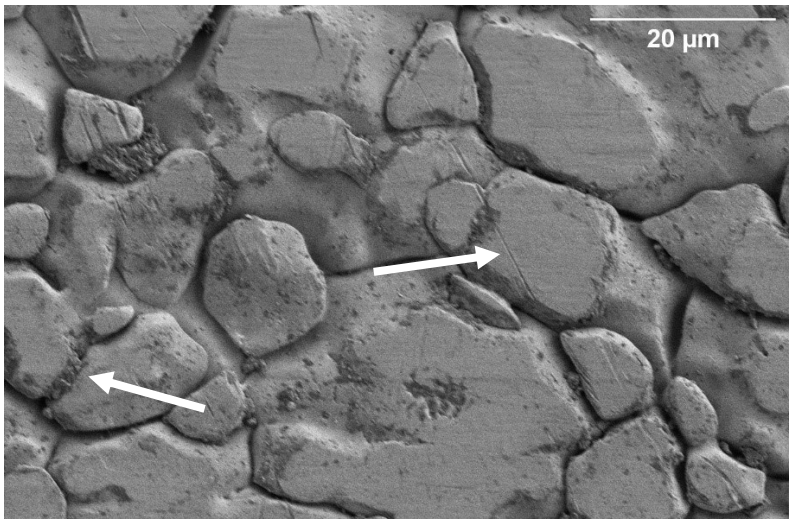

Figure 62 ETD-SEM image of non-treated reference surface with 1500x magnification. Debris particles and polishing-induced line marks of the surface are highlighted with arrows.

Figure 62 shows the non-treated reference surface at 1500x magnification, providing a closer examination of the fine morphological details within the grains and along the grain boundaries. The grain interiors appear smooth, with occasional nanoscale debris particles and polishing-induced line marks. The grain boundaries themselves reveal shallow depressions and, in some cases, localised accumulations of fine particulate matter, possibly remnants of polishing compounds or oxide fragments that have preferentially adhered to these lower-energy sites. Subtle differences in the low-angle backscattered image within individual grains may reflect variations in crystallographic orientation or the presence of very fine sub-grain features. The absence of melt–re-solidification structures, microcracks, or irregular protrusions further confirms that this surface has not undergone thermal modification, reinforcing its role as a reference surface for assessing laser-induced morphological changes.

The T1-SEM image with 1500x magnification of non-treated reference surface is presented in Figure 63.

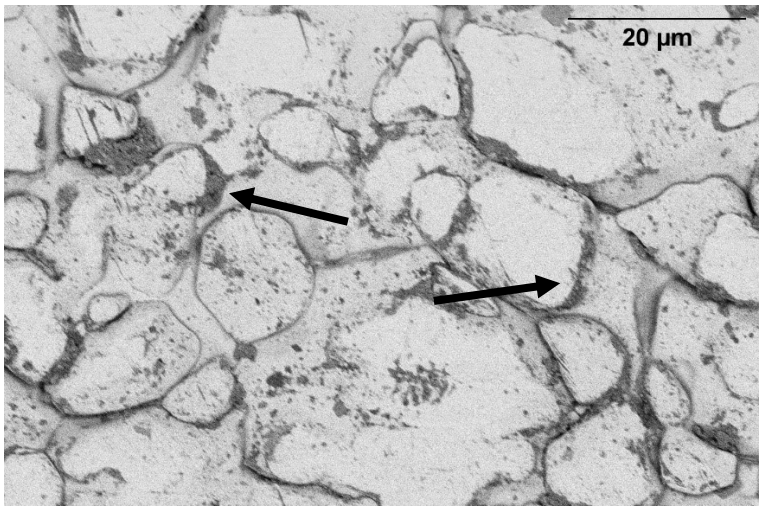

Figure 63 T1-SEM image of non-treated reference surface with 1500x magnification. Darker regions along grain boundaries of the surface are highlighted with arrows.

Figure 63 shows a T1-SEM image of the non-treated reference surface at 1500x magnification. The T1 detector captures high-angle backscattered electrons, producing atomic number (Z) contrast that reveals subtle compositional variations across the stainless steel surface microstructure. Brighter regions correspond to areas enriched in heavier elements, while darker zones indicate regions with lighter elements or lower atomic number. The image delineates the grain structure previously observed with ETD detector (see Figure 62), but here the boundaries appear more pronounced in contrast due to possible segregation of alloying elements during solidification. Darker regions along grain boundaries may suggest the presence of lighter-element phases, minor oxidation, or contamination introduced during manufacturing or handling. Conversely, occasional bright spots within grain interiors could indicate small inclusions or compositional heterogeneities, potentially originating from the steelmaking process. The overall contrast uniformity across most grains indicates that the base material is compositionally consistent, with only minor localised variations. This non-treated reference surface condition provides a baseline for identifying laser-induced compositional redistribution or oxide formation in processed surfaces, where higher thermal input may alter the Z-contrast signature.

The ETD-SEM image with 500x magnification of L1 surface is presented in Figure 64.

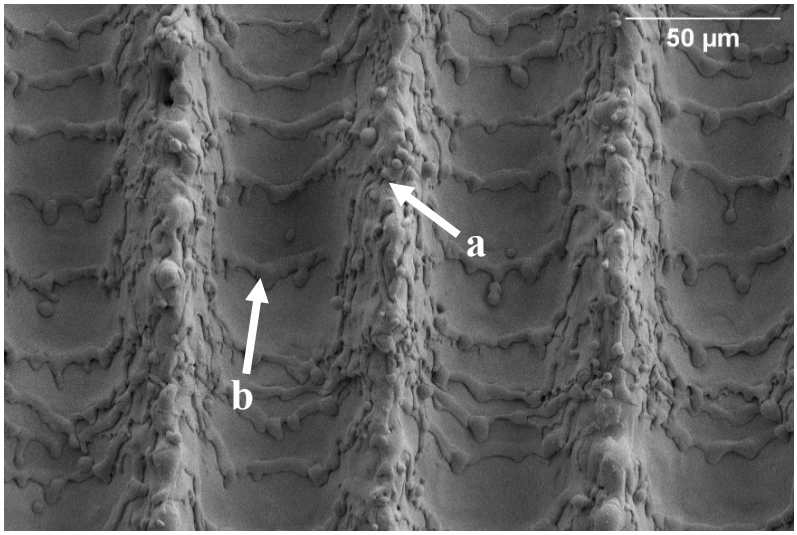

Figure 64 ETD-SEM image of L1 surface with 500x magnification.

Figure 64 presents an ETD-SEM image of the L1 laser textured surface at 500x magnification. The L1 surface was laser processed with line pattern and laser fluence of 35 J/mm^2. The surface displays a series of parallel laser tracks aligned with the scanning direction, separated by distinct ridges formed during the overlapping of successive pulses (indicated by arrow a in Figure 64). These ridges exhibit an irregular morphology with molten material resolidified into rounded protrusions and droplets, indicating localized melting and re-solidification dynamics inherent to the nanosecond pulsed laser process. Between the ridges, the track interiors (marked by arrow b) appear relatively smooth but still contain fine particulate deposits and shallow surface undulations, suggesting partial re-deposition of ablated material and surface-tension-driven flow during the molten state. The ridge height and width variation may be attributed to fluctuations in energy delivery along the scan path or local differences in substrate absorptivity. The observed periodic structure corresponds closely to the programmed scanning parameters and fill pitch (0.02 mm), with the distinct ridge–valley topography expected to influence subsequent wetting behaviour by introducing directional anisotropy. The degree of molten material accumulation along the ridges also suggests that flash overlap and heat accumulation effects are present at the selected fluence and repetition settings for the L1 surface, potentially enhancing microstructural reflow at the track boundaries.

The ETD-SEM image with 1500x magnification of raised ridge on the L1 surface is presented in Figure 65.

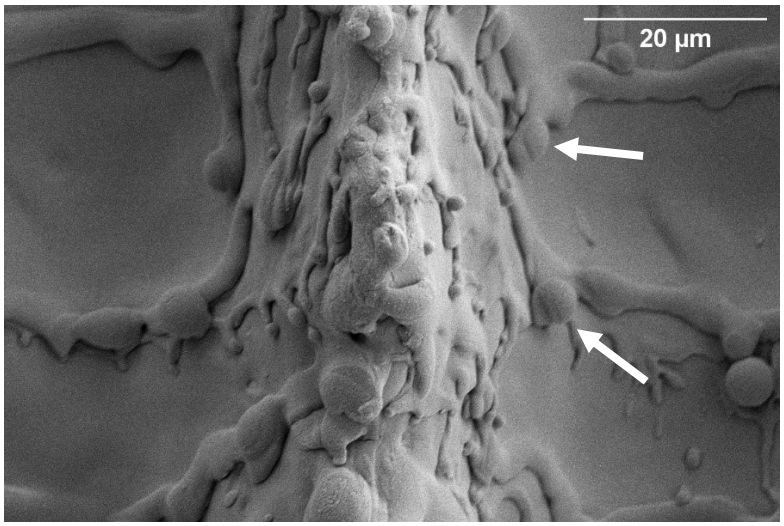

Figure 65 ETD-SEM image of raised ridge on L1 surface with 1500x magnification. Spherical and semi-spherical droplets of the surface are highlighted with arrows.

Figure 65 shows an ETD-SEM image of the laser textured surface L1, processed with line pattern and laser fluence of 35 J/mm^2, at 1500x magnification, focusing on the ridge region formed between adjacent laser scan tracks. The ridge exhibits an irregular topography with evidence of extensive molten material reflow and solidification. Spherical and semi-spherical resolidified droplets are abundant along the crest (see Figure 65), ranging from submicron sizes to several micrometres in diameter, indicative of melt ejection and redeposition during pulse overlap. The surface texture on these resolidified features appears rough, suggesting rapid solidification that may have trapped fine-scale microstructures or oxide layers. Between the droplets, the ridge surface displays flow-like patterns, consistent with viscous melt movement before solidification. The valley regions on either side of the ridge are comparatively smoother, with occasional small particulates, likely representing either condensed vapour phase material or molten splashes that settled in lower areas. This higher magnification view complements the 500x (see Figure 64) overview by revealing the microstructural consequences of the chosen fluence (35 J/mm^2) and pulse overlap parameters (frequency 20 kHz, fill pitch 0.02 mm) for L1. The pronounced droplet formation and ridge height variation suggest that localised heat accumulation influenced melt pool dynamics, potentially affecting not only surface roughness but also wettability by introducing microscale hierarchical features along the laser track boundaries.

The ETD-SEM image with 500x magnification of L2 surface is presented in Figure 66.

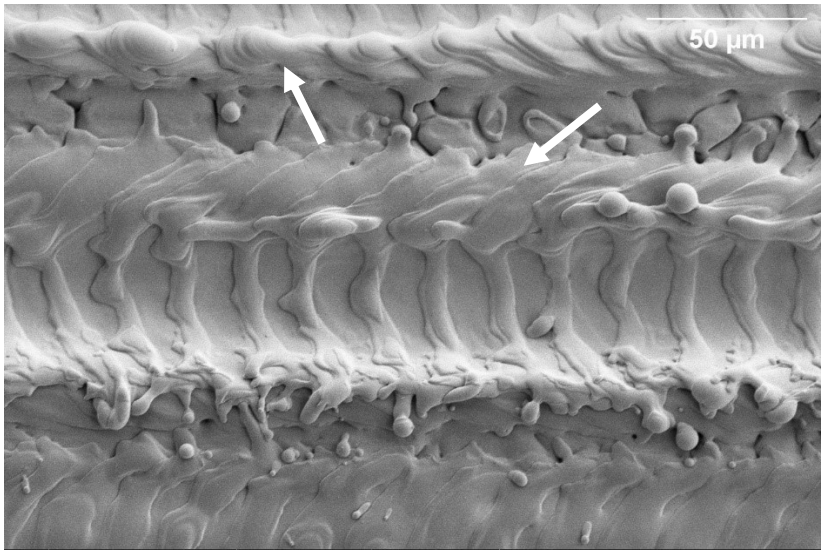

Figure 66 ETD-SEM image of ridge on L2 surface with 500x magnification. Ridges of the surface formed during the laser process are highlighted with arrows.

Figure 66 presents an ETD-SEM image of the L2 laser textured surface at 500x magnification. L2 surface was laser processed with line pattern and laser fluence of 141 J/mm^2. The surface morphology consists of parallel laser tracks with shallow valleys and moderately elevated ridges along their boundaries. The ridges are more uniform and less irregular than those observed on the L1 surface (see Figure 64), reflecting the influence of the higher pulse repetition rate (100 kHz) and increased pulse overlap in parallel to scanning direction (frequency of 100 kHz), which promote smoother material redistribution during re-solidification. Flow-like patterns are visible at the ridge edges, indicative of molten material displacement from the irradiated zones toward the periphery of each track. Spherical and semi-spherical particles, likely formed from ejected molten droplets that re-solidified upon redeposition, are scattered across the surface but appear in lower density than in L1 surface, suggesting reduced spatter generation at the higher fluence (141 J/mm²) under these scanning conditions. The track interiors are smooth and continuous, with minimal deep localised depressions, consistent with a more stable melt pool formation and reduced pulse-to-pulse height variation. The overall morphology suggests that the processing parameters of L2 surface result in a more uniform and less topographically extreme surface than L1 surface, while still maintaining pronounced track–ridge definition.

The ETD-SEM image with 1500x magnification of non-treated area adjacent to laser tracks on the L2 surface is presented in Figure 67.

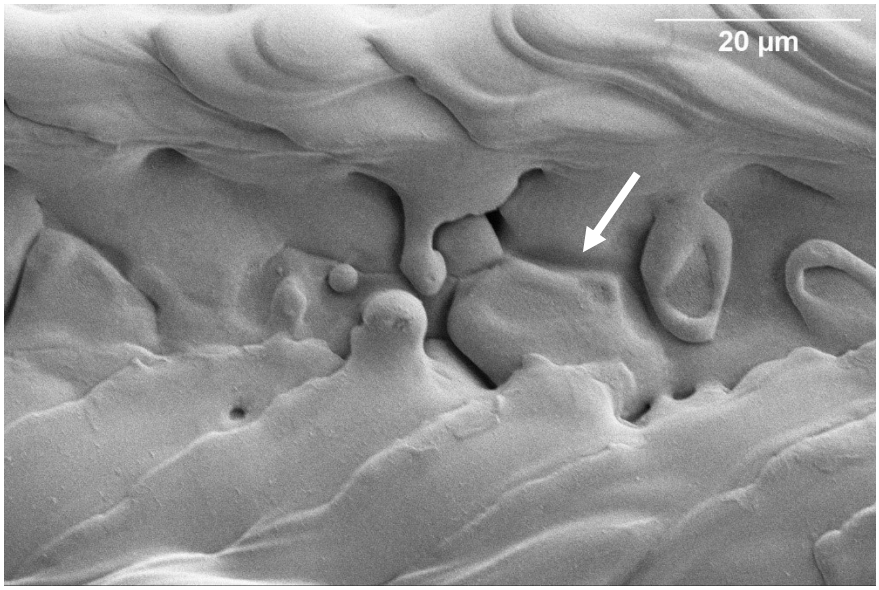

Figure 67 ETD-SEM image of non-treated area adjacent to laser tracks on L2 surface with 1500x magnification. Grain structure between ridges of the surface is highlighted with arrow.

Figure 67 shows an ETD-SEM image of the L2 laser textured surface taken between adjacent laser tracks at 1500x magnification. The surface was laser processed with line pattern and laser fluence of 141 J/mm^2. The morphology in this inter-track region is smooth compared to the ridge zones, with only moderate surface undulations and isolated resolidified features. Small spherical and semi-spherical droplets, ranging from submicron size to a few micrometres, are scattered across the area, indicating limited spatter deposition from neighbouring melt zones. Some elongated, flow-like structures are present, suggesting minor melt displacement during the laser process, but without the pronounced height variations seen in ridge regions. The presence of shallow depressions and fine-scale protrusions reflects partial re-melting and surface tension-driven redistribution, likely influenced by heat conduction from adjacent tracks. In the centre of the image, between the ridges, grain structures typical of the non-treated reference surface (see Figure 62) are discernible, implying that parts of the inter-track region remained unmodified by the laser process. The overall uniformity of the surface in this region points to a higher degree of pulse overlap and a more stable melt pool behaviour under the L2 parameters, which reduces extreme topographical features while still leaving evidence of localised droplet ejection and redeposition.

The ETD-SEM image with 500x magnification of G1 surface is presented in Figure 68.

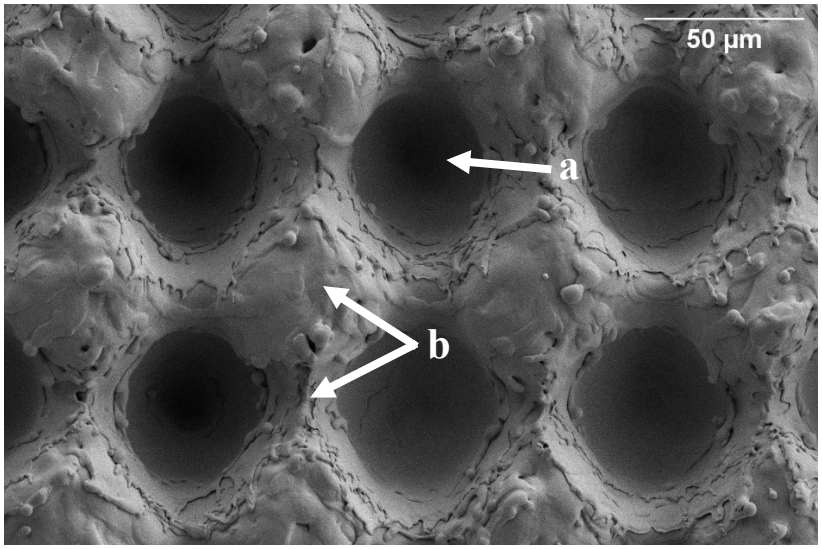

Figure 68 ETD-SEM image of ridge on G1 surface with 500x magnification.

Figure 68 presents an ETD-SEM image of the G1 laser textured surface at 500x magnification, revealing the characteristic grit pattern morphology formed by overlapping of the laser pulses. G1 surface was laser processed with grid pattern and laser fluence of 35 J/mm^2. The surface consists of a periodic arrangement of closely spaced, bowl-shaped depressions surrounded by raised ridges where molten material has resolidified (indicated by arrow a in Figure 68). These depressions represent areas of localized ablation where laser energy concentration was highest, leading to material removal and melting. The ridges surrounding the depressions (marked by arrow b) exhibit irregular contours and contain numerous spherical and semi-spherical droplets, ranging from submicron to several micrometres in size. These features are indicative of melt ejection, redeposition, and surface-tension-driven flow during rapid solidification. The interiors of the depressions appear comparatively smooth, suggesting limited re-deposition within the ablated zones, while the ridge regions display pronounced flow-like textures consistent with rapid re-solidification dynamics. The uniformity of the pattern reflects the programmed pulse overlap (frequency 20 kHz) and fill pitch parameters (0.02 mm) for the G1 surface. However, the substantial ridge height suggests localized heat input and material displacement. This hierarchical surface topography, defined by primary pits and secondary melt-derived protrusions, is expected to influence functional surface properties, particularly wettability and potential coating adhesion.

The T3-SEM image with 500x magnification of G1 surface is presented in Figure 69.

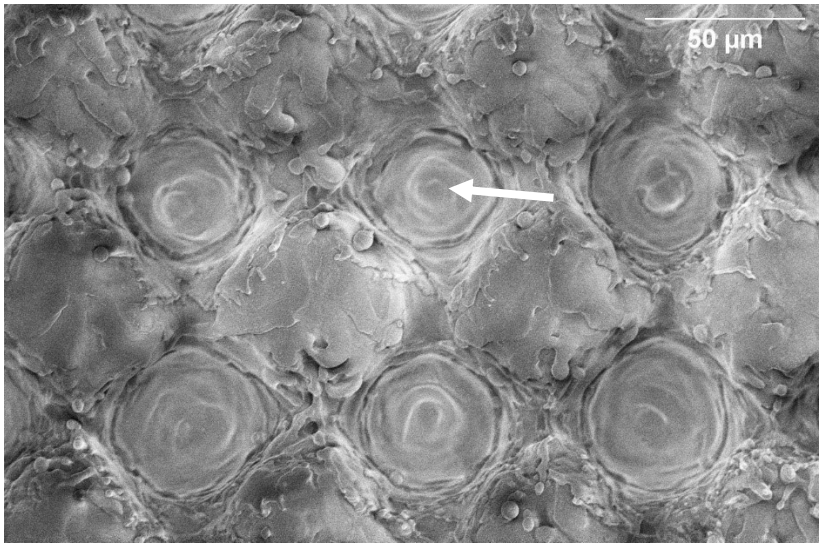

Figure 69 T3-SEM image of ridge on G1 surface with 500x magnification. Bowl-shaped depression of the surface is highlighted with arrow.

Figure 69 shows a T3-SEM image of the G1 laser textured surface, processed with grid pattern and laser fluence of 35 J/mm^2, at 500x magnification. Compared to the ETD image of the G1 surface (see Figure 68), the T3 detector provides clearer visibility of the depression bottoms and reveals finer details of the local topography. The periodic array of circular depressions remains evident, each bordered by resolidified ridges containing irregular edges and small spherical droplets. However, in this image the concentric ring-like features inside the depressions can be more distinctly observed, indicating multiple pulse overlaps at the same locations (see Figure 69). The detector enhances the contrast of inclined surfaces, making the ridge zones appear brighter and emphasising small-scale protrusions and melt redistribution patterns. Within the depressions, the smoother interiors and faint layered textures are more apparent than in the ETD image of the surface, suggesting limited redeposition but clear evidence of cumulative melting effects. Overall, the T3 imaging mode complements the ETD observations by providing a more detailed view of the pit interiors and subtle melt dynamics, offering additional insights into how heat accumulation and material flow shaped the G1 surface during processing.

The T3-SEM image with 1500x magnification of raised ridge on the G1 surface is presented in Figure 70.

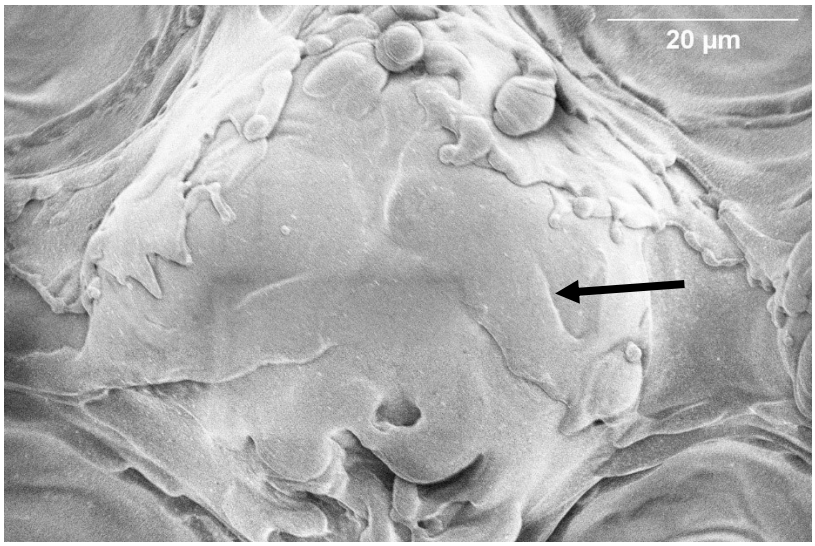

Figure 70 T3-SEM image of raised ridge on G1 surface with 1500x magnification. Flow pattern of the ridge formed during the laser processing is highlighted with arrow.

Figure 70 presents a T3-SEM image of the G1 laser textured surface, focusing on raised ridge, or a hill structure, located between adjacent laser tracks at 1500x magnification. G1 surface was laser processed with grid pattern and laser fluence of 35 J/mm^2. The T3 detector provides pronounced topographic and compositional contrast, revealing the smooth, solidified melt surface interspersed with occasional nanoscale particles and small spherical droplets. The hill crest exhibits layered flow patterns (see Figure 70), suggesting directional melt movement during the solidification phase. Brighter regions correspond to elevated topography and potentially slight compositional variations, while darker depressions may indicate areas of lower density or smoother surface finish. The relatively uniform texture of the hill contrasts with the more irregular morphology observed along ridge edges, implying more stable melt pool dynamics in these inter-track regions. The presence of isolated droplets suggests limited but persistent melt ejection, even in zones where the thermal input is lower than directly under the laser beam focus.

The T3-SEM image with 1500x magnification of bowl-shaped depression on the G1 surface is presented in Figure 71.

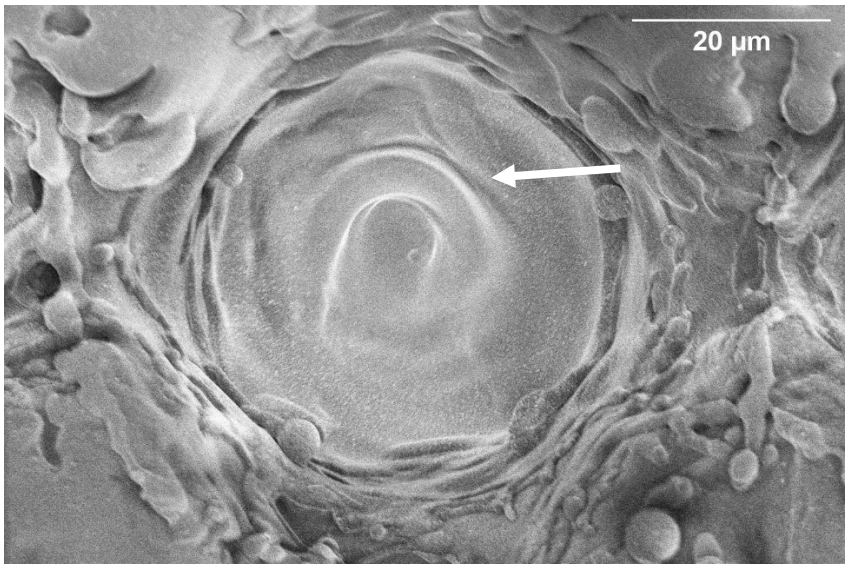

Figure 71 T3-SEM image of bowl-shaped depression on G1 surface with 1500x magnification. Ripple patterns of the bowl-shaped depression of the surface is highlighted with arrow.

Figure 71 presents a T3-SEM image of the G1 laser textured surface captured within the interior of a bowl-shaped depression of the surface at 1500x magnification. G1 surface was laser processed with grid pattern and laser fluence of 35 J/mm^2. The central region of the track displays a distinct concentric ripple pattern radiating outward from a shallow central depression (see Figure 71), indicative of melt pool solidification dynamics and possible recoil pressure effects during laser-material interaction. The T3 detector enhances both topographic and compositional contrast, highlighting subtle variations in the surface morphology. Surrounding the central zone, smooth re-solidified melt surfaces transition into irregular edges with fine droplets and solidified splashes, suggesting localized melt ejection near the track boundaries. The brighter fringes correspond to elevated, resolidified rims, while darker central regions indicate smoother, lower-lying melt zones. The circular symmetry and smoothness of the interior imply relatively stable melt pool conditions within the track, contrasting with the more turbulent morphology found at inter-track ridges.

The ETD-SEM image with 500x magnification of G2 surface is presented in Figure 72.

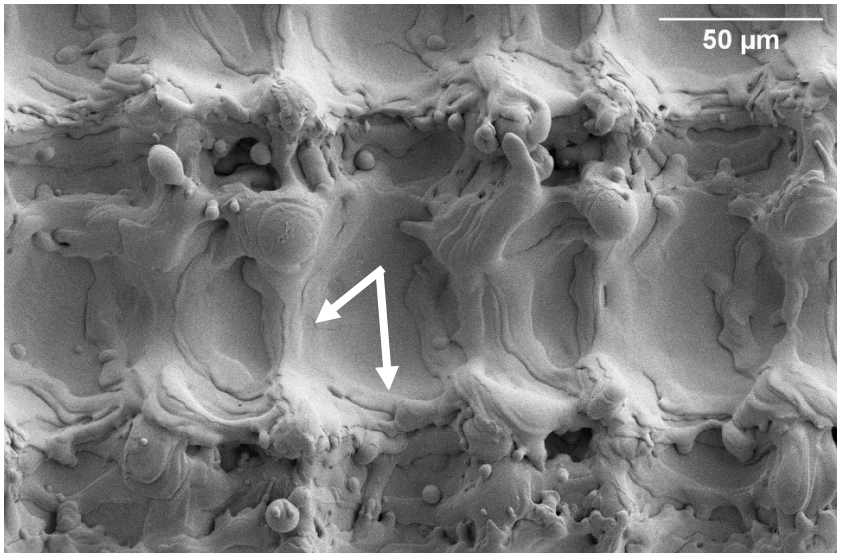

Figure 72 ETD-SEM image of G2 surface with 500x magnification. Ridges of the surface formed during the laser processing are highlighted with arrows.

Figure 72 presents an ETD-SEM image of the G2 laser textured surface, processed with grid pattern and laser fluence of 141 J/mm^2, at 500x magnification. The ETD image reveals an irregular topography dominated by interconnected molten ridges and valleys caused from the overlapping of adjacent laser spots. The ridge regions are populated with numerous resolidified droplets ranging from submicron sizes to several micrometres in diameter, indicative of extensive melt ejection and redeposition during processing. Flow-like textures and layered solidification fronts are visible along the ridge flanks, suggesting repeated thermal cycling and viscous melt movement before rapid cooling. The valley areas between ridges appear comparatively smoother but still contain fine particulate deposits and occasional shallow depressions, likely formed by localised vaporisation and partial melt recoil. The pronounced variation in height and morphology across the surface reflects the cumulative effect of high pulse overlap (frequency 100 kHz) and circular spot geometry in G2, producing a complex three-dimensional texture expected to influence wetting and light-scattering behaviour.

The ETD-SEM image with 1500x magnification of raised ridge on the G2 surface is presented in Figure 73.

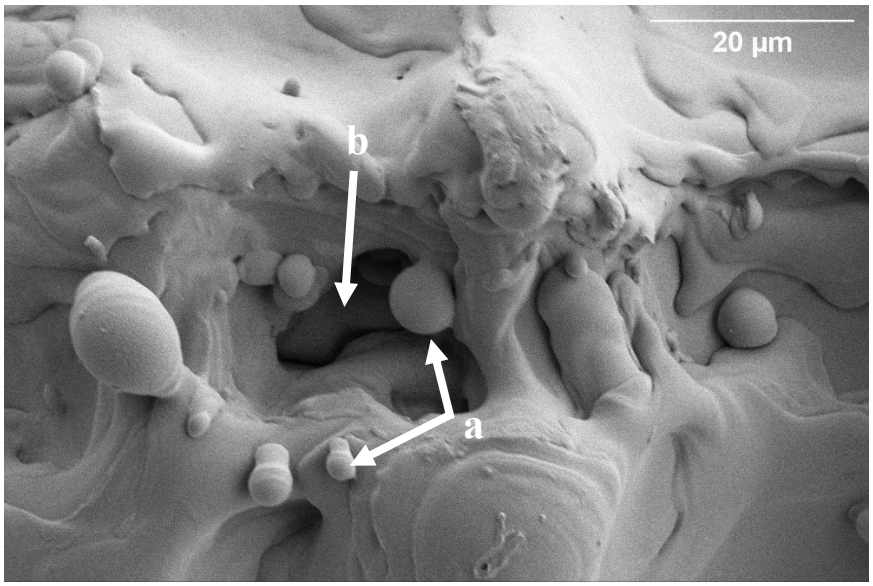

Figure 73 ETD-SEM image of raised ridge on G2 surface with 1500x magnification.

Figure 73 presents a 1500x magnification ETD-SEM view of the G2 surface focusing on the inter-track ridge region. G2 surface was laser processed with grid pattern and laser fluence of 141 J/mm^2. The surface is dominated by an intricate arrangement of resolidified melt features, including spherical and semi-spherical droplets varying from submicron sizes to over 5 µm in diameter, formed via melt ejection and rapid cooling. These droplets, indicated by arrow a in Figure 73, are distributed across the ridge structures and in some cases partially fused into the surface, suggesting deposition while the material was still molten. Between the ridges, cavities and shadowed depressions (marked by arrow b) are visible, likely originating from trapped vapour bubbles or incomplete material reflow during rapid solidification. The surrounding surface exhibits smooth, flow-patterned layers with occasional protrusions and sharp-edged solidification fronts, characteristic of directional melt flow prior to freezing. The observed morphology reflects the combined effects of high local fluence, thermal accumulation, and complex melt dynamics, all contributing to the hierarchical roughness and elevated surface area typical of the G2 texture. This intricate microstructure indicates enhanced melt mobility and localized remelting, which may affect the surface's wetting and coating adhesion behaviour.

The T3-SEM image with 1500x magnification of raised ridge on the G2 surface is presented in Figure 74.

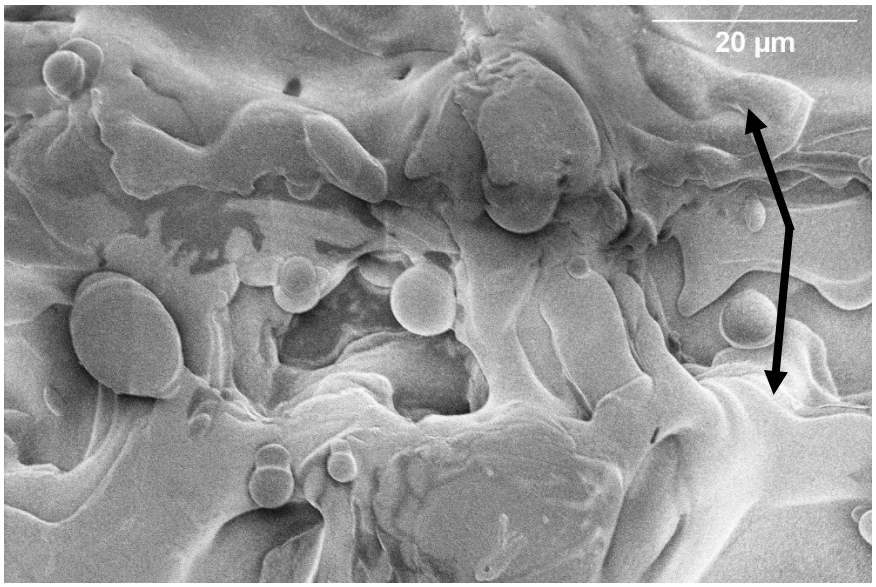

Figure 74 T3-SEM image of raised ridge on G2 surface with 1500x magnification. Flow-like solidification fronts are highlighted with arrows.

Figure 74 shows a T3-SEM image revealing the inter-track ridge morphology of the G2 surface at 1500x magnification. The surface was laser processed with grid pattern and laser fluence of 141 J/mm^2. Compared to the ETD image (see Figure 73), the T3 detector reveals finer details inside the cavities and along the ridge flanks, enhancing the visibility of steep or inclined surfaces. The surface exhibits a heterogeneous microstructure dominated by resolidified melt features and spherical spatter particles, ranging from submicron sizes to approximately 6–8 µm in diameter. Many droplets appear more clearly defined in this image compared to ETD image of the G2 surface, with their partial fusion into the ridge surface highlighted by improved edge contrast. The surrounding matrix displays layered solidification fronts with flow-like textures (see Figure 74), but in this case the T3 imaging mode emphasises subtle undercuts, irregular voids, and local variations in surface density, suggesting incomplete coalescence of melt pools and possible vapour entrapment. These observations provide complementary insights to the ETD view, showing that the G2 ridge morphology combines dense droplet deposition with pronounced micro-scale roughness, contributing to the high surface area generated under high-fluence conditions.

Coating

SEM imaging and analysis were performed on the coated laser textured surfaces L1, L2, G1, and G2, as well as on the coated non-treated reference surface. Key results obtained using the ETD, T1, and T3 detectors of FE-SEM are presented in Figures 75-89.

The ETD-SEM image with 500x magnification of coated non-treated reference surface is presented in Figure 75.

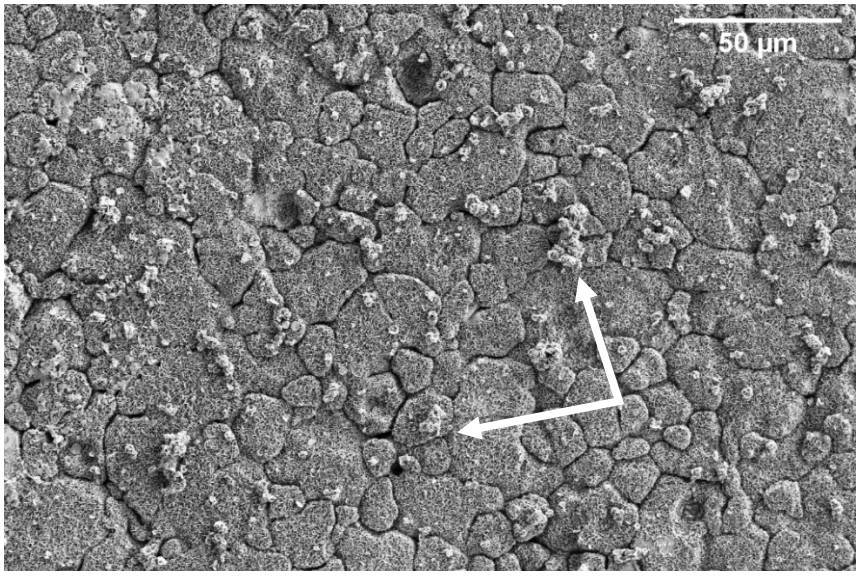

Figure 75 ETD-SEM image of coated non-treated reference surface with 500x magnification. Agglomerates distributed across the surface are highlighted with arrows.

Figure 75 presents an ETD-SEM image of the coated non-treated reference surface at 500x magnification. The overall granular microstructure of the stainless steel substrate remains visible beneath the thin coating layer, indicating that the coating has conformed closely to the existing topography without masking the underlying features. Grain boundaries are still distinguishable, and the surface exhibits fine-scale irregularities that are consistent with polishing-induced morphology. Localised bright spots and agglomerates are distributed across the surface (see Figure 75), likely corresponding to coating particles that accumulated unevenly during deposition.

The ETD-SEM image with 1500x magnification of coated non-treated reference surface is presented in Figure 76.

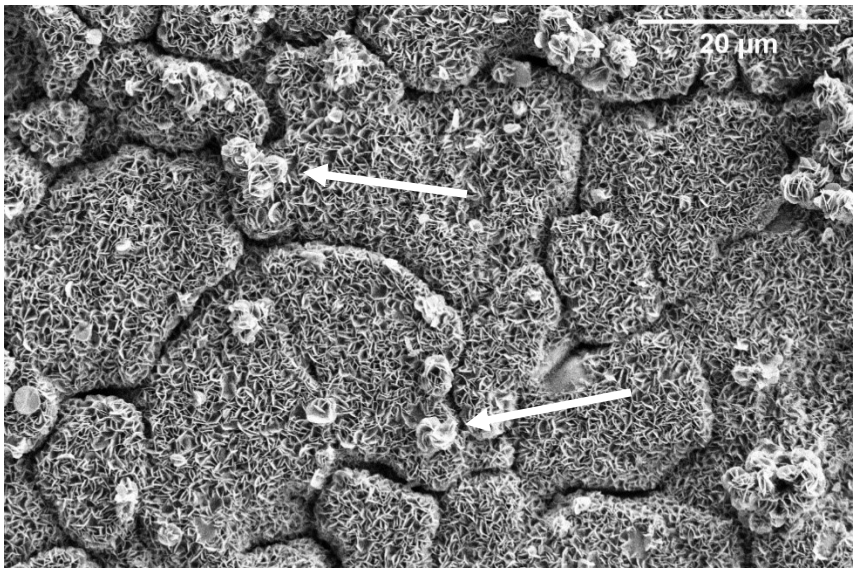

Figure 76 ETD-SEM image of coated non-treated reference surface with 1500x magnification. Agglomerates distributed across the surface are highlighted with arrows.

Figure 76 presents an ETD-SEM image of the coated non-treated reference surface at 1500x magnification. At this higher magnification, the coating layer can be observed in greater detail, revealing a porous, sponge-like morphology distributed across both grain interiors and boundaries. The fine-scale texture suggests that the coating has solidified into a network of interconnected structures, producing an increased surface area compared to the smoother substrate visible before coating. Bright agglomerates and clustered particles are evident in several regions (see Figure 76), indicating local variations in deposition thickness. The microstructure suggests that the coating has adhered uniformly across the reference surface while introducing nanoscale roughness that may influence subsequent wettability and surface interactions.

The T1-SEM image with 1500x magnification of coated non-treated reference surface is presented in Figure 77.

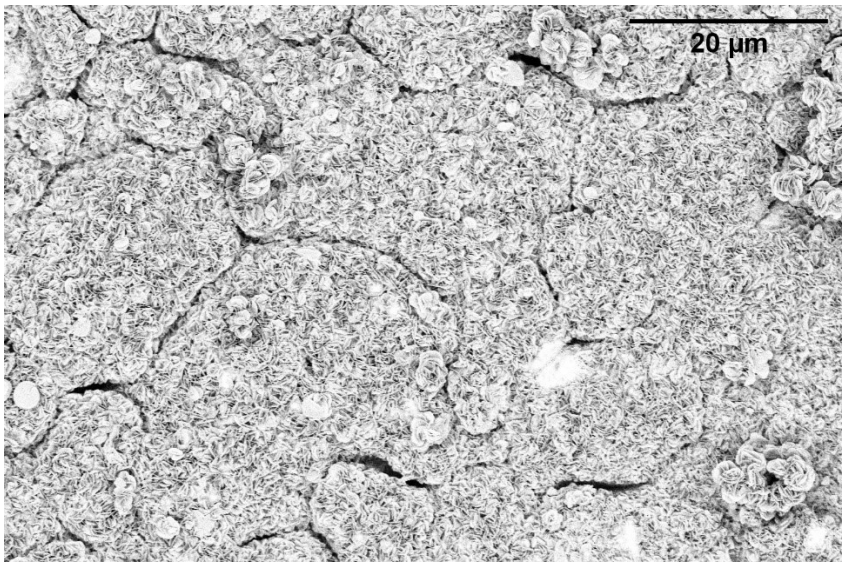

Figure 77 T1-SEM image of coated non-treated reference surface with 1500x magnification.

Figure 77 shows a T1-SEM image of the coated non-treated reference surface at 1500x magnification. The use of the T1 detector emphasizes atomic number contrast, making variations in composition across the coating and substrate more visible than in ETD imaging. Brighter regions correspond to particle agglomerates enriched in heavier elements, which appear as small clustered formations on top of the coating layer. In contrast, the darker regions trace the underlying grain boundaries, suggesting areas with thinner coating or the presence of phases containing lighter elements. The coating microstructure retains its porous, fine-textured appearance, but the compositional differences highlighted here reveal that deposition is not completely homogeneous. These localized variations may influence coating stability and adhesion performance, particularly if certain areas act as preferential sites for delamination or surface chemical interaction.

The ETD-SEM image with 1500x magnification of raised ridge on the coated L1 surface is presented in Figure 78.

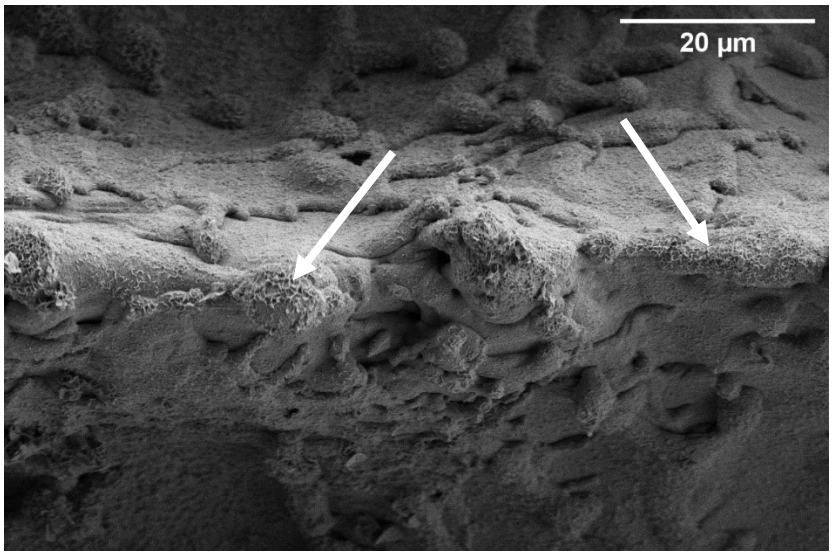

Figure 78 ETD-SEM image of raised ridge on coated L1 surface with 1500x magnification. Irregularities in coating are highlighted with arrows.

Figure 78 shows an ETD-SEM image of the coated L1 surface at 1500x magnification, focusing on a raised ridge formed during the laser texturing process. The ridge displays an irregular morphology, characterized by re-solidified melt structures with cavities and porous zones. The coating layer conforms closely to this rough topography, covering both the ridge crest and the vertical flanks. The image also reveals local irregularities where the coating appears thinner or partially disrupted (see Figure 78), particularly along steep surfaces and within voids. These features indicate that while the coating adheres to the complex ridge geometry, deposition is not entirely uniform at the microscale. The porous and layered appearance of the underlying laser-induced structure likely promotes mechanical interlocking of the coating, but at the same time creates areas prone to local stress concentration, which may reduce long-term adhesion reliability.

The ETD-SEM image with 1500x magnification of laser track on the coated L1 surface is presented in Figure 79.

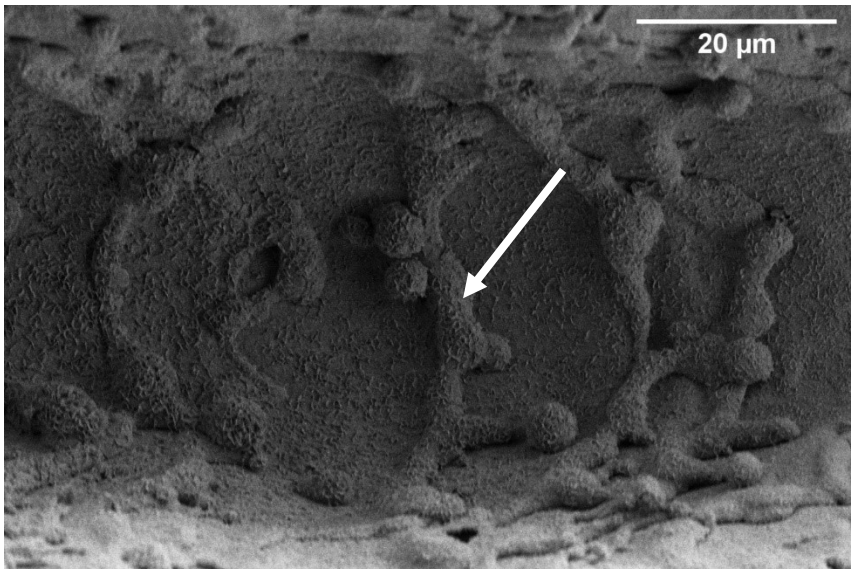

Figure 79 ETD-SEM image of laser tracks on coated L1 surface with 1500x magnification. Re-solidified extrusion with deposited coating is highlighted with arrow.

Figure 78 shows an ETD-SEM image of the coated L1 surface at 1500x magnification, focusing on the morphology of individual laser tracks. The periodic track structure remains visible despite coating deposition, with rounded protrusions and cavities delineating the track boundaries. The coating conforms closely to these laser-induced features, but its thickness appears uneven in areas of high roughness, particularly along steep walls and near spherical re-solidification extrusions (see Figure 79). Within the track interiors, the surface appears relatively smooth and uniformly covered, whereas the boundary regions exhibit more irregular deposition, suggesting local variations in coating wetting and spreading behaviour. The image indicates that while the coating successfully preserves the underlying microstructure of the laser tracks, the highly textured morphology imposes challenges for achieving fully homogeneous coverage, which may influence functional behaviour such as wettability and adhesion under mechanical stress.

The T1-SEM image with 1500x magnification of raised ridge on the L1 surface is presented in Figure 80.

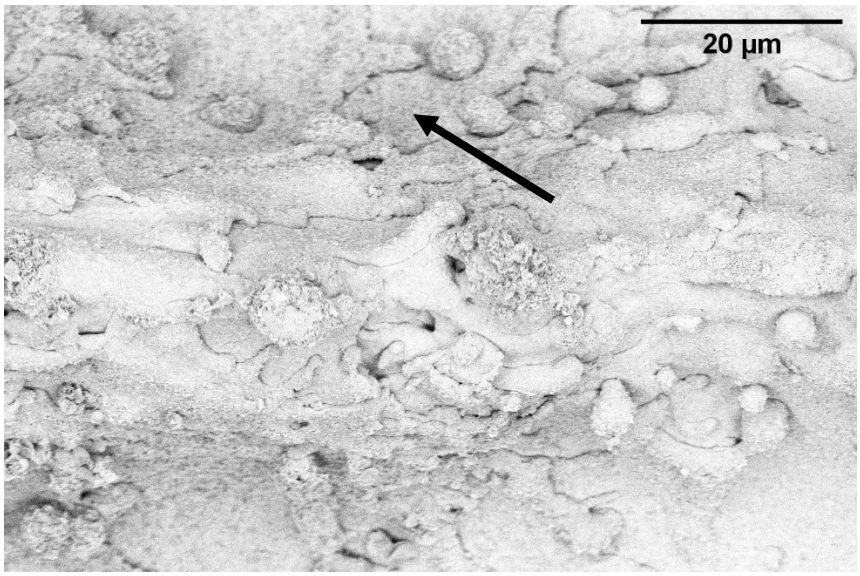

Figure 80 T1-SEM image of raised ridge on coated L1 surface with 1500x magnification. Darker regions suggesting thinner coating coverage is highlighted with arrow.

Figure 80 presents a T1-SEM image of the coated L1 surface at 1500x magnification, focusing on a raised ridge formed during laser processing. The T1 detector enhances compositional contrast, revealing variations in coating distribution across the ridge structure. Brighter regions are observed at the ridge peaks, likely corresponding to thicker coating layers or areas enriched with higher atomic number elements. In contrast, darker zones along the flanks and valleys suggest thinner coverage or localised porosity. The ridge morphology, characterised by clusters of semi-spherical protrusions and irregular solidified features, remains preserved under the coating, demonstrating the conformal nature of the layer. The observed brightness variations indicate that coating deposition is not fully uniform (see Figure 80), with preferential accumulation at elevated areas. This non-uniformity may influence the surface's functional behaviour, particularly under conditions where adhesion or wettability is governed by local film thickness and continuity.

The ETD-SEM image with 1500x magnification of non-treated area adjacent to laser tracks on the coated L2 surface is presented in Figure 81.

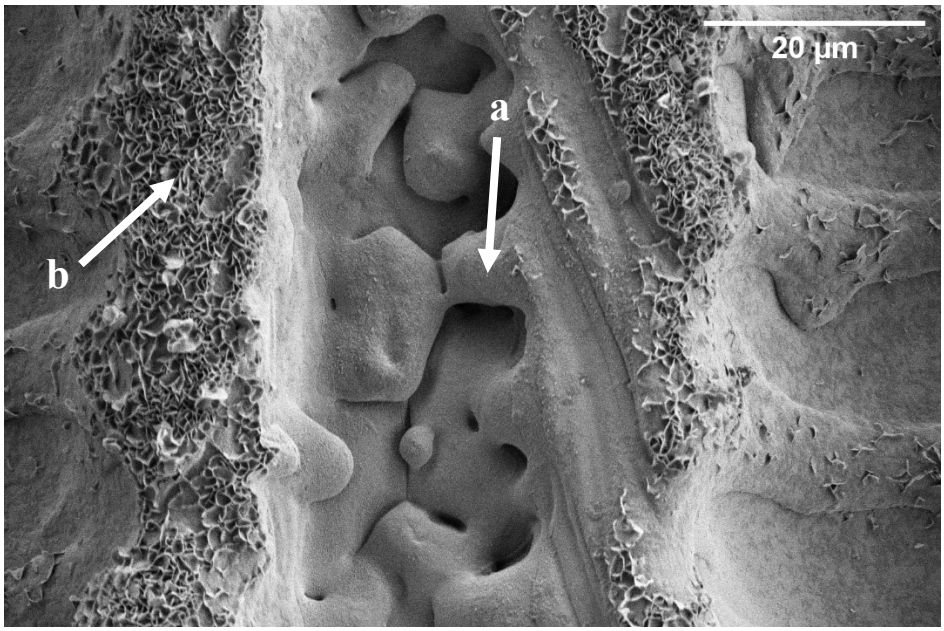

Figure 81 ETD-SEM image of non-treated area adjacent to laser tracks on coated L2 surface with 1500x magnification.

Figure 81 presents an ETD-SEM image of the coated L2 surface at 1500x magnification, showing a non-treated inter-track region adjacent to laser-modified areas. he central depression, indicated by arrow a in Figure 81, exhibits a smooth morphology with rounded cavities that are mostly covered by a thin and continuous coating layer. This region represents an untextured zone between laser tracks where the coating has spread evenly and solidified conformally due to the absence of intense laser-induced topography. In contrast, the rougher coating accumulation observed along the raised ridges (marked by arrow b) appears less uniform and contains clusters of fine particulate deposits and irregular agglomerates. These features suggest preferential coating adherence and local thickening at elevated ridge boundaries, likely caused by increased surface energy and microstructural roughness introduced during laser processing. The smooth morphology of the depression indicates limited melt disturbance and reduced thermal input compared to the ridge regions. Overall, the observed variation in coating distribution across valleys and ridges implies that local topography and energy gradients govern how the thin film spreads and stabilizes on the L2 textured surface, influencing its uniformity and potential adhesion performance.

The ETD-SEM image with 1500x magnification of laser track on the coated L2 surface is presented in Figure 82.

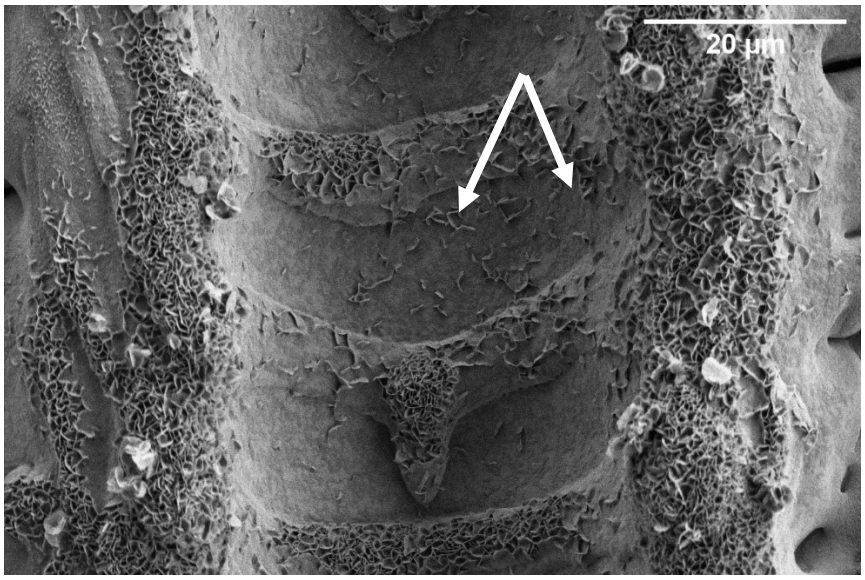

Figure 82 ETD-SEM image of laser tracks on coated L2 surface with 1500x magnification. Irregulates of coating on laser track are highlighted with arrows.

Figure 81 shows an ETD-SEM image of the coated L2 surface at 1500x magnification, focusing on the morphology of laser tracks and their surrounding raised ridges. The interiors of the tracks appear smooth, covered by a thin and uniform coating layer with only minor surface irregularities. The ridge flanks exhibit markedly rougher textures, with clusters of resolidified material and particulate accumulations, which are further emphasised by the coating adhering preferentially to these elevated and irregular areas. The coating highlights the underlying ridge geometry, forming thicker deposits along the ridge boundaries while leaving the flatter track interiors comparatively even. This suggests that the coating spreads conformally across smoother regions but tends to accumulate in areas of high surface roughness, where increased surface area and microcavities enhance anchoring. The observed differences between smooth track interiors and rough ridge flanks underline how localised topography dictates coating distribution on laser-textured L2 surfaces.

The ETD-SEM image with 1500x magnification of raised ridge on the coated G1 surface is presented in Figure 83.

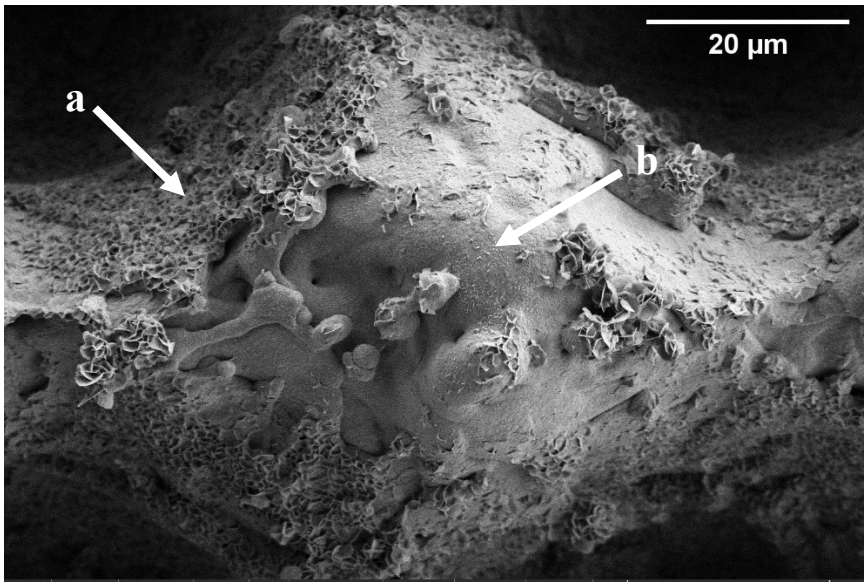

Figure 83 ETD-SEM image of raised ridge on coated G1 surface with 1500x magnification.

Figure 83 presents an ETD-SEM image of the coated G1 surface at 1500x magnification, focusing on a raised ridge structure formed at the intersection of the grid pattern. he ridge morphology is irregular, consisting of uneven solidification fronts, cavities, and protrusions shaped by molten material displacement during laser processing. The area indicated by arrow a in Figure 83 shows irregular surface features covered with an uneven coating layer, where microcavities and roughness promote preferential accumulation of the coating. The coating appears thicker and more clustered on these elevated regions, conforming to the complex topography formed by overlapping laser pulses. In contrast, the inter-track region marked by arrow b displays a smoother surface with more uniform coating coverage, reflecting reduced melt disturbance and steadier heat dissipation in these areas. The ridge regions, however, contain solidified droplets and fragmented textures, indicative of repeated melt–solidification cycles and unstable melt-pool dynamics under the selected low fluence and grid-pattern settings. Compared to the smoother inter-track areas, the ridge demonstrates more heterogeneous coating distribution, suggesting that coating anchoring is primarily governed by local microstructural variations. These observations indicate that, on the G1 surface, the intersecting grid geometry increases microstructural complexity and enhances surface roughness, yet simultaneously promotes uneven coating accumulation, potentially increasing the likelihood of local delamination under stress.

The T1-SEM image with 1500x magnification of raised ridge on the coated G1 surface is presented in Figure 84.

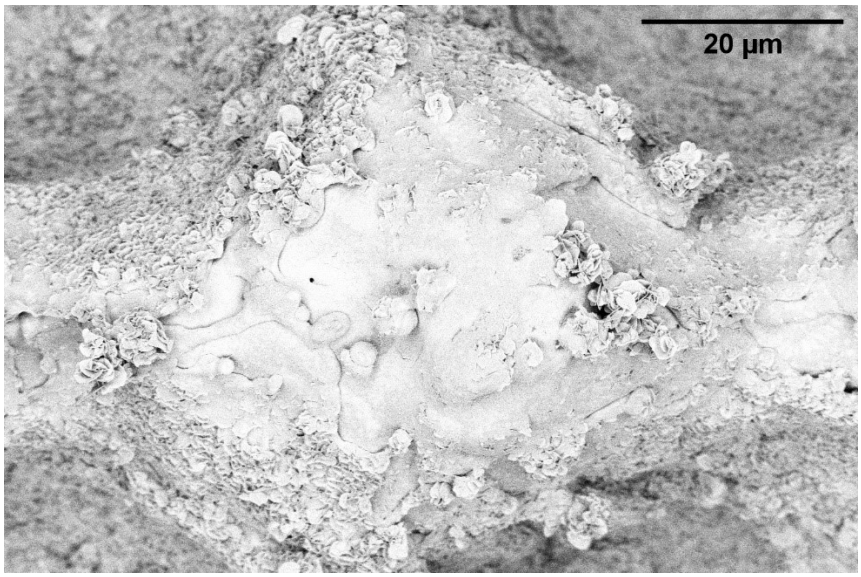

Figure 84 T1-SEM image of raised ridge on coated G1 surface with 1500x magnification.

Figure 84 shows a T1-SEM image of the coated G1 surface at 1500x magnification, focusing on a raised ridge structure. Compared to the ETD image of the same area (see Figure 82), the T1 detector reveals compositional contrast that highlights differences in coating deposition and underlying substrate features. Brighter regions along the ridge crest indicate zones of higher atomic number contrast, which may correspond to preferential coating accumulation or localized enrichment of alloying elements. The coating distribution appears heterogeneous, with thicker coverage at the ridge top and thinner areas along the slopes, where the rough and irregular topography likely hindered uniform spreading. Small bright inclusions are also visible, potentially corresponding to re-solidified oxide particles or high-density debris embedded in the coating layer. These variations confirm that the grid-patterned geometry creates complex local conditions during both laser processing and subsequent coating application, leading to uneven microstructural features that could influence adhesion performance.

The T3-SEM image with 1500x magnification of bowl-shaped depression on the coated G1 surface is presented in Figure 85.

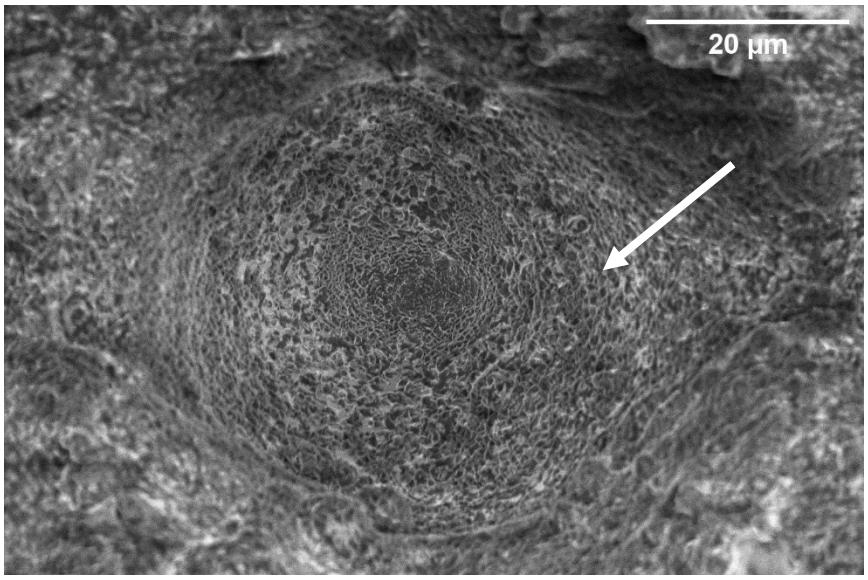

Figure 85 T3-SEM image of bowl-shaped depression on coated G1 surface with 1500x magnification. Ripple like surface structure, suggesting uneven coating, is highlighted with arrow.

Figure 85 presents a T3-SEM image of the coated G1 surface at 1500x magnification, focusing on a bowl-shaped depression. The depression interior exhibits concentric ripple-like textures, consistent with successive laser pulses overlapping within the same region. The coating layer appears to follow the underlying morphology, but variations in contrast indicate uneven distribution across the depression. Brighter zones suggest localized thickening of the coating, while darker areas correspond to thinner coverage or possible porosity at the base of the depression. The smooth central region transitions into rougher peripheries where fine droplets and redeposited material are visible, suggesting that melt dynamics during processing created flow patterns subsequently emphasized by the coating layer. These observations highlight how the geometry of grid-processed depressions promotes non-uniform coating spreading, with thicker accumulation along slopes and rims and thinner layers at the depression floor.

The ETD-SEM image with 1500x magnification of raised ridge on the coated G2 surface is presented in Figure 86.

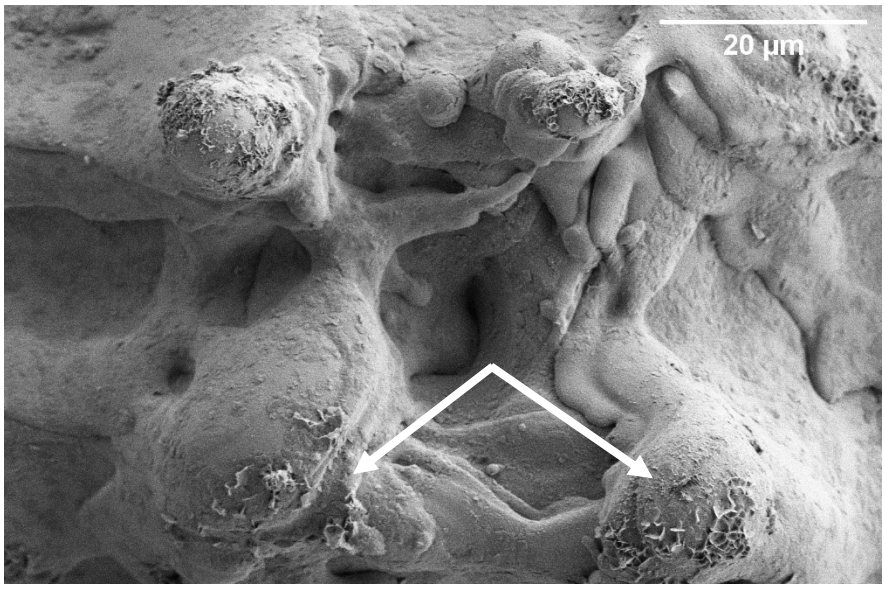

Figure 86 ETD-SEM image of raised ridge on coated G2 surface with 1500x magnification. Ripple like structures of uneven coating are highlighted with arrows.

Figure 86 shows an ETD-SEM image of a raised ridge on the coated G2 surface at 1500x magnification. The ridge morphology is dominated by complex melt re-solidification features, including smooth, flow-like fronts that indicate lateral movement of molten material before cooling. Spherical and semi-spherical droplets are embedded within the ridge surface, some partially fused, suggesting redeposition during the molten state. In addition, cavity-like voids and undercut regions are visible along the ridge flanks, likely formed by trapped vapour bubbles or incomplete reflow during solidification. The coating layer appears to conform closely to this irregular microstructure, covering both elevated and recessed features. Unevenness of coating can be seen as ripple-like structures on top of the formed ridges, as seen in Figure 86. These observations highlight the combined effects of high fluence and grid geometry, which produced pronounced material displacement and complex hierarchical roughness now preserved under the coating layer.

The T3-SEM image with 1500x magnification of raised ridge on the coated G2 surface is presented in Figure 87.

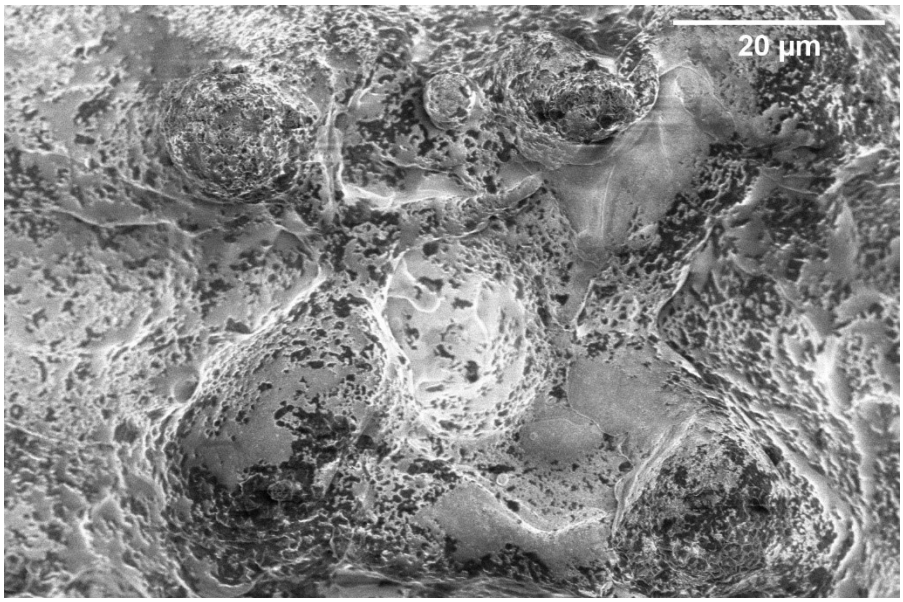

Figure 87 T3-SEM image of raised ridge on coated G2 surface with 1500x magnification.

Figure 87 shows a T3-SEM image of the raised ridge on the coated G2 surface at 1500x magnification. The T3 detector enhances the visibility of inclined surfaces and compositional contrast, revealing intricate details of the melt-solidification structures. The ridge displays a heterogeneous morphology with distinct layered flow textures that indicate repeated re-solidification events. Embedded spherical droplets of varying sizes are clearly visible, some clustered and partially fused into the ridge surface, suggesting redeposition during molten conditions. Localised voids and darker recessed regions appear along the ridge flanks, likely originating from incomplete melt coalescence or vapour entrapment during cooling. The coating layer conforms to these irregularities, but variations in brightness suggest that the thickness may not be uniform, particularly near droplet clusters and void edges. Compared to the ETD image of the same region (Figure 86), the T3 imaging highlights subtle undercuts and finer structural contrasts, providing a complementary view of the complex hierarchical roughness characteristic of the high-fluence grid-textured G2 surface.

The ETD-SEM image with 1500x magnification of laser track on the coated G2 surface is presented in Figure 88.

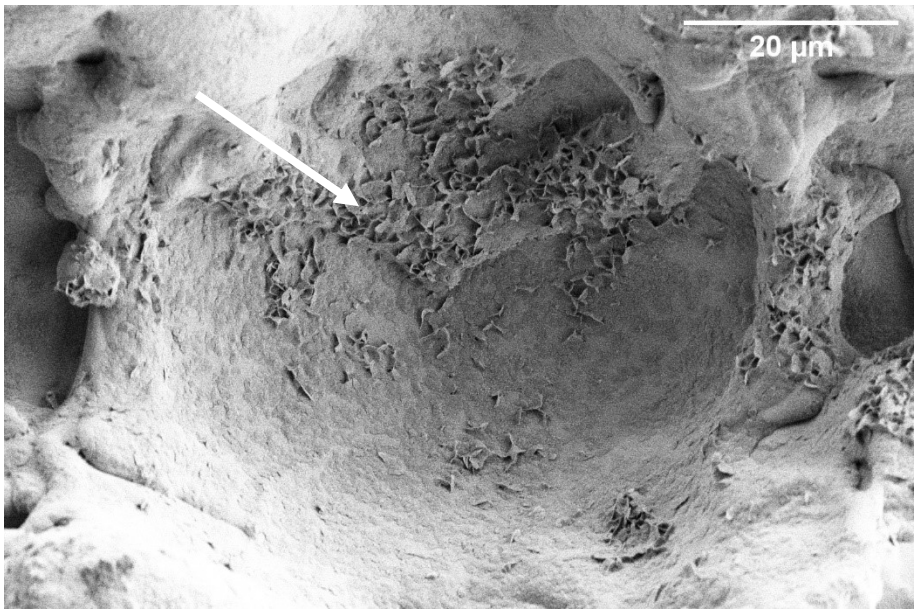

Figure 88 ETD-SEM image of laser track on coated G2 surface with 1500x magnification. Ripple like coating formation are highlighted with arrow.

Figure 88 presents an ETD-SEM image of a laser track on the coated G2 surface at 1500x magnification. The image shows a bowl-shaped depression corresponding to the ablation zone of a single laser pass. As ETD imaging emphasizes topographical contrasts, the lower floor of the depression appears relatively smooth, indicating stable remelting and re-solidification under the applied high fluence (141 J/mm²). The upper boundary of the depression exhibits ripple-like coating features and clusters of redeposited particles, pointing to inhomogeneous spreading of the coating across the textured substrate. The presence of these ripples along the upper edge, combined with the smoother appearance of the depression floor, suggests that the coating layer did not fully conform to the underlying microtopography. This heterogeneity highlights the interplay between laser-induced morphology and coating deposition, where depressions tend to accumulate a thinner and more uniform layer, while edges promote local particle build-up and ripple-like textures.

The T3-SEM image with 1500x magnification of laser track on the coated G2 surface is presented in Figure 89.

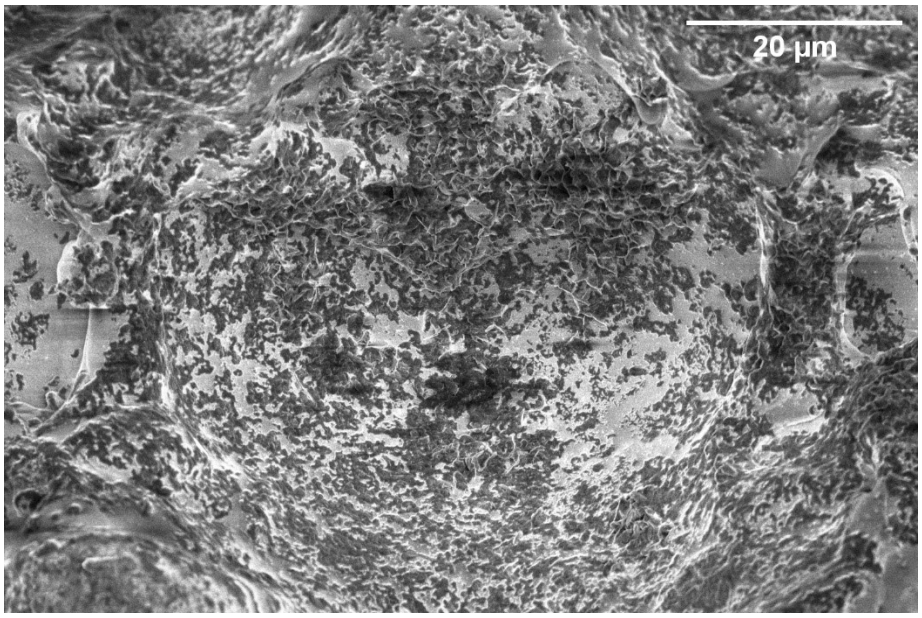

Figure 89 T3-SEM image of laser track on coated G2 surface with 1500x magnification.

Figure 88 presents a T3-SEM image of a laser track on the coated G2 surface at 1500x magnification. Compared to the ETD view of the same region (Figure 88), the T3 detector enhances topographic contrast, revealing more clearly the distribution of redeposited particles inside the depression. The floor of the depression is covered with a dense layer of irregular particles and flake-like features, suggesting extensive re-condensation of vapour-phase material or fragmentation of molten droplets during rapid solidification. These clustered deposits appear heterogeneously distributed, with some regions showing thick particle accumulation, while other areas remain relatively smooth. The ridge edges framing the depression are more irregular and textured than in the ETD image, displaying fine protrusions and void-like features that reflect unstable melt displacement at the track boundaries. These observations indicate that while the depression floor was smoothed by remelting, subsequent coating deposition and particle re-condensation introduced additional nanoscale roughness. The heterogeneous coverage may influence coating adhesion and wetting behaviour by creating zones of variable thickness and microstructural density.

8.5 Contact angle measurements

Pre-treatment

Contact angle measurements were performed on the laser textured surfaces L1, L2, G1, and G2, as well as on the non-treated reference surface, which served as the baseline prior to laser

processing. L1 surface was processed with line pattern and laser fluence of 35 J/mm^2, L2 line pattern and laser fluence of 141 J/mm^2, G1 has been processed with grid pattern and laser fluence of 35 J/mm^2, G2 grid pattern and laser fluence of 141 J/mm^2. Key results obtained from the measurements are presented in Figures 90-92.

The contact angle measurement of non-treated reference surface is presented in Figure 90.

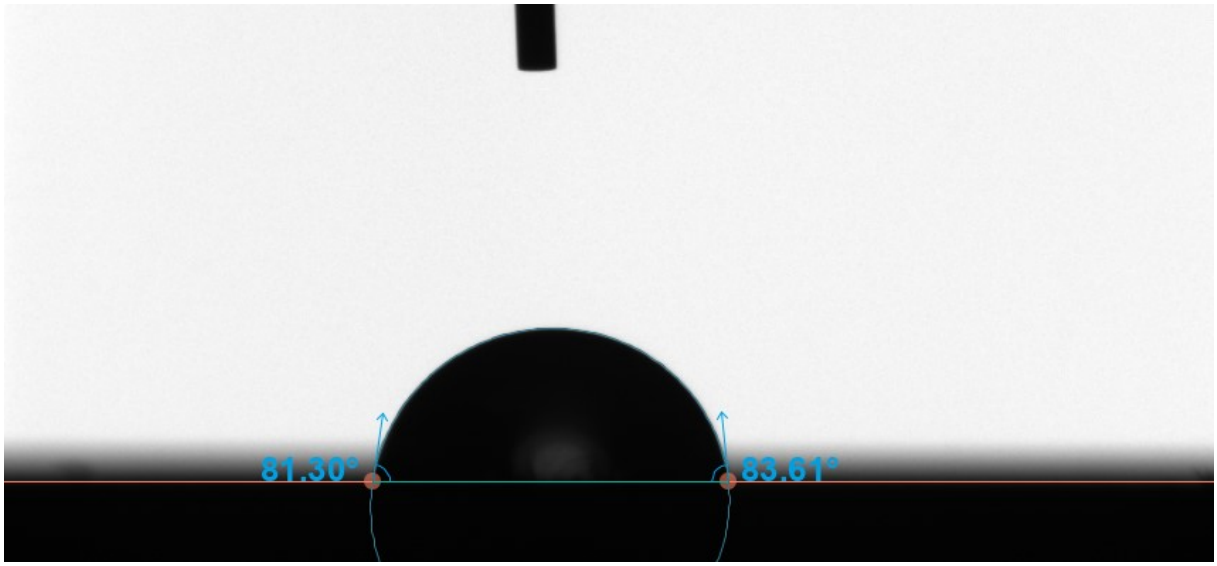

Figure 90 Contact angle measurement of non-treated reference surface.

Figure 90 presents the contact angle measurement for the non-treated reference surface. The sessile drop analysis yielded contact angles of 81.3° (left side) and 83.6° (right side), causing an average value of 82.5°. Since the contact angle remains below 90°, the surface is not hydrophobic but instead exhibits hydrophilic behaviour. This wettability is characteristic of stainless steel with a native oxide layer and standard mechanical finish, providing only limited resistance to wetting [194]. The near-symmetry of the measured angles on both sides of the droplet suggests that the surface is macroscopically homogeneous in terms of wettability, with no pronounced directional effects. This result serves as a baseline for evaluating the effects of laser texturing, enabling direct comparison of changes in surface chemistry or topography and their impact on enhancing or suppressing hydrophobic behaviour.

The contact angle measurement of laser textured G1 surface is presented in Figure 91.

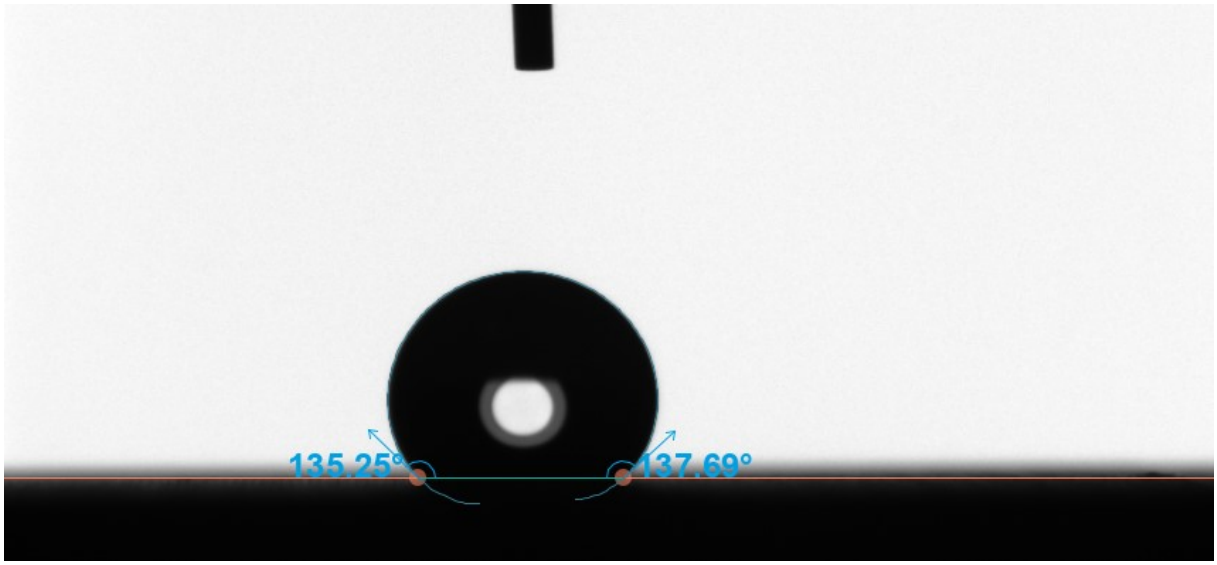

Figure 91 Contact angle measurement of G1 surface processed with grid pattern and fluence of 35 J/mm^2.

Figure 91 shows the contact angle measurement for the G1 laser textured surface. The surface was laser processed with grid pattern and laser fluence of 35 J/mm^2. The measured contact angles were 135.25° (left side) and 137.69° (right side), giving an average of approximately 136.5°. This represents an increase compared to the non-treated reference surface (≈82.5°), indicating a clear transition from moderately hydrophilic to strongly hydrophobic behaviour. The high contact angle values suggest that the grid-patterned microstructure produced by the laser texturing effectively traps air pockets between the surface asperities, thereby reducing the solid–liquid contact fraction in accordance with the Cassie–Baxter wetting regime. The minimal asymmetry between the left and right measurements indicates a relatively isotropic wetting response, which is consistent with the symmetric nature of the grid pattern. This result demonstrates that even at the microscale, the uniform distribution of features can promote stable droplet shapes with minimal pinning, contributing to enhanced water repellence.

The contact angle measurements for laser textured surfaces L1, L2, G1 and G2, and non-treated reference surface are presented in Figure 92.

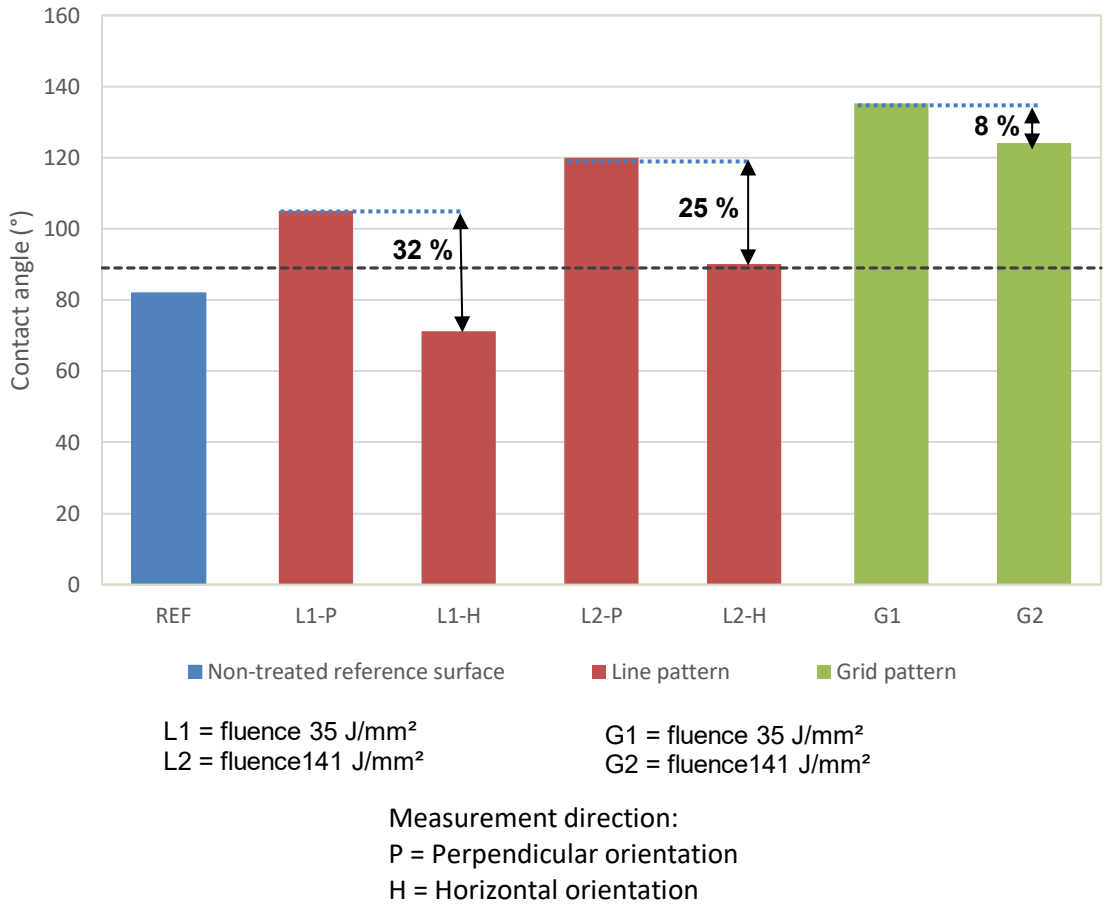

Figure 92 Contact angles of non-treated reference surface (REF) and laser textured surfaces L1, L2, G1 and G2. Contact angle for surfaces L1 and L2 has been measured from two different orientations P and H. Dotted line represents value of contact angle 90°, which separates hydrophilic (<90°) from hydrophobic (>90°) surfaces.

Figure 92 summarises the average contact angle values measured for all tested surfaces, including the non-treated reference (REF), line patterned (L1, L2) and grid patterned (G1, G2) textures. The L1 and G1 surfaces were processed with laser fluence of 35 J/mm^2, and the L2 and G2 surfaces with laser fluence of 141 J/mm^2. For the line patterned surfaces, measurements were taken in two orientations: perpendicular (P) and horizontal (H) to the laser scanning direction, to account for potential anisotropy in wetting behaviour. The dashed horizontal line at 90° separates hydrophilic (<90°) from hydrophobic (>90°) surfaces.

As shown in Figure 92, The non-treated reference surface (contact angle value of 82.0°) is hydrophilic, whereas L1-P (contact angle value of 105.0°) and L2-P (contact angle value of 120.0°) exceed the hydrophobic threshold. In contrast, L1-H (contact angle value of 71.2°) and

L2-H (contact angle value of 90.1°) show lower angles, indicating that wetting behaviour is direction-dependent for line textures, with reduced hydrophobicity along the parallel measurement direction. This anisotropy is further highlighted in the Figure 92: L1 surface shows a 32 % difference between perpendicular and horizontal measurements, while L2 surface shows a 25 % difference. Such variation likely arises from capillary action and droplet elongation along the grooves formed during laser scanning. The comparison between L1 and L2 also shows that the higher laser fluence of 141 J/mm² used for processing L2 surface, produced higher contact angles in both orientations compared to L1 surface, processed with 35 J/mm². This suggests that the increased fluence generated deeper or more defined grooves, enhancing air entrapment and promoting stronger hydrophobicity. Among all surfaces, the surfaces laser textured with grid pattern exhibited the highest and most isotropic hydrophobicity, with G1 surface having a contact angle value of 135.3° and G2 surface at 124.1°. The difference between contact angles of surfaces G1 and G2 corresponds to 8 %, which can be attributed to the higher fluence of 141 J/mm² used in processing G2 surface compared to 35 J/mm² in G1 surface. While higher fluence enhanced hydrophobicity for line textures, in grid patterns it appears to have promoted excessive melting and smoother re-solidification of the ridges, thereby reducing the effectiveness of air trapping. The low directional variation of the grid structures confirms that the intersecting pattern efficiently suppresses anisotropy in wetting behaviour by providing uniformly distributed microcavities.

These results demonstrate that surface geometry, orientation of measurement, and texturing parameters collectively govern the wettability of laser processed stainless steel. While increased fluence enhances hydrophobicity in line textures, its effect in grid patterns can be more complex, depending on how the melt dynamics influence ridge and cavity formation.

Coating

Contact angle measurements were performed on the coated laser textured surfaces L1, L2, G1, and G2, as well as on the coated non-treated reference surface. L1 surface was processed with line pattern and laser fluence of 35 J/mm^2, L2 line pattern and laser fluence of 141 J/mm^2, G1 has been processed with grid pattern and laser fluence of 35 J/mm^2, G2 grid pattern and laser fluence of 141 J/mm^2.

The contact angle measurements of the coated laser textured surfaces L1, L2, G1 and G2, and coated non-treated reference surface, are presented in Figure 93. During the contact angle measurements, no stable droplet formation could be recorded on the coated G2 surface, as the

water droplet spread instantaneously across the surface. This behaviour indicates that the G2 surface exhibited superhydrophilic characteristics after coating, preventing reliable angle determination. Therefore, no numerical contact angle values are reported for G2 in Figure 92.

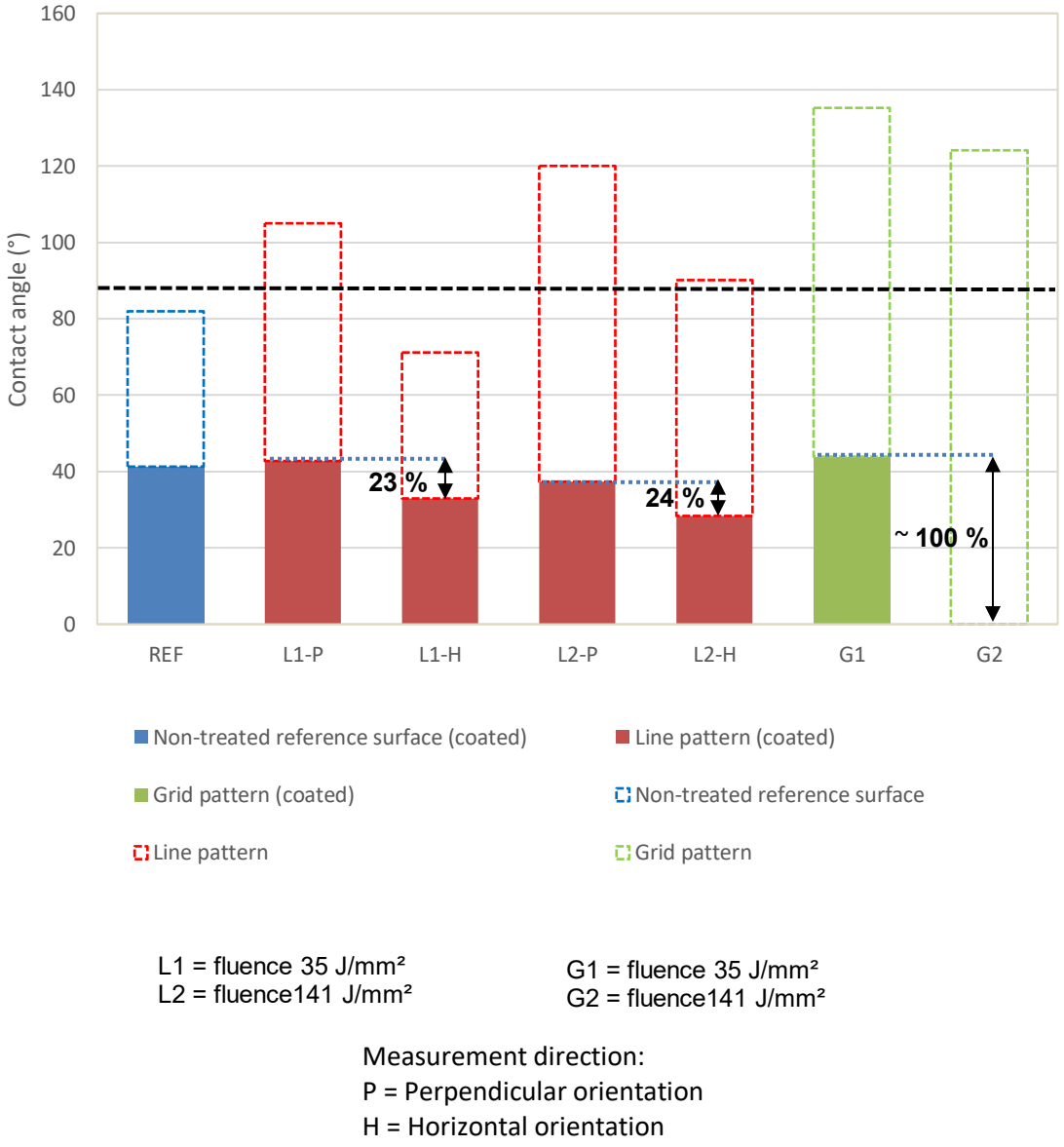

Figure 93 Contact angles of coated non-treated reference surface (REF) and coated laser textured surfaces L1, L2, G1 and G2, and corresponding results of non-coated surfaces. Contact angle for surfaces L1 and L2 has been measured from two different orientations P and H. Dotted line represents value of contact angle 90°, which separates hydrophilic (<90°) from hydrophobic (>90°) surfaces.

Figure 93 summarises the contact angle values of the coated non-treated reference surface (REF) and the coated laser textured surfaces L1, L2, G1, and G2, and compares them against their uncoated counterparts. The dashed line at 90° indicates the hydrophobic threshold, separating hydrophilic (<90°) from hydrophobic (>90°) behaviour. For the line patterned

surfaces, measurements were taken in two orientations: perpendicular (P) and horizontal (H) to the laser scanning direction, to account for potential anisotropy in wetting behaviour. The dashed horizontal line at 90° separates hydrophilic (<90°) from hydrophobic (>90°) surfaces. The data demonstrate that coating systematically reduced the contact angle values of all surfaces, strongly diminishing or completely eliminating hydrophobicity.

The coated reference surface exhibited a reduction of approximately 50 % compared to the uncoated condition, shifting the wettability clearly into the hydrophilic regime. This confirms that the coating layer modifies the surface chemistry by introducing a more polar oxide-based composition, which increases surface energy and promotes water spreading. At the same time, the coating smoothens the fine-scale surface irregularities created by laser texturing, thereby suppressing microstructural effects such as air entrapment and capillary barriers that would otherwise contribute to water repellence.

As seen in Figure 93, for surfaces laser textured with line pattern (L1 and L2), the reductions in contact angle between non-coated and coated surfaces, ranged from 54–69 %, depending on orientation. Specifically, L1-P decreased by 59 % and L1-H by 54 %, while L2-P and L2-H both decreased by 69 % compared to their uncoated states. Despite these reductions, anisotropy between perpendicular and horizontal orientations remained visible: L1 surface showed a 23 % difference between P and H orientations, while L2 surface showed a 24 % difference. This demonstrates that the line textures retain some directional dependence of wetting behaviour even after coating, although the absolute values are well below the hydrophobic threshold.

As seen in Figure 93, G1 surface exhibited a 68 % reduction compared to its uncoated state, while G2 surface showed a complete 100 % reduction, losing hydrophobicity entirely. In addition, a pronounced difference was observed between the two grid-patterned surfaces: contact angle of G1 surface was approximately 100 % higher than that of G2 surface. This indicates that while both grid textures lost hydrophobicity, G1 surface retained more air-trapping capability than G2 surface, which was almost entirely neutralised by the coating.

The results demonstrate that the coating significantly reduces hydrophobicity across all surfaces, with grid-patterned textures being most strongly affected. While line textures still show measurable anisotropy (23–24 % between orientations), their absolute values have dropped below the hydrophobic threshold. The grid textures, on the other hand, lose their isotropic wetting advantage, with G2 surface showing complete suppression. This confirms that

the coating forms a thin, homogeneous film that fills or levels the microcavities introduced by laser texturing, thereby diminishing the surface's ability to sustain Cassie–Baxter-type wetting.

8.6 Adhesion testing

Tape adhesion testing was performed on the coated laser textured surfaces L1, L2, G1, and G2, as well as on the coated non-treated reference surface. L1 surface was processed with line pattern and laser fluence of 35 J/mm^2, L2 line pattern and laser fluence of 141 J/mm^2, G1 has been processed with grid pattern and laser fluence of 35 J/mm^2, G2 grid pattern and laser fluence of 141 J/mm^2. All surfaces were coated with CoOH -coating.

The macro images of the coated surfaces after cross-hatch scoring prior to tape adhesion testing is shown in Figure 94.

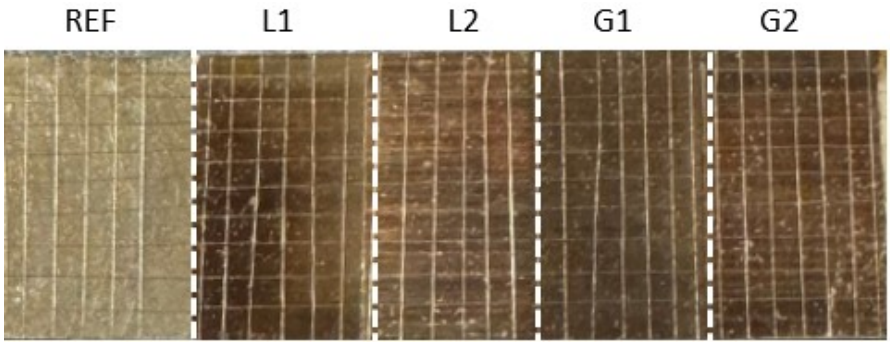

Figure 94 Macro image of the non-treated reference surface (REF) and laser textured surfaces (L1, L2, G1, G2) after the cross-cut tape adhesion test.

Figure 94 presents a macro image of the tested stainless steel surfaces after the cross-cut scoring and prior to the adhesion tape pull. The coated non-treated reference surface (REF) and the coated laser textured surfaces (L1, L2, G1, and G2) are displayed side by side. The cross-hatch lines are clearly visible across all surfaces, indicating that the scoring penetrated consistently through the coating layer down to the substrate. This uniformity ensures comparability of the subsequent adhesion test, as each sample exhibits an equivalent grid structure for assessing coating detachment. The image also highlights minor differences in the overall surface tone between the samples, which reflect the underlying textures introduced by laser processing but do not yet indicate coating failure. These scored macro images therefore provide the baseline state from which the extent of coating removal during the tape test can be reliably evaluated.

The microscopy images with 1x magnification showing the tape adhesion measurement result of coated non-treated reference surface, are shown in Figure 95.

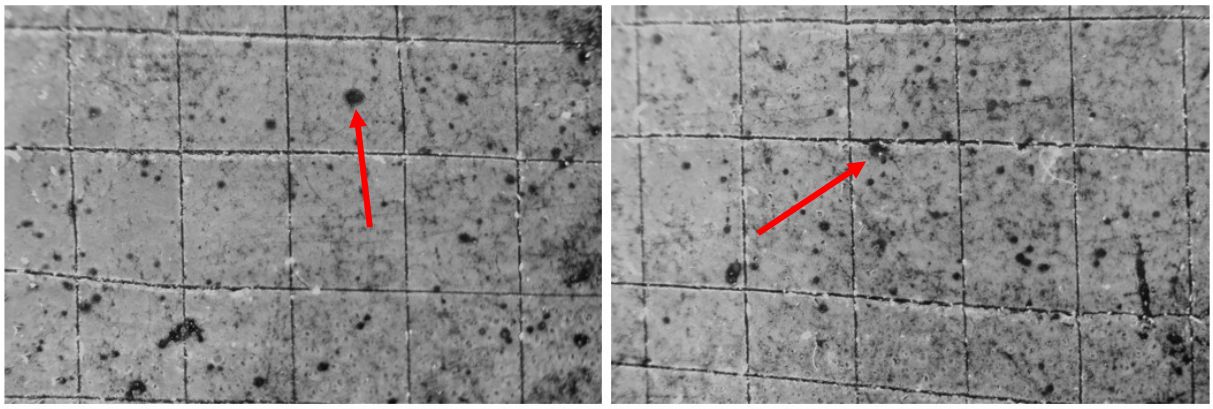

Figure 95 Tape adhesion testing result for coated non-treated reference surface. Black speckles detected in the tape surface, showing possible surface contamination, are highlighted with arrows.

Figure 95 shows the tape adhesion test result for the coated non-treated reference surface. The tape exhibits almost complete detachment of the coating layer, as evidenced by the predominantly light regions corresponding to areas where the coating has been removed. The remaining dark regions are minimal and indicate only small patches of coating that adhered to the substrate. According to the reference grading scale, this result corresponds to grade 0 (100 % detachment). The presence of scattered black speckles is most likely due to surface contamination or debris adhered to the tape rather than intact coating, as seen in Figure 95. These findings confirm that the coating exhibited negligible adhesion to the untreated stainless steel surface, establishing a baseline condition against which the adhesion performance of the laser-textured samples can be evaluated.

The microscopy images with 1x magnification showing the tape adhesion measurement result of coated L1 surface, are shown in Figure 96.

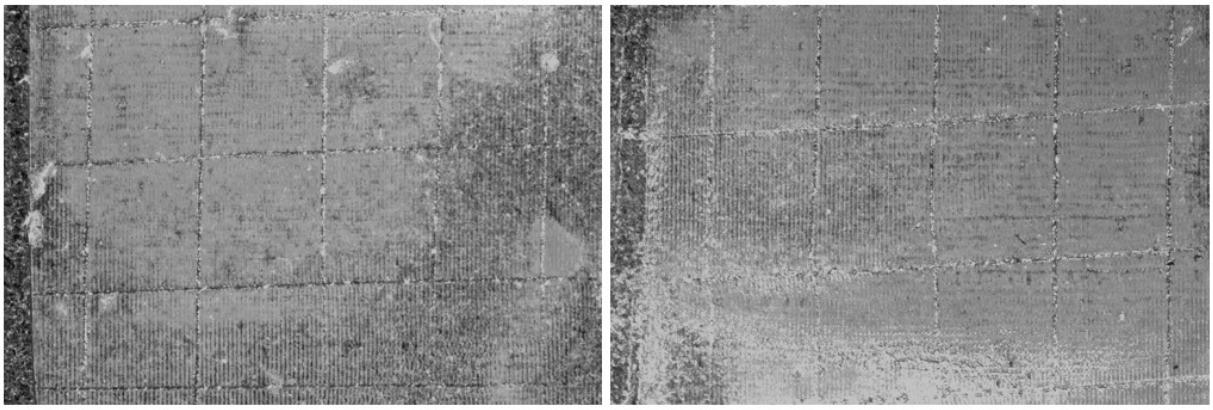

Figure 96 Tape adhesion testing result for coated L1 surface, processed with line pattern and fluence of 35 J/mm^2.

Figure 96 shows the tape adhesion test results for the coated L1 surface, processed with line pattern and fluence of 35 J/mm^2. In contrast to the non-treated reference surface, only partial detachment of the coating is observed. Light regions within the cross-hatched squares indicate areas where the coating was removed, while the darker regions correspond to intact coating that remained adhered to the substrate. The extent of detachment can be estimated at approximately 60 %, corresponding to grade 2 on the adhesion scale. This represents a clear improvement compared to the reference surface, where complete delamination occurred. The enhanced adhesion is likely related to the laser-induced surface roughness and unidirectional grooves, which increase the effective surface area and promote mechanical interlocking of the coating. Local variations in brightness and patchiness suggest some heterogeneity in coating anchoring, which may be attributed to differences in groove depth or oxide formation during laser processing.

The microscopy image with 1x magnification showing the tape adhesion measurement result of coated L2 surface, are shown in Figure 97.

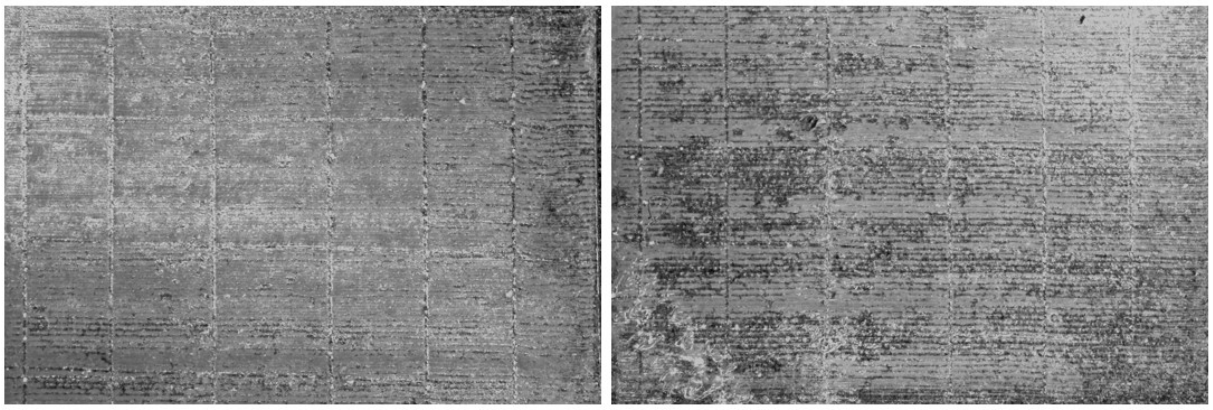

Figure 97 Tape adhesion testing result for coated L2 surface, processed with line pattern and fluence of 141 J/mm^2.

Figure 97 shows the tape adhesion testing result for the coated L2 surface (line pattern, fluence of 141 J/mm^2), processed with a line pattern and a fluence of 141 J/mm^2. After the test, partial detachment of the coating can be observed, particularly in the central regions of the cross-hatched squares. The detached areas appear as lighter regions, while darker regions indicate areas where the coating remains attached to the substrate. The overall degree of removal is estimated at around 40 %, which corresponds to grade 3 on the adhesion scale. This indicates a moderate adhesion strength: the coating adheres more effectively than on the reference surface (grade 0) and on the L1 surface (grade 2).

The microscopy image with 1x magnification showing the tape adhesion measurement result of coated G1 surface, are shown in Figure 98.

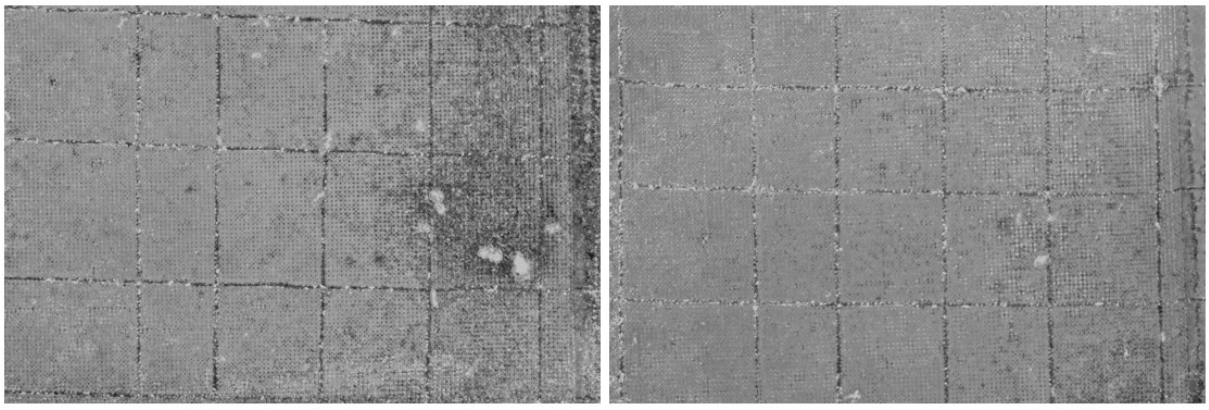

Figure 98 Tape adhesion testing result for coated G1 surface, processed with grid pattern and fluence of 35 J/mm^2.

Figure 98 shows the tape adhesion testing result for the coated G1 surface, processed with a grid pattern and a fluence of 35 J/mm². The images indicate that a significant portion of the coating detached after the tape removal, visible as lighter regions across the cross-hatched squares. The estimated removal area corresponds to approximately 80 %, which is classified as grade 1 on the adhesion scale. This result suggests relatively poor adhesion of the coating on the G1 surface, with only limited areas of the coating remaining intact. Compared to the other tested surfaces, adhesion testing results on G1 surface shows one of the weakest adhesion performances, indicating that the specific combination of grid pattern and lower fluence may have reduced coating–substrate bonding strength.

The microscopy image with 1x magnification showing the tape adhesion measurement result of coated G2 surface, are shown in Figure 99.

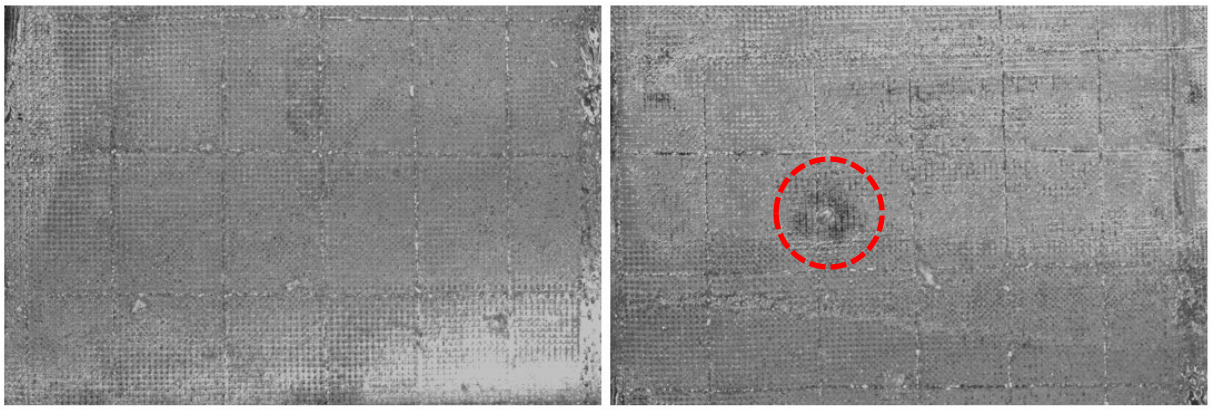

Figure 99 Tape adhesion testing result for coated G2 surface, processed with grid pattern and fluence of 141 J/mm^2. One are without detached coating can be detected.

Figure 99 shows the tape adhesion testing result for the coated G2 surface, processed with a grid pattern and a fluence of 141 J/mm². The tape exhibits complete removal of the coating layer, as the cross-hatched squares appear fully detached, excluding one area marked in Figure 99. This corresponds to grade 0 on the adhesion scale, indicating 100 % coating loss. The result demonstrates very poor adhesion of the coating to the G2 surface, suggesting that the combination of high fluence and grid pattern did not provide favourable conditions for coating–substrate bonding.

Adhesion test results show that laser texturing of stainless steel surface influences coating adhesion, and its effectiveness is depended on the applied laser parameters and surface geometry. Line-patterned surfaces were observed to achieve stronger adhesion compared to grid-patterned textures, suggesting that the unidirectional grooves provide more favourable conditions for coating anchoring and mechanical interlocking.

9 Further analysis

Further analysis was carried out to compare the morphology of the laser-textured surfaces before and after coating using SEM-ETD imaging. Figure 100 presents side-by-side images of the non-treated reference surface and the four laser-processed textures (L1, L2, G1, G2) in both pre-treated and coated states. Images at 500x and 1500x magnifications reveal how the coating layer interacts with the laser-induced topography and whether it alters or preserves the underlying microstructural features.

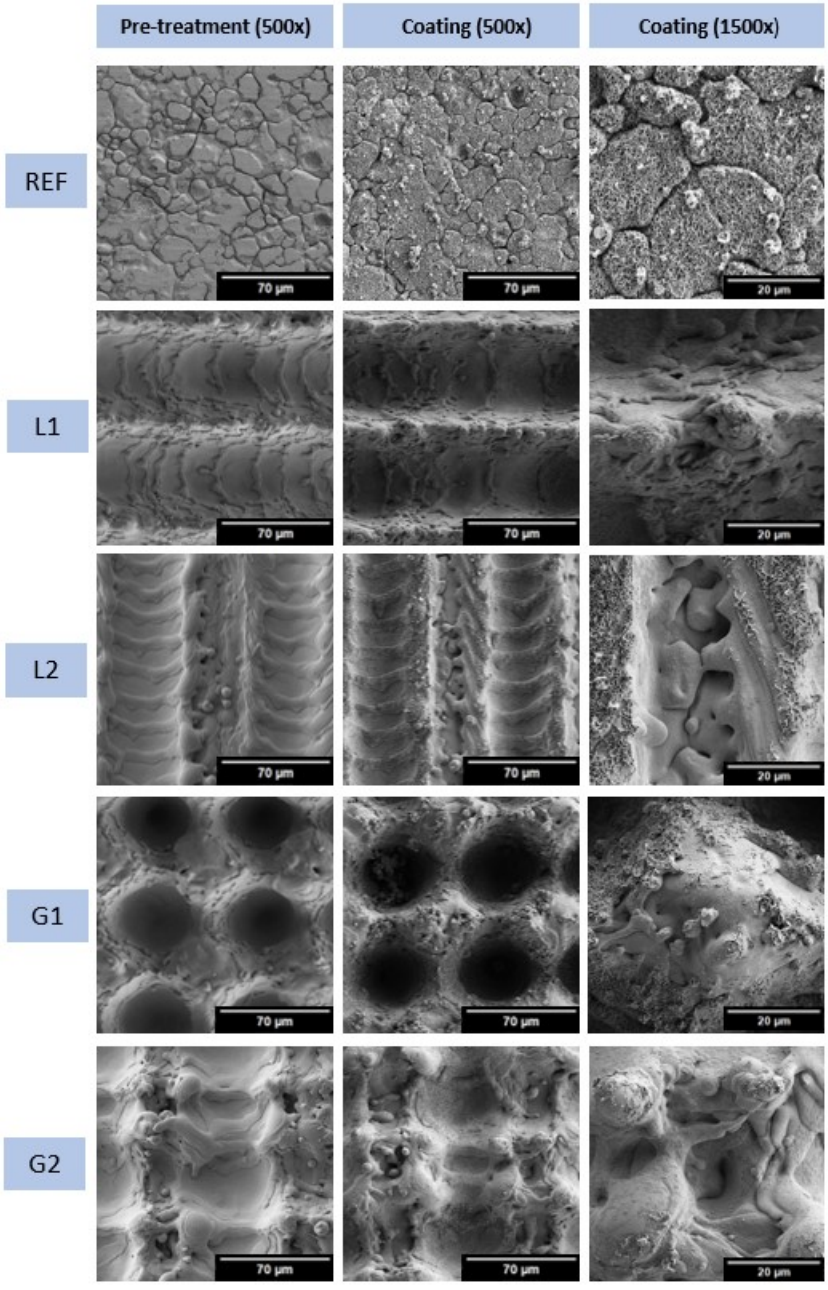

Figure 100 SEM-ETD images of surfaces with laser texturing as a pre-treatment, with 500x magnification, and coating after pre-treatment, with 500x and 1500x magnification: L1 (line pattern,

fluence 35 J/mm^2), L2 (line pattern, fluence 141 J/mm^2), G1 (grid pattern, fluence 35 J/mm^2), and G2 (grid pattern, fluence 141 J/mm^2).

As shown in Figure 100, the non-treated reference surface exhibits a granular morphology prior to coating, with clearly visible grain boundaries and polishing-induced irregularities. After coating, these features are still discernible, but the surface appears rougher and populated with fine-scale particulates, indicating that the coating layer replicated the underlying morphology rather than levelling it out. For the line-patterned surfaces (L1 and L2), the pre-treatment images reveal distinct periodic ridges and valleys aligned with the scanning direction. Following coating, these periodic features remain clearly visible, demonstrating that the coating has conformed to the existing laser-induced structures instead of obscuring them. In L1 surface, ridges appear slightly smoother, consistent with partial filling of sharp asperities, whereas in L2 surface, the coating accentuates the already smoother ridge–valley transitions generated by the higher fluence and pulse overlap. The grid-patterned surfaces (G1 and G2) display the most pronounced morphological changes after laser processing, with deep bowl-shaped depressions and raised ridges visible in the pre-treatment state. After coating, these depressions and intersections remain preserved, although the coated images highlight subtle heterogeneities in coating deposition. In particular, G1 surface shows areas where the coating layer appears thicker at the ridge peripheries, consistent with earlier higher-magnification observations of ripple-like textures. In contrast, G2 surface demonstrates a more uniform coverage across the ridges and depressions, though slight variations in contrast suggest minor local differences in coating thickness.

The SEM comparisons confirm that the coating layer is thin and conformal, adhering closely to the underlying laser-induced textures without obscuring their periodicity or geometry. The non-treated reference surface shows minimal adhesion and higher detachment in adhesion tests, whereas the textured surfaces, especially those with line and grid patterns, provide mechanical interlocking sites that enhance adhesion. Moreover, the persistence of ridges, depressions, and re-solidification features after coating demonstrates that functional surface characteristics introduced by laser texturing are preserved. These results align with the adhesion test findings, supporting the conclusion that surface morphology strongly governs coating behaviour, and that higher fluence grid patterns (G2) provide the most stable and uniform coating–substrate interface.

In addition to adhesion performance, the results also underline the limitations of cobalt hydroxide deposition on laser-treated stainless steel. Unlike the untreated reference samples,

which showed homogeneous and uniform coating coverage, the patterned surfaces often exhibited heterogeneous deposition with local variations in thickness and surface coverage. This outcome is likely not only a consequence of the increased micro-roughness introduced by laser structuring, but also of the oxide layer formed during laser irradiation, which may have impeded subsequent deposition and nucleation of the cobalt hydroxide layer. These findings suggest that while laser-induced textures provide favourable topographical anchoring sites, their chemical modification can simultaneously hinder coating growth, reducing uniformity and coverage. Consequently, the untreated surfaces demonstrated coating homogeneity, whereas the laser-textured substrates revealed a more complex interplay between mechanical interlocking and chemical compatibility of the deposited layer.

The results obtained in this thesis show both consistencies and deviations compared to earlier reports on laser-induced hydrophobicity of stainless steel and other metallic materials. In several respects, the observations confirm established mechanisms described in the literature, such as the role of hierarchical roughness in enabling Cassie–Baxter wetting and the strong anisotropy of line textures. At the same time, some findings diverge from common trends, particularly in the behaviour of grid patterns at higher fluence, where excessive remelting diminished hydrophobicity instead of enhancing it. By placing these results in the context of prior studies, the interplay between laser parameters, surface geometry, and wettability can be more clearly defined.

The contact angle measurements obtained in this thesis are consistent with reported literature on laser-induced hydrophobicity but also reveal distinct deviations. The non-treated reference surface (contact angle value of 82°) showed hydrophilic behaviour, which matches typical stainless steel values with native oxide layers reported by Dongre et al. (2021) [123]. After laser texturing, contact angles increased above the value of 100° for several surfaces, confirming the transition toward Cassie–Baxter wetting states, in agreement with earlier reports that pulsed laser irradiation can promote hydrophobicity by generating hierarchical textures. Specifically, the surface laser textured with line pattern and fluence of 35 J/mm^2 (L1) reached an average contact angle value of 105.0° in the perpendicular orientation, while L2 exhibited an even higher contact angle value of 120.0°. The surfaces laser textured with grid pattern surfaces showed the strongest hydrophobic response, with G1 surface (fluence of 35 J/mm^2) reaching contact angle value of 135.3° and G2 surface (fluence of 141 J/mm^2) the value of 124.1°, both values above the non-treated reference surface (contact angle value of 82.0°). These measured contact angle values are consistent with literature findings, as Rafieazad et al. (2018) [120] have

reported contact angles of up to 145° on stainless steel surfaces textured with a nanosecond pulsed fibre laser, and Yang et al. (2016) [125] have demonstrated values exceeding 150° on titanium surfaces textured with a nanosecond pulsed laser. The fact that several of the tested surfaces approached or exceeded the 120° threshold highlights that the applied processing parameters were sufficient to induce effective air trapping and reduced liquid–solid contact, characteristic of Cassie–Baxter wetting.

Anisotropy in line textures was clearly observed in the experiments. The perpendicular measurement orientations (L1P: contact angle value of 105°, L2P: contact angle value of 120°) were hydrophobic, while horizontal measurement orientations (L1H: contact angle value of 71°, L2H: contact angle value of 90°) were hydrophilic or marginal. The anisotropy reached 32 % for L1 surface (fluence of 35 J/mm^2) and 25 % for L2 surface (fluence of 141 J/mm^2). This matches the findings of Yang et al. (2016) [125], who have showed that using line and groove textures on titanium produces strong directional wetting effects, as droplets elongated and penetrated grooves along the scan direction. The results of this thesis further demonstrate that using a higher fluence for laser texturing with line pattern (value of 141 J/mm^2) enhanced hydrophobicity in both orientations compared to lower fluence (value of 141 J/mm^2), consistent with Kam et al. (2012) [119], who have reported that increased fluence and optimised cone aspect ratios improved contact angles on stainless steel surfaces.

Since no measurable anisotropy was observed for grid-patterned surfaces in preliminary experiments, the contact angles of G1 surface and G2 surface were measured in a single orientation. The G1 surface (fluence of 35 J/mm²) reached an average contact angle of 135°, while the G2 surface (fluence of 141 J/mm²) reached an average value of 124°. The difference between the results of the two grid textured surfaces can be attributable to processing parameters rather than anisotropy. This isotropy aligns with the findings of Yang et al. (2016) [125], who have reported that surfaces textured with grid patterns promote uniform air trapping and suppress directional wetting effects. However, in contrast to the line textures, for surfaces textured with grid pattern, the higher laser processing fluence of G2 surface (fluence of 141 J/mm²) led to 8 % lower contact angle compared to G1 surface which was processed with lower fluence (fluence of 35 J/mm²). SEM and 3D topography analyses further clarify this discrepancy: profile measurements showed that G1 surface had peak-to-valley amplitudes of approximately 60 µm, while G2 surface exhibited shallower grooves of about 20–25 µm. These differences reflect the influence of higher fluence combined with a larger fill pitch in G2, which promoted remelting and smoothing of the ridges. As a result, although higher fluence enhanced

hydrophobicity in line textures, in grid textures excessive melting and reduced groove depth diminished effective air trapping. A comparable effect was reported by Rico et al. (2019) [122], who have showed that Cassie–Baxter surfaces lose efficiency when over-melted, even if the overall roughness amplitude remains high.

Surface roughness and topography metrics provide further support for the wettability results. L1 surface (fluence of 35 J/mm²) produced the highest arithmetical average roughness among the laser textured surfaces, with a *Sa* value of 14.3 µm. In contrast, L2 surface (fluence of 141 J/mm²) exhibited a lower *Sa* value of 8.4 µm but a much higher mean peak-to-valley height (*Sz* value of 115 µm) compared to L1 surface (*Sz* value of 73 µm). This indicates that L2 formed deeper valleys due to the larger fill pitch (fill pitch of 0.02 mm for L1 surface, and fill pitch of 0.1 mm for L2 surface), enhancing its ability to trap air and explaining the higher contact angles measured for this surface. In the laser textured surfaces with grid pattern, G1 surface (fluence of 35 J/mm²) showed both the highest *Sa* value (value of 16.4 µm) and *Sz* value (value of 124 µm). These results correlated with the highest measured contact angle, confirming that pronounced hierarchical roughness favours stable Cassie–Baxter wetting states, as also demonstrated by Rafieazad et al. (2018) [120] and Yang et al. (2016) [125]. In contrast, G2 surface (fluence of 141 J/mm²) exhibited lower roughness values (*Sa* value of 10.6 µm, *Sz* value of 73 µm) and a reduced contact angle compared to G1 surface, consistent with excessive remelting and smoother ridge morphology at higher fluence. The non-treated reference surface, by comparison, showed minimal roughness (*Sa* value of 1.0 µm, *Sz* value of 19 µm), reflecting its hydrophilic behaviour with a contact angle of ~82°. Taken together, these results highlight that both average roughness and maximum height values must be considered: while *Sa* reflects overall surface modulation, *Sz* and groove depth are critical for understanding air entrapment capacity and the caused wetting state.

SEM analysis further clarifies the observed wetting trends. L1 surface (line pattern) and G1 surface (grid pattern), processed at lower fluence (fluence of 35 J/mm²), showed irregular ridges with abundant resolidified droplets, which enhance air pocket formation. Surfaces laser textured with higher laser fluence of 141 J/mm², L2 (line pattern) and G2 (grid pattern), in contrast, displayed smoother morphologies due to higher pulse overlap and remelting, which reduced surface modulation and suppressed extreme hydrophobicity. Rafieazad et al. (2018) [120] similarly have noted that while laser-induced hydrophobicity was achieved on 17-4 PH stainless steel, excessive remelting reduced the ability of textures to entrap air, especially under immersion.

These findings highlight that laser-induced hydrophobicity cannot be attributed to fluence alone, but instead is caused from the interplay of geometry, fill pitch, pulse frequency, and melt dynamics. The trends observed in this thesis support established literature findings: line textures induce anisotropic wetting, whereas grid textures promote isotropy. However, the reduced hydrophobicity of G2 (fluence of 141 J/mm²) surface compared to G1 surface (fluence of 35 J/mm²) demonstrates that higher fluence does not universally enhance performance. Instead, as reported by Dongre et al. (2021) [123] and Rico et al. (2019) [122], over-melted structures can compromise the Cassie–Baxter state despite increased energy input. The present results therefore extend existing studies by demonstrating how parameter combinations can invert expected trends, particularly in grid geometries on stainless steel substrate.

10 Conclusions

This thesis examined the use of a 100 W nanosecond fibre laser to modify stainless steel surfaces through line and grid texturing patterns, with the aim of enhancing hydrophobicity and improving coating adhesion. The results demonstrate that laser surface texturing can substantially alter both surface morphology and functional properties, although its effects depend strongly on the applied geometry and fluence.

From the literature review, it was established that hierarchical roughness produced by pulsed laser texturing can induce hydrophobicity on metallic surfaces, with Cassie–Baxter wetting states achieved when micro- and nanostructures trap air beneath water droplets. Prior studies also emphasised that line textures typically create anisotropic wetting due to directional grooves, while grid textures provide isotropy through intersecting cavities. Furthermore, laser-induced oxide formation and surface chemistry were highlighted as key factors influencing not only wettability but also coating behaviour, with both beneficial and detrimental effects reported depending on processing conditions.

The non-treated reference surface exhibited a hydrophilic contact angle of 82°, consistent with stainless steel covered by a native oxide layer. Laser texturing increased hydrophobicity significantly. Line-patterned surfaces reached contact angles of 105° (L1-P) and 120° (L2-P) when measured perpendicular to the scanning direction, while parallel orientations yielded much lower values of 71° for L1-H and 90° for L2-H. This confirmed strong anisotropy, with differences of up to 32 % between orientations. Grid patterns, in contrast, produced isotropic wetting: G1 reached 135° and G2 124°, both well above the hydrophobic threshold. After coating deposition, all surfaces lost hydrophobicity, with contact angles decreasing by 54–69 % for L1 and L2, and by 68 % for G1. On G2, the effect was even more extreme, as the droplet spread instantly, indicating superhydrophilicity.

Surface roughness measurements supported these observations. The line-patterned L1 surface showed the highest average roughness *Sa* (value of 14.3 µm) with a *Sz* value of 73 µm, whereas L2 was smoother (*Sa* value of 8.4 µm) but exhibited deeper valleys, with *Sz* value increasing to 115 µm due to its larger fill pitch. Among the grid patterns, G1 had the most pronounced roughness (*Sa* value of 16.4 µm, *Sz* value of 124 µm), while G2 surface was less extreme (*Sa* value of 10.6 µm, *Sz* value of 73 µm), reflecting excessive remelting at higher fluence. After coating, roughness values decreased especially in L2 and G2, where *Sz* value dropped by 60 %

and 41 %, respectively, indicating that the coating preferentially filled deeper valleys and smoothed out extremes.

Adhesion testing revealed that the untreated reference surface exhibited complete coating removal (100 %, grade 0). Laser texturing improved adhesion only for line-patterned surfaces: L1 showed ~60 % removal (grade 2), and L2 performed better with ~40 % removal (grade 3). Grid patterns provided weaker adhesion, with G1 losing ~80 % of coating (grade 1) and G2 again showing complete detachment (grade 0). SEM analyses further indicated that cobalt hydroxide deposition was less effective on laser-textured surfaces, where oxide layers formed during processing and heterogeneous roughness hindered uniform nucleation. In contrast, the untreated reference surface displayed a homogeneous and continuous coating layer, highlighting that laser texturing does not universally benefit deposition quality.

The results show that laser surface texturing with a 100 W nanosecond fibre laser can be used to fabricate hydrophobic structures on stainless steel, with contact angles up to 135° for grid textures. However, the beneficial effects are geometry-dependent: line textures produce anisotropic wetting, while grid textures enable isotropy but may lose effectiveness at high fluence due to remelting. Adhesion tests demonstrated that line textures promote mechanical interlocking and improve coating stability compared to the untreated surface, but grid textures did not enhance adhesion, and in some cases, adhesion was even reduced.

Based on these findings, the research questions can be answered:

1. *Can a nanosecond fibre laser be used to improve hydrophobic properties on stainless steel surfaces?* A 100 W nanosecond fibre laser can improve hydrophobicity, achieving contact angles up to 135° (G1) compared to 82° on the non-treated stainless steel surface.

2. *How do different surface texturing geometries affect the hydrophobicity of the surface of stainless steel electrodes?* Surface texturing geometry is decisive: line textures induce anisotropic wetting (differences up to 32 % between orientations), while grid textures provide isotropic wetting but are sensitive to fluence, with excessive remelting reducing hydrophobicity.

3. *Can laser surface texturing improve the adhesion of catalytic coatings to stainless steel electrodes?* Laser surface texturing did not consistently improve the adhesion of cobalt hydroxide coatings, as line textures showed partial improvements (grades 2–3), but grid

textures provided poor results, and coating deposition was most homogeneous on untreated surfaces.

11 Further studies

The results obtained in this thesis are limited by the low number of specimens and restricted parameter sets, meaning that the findings represent an experimental-level exploration rather than fully validated outcomes. To strengthen the reliability of the conclusions, further studies should be conducted with multiple repetitions for each parameter set to provide statistically significant evidence of reproducibility.

Additional analysis methods could be employed to achieve a deeper understanding of the laser–material interactions. For example, complementary surface characterization using atomic force microscopy (AFM), focused ion beam scanning electron microscopy (FIB-SEM) cross-sections, or XPS would allow more detailed correlation between micro- and nanoscale surface morphology, surface chemistry, and wettability. Extending the contact angle measurements over longer time intervals and under controlled environmental conditions (e.g., air, deionised water, or saline solutions) would provide insight into the temporal stability of the hydrophobic state, as earlier studies have shown that wettability can evolve over days or weeks after laser texturing.

Functional performance tests are another important direction. Corrosion resistance under saline exposure and wear resistance under mechanical abrasion should be systematically evaluated, as literature indicates that laser texturing alone may not always provide protection in different environments. In addition, anti-icing tests, droplet mobility and hysteresis measurements would allow the functional implications of the textures to be assessed beyond static contact angle data.

Further process development should also include a more systematic parametric study of fluence, pulse frequency, and fill pitch. The present results already suggest that excessive remelting and smoothing at high fluence can reduce air entrapment in grid patterns, consistent with earlier reports. Expanding this parameter space would enable identification of optimal regimes for stable Cassie–Baxter wetting states.

Finally, comparative studies with alternative surface modification techniques, such as sandblasting, chemical etching, or coating deposition (e.g., silane or CFx layers), either individually or in combination with laser texturing, would be valuable. These comparisons would not only benchmark the performance of laser-based methods against conventional techniques but also identify potential hybrid strategies for achieving durable and application-specific hydrophobic surfaces.

References

[1] W. Pfleging, “Recent progress in laser texturing of battery materials: a review of tuning electrochemical performances, related material development, and prospects for large-scale manufacturing,” *Int. J. Extreme Manuf.*, vol. 3, no. 1, p. 012002, Dec. 2020, doi: 10.1088/2631-7990/abca84.

[2] B. Rego De Vasconcelos and J.-M. Lavoie, “Recent Advances in Power-to-X Technology for the Production of Fuels and Chemicals,” *Front. Chem.*, vol. 7, p. 392, Jun. 2019, doi: 10.3389/fchem.2019.00392.

[3] F. V. Vázquez *et al.*, “Power-to-X technology using renewable electricity and carbon dioxide from ambient air: SOLETAIR proof-of-concept and improved process concept,” *J. CO2 Util.*, vol. 28, pp. 235–246, Dec. 2018, doi: 10.1016/j.jcou.2018.09.026.

[4] D. Givirovskaia *et al.*, “Efficient water splitting with a MOF-74(Ni)-derived composite electrocatalyst prepared via microwave- and laser-assisted synthesis,” *Nano Res.*, vol. 18, no. 2, p. 94907100, Feb. 2025, doi: 10.26599/NR.2025.94907100.

[5] M. Genovese, A. Schlüter, E. Scionti, F. Piraino, O. Corigliano, and P. Fragiacomo, “Power-to-hydrogen and hydrogen-to-X energy systems for the industry of the future in Europe,” *Int. J. Hydrog. Energy*, vol. 48, no. 44, pp. 16545–16568, May 2023, doi: 10.1016/j.ijhydene.2023.01.194.

[6] I. Garagounis, A. Vourros, D. Stoukides, D. Dasopoulos, and M. Stoukides, “Electrochemical Synthesis of Ammonia: Recent Efforts and Future Outlook,” *Membranes*, vol. 9, no. 9, p. 112, Aug. 2019, doi: 10.3390/membranes9090112.

[7] D. Ding, M. Liu, and M. Liu, “Enhancing SOFC Electrode Performance Through Surface Modification,” *ECS Trans.*, vol. 57, no. 1, pp. 1801–1810, Oct. 2013, doi: 10.1149/05701.1801ecst.

[8] P. Blanck, D. Schmider, R. J. Kee, J. Dailly, and O. Deutschmann, “Microstructural optimizations of an iron-containing electrode for electrochemical ammonia synthesis on a proton-conducting ceramic membrane,” *Ceram. Int.*, p. S0272884225022825, Jun. 2025, doi: 10.1016/j.ceramint.2025.05.149.

[9] S. Giddey, S. P. S. Badwal, and A. Kulkarni, “Review of electrochemical ammonia production technologies and materials,” *Int. J. Hydrog. Energy*, vol. 38, no. 34, pp. 14576–14594, Nov. 2013, doi: 10.1016/j.ijhydene.2013.09.054.

[10] R. B. Smith and M. Z. Bazant, “Multiphase Porous Electrode Theory,” *J. Electrochem. Soc.*, vol. 164, no. 11, pp. E3291–E3310, 2017, doi: 10.1149/2.0171711jes.

[11] D. Kim *et al.*, “Manipulating wettability of catalytic surface for improving ammonia production from electrochemical nitrogen reduction,” *J. Colloid Interface Sci.*, vol. 633, pp. 53–59, Mar. 2023, doi: 10.1016/j.jcis.2022.11.052.

[12] M. Danish, “Contact Angle Studies of Hydrophobic and Hydrophilic Surfaces,” in *Handbook of Magnetic Hybrid Nanoalloys and their Nanocomposites*, S. Thomas and A. Rezazadeh Nochehdehi, Eds., Cham: Springer International Publishing, 2022, pp. 761–782. doi: 10.1007/978-3-030-90948-2_24.

[13] A. B. D. Cassie and S. Baxter, “Wettability of porous surfaces,” *Trans. Faraday Soc.*, vol. 40, p. 546, 1944, doi: 10.1039/tf9444000546.

[14] Shubhava, A. Jayarama, G. K. Kannarpady, S. Kale, S. Prabhu, and R. Pinto, “Chemical etching of glasses in hydrofluoric Acid: A brief review,” *Mater. Today Proc.*, vol. 55, pp. 46–51, 2022, doi: 10.1016/j.matpr.2021.12.110.

[15] M. Yu, X. Zeng, Q. Song, L. Liu, and J. Li, “Examining regeneration technologies for etching solutions: a critical analysis of the characteristics and potentials,” *J. Clean. Prod.*, vol. 113, pp. 973–980, Feb. 2016, doi: 10.1016/j.jclepro.2015.10.131.

[16] Y.-H. Chang *et al.*, “Improvement of the inter-electrode reproducibility of screen-printed carbon electrodes by oxygen plasma etching and an image color level method for quality control,” *Mater. Sci. Eng. C*, vol. 31, no. 7, pp. 1265–1270, Oct. 2011, doi: 10.1016/j.msec.2011.01.001.

[17] K. Artur, R. Norbert, O. Łukasz, P. Jacek, S. Marcin, and B. Jozef, “Laser Surface Texturing: Characteristics and Applications,” *Syst. Saf. Hum. - Tech. Facil. - Environ.*, vol. 5, no. 1, pp. 240–248, Dec. 2023, doi: 10.2478/czoto-2023-0026.
[18] J. P. Davim, Ed., *Laser in manufacturing*. London: ISTE, 2012.
[19] A. Peethan, V. K. Unnikrishnan, S. Chidangil, and S. D. George, “Laser-Assisted Tailoring of Surface Wettability - Fundamentals and Applications: A Critical Review,” *Rev. Adhes. Adhes.*, vol. 7, no. 4, pp. 331–366, Dec. 2019, doi: 10.7569/RAA.2019.097312.
[20] S. N. Grigoriev, M. A. Volosova, and A. A. Okunkova, “Advances in Laser Materials Processing,” *Metals*, vol. 12, no. 6, p. 917, May 2022, doi: 10.3390/met12060917.
[21] Market Report Analytics, “Laser Surface Texturing and Patterning Market – Global Forecast 2023–2028,” Market Report Analytics, Apr. 2025. [Online]. Available: https://www.marketreportanalytics.com/reports/laser-surface-texturing-and-patterning-76449
[22] J. Yang, J. Pan, and S. Du, “Understanding Surface/Interface-Induced Chemical and Physical Properties at Atomic Level by First Principles Investigations,” *WIREs Comput. Mol. Sci.*, vol. 15, no. 3, p. e70030, May 2025, doi: 10.1002/wcms.70030.
[23] R. S. McDonald, “Surface Functionality of Amorphous Silica by Infrared Spectroscopy,” *J. Phys. Chem.*, vol. 62, no. 10, pp. 1168–1178, Oct. 1958, doi: 10.1021/j150568a004.
[24] *Photoactive Inorganic Nanoparticles*. Elsevier, 2019. doi: 10.1016/C2017-0-01254-5.
[25] L. Tang, P. Thevenot, and W. Hu, “Surface Chemistry Influences Implant Biocompatibility,” *Curr. Top. Med. Chem.*, vol. 8, no. 4, pp. 270–280, Mar. 2008, doi: 10.2174/156802608783790901.
[26] G.-H. Yan *et al.*, “Effects of carbon dots surface functionalities on cellular behaviors – Mechanistic exploration for opportunities in manipulating uptake and translocation,” *Colloids Surf. B Biointerfaces*, vol. 181, pp. 48–57, Sep. 2019, doi: 10.1016/j.colsurfb.2019.05.027.
[27] F. Arena, G. Mezzatesta, G. Zafarana, G. Trunfio, F. Frusteri, and L. Spadaro, “Effects of oxide carriers on surface functionality and process performance of the Cu–ZnO system in the synthesis of methanol via CO2 hydrogenation,” *J. Catal.*, vol. 300, pp. 141–151, Apr. 2013, doi: 10.1016/j.jcat.2012.12.019.
[28] C. Liu, Z. Jin, H. Zhao, and L. Wang, “Triple-action smart nanocontainers enhanced protective coatings with superior active and passive properties,” *Prog. Org. Coat.*, vol. 148, p. 105887, Nov. 2020, doi: 10.1016/j.porgcoat.2020.105887.
[29] M. Rocca, T. S. Rahman, and L. Vattuone, Eds., *Springer Handbook of Surface Science*. in Springer Handbooks. Cham: Springer International Publishing, 2020. doi: 10.1007/978-3-030-46906-1.
[30] M. Kutz, Ed., *Mechanical Engineers’ Handbook: Materials and Mechanical Design*, 1st ed. Wiley, 2005. doi: 10.1002/0471777447.
[31] C. Wu, P. Selvaraj, Y. Tsai, C. Huang, C. Sun, and K. Cheng, “Stimuli-Responsive Smart Glass with Switchable Unidirectional Light Source for Enhanced Privacy/Indoor Illumination,” *Adv. Opt. Mater.*, vol. 13, no. 8, p. 2403088, Mar. 2025, doi: 10.1002/adom.202403088.
[32] S. K. Sethi and G. Manik, “Recent Progress in Super Hydrophobic/Hydrophilic Self-Cleaning Surfaces for Various Industrial Applications: A Review,” *Polym.-Plast. Technol. Eng.*, vol. 57, no. 18, pp. 1932–1952, Dec. 2018, doi: 10.1080/03602559.2018.1447128.
[33] K. Kato, “Wear in relation to friction — a review,” *Wear*, vol. 241, no. 2, pp. 151–157, Jul. 2000, doi: 10.1016/S0043-1648(00)00382-3.
[34] L. Wu *et al.*, “Optical Functional Materials Inspired by Biology,” *Adv. Opt. Mater.*, vol. 4, no. 2, pp. 195–224, Feb. 2016, doi: 10.1002/adom.201500428.
[35] K. Yuan *et al.*, “Engineering the Thermal Conductivity of Functional Phase-Change Materials for Heat Energy Conversion, Storage, and Utilization,” *Adv. Funct. Mater.*, vol. 30, no. 8, p. 1904228, Feb. 2020, doi: 10.1002/adfm.201904228.
[36] P.-Y. Chen, J. McKittrick, and M. A. Meyers, “Biological materials: Functional adaptations and bioinspired designs,” *Prog. Mater. Sci.*, vol. 57, no. 8, pp. 1492–1704, Nov. 2012, doi: 10.1016/j.pmatsci.2012.03.001.
[37] G. Ding, X. Yu, F. Dong, Z. Ji, and J. Wang, “Using Silane Coupling Agent Coating on Acidic Aggregate Surfaces to Enhance the Adhesion between Asphalt and Aggregate: A Molecular

Dynamics Simulation," *Materials*, vol. 13, no. 23, p. 5580, Dec. 2020, doi: 10.3390/ma13235580.
[38] L. Zhang *et al.*, "Transparent hydrophilic-oleophobic waterborne coating for multifunctional applications," *Prog. Org. Coat.*, vol. 191, p. 108454, Jun. 2024, doi: 10.1016/j.porgcoat.2024.108454.
[39] J. F. Mano, "Stimuli-Responsive Polymeric Systems for Biomedical Applications," *Adv. Eng. Mater.*, vol. 10, no. 6, pp. 515–527, Jun. 2008, doi: 10.1002/adem.200700355.
[40] P. M. Martin and P. Martin, *Introduction to surface engineering and functionally engineered materials*. Salem, Mass: Scrivener, 2011.
[41] F. Saubade *et al.*, "Principal Component Analysis to Determine the Surface Properties That Influence the Self-Cleaning Action of Hydrophobic Plant Leaves," *Langmuir*, vol. 37, no. 27, pp. 8177–8189, Jul. 2021, doi: 10.1021/acs.langmuir.1c00853.
[42] B. Fubini, "Surface Chemistry and Quartz Hazard," *Ann. Occup. Hyg.*, vol. 42, no. 8, pp. 521–530, Nov. 1998, doi: 10.1016/S0003-4878(98)00066-0.
[43] N. Parhizkar, T. Shahrabi, and B. Ramezanzadeh, "A new approach for enhancement of the corrosion protection properties and interfacial adhesion bonds between the epoxy coating and steel substrate through surface treatment by covalently modified amino functionalized graphene oxide film," *Corros. Sci.*, vol. 123, pp. 55–75, Jul. 2017, doi: 10.1016/j.corsci.2017.04.011.
[44] N. J. Shirtcliffe, G. McHale, M. I. Newton, G. Chabrol, and C. C. Perry, "Dual-Scale Roughness Produces Unusually Water-Repellent Surfaces," *Adv. Mater.*, vol. 16, no. 21, pp. 1929–1932, Nov. 2004, doi: 10.1002/adma.200400315.
[45] I. Demirci, S. Mezghani, M. Yousfi, H. Zahouani, and M. E. Mansori, "The Scale Effect of Roughness on Hydrodynamic Contact Friction," *Tribol. Trans.*, vol. 55, no. 5, pp. 705–712, Sep. 2012, doi: 10.1080/10402004.2012.694990.
[46] J. Morehead and M. Zou, "Superhydrophilic surface on Cu substrate to enhance lubricant retention," *J. Adhes. Sci. Technol.*, vol. 28, no. 8–9, pp. 833–842, Apr. 2014, doi: 10.1080/01694243.2012.697751.
[47] X. Du, B. Chen, R. Liu, and C. Li, "Research on Fractal Model of Load Distribution and Axial Stiffness of Planetary Roller Screw Mechanism Considering Surface Roughness and Friction Factor," *Adv. Theory Simul.*, vol. 5, no. 4, p. 2100399, Apr. 2022, doi: 10.1002/adts.202100399.
[48] X. Mei, L. Zhang, and Y. Zhu, "Investigation into the effect of the aspect ratio of cylindrical surface microstructure on von Willebrand factor damage," *Int. J. Artif. Organs*, vol. 45, no. 3, pp. 322–330, Mar. 2022, doi: 10.1177/03913988211070309.
[49] S. Hajimirza, G. El Hitti, A. Heltzel, and J. Howell, "Specification of Micro-Nanoscale Radiative Patterns Using Inverse Analysis for Increasing Solar Panel Efficiency," *J. Heat Transf.*, vol. 134, no. 10, p. 102702, Oct. 2012, doi: 10.1115/1.4006209.
[50] A. Urrutia, P. J. Rivero, J. Goicoechea, and F. J. Arregui, "Micro/nanodeposition techniques for enhanced optical fiber sensors," in *Handbook of Nanomaterials for Sensing Applications*, Elsevier, 2021, pp. 531–573. doi: 10.1016/B978-0-12-820783-3.00018-X.
[51] Y. S. Lin and S. G. Deng, "Sol-gel preparation of nanostructured adsorbents," in *Studies in Surface Science and Catalysis*, vol. 120, Elsevier, 1999, pp. 653–686. doi: 10.1016/S0167-2991(99)80568-0.
[52] M. Patel, S. Ahn, and W.-G. Koh, "Topographical pattern for neuronal tissue engineering," *J. Ind. Eng. Chem.*, vol. 114, pp. 19–32, Oct. 2022, doi: 10.1016/j.jiec.2022.07.006.
[53] L. Cheng *et al.*, "A review on the wettability and residual stress of AMB AlN/metal joints," *Mater. Sci. Semicond. Process.*, vol. 174, p. 108181, May 2024, doi: 10.1016/j.mssp.2024.108181.
[54] K. Kendall, "Adhesion: Molecules and Mechanics," *Science*, vol. 263, no. 5154, pp. 1720–1725, Mar. 1994, doi: 10.1126/science.263.5154.1720.
[55] L.-M. Berger, "Coatings by Thermal Spray," in *Comprehensive Hard Materials*, Elsevier, 2014, pp. 471–506. doi: 10.1016/B978-0-08-096527-7.00017-9.
[56] T. Wan, B. Wang, Q. Han, J. Chen, B. Li, and S. Wei, "A review of superhydrophobic shape-memory polymers: Preparation, activation, and applications," *Appl. Mater. Today*, vol. 29, p. 101665, Dec. 2022, doi: 10.1016/j.apmt.2022.101665.

[57] A. Chivate and C. Zhou, “Additive manufacturing of micropatterned functional surfaces: a review,” *Int. J. Extreme Manuf.*, vol. 6, no. 4, p. 042004, Aug. 2024, doi: 10.1088/2631-7990/ad4240.

[58] L. Wen, J. C. Weaver, and G. V. Lauder, “Biomimetic shark skin: design, fabrication and hydrodynamic function,” *J. Exp. Biol.*, vol. 217, no. 10, pp. 1656–1666, May 2014, doi: 10.1242/jeb.097097.

[59] L. Zhang, J. Wu, M. N. Hedhili, X. Yang, and P. Wang, “Inkjet printing for direct micropatterning of a superhydrophobic surface: toward biomimetic fog harvesting surfaces,” *J. Mater. Chem. A*, vol. 3, no. 6, pp. 2844–2852, 2015, doi: 10.1039/C4TA05862C.

[60] L. Wu *et al.*, “Printing Patterned Fine 3D Structures by Manipulating the Three Phase Contact Line,” *Adv. Funct. Mater.*, vol. 25, no. 15, pp. 2237–2242, Apr. 2015, doi: 10.1002/adfm.201404559.

[61] T. Young, “III. An essay on the cohesion of fluids,” *Philos. Trans. R. Soc. Lond.*, vol. 95, pp. 65–87, Dec. 1805, doi: 10.1098/rstl.1805.0005.

[62] R. N. Wenzel, “RESISTANCE OF SOLID SURFACES TO WETTING BY WATER,” *Ind. Eng. Chem.*, vol. 28, no. 8, pp. 988–994, Aug. 1936, doi: 10.1021/ie50320a024.

[63] I. Rea, P. Giardina, S. Longobardi, and L. De Stefano, “Protein-modified porous silicon films for biomedical applications,” in *Porous Silicon for Biomedical Applications*, Elsevier, 2014, pp. 104–128. doi: 10.1533/9780857097156.1.104.

[64] G. I. Mantanis and R. A. Young, “Wetting of wood,” *Wood Sci. Technol.*, vol. 31, no. 5, pp. 339–353, Oct. 1997, doi: 10.1007/BF01159153.

[65] N. Eustathopoulos, M. G. Nicholas, and B. Drevet, *Wettability at high temperatures*, 1st ed. in Pergamon materials series, no. v. 3. Amsterdam New York: Pergamon, 1999.

[66] J. W. Gibbs and J. W. Gibbs, “The scientific papers of J. Willard Gibbs. 1: Thermodynamics,” Repr., Woodbridge, Conn: Ox Bow Pr, 1970.

[67] P. M. Hansson, A. Swerin, J. Schoelkopf, P. A. C. Gane, and E. Thormann, “Influence of Surface Topography on the Interactions between Nanostructured Hydrophobic Surfaces,” *Langmuir*, vol. 28, no. 21, pp. 8026–8034, May 2012, doi: 10.1021/la300628m.

[68] Y. G. Bushuev, “Effects of Size and Porosity on the Hydrophobicity of Hierarchical Nanoparticles,” *Nano Lett.*, vol. 25, no. 8, pp. 3351–3356, Feb. 2025, doi: 10.1021/acs.nanolett.5c00058.

[69] Y. Yoon, D. Kim, and J.-B. Lee, “Hierarchical micro/nano structures for super-hydrophobic surfaces and super-lyophobic surface against liquid metal,” *Micro Nano Syst. Lett.*, vol. 2, no. 1, p. 3, Dec. 2014, doi: 10.1186/s40486-014-0003-x.

[70] J. Long *et al.*, “Cassie-State Stability of Metallic Superhydrophobic Surfaces with Various Micro/Nanostructures Produced by a Femtosecond Laser,” *Langmuir*, vol. 32, no. 4, pp. 1065–1072, Feb. 2016, doi: 10.1021/acs.langmuir.5b04329.

[71] E. J. De Souza, L. Gao, T. J. McCarthy, E. Arzt, and A. J. Crosby, “Effect of Contact Angle Hysteresis on the Measurement of Capillary Forces,” *Langmuir*, vol. 24, no. 4, pp. 1391–1396, Feb. 2008, doi: 10.1021/la702188t.

[72] A. Nakajima, “Design of a Transparent Hydrophobic Coating,” *J. Ceram. Soc. Jpn.*, vol. 112, no. 1310, pp. 533–540, 2004, doi: 10.2109/jcersj.112.533.

[73] G. McHale, N. J. Shirtcliffe, and M. I. Newton, “Contact-Angle Hysteresis on Super-Hydrophobic Surfaces,” *Langmuir*, vol. 20, no. 23, pp. 10146–10149, Nov. 2004, doi: 10.1021/la0486584.

[74] C. W. Extrand, “Model for Contact Angles and Hysteresis on Rough and Ultraphobic Surfaces,” *Langmuir*, vol. 18, no. 21, pp. 7991–7999, Oct. 2002, doi: 10.1021/la025769z.

[75] M. Nosonovsky and B. Bhushan, “Hierarchical roughness optimization for biomimetic superhydrophobic surfaces,” *Ultramicroscopy*, vol. 107, no. 10–11, pp. 969–979, Oct. 2007, doi: 10.1016/j.ultramic.2007.04.011.

[76] A. Shastri, P. M. Gore, and B. Kandasubramanian, “Engineering superhydrophobicity: a survey of coating techniques for silicone-based oil–water separation membranes,” *Environ. Sci. Pollut. Res.*, vol. 31, no. 29, pp. 41854–41872, Jun. 2024, doi: 10.1007/s11356-024-33686-z.

[77] C. G. L. Furmidge, “Studies at phase interfaces. I. The sliding of liquid drops on solid surfaces and a theory for spray retention,” *J. Colloid Sci.*, vol. 17, no. 4, pp. 309–324, Apr. 1962, doi: 10.1016/0095-8522(62)90011-9.

[78] C. W. Extrand and Y. Kumagai, “Liquid Drops on an Inclined Plane: The Relation between Contact Angles, Drop Shape, and Retentive Force,” *J. Colloid Interface Sci.*, vol. 170, no. 2, pp. 515–521, Mar. 1995, doi: 10.1006/jcis.1995.1130.

[79] B. He, J. Lee, and N. A. Patankar, “Contact angle hysteresis on rough hydrophobic surfaces,” *Colloids Surf. Physicochem. Eng. Asp.*, vol. 248, no. 1–3, pp. 101–104, Nov. 2004, doi: 10.1016/j.colsurfa.2004.09.006.

[80] *Surface Modification of Metals and Alloys*. MDPI, 2021. doi: 10.3390/books978-3-0365-1011-8.

[81] K. A. Whitehead and J. Verran, “The Effect of Surface Topography on the Retention of Microorganisms,” *Food Bioprod. Process.*, vol. 84, no. 4, pp. 253–259, Dec. 2006, doi: 10.1205/fbp06035.

[82] M. Rosentritt, S. Schneider-Feyrer, and L. Kurzendorfer, “Comparison of surface roughness parameters Ra/Sa and Rz/Sz with different measuring devices,” *J. Mech. Behav. Biomed. Mater.*, vol. 150, p. 106349, Feb. 2024, doi: 10.1016/j.jmbbm.2023.106349.

[83] K. J. Kubiak, M. C. T. Wilson, T. G. Mathia, and Ph. Carval, “Wettability versus roughness of engineering surfaces,” *Wear*, vol. 271, no. 3–4, pp. 523–528, Jun. 2011, doi: 10.1016/j.wear.2010.03.029.

[84] H. S. Rabbani, B. Zhao, R. Juanes, and N. Shokri, “Pore geometry control of apparent wetting in porous media,” *Sci. Rep.*, vol. 8, no. 1, p. 15729, Oct. 2018, doi: 10.1038/s41598-018-34146-8.

[85] W. Fang, H.-Y. Guo, B. Li, Q. Li, and X.-Q. Feng, “Revisiting the Critical Condition for the Cassie–Wenzel Transition on Micropillar-Structured Surfaces,” *Langmuir*, vol. 34, no. 13, pp. 3838–3844, Apr. 2018, doi: 10.1021/acs.langmuir.8b00121.

[86] F. Bernardoni and A. Y. Fadeev, “Adsorption and wetting characterization of hydrophobic SBA-15 silicas,” *J. Colloid Interface Sci.*, vol. 356, no. 2, pp. 690–698, Apr. 2011, doi: 10.1016/j.jcis.2011.01.033.

[87] R. N. Wenzel, “RESISTANCE OF SOLID SURFACES TO WETTING BY WATER,” *Ind. Eng. Chem.*, vol. 28, no. 8, pp. 988–994, Aug. 1936, doi: 10.1021/ie50320a024.

[88] D. E. Smith and A. D. J. Haymet, “Free energy, entropy, and internal energy of hydrophobic interactions: Computer simulations,” *J. Chem. Phys.*, vol. 98, no. 8, pp. 6445–6454, Apr. 1993, doi: 10.1063/1.464809.

[89] B. Kronberg, “The hydrophobic effect,” *Curr. Opin. Colloid Interface Sci.*, vol. 22, pp. 14–22, Apr. 2016, doi: 10.1016/j.cocis.2016.02.001.

[90] J. Chang, X. He, Z. Yang, X. Bai, and C. Yuan, “Effects of chemical composition on the hydrophobicity and antifouling performance of epoxy-based self-stratifying nanocomposite coatings,” *Prog. Org. Coat.*, vol. 167, p. 106827, Jun. 2022, doi: 10.1016/j.porgcoat.2022.106827.

[91] B.-Y. Wang, C. K. Tseng, C.-M. Shih, Y.-L. Pai, H.-P. Kuo, and S. J. Lue, “Polytetrafluoroethylene (PTFE)/silane cross-linked sulfonated poly(styrene–ethylene/butylene–styrene) (sSEBS) composite membrane for direct alcohol and formic acid fuel cells,” *J. Membr. Sci.*, vol. 464, pp. 43–54, Aug. 2014, doi: 10.1016/j.memsci.2014.03.076.

[92] S. Lopez De Armentia, M. Pantoja, J. Abenojar, and M. A. Martinez, “Development of Silane-Based Coatings with Zirconia Nanoparticles Combining Wetting, Tribological, and Aesthetical Properties,” *Coatings*, vol. 8, no. 10, p. 368, Oct. 2018, doi: 10.3390/coatings8100368.

[93] G. Xie *et al.*, “Light- and Electric-Field-Controlled Wetting Behavior in Nanochannels for Regulating Nanoconfined Mass Transport,” *J. Am. Chem. Soc.*, vol. 140, no. 13, pp. 4552–4559, Apr. 2018, doi: 10.1021/jacs.7b13136.

[94] Z. Zhu *et al.*, “Tunable Surface Wettability via Terahertz Electrowave Controlled Vicinal Subnanoscale Water Layer,” *Nano Lett.*, vol. 24, no. 10, pp. 3243–3248, Mar. 2024, doi: 10.1021/acs.nanolett.4c00248.

[95] J. Bonse, S. Hohm, S. V. Kirner, A. Rosenfeld, and J. Kruger, "Laser-Induced Periodic Surface Structures— A Scientific Evergreen," *IEEE J. Sel. Top. Quantum Electron.*, vol. 23, no. 3, p. 7581030, May 2017, doi: 10.1109/JSTQE.2016.2614183.
[96] G. Hu, Y. Song, and Y. Guan, "Tailoring metallic surface properties induced by laser surface processing for industrial applications," *Nanotechnol. Precis. Eng.*, vol. 2, no. 1, pp. 29–34, Mar. 2019, doi: 10.1016/j.npe.2019.03.003.
[97] S. Banik, R. Indhu, N. Arunachalam, and M. S. R. Rao, "Femtosecond laser-induced surface structuring for improved surface characteristics of single crystal diamond," *Diam. Relat. Mater.*, vol. 154, p. 112240, Apr. 2025, doi: 10.1016/j.diamond.2025.112240.
[98] Y. Cai, J. Aslam, J. Xue, Q. Song, H. Ma, and Z. Liu, "Enhancement of tribological performance with Laser surface texturing: A review," *Proc. Inst. Mech. Eng. Part J J. Eng. Tribol.*, p. 13506501251330449, Apr. 2025, doi: 10.1177/13506501251330449.
[99] I. Etsion, "Improving Tribological Performance of Mechanical Components by Laser Surface Texturing".
[100] D. Bäuerle, "Laser-Induced Chemical Reactions," in *Chemical Processing with Lasers*, vol. 1, in Springer Series in Materials Science, vol. 1. , Berlin, Heidelberg: Springer Berlin Heidelberg, 1986, pp. 36–57. doi: 10.1007/978-3-662-02505-5_3.
[101] F. Piscitelli, R. De Palo, and A. Volpe, "Enhancing Coating Adhesion on Fibre-Reinforced Composite by Femtosecond Laser Texturing," *Coatings*, vol. 13, no. 5, p. 928, May 2023, doi: 10.3390/coatings13050928.
[102] C. H. Lau *et al.*, "The effect of functionalization on structure and electrical conductivity of multi-walled carbon nanotubes," *J. Nanoparticle Res.*, vol. 10, no. S1, pp. 77–88, Dec. 2008, doi: 10.1007/s11051-008-9376-1.
[103] Y. Aono, A. Hirata, and H. Tokura, "Non-textured laser modification of silica glass surface: Wettability control and flow channel formation," *Appl. Surf. Sci.*, vol. 371, pp. 530–537, May 2016, doi: 10.1016/j.apsusc.2016.03.040.
[104] P. Van Assenbergh, E. Meinders, J. Geraedts, and D. Dodou, "Nanostructure and Microstructure Fabrication: From Desired Properties to Suitable Processes," *Small*, vol. 14, no. 20, p. 1703401, May 2018, doi: 10.1002/smll.201703401.
[105] T. D. B. Jacobs, L. Pastewka, and Guest Editors, "Surface topography as a material parameter," *MRS Bull.*, vol. 47, no. 12, pp. 1205–1210, Dec. 2022, doi: 10.1557/s43577-022-00465-5.
[106] W. A. Weyl, "SURFACE STRUCTURE AND SURFACE PROPERTIES OF CRYSTALS AND GLASSES*," *J. Am. Ceram. Soc.*, vol. 32, no. 11, pp. 367–374, Nov. 1949, doi: 10.1111/j.1151-2916.1949.tb18915.x.
[107] D. S. Gnanamuthu, "Laser Surface Treatment," *Opt. Eng.*, vol. 19, no. 5, Oct. 1980, doi: 10.1117/12.7972604.
[108] Y. Bouraoui, L. Rathmann, C. Niehaves, M. Mikulewitsch, A. Fischer, and T. Radel, "Material removal in laser chemical processing with modulated laser power," *J. Laser Appl.*, vol. 36, no. 1, p. 012013, Feb. 2024, doi: 10.2351/7.0001109.
[109] G. Saccone and N. Favaloro, "Dust Mitigation Strategies Enabling Moon Exploration Missions," *Aerotec. Missili Spaz.*, vol. 104, no. 3, pp. 233–246, Jun. 2025, doi: 10.1007/s42496-024-00225-5.
[110] D. Moskal, J. Martan, and M. Honner, "Scanning Strategies in Laser Surface Texturing: A Review," *Micromachines*, vol. 14, no. 6, p. 1241, Jun. 2023, doi: 10.3390/mi14061241.
[111] A. Riveiro, A. L. B. Maçon, J. Del Val, R. Comesaña, and J. Pou, "Laser Surface Texturing of Polymers for Biomedical Applications," *Front. Phys.*, vol. 6, p. 16, Feb. 2018, doi: 10.3389/fphy.2018.00016.
[112] G. Lin *et al.*, "Enhanced wear resistance of laser cladded WC-Ni composite coatings by picosecond laser surface texturing," *Tribol. Int.*, vol. 204, p. 110517, Apr. 2025, doi: 10.1016/j.triboint.2025.110517.
[113] B. Stolz and R. Poprawe, "Surface conductivity modification of ceramics with laser radiation," *Surf. Coat. Technol.*, vol. 112, no. 1–3, pp. 394–400, Feb. 1999, doi: 10.1016/S0257-8972(98)00739-7.
[114] V. Tunakova, Z. Hrubosova, M. Tunak, M. Kasparova, and J. Mullerova, "Laser surface modification of electrically conductive fabrics: Material performance improvement and design

effects," *Opt. Laser Technol.*, vol. 98, pp. 178–189, Jan. 2018, doi: 10.1016/j.optlastec.2017.07.017.
[115] D. Shiffman, "Pixels," in *Learning Processing*, Elsevier, 2015, pp. 3–17. doi: 10.1016/B978-0-12-394443-6.50001-9.
[116] B. Toukoniitty, J.-P. Mikkola, D. Yu. Murzin, and T. Salmi, "Utilization of electromagnetic and acoustic irradiation in enhancing heterogeneous catalytic reactions," *Appl. Catal. Gen.*, vol. 279, no. 1–2, pp. 1–22, Jan. 2005, doi: 10.1016/j.apcata.2004.10.044.
[117] M. Petkovšek, M. Hočevar, and P. Gregorčič, "Surface functionalization by nanosecond-laser texturing for controlling hydrodynamic cavitation dynamics," *Ultrason. Sonochem.*, vol. 67, p. 105126, Oct. 2020, doi: 10.1016/j.ultsonch.2020.105126.
[118] M. Saqib *et al.*, "Tailoring surface properties, biocompatibility and corrosion behavior of stainless steel by laser induced periodic surface treatment towards developing biomimetic stents," *Surf. Interfaces*, vol. 34, p. 102365, Nov. 2022, doi: 10.1016/j.surfin.2022.102365.
[119] D. H. Kam, S. Bhattacharya, and J. Mazumder, "Control of the wetting properties of an AISI 316L stainless steel surface by femtosecond laser-induced surface modification," *J. Micromechanics Microengineering*, vol. 22, no. 10, p. 105019, Oct. 2012, doi: 10.1088/0960-1317/22/10/105019.
[120] M. Rafieazad, J. A. Jaffer, C. Cui, X. Duan, and A. Nasiri, "Nanosecond Laser Fabrication of Hydrophobic Stainless Steel Surfaces: The Impact on Microstructure and Corrosion Resistance," *Materials*, vol. 11, no. 9, p. 1577, Sep. 2018, doi: 10.3390/ma11091577.
[121] P. Gregorčič, M. Conradi, L. Hribar, and M. Hočevar, "Long-Term Influence of Laser-Processing Parameters on (Super)hydrophobicity Development and Stability of Stainless-Steel Surfaces," *Materials*, vol. 11, no. 11, p. 2240, Nov. 2018, doi: 10.3390/ma11112240.
[122] V. J. Rico *et al.*, "Hydrophobicity, Freezing Delay, and Morphology of Laser-Treated Aluminum Surfaces," *Langmuir*, vol. 35, no. 19, pp. 6483–6491, May 2019, doi: 10.1021/acs.langmuir.9b00457.
[123] G. Dongre, A. Rajurkar, R. Raut, and S. Jangam, "Preparation of super-hydrophobic textures by using nanosecond pulsed laser," *Mater. Today Proc.*, vol. 42, pp. 1145–1151, 2021, doi: 10.1016/j.matpr.2020.12.497.
[124] W.-S. Chu, M. M. Shehroze, N. G. Tran, T. Dinh, S.-T. Hong, and D.-M. Chun, "Green Fabrication of Superhydrophobic Surfaces Using Laser Surface Texturing Without Toxic Chemicals: A Review," *Int. J. Precis. Eng. Manuf.*, vol. 25, no. 5, pp. 1101–1123, May 2024, doi: 10.1007/s12541-024-00962-4.
[125] C. Yang, X. Mei, Y. Tian, D. Zhang, Y. Li, and X. Liu, "Modification of wettability property of titanium by laser texturing," *Int. J. Adv. Manuf. Technol.*, vol. 87, no. 5–8, pp. 1663–1670, Nov. 2016, doi: 10.1007/s00170-016-8601-9.
[126] W. F. Furter, Ed., *A century of chemical engineering: edited by William F. Furter*. New York: Plenum Press, 1982.
[127] W. F. Furter and American Chemical Society, Eds., *A Century of chemical engineering*. New York: Plenum Press, 1982.
[128] N. Pernicone, "Wustite as a new precursor of industrial ammonia synthesis catalysts," *Appl. Catal. Gen.*, vol. 251, no. 1, pp. 121–129, Sep. 2003, doi: 10.1016/S0926-860X(03)00313-2.
[129] The Royal Society, "Ammonia: Zero-carbon Fertiliser, Fuel and Energy Store," London, 2020.
[130] "Green ammonia synthesis," *Nat. Synth.*, vol. 2, no. 7, pp. 581–582, Jun. 2023, doi: 10.1038/s44160-023-00362-y.
[131] V. Kyriakou, I. Garagounis, E. Vasileiou, A. Vourros, and M. Stoukides, "Progress in the Electrochemical Synthesis of Ammonia," *Catal. Today*, vol. 286, pp. 2–13, May 2017, doi: 10.1016/j.cattod.2016.06.014.
[132] M. Appl, "The Haber-Bosch Heritage: The Ammonia Production Technology," presented at the 50th Anniversary of the IFA Technical Conference, Sevilla, Spain, Sep. 1997.
[133] H. Shen *et al.*, "Electrochemical ammonia synthesis: Mechanistic understanding and catalyst design," *Chem*, vol. 7, no. 7, pp. 1708–1754, Jul. 2021, doi: 10.1016/j.chempr.2021.01.009.
[134] J. Kim, S. Sengodan, S. Kim, O. Kwon, Y. Bu, and G. Kim, "Proton conducting oxides: A review of materials and applications for renewable energy conversion and storage," *Renew. Sustain. Energy Rev.*, vol. 109, pp. 606–618, Jul. 2019, doi: 10.1016/j.rser.2019.04.042.

[135] M. H. Pishbin, A. R. Mohammadi, and M. Nasri, “Optimisation of Manufacturing Parameters for an Ni–Ag Fuel Cell Electrode,” *Fuel Cells*, vol. 7, no. 4, pp. 291–297, Aug. 2007, doi: 10.1002/fuce.200600027.
[136] X. Yang *et al.*, “Enzyme-Mimetic Single-Atom Catalyst Design for Green Ammonia Synthesis,” *Adv. Energy Mater.*, p. 2501867, Jun. 2025, doi: 10.1002/aenm.202501867.
[137] A. Lal, H. Porat, A. Dutta, M. K. Yadav, and A. Borenstein, “Laser-Induced HKUST-1 Derived Porous Electrocatalyst: an Innovative Approach to Boost Sustainable Ammonia Synthesis,” *Adv. Sustain. Syst.*, p. e00441, Jun. 2025, doi: 10.1002/adsu.202500441.
[138] J. H. Montoya, C. Tsai, A. Vojvodic, and J. K. Nørskov, “The Challenge of Electrochemical Ammonia Synthesis: A New Perspective on the Role of Nitrogen Scaling Relations,” *ChemSusChem*, vol. 8, no. 13, pp. 2180–2186, Jul. 2015, doi: 10.1002/cssc.201500322.
[139] K. Li *et al.*, “Increasing Current Density of Li-Mediated Ammonia Synthesis with High Surface Area Copper Electrodes,” *ACS Energy Lett.*, vol. 7, no. 1, pp. 36–41, Jan. 2022, doi: 10.1021/acsenergylett.1c02104.
[140] X. Wang, J. Yin, J. Xu, H. Wang, and G. Ma, “Chemical Stability, Ionic Conductivity of $BaCe_{0.9-x}Zr_xSm_{0.10}O_{3-\alpha}$ and Its Application to Ammonia Synthesis at Atmospheric Pressure,” *Chin. J. Chem.*, vol. 29, no. 6, pp. 1114–1118, Jun. 2011, doi: 10.1002/cjoc.201190209.
[141] G. A. Somorjai and N. Materer, “Surface structures in ammonia synthesis,” *Top. Catal.*, vol. 1, no. 3–4, pp. 215–231, Sep. 1994, doi: 10.1007/BF01492277.
[142] K. S. Yin and M. Venugopalan, “Plasma chemical synthesis. I. Effect of electrode material on the synthesis of ammonia,” *Plasma Chem. Plasma Process.*, vol. 3, no. 3, pp. 343–350, Sep. 1983, doi: 10.1007/BF00564632.
[143] M. Iwamoto, M. Akiyama, K. Aihara, and T. Deguchi, “Ammonia Synthesis on Wool-Like Au, Pt, Pd, Ag, or Cu Electrode Catalysts in Nonthermal Atmospheric-Pressure Plasma of N_2 and H_2,” *ACS Catal.*, vol. 7, no. 10, pp. 6924–6929, Oct. 2017, doi: 10.1021/acscatal.7b01624.
[144] L. Zhao, Y. Peng, P. Dou, Y. Li, T. He, and F. Ran, “Surface chemistry of electrode materials toward improving electrolyte-wettability: A method review,” *InfoMat*, vol. 6, no. 11, p. e12597, Nov. 2024, doi: 10.1002/inf2.12597.
[145] K. Wang, X. Li, and J. Chen, “Surface and Interface Engineering of Electrode Materials for Lithium-Ion Batteries,” *Adv. Mater.*, vol. 27, no. 3, pp. 527–545, Jan. 2015, doi: 10.1002/adma.201402962.
[146] J. Bai, W. Wang, and J. Liu, “Bioinspired Hydrophobicity for Enhancing Electrochemical CO_2 Reduction,” *Chem. – Eur. J.*, vol. 29, no. 68, p. e202302461, Dec. 2023, doi: 10.1002/chem.202302461.
[147] J. Lin, S. Yan, C. Zhang, Q. Hu, and Z. Cheng, “Hydrophobic Electrode Design for CO_2 Electroreduction in a Microchannel Reactor,” *ACS Appl. Mater. Interfaces*, vol. 14, no. 6, pp. 8623–8632, Feb. 2022, doi: 10.1021/acsami.1c23744.
[148] L. Dong *et al.*, “Insights into hydrophobicity-tuned catalyst microenvironment in gas diffusion electrode for boosting CO_2 electrolysis,” *AIChE J.*, vol. 70, no. 6, p. e18408, Jun. 2024, doi: 10.1002/aic.18408.
[149] H. Shen *et al.*, “Electrochemical ammonia synthesis: Mechanistic understanding and catalyst design,” *Chem*, vol. 7, no. 7, pp. 1708–1754, Jul. 2021, doi: 10.1016/j.chempr.2021.01.009.
[150] G. S. Avcioglu, B. Ficicilar, and I. Eroglu, “Improved PEM fuel cell performance with hydrophobic catalyst layers,” *Int. J. Hydrog. Energy*, vol. 43, no. 40, pp. 18632–18641, Oct. 2018, doi: 10.1016/j.ijhydene.2018.03.045.
[151] L. L. Faulkner and A. J. Bard, *Electrochemical methods and applications*, 2nd ed. New Yor: Wiley, 2001.
[152] L. Li *et al.*, “Overcoming Gas Mass Transfer Limitations Using Gas-Conducting Electrodes for Efficient Nitrogen Reduction,” *ACS Nano*, vol. 19, no. 1, pp. 1080–1089, Jan. 2025, doi: 10.1021/acsnano.4c12909.
[153] H. He *et al.*, “Hydrophobicity Tailoring of Ferric Covalent Organic Framework/MXene Nanosheets for High-Efficiency Nitrogen Electroreduction to Ammonia,” *Adv. Sci.*, vol. 10, no. 15, p. 2206933, May 2023, doi: 10.1002/advs.202206933.

[154] X. Xiong *et al.*, “Washing effects on electrochemical performance and storage characteristics of LiNi0.8Co0.1Mn0.1O2 as cathode material for lithium-ion batteries,” *J. Power Sources*, vol. 222, pp. 318–325, Jan. 2013, doi: 10.1016/j.jpowsour.2012.08.029.
[155] Z. Zhao *et al.*, “Engineering Reaction Pathway to Harmonize the Competition between NRR and HER for Efficient Photocatalytic Ammonia Synthesis,” *ACS Catal.*, vol. 14, no. 15, pp. 11626–11634, Aug. 2024, doi: 10.1021/acscatal.4c02430.
[156] M. Goldman *et al.*, “Novel Front Contacts for Hydrophobic Gas Diffusion Layers Enable High Energy Efficiency and Durability for Electrochemical CO $_2$ Reduction to C $_{2+}$ Products.,” *ECS Meet. Abstr.*, vol. MA2024-02, no. 62, pp. 4234–4234, Nov. 2024, doi: 10.1149/MA2024-02624234mtgabs.
[157] G. C. Sarti, C. Gostoli, and S. Matulli, “Low energy cost desalination processes using hydrophobic membranes,” *Desalination*, vol. 56, pp. 277–286, Jan. 1985, doi: 10.1016/0011-9164(85)85031-1.
[158] V. Vediyappan *et al.*, “Pressurized water electrolysis using hydrophobic gas diffusion layer with a new electrolyzer cell structure,” *Solid State Ion.*, vol. 416, p. 116678, Nov. 2024, doi: 10.1016/j.ssi.2024.116678.
[159] M. Jouny, W. Luc, and F. Jiao, “High-rate electroreduction of carbon monoxide to multi-carbon products,” *Nat. Catal.*, vol. 1, no. 10, pp. 748–755, Aug. 2018, doi: 10.1038/s41929-018-0133-2.
[160] L. Li *et al.*, “High-Rate Alkaline Water Electrolysis at Industrially Relevant Conditions Enabled by Superaerophobic Electrode Assembly,” *Adv. Sci.*, vol. 10, no. 4, p. 2206180, Feb. 2023, doi: 10.1002/advs.202206180.
[161] A. M. Helmenstine, “Aqueous Solution Definition in Chemistry,” ThoughtCo. [Online]. Available: thoughtco.com/definition-of-aqueous-solution-604370
[162] M. Wang *et al.*, “High-performance and durable cathode catalyst layer with hydrophobic C@PTFE particles for low-Pt loading membrane assembly electrode of PEMFC,” *Energy Convers. Manag.*, vol. 191, pp. 132–140, Jul. 2019, doi: 10.1016/j.enconman.2019.04.014.
[163] S. Khorsand, K. Raeissi, and F. Ashrafizadeh, “Corrosion resistance and long-term durability of super-hydrophobic nickel film prepared by electrodeposition process,” *Appl. Surf. Sci.*, vol. 305, pp. 498–505, Jun. 2014, doi: 10.1016/j.apsusc.2014.03.123.
[164] H. Shen *et al.*, “Electrochemical ammonia synthesis: Mechanistic understanding and catalyst design,” *Chem*, vol. 7, no. 7, pp. 1708–1754, Jul. 2021, doi: 10.1016/j.chempr.2021.01.009.
[165] J. Hong *et al.*, “Plasma Catalytic Synthesis of Ammonia Using Functionalized-Carbon Coatings in an Atmospheric-Pressure Non-equilibrium Discharge,” *Plasma Chem. Plasma Process.*, vol. 36, no. 4, pp. 917–940, Jul. 2016, doi: 10.1007/s11090-016-9711-8.
[166] I. Ielo *et al.*, “Nanostructured Surface Finishing and Coatings: Functional Properties and Applications,” *Materials*, vol. 14, no. 11, p. 2733, May 2021, doi: 10.3390/ma14112733.
[167] J.-K. Lee, “Substrate Effect on the Microstructure and Electrochemical Properties in the Deposition of a Thin Film LiCoO[sub 2] Electrode,” *Electrochem. Solid-State Lett.*, vol. 2, no. 10, p. 512, 1999, doi: 10.1149/1.1390887.
[168] Q. Li, X. Chen, and Y. Yang, “Biomass-Derived Nitrogen-Doped Porous Carbon for Highly Efficient Ambient Electro-Synthesis of NH3,” *Catalysts*, vol. 10, no. 3, p. 353, Mar. 2020, doi: 10.3390/catal10030353.
[169] Z.-Y. Wu *et al.*, “Electrochemical ammonia synthesis via nitrate reduction on Fe single atom catalyst,” *Nat. Commun.*, vol. 12, no. 1, p. 2870, May 2021, doi: 10.1038/s41467-021-23115-x.
[170] X. Lv, C. Weng, and Z. Yuan, “Ambient Ammonia Electrosynthesis: Current Status, Challenges, and Perspectives,” *ChemSusChem*, vol. 13, no. 12, pp. 3061–3078, Jun. 2020, doi: 10.1002/cssc.202000670.
[171] W. Chang, A. Jain, F. Rezaie, and K. Manthiram, “Lithium-mediated nitrogen reduction to ammonia via the catalytic solid–electrolyte interphase,” *Nat. Catal.*, vol. 7, no. 3, pp. 231–241, Mar. 2024, doi: 10.1038/s41929-024-01115-6.
[172] Y.-Y. Lou *et al.*, “Phase-dependent Electrocatalytic Nitrate Reduction to Ammonia on Janus Cu@Ni Tandem Catalyst,” *ACS Catal.*, vol. 14, no. 7, pp. 5098–5108, Apr. 2024, doi: 10.1021/acscatal.4c00479.

[173] Y. Wang *et al.*, “Crystal Phase Engineering of Ultrathin Alloy Nanostructures for Highly Efficient Electroreduction of Nitrate to Ammonia,” *Adv. Mater.*, vol. 36, no. 14, p. 2313548, Apr. 2024, doi: 10.1002/adma.202313548.
[174] P. Shende, P. Kasture, and R. S. Gaud, “Nanoflowers: the future trend of nanotechnology for multi-applications,” *Artif. Cells Nanomedicine Biotechnol.*, vol. 46, no. sup1, pp. 413–422, Oct. 2018, doi: 10.1080/21691401.2018.1428812.
[175] C. Guo, L. Shen, Y. Tang, F. Ciucci, and Z. Tang, “Cu Nanowires Encapsulated by ZIF67 for Efficient Ammonia Electrosynthesis from Nitrate,” *ChemSusChem*, vol. 18, no. 8, p. e202401418, Apr. 2025, doi: 10.1002/cssc.202401418.
[176] Q. Yan, R. Zhao, L. Yu, Z. Zhao, L. Liu, and J. Xi, “Enhancing Compatibility of Two-Step Tandem Catalytic Nitrate Reduction to Ammonia Over P-Cu/Co(OH) $_2$,” *Adv. Mater.*, vol. 36, no. 45, p. 2408680, Nov. 2024, doi: 10.1002/adma.202408680.
[177] H. Li, Y. Lin, J. Duan, Q. Wen, Y. Liu, and T. Zhai, “Stability of electrocatalytic OER: from principle to application,” *Chem. Soc. Rev.*, vol. 53, no. 21, pp. 10709–10740, 2024, doi: 10.1039/D3CS00010A.
[178] Y. Wu *et al.*, “Thiol Ligand-Modified Au for Highly Efficient Electroreduction of Nitrate to Ammonia,” *Precis. Chem.*, vol. 2, no. 3, pp. 112–119, Mar. 2024, doi: 10.1021/prechem.3c00107.
[179] L. Peng *et al.*, “Stabilizing the Unstable: Chromium Coating on NiMo Electrode for Enhanced Stability in Intermittent Water Electrolysis,” *ACS Appl. Mater. Interfaces*, vol. 14, no. 36, pp. 40822–40833, Sep. 2022, doi: 10.1021/acsami.2c09004.
[180] T. D. Singewald *et al.*, “Systematic variation of inorganic additives and their impact on interfacial delamination processes of automotive coating systems,” *Prog. Org. Coat.*, vol. 173, p. 107172, Dec. 2022, doi: 10.1016/j.porgcoat.2022.107172.
[181] M. Shirkhanzadeh and M. Azadegan, “Formation of carbonate apatite on calcium phosphate coatings containing silver ions,” *J. Mater. Sci. Mater. Med.*, vol. 9, no. 7, pp. 385–391, Jul. 1998, doi: 10.1023/A:1013231529439.
[182] J. W. Martin, “Methodologies for predicting the service lives of coating systems,” 1998.
[183] J. Xu *et al.*, “Enhancement of ammonia corrosion resistance of coatings through improving dispersion and binding site of graphene oxide in silane coatings,” *J. Alloys Compd.*, vol. 989, p. 174174, Jun. 2024, doi: 10.1016/j.jallcom.2024.174174.
[184] C.-C. Huang, Y.-J. Huang, H.-S. Wang, F.-G. Tseng, and Y.-C. Su, “A well-dispersed catalyst on porous silicon micro-reformer for enhancing adhesion in the catalyst-coating process,” *Int. J. Hydrog. Energy*, vol. 39, no. 15, pp. 7753–7764, May 2014, doi: 10.1016/j.ijhydene.2014.03.029.
[185] A. Emblem and M. Hardwidge, “Adhesives for packaging,” in *Packaging Technology*, Elsevier, 2012, pp. 381–394. doi: 10.1533/9780857095701.2.381.
[186] H. Weiss, “Adhesion of advanced overlay coatings: mechanisms and quantitative assessment,” *Surf. Coat. Technol.*, vol. 71, no. 2, pp. 201–207, Mar. 1995, doi: 10.1016/0257-8972(94)01022-B.
[187] X. Zou *et al.*, “Laser surface treatment to enhance the adhesive bonding between steel and CFRP: Effect of laser spot overlapping and pulse fluence,” *Opt. Laser Technol.*, vol. 159, p. 109002, Apr. 2023, doi: 10.1016/j.optlastec.2022.109002.
[188] M. Suermann, T. Gimpel, L. V. Bühre, W. Schade, B. Bensmann, and R. Hanke-Rauschenbach, “Femtosecond laser-induced surface structuring of the porous transport layers in proton exchange membrane water electrolysis,” *J. Mater. Chem. A*, vol. 8, no. 9, pp. 4898–4910, 2020, doi: 10.1039/C9TA12127G.
[189] R. Kromer *et al.*, “Laser surface patterning to enhance adhesion of plasma sprayed coatings,” *Surf. Coat. Technol.*, vol. 278, pp. 171–182, Sep. 2015, doi: 10.1016/j.surfcoat.2015.07.022.
[190] Y. A. Albrimi, A. Eddib, J. Douch, Y. Berghoute, M. Hamdani, and R. M. Souto, “Electrochemical Behaviour of AISI 316 Austenitic Stainless Steel in Acidic Media Containing Chloride Ions,” *Int. J. Electrochem. Sci.*, vol. 6, no. 10, pp. 4614–4627, Oct. 2011, doi: 10.1016/S1452-3981(23)18352-0.

[191] J. Snitzer and X. Lou, “Sensitization of 316L Stainless Steel made by Laser Powder Bed Fusion Additive Manufacturing,” *Corrosion*, vol. 79, no. 2, pp. 240–251, Feb. 2023, doi: 10.5006/4241.
[192] S. Ravi-Kumar, B. Lies, X. Zhang, H. Lyu, and H. Qin, “Laser ablation of polymers: a review,” *Polym. Int.*, vol. 68, no. 8, pp. 1391–1401, Aug. 2019, doi: 10.1002/pi.5834.
[193] D. Gunes and B. Karagoz, “Synthesis of Core–Shell Polyborosiloxanes as a Heat-Resistant Platform,” *ACS Omega*, vol. 7, no. 48, pp. 43877–43882, Dec. 2022, doi: 10.1021/acsomega.2c05056.
[194] S. Tardio, M.-L. Abel, R. H. Carr, J. E. Castle, and J. F. Watts, “Comparative study of the native oxide on 316L stainless steel by XPS and ToF-SIMS,” *J. Vac. Sci. Technol. Vac. Surf. Films*, vol. 33, no. 5, p. 05E122, Sep. 2015, doi: 10.1116/1.4927319.

Appendices

Appendix 1 Preliminary testing parameters

Table 5 Nanosecond pulsed laser parameters used in preliminary testing of surface texturing. Highlighted rows show the chosen parameters sets for further experiments.

Sample	Power (W)	Pulse width (s)	Pulse frequency (kHz)	Scanning speed (mm/s)	Pattern	Fill pitch (mm)	Repetition times
1	20	1.00E-09	100	1500	grid	0.4	1
2	20	1.00E-09	100	1500	grid	0.4	3
3	20	1.00E-09	100	1500	grid	0.4	5
4	40	1.00E-09	100	1500	grid	0.4	1
5	40	1.00E-09	100	1500	grid	0.4	3
6	40	1.00E-09	85	1500	grid	0.4	1
7	40	1.00E-09	85	1500	grid	0.4	2
8	20	1.00E-09	100	1500	grid	0.2	1
9	20	1.00E-09	100	1500	grid	0.2	3
10	20	1.00E-09	100	1500	grid	0.2	5
11	10	1.00E-07	20	1500	grid	0.02	3
12	10	1.00E-07	20	1500	grid	0.02	5
13	10	1.00E-07	20	1500	grid	0.02	7
14	10	1.00E-07	20	1500	grid	0.1	3
15	10	1.00E-07	20	1500	grid	0.1	5
16	10	1.00E-07	20	1500	grid	0.1	7
17	20	1.00E-08	100	2000	grid	0.04	3
18	20	1.00E-08	100	2000	grid	0.04	5
19	20	1.00E-08	100	2000	grid	0.04	7
20	30	1.00E-08	100	2000	grid	0.1	1
21	30	1.00E-08	100	2000	grid	0.1	3
22	30	1.00E-08	100	2000	grid	0.1	5
23	40	1.00E-07	100	2000	grid	0.1	1
24	40	1.00E-07	100	2000	grid	0.1	3
25	40	1.00E-07	100	2000	grid	0.1	5
26	40	1.00E-07	100	2000	grid	0.05	1
27	40	1.00E-07	100	2000	grid	0.05	3
28	40	1.00E-07	100	2000	grid	0.05	5
29	40	1.00E-07	100	2000	grid	0.02	1
30	40	1.00E-07	100	2000	grid	0.02	3

Appendix 2 Example calculation of laser fluence

The laser fluence of each chosen laser parameter are calculated as shown in Equation (8), using values in Table 4 and laser beam diameter of 60 µm.

$$F = \frac{P}{t \cdot A} = \frac{10\ W}{100\ ns \cdot \pi\ (\frac{60}{2}\mu m)^2} = 35.37\ \frac{\mathrm{J}}{\mathrm{mm}^2} \approx 35\ \frac{\mathrm{J}}{\mathrm{mm}^2} \quad (8)$$

Appendix 3 3D topography images

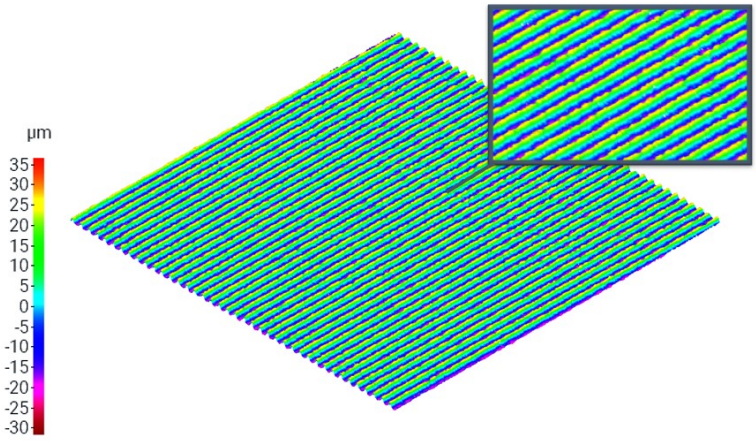

Figure 101 3D topography image of the L1 processed with line pattern and laser fluence of 35 J/mm^2 surface.

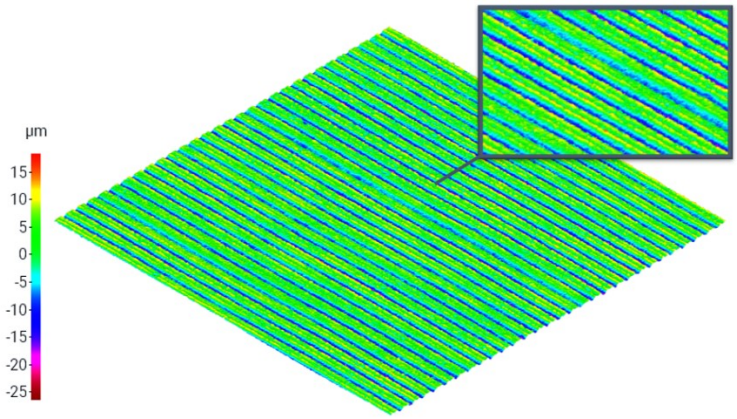

Figure 102 3D topography image of the L2 processed with line pattern and laser fluence of 141 J/mm^2 surface.

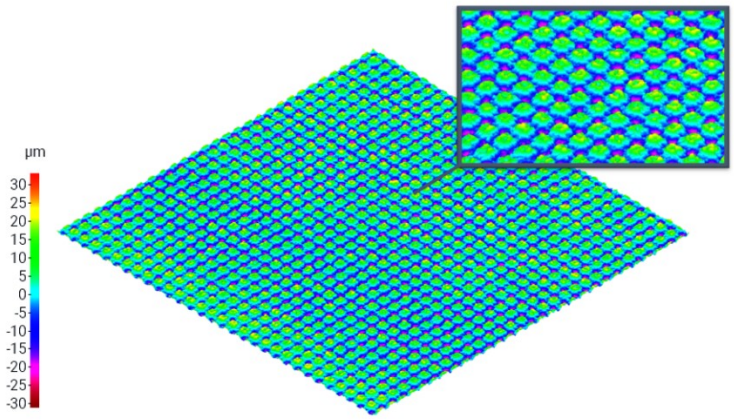

Figure 103 3D topography image of the G2 processed with grid pattern and laser fluence of 141 J/mm^2 surface.

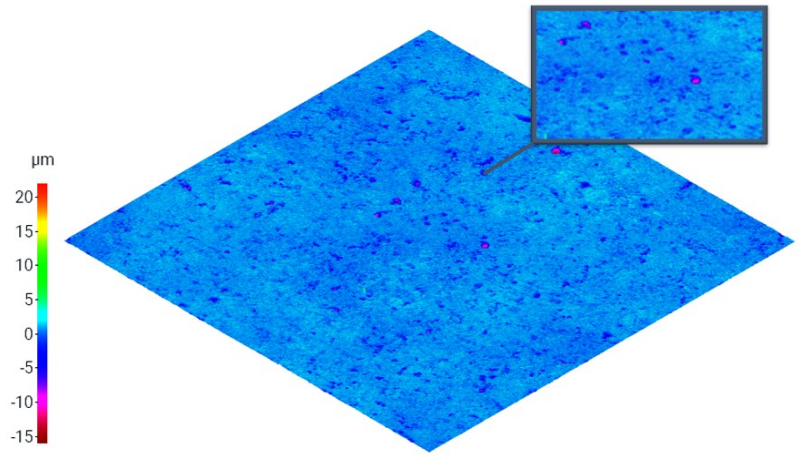

Figure 104 3D topography image of the coated non-treated reference surface.

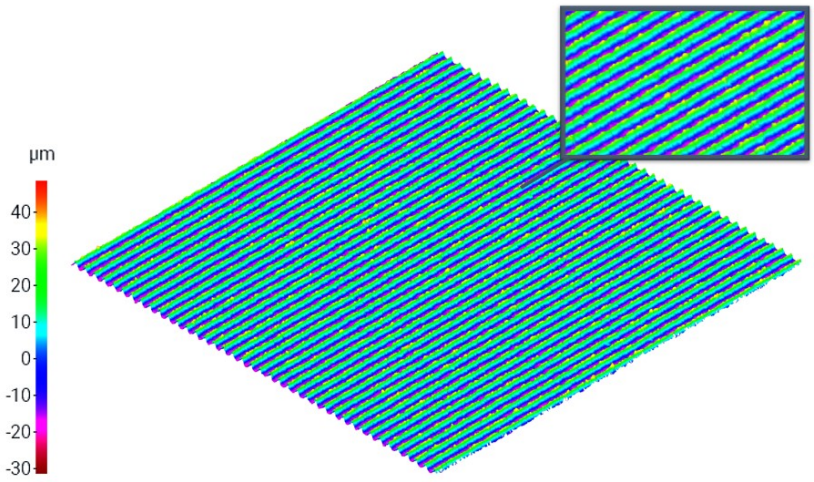

Figure 105 3D topography image of the coated L1 processed with line pattern and laser fluence of 35 J/mm^2 surface.

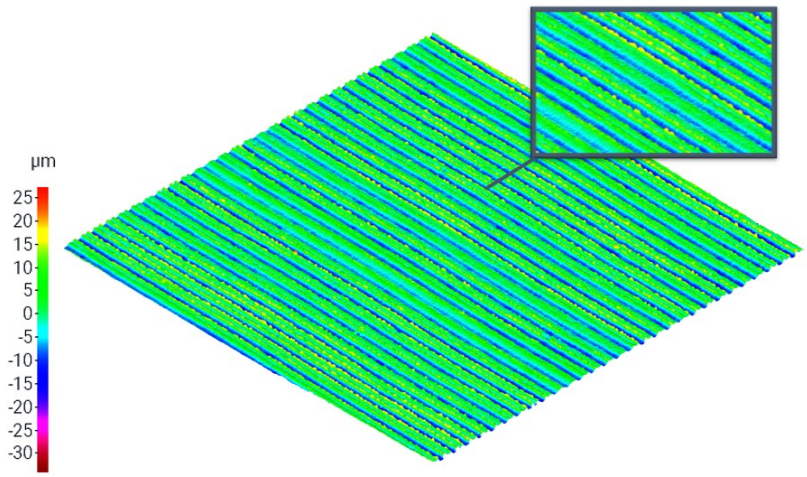

Figure 106 3D topography image of the coated L2 processed with line pattern and laser fluence of 141 J/mm^2 surface.

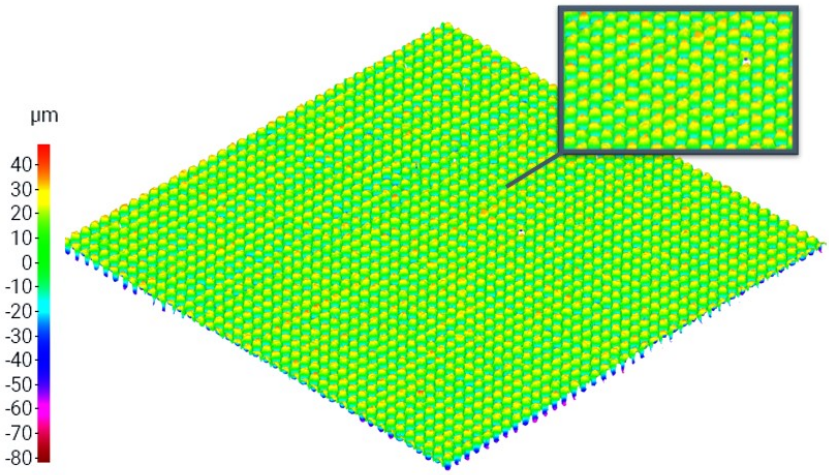

Figure 107 3D topography image of the coated G1 processed with grid pattern and laser fluence of 35 J/mm^2 surface.

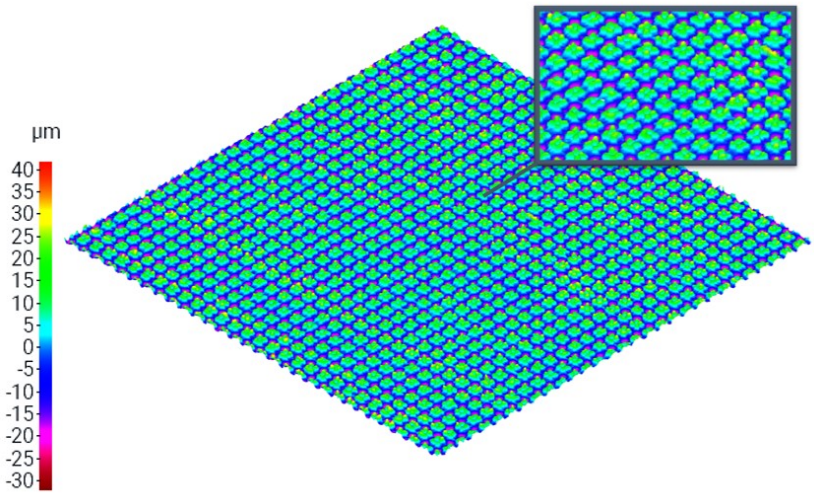

Figure 108 3D topography image of the coated G2 processed with line pattern and laser fluence of 141 J/mm^2 surface.

Appendix 4 Roughness values

Table 6 Roughness values *Sa* and *Sz* for non-treated reference surface, and for surfaces L1, L2, G1 and G2, and for coated non-treated reference surface, and for coated surfaces L1, L2, G1 and G2.

	Sa (µm)	*Sz* (µm)
REF	1.1	19.1
L1	14.3	73.4
L2	8.42	115
G1	16.4	123
G2	10.6	73.0
REF (coated)	0.600	18.8
L1 (coated)	14.6	74.6
L2 (coated)	6.60	46.5
G1 (coated)	20.5	124
G2 (coated)	11.0	86.5

Appendix 5 Contact angle values

Table 7 Measured contact angles for non-treated reference surface, and for laser textured surfaces L1, L2, G1 and G2. Surfaces with line pattern (L1 and L2) have been measured from two different orientations (P = perpendicular horizontal to laser tracks, H = horizontal to laser tracks). Measured averages for each surface is shown in table.

	Contact angle (°)				Average
REF	69.805	98.642	83.511	75.977	81.984
L1-P	104.073	116.383	82.133	117.486	105.019
L1-H	70.272	69.647	73.802	-	71.240
L2-P	120.234	130.434	125.686	103.529	119.971
L2-H	75.650	99.645	75.139	110.027	90.115
G1	119.644	142.982	136.524	142.111	135.315
G2	113.824	132.635	112.460	137.313	124.058

Table 8 Measured contact angles for coated non-treated reference surface, and for coated laser textured surfaces L1, L2, G1 and G2. Surfaces with line pattern (L1 and L2) have been measured from two different orientations (P = perpendicular horizontal to laser tracks, H = horizontal to laser tracks). Measured averages for each surface is shown in table.

	Contact angle (°)				Average
REF (coated)	45.902	47.208	38.128	33.914	41.288
L1-P (coated)	37.846	49.982	38.105	44.799	42.683
L1-H (coated)	30.577	40.561	31.201	29.606	32.986
L2-P (coated)	51.432	28.446	32.969	36.469	37.329
L2-H (coated)	23.393	39.051	21.183	29.897	28.381
G1 (coated)	52.943	31.205	52.866	38.337	43.838
G2 (coated)	-	-	-	-	-

Appendix 6 Line profiles

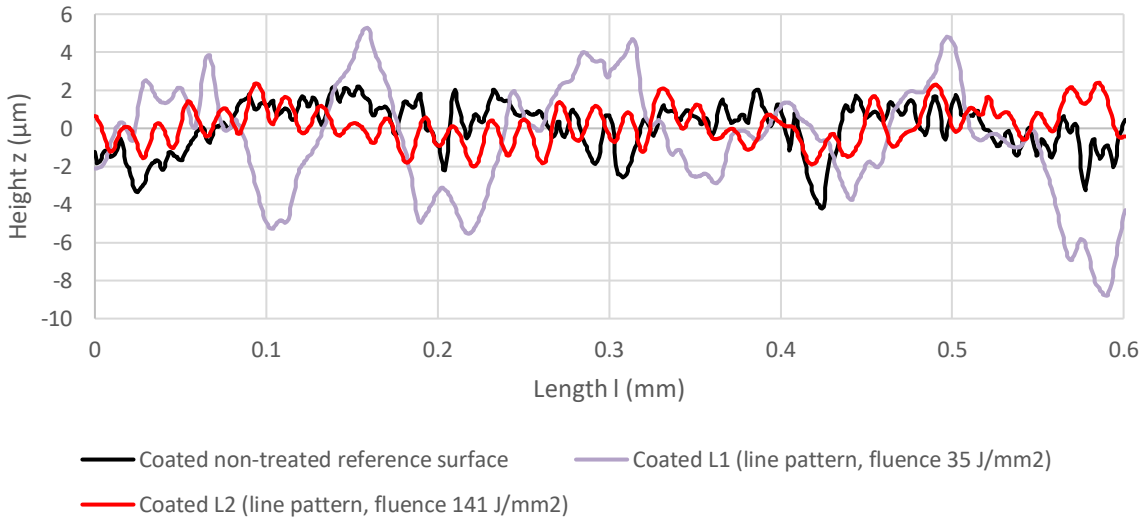

Figure 109 Line profiles along laser tracks of coated non-treated reference surface, and coated laser textured surfaces L1 and L2.

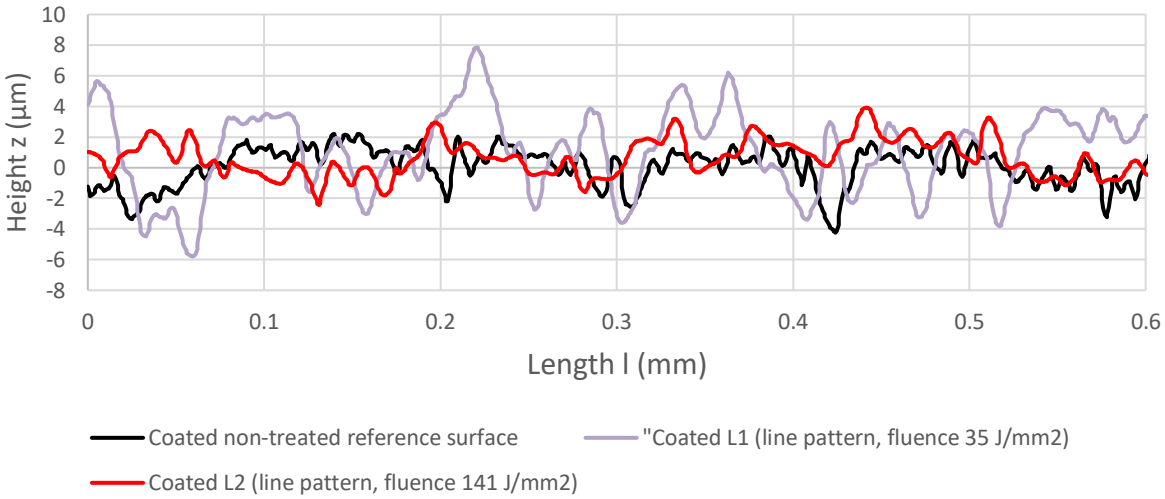

Figure 110 Line profiles between laser tracks of coated non-treated reference surface, and coated laser textured surfaces L1 and L2.

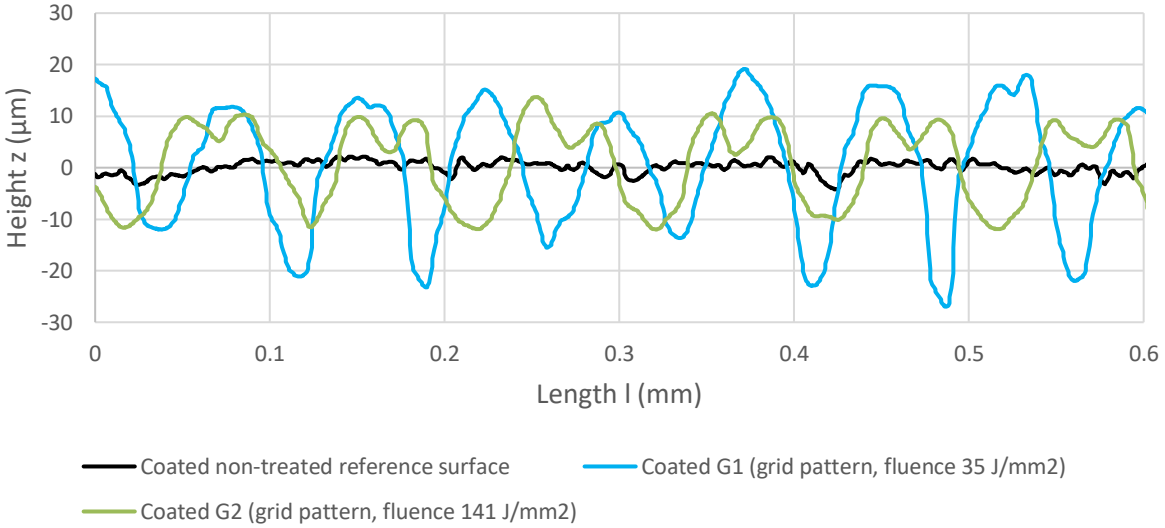

Figure 111 Line profiles between laser tracks of coated non-treated reference surface, and coated laser textured surfaces G1 and G2.